Universitatea Politehnica Timişoara
Facultatea de Electronică şi Telecomunicații

Corina-Alda Nafornița

Habilitation Thesis
Teză de Abilitare

2015

Table of contents

1. Abstract

1.1 Abstract

I have received the Ph.D. degree in Electronics and Telecommunications in 2008, from the Technical University of Cluj-Napoca, Romania. In 2003, I joined the Department of Communications at "Politehnica" University of Timisoara, where I currently hold the position of Associate Professor (since 2013). My activity is carried out in the framework of the Intelligent Signal Processing Adelaida Mateescu Research Centre, at Politehnica Univ. Timisoara. My research interests include: signal and image processing, statistical signal processing, multimedia security, watermarking, wavelets, radar signal processing.

Consequently, this thesis covers the research activities published in papers, books and book chapters in the period 2008-2014, which were performed after the PhD thesis.

My PhD thesis was written under the guidance of **Professor Monica Borda** (from Technical University of Cluj-Napoca) and **Professor Alexandru Isar** (from Politehnica University Timisoara), with the subject of *Contributions to Image watermarking in the wavelet domain*. My research efforts in the **image watermarking** field were continued, for example I have proposed using the Hyperanalytic Wavelet domain to embed the watermark, or to use turbocodes for a high degree of robustness.

I have co-authored research papers in the field of **image denoising** using the Hyperanalytic Wavelet transform in collaboration with Professor Alexandru Isar, dr. Ioana Firoiu, Professor Dorina Isar and Professor Jean-Marc Boucher (Telecom Bretagne, Brest, France).

I have co-authored a paper that presents the implementation of a new complex 2D wavelet transform, namely the **Hyperanalytic wavelet transform, (HWT)**; this was used for watermarking and denoising with a better performance than other quasi shift-invariant complex transforms. A research preoccupation was the **statistical analysis of 2D wavelet transforms** including the 2D Discrete Wavelet Transform (DWT) and the HWT.

I suggested **improving the directional selectivity** of the HWT by using H**yperanalytic Wavelet Packets Transform** (HWPT). For anisotropic images, to distinguish between preferential directions, we have proposed to use the HWPT, and on each direction the smoothness is estimated via the **Hurst exponent**.

I have improved further the **Hurst exponent estimation** techniques by applying a **LASSO based regularization** in the wavelet domain and I applied this estimation method to solve an image denoising problem where the regularity is considered to vary piecewise.

We have considered the HWT coefficients being circularly distributed, with complex Gaussian distribution. We computed a closed form for the **Kullback-Leibler divergence for the Complex Generalized Gaussian Distribution (CGGD)**.

A new method for **texture clustering** based on the information-geometry tools (barycentric distribution for each cluster) is proposed. These activities were carried out in the framework of an international research project Brancusi, funded by UEFISCDI and EGIDE,

for which I was grant director on the Romanian side. The grant director on the French side was Professor Yannick Berthoumieu, ENSEIRB MATMECA, Bordeaux, France.

Image contrast enhancement was performed for images that were exposed to non-uniform lightening, using a complex wavelet transform and a bivariate model for the coefficients. The method implies both denoising and contrast enhancement in the Double Tree Complex Wavelet Transform (DTCWT) domain.

Recently, in the framework of an European Project (FP7-ARTRAC), I have worked in the field of **RADAR signal processing**, proposing denoising to improve probability of detection for the envelope detector; as well as a method to build the range-Doppler map for multiple targets in the automotive field.

Other research activities were biomedical signal processing (electrocardiograms and magnetocardiograms signals), such as denoising, compression and wander baseline reduction. In communications we proposed methods for the reduction of the Peak-to-Average Power Ratio (PAPR) of the Orthogonal Frequency Division Multiplexing (OFDM) transmitted signal.

I am an IEEE member since 2003, reviewer for several journals and Technical Program Committee (TPC) member for prestigious international conferences. In April-June 2011 I was invited researcher at Lab. Intégration du Matériau au Système, ENSEIRB Bordeaux and in Sept-Oct. 2009 I was Invited Professor at "Lab. Intégration du Matériau au Système", Universite Bordeaux I, where I awarded an EGIDE scholarship for research (Oct. 2009).

I am currently Scientific Secretary for the Scientific Bulletin of "Politehnica" University of Timisoara, Transactions on Electronics and Communications (2006-) and I served as Publication chair for the IEEE International Symposium of Electronics and Telecommunications, editions 2014, 2012 and 2010 and member in the organizing committee for editions 2004, 2006 and 2008. In 2012 and 2014 I was also a Session Chair at the ISETC symposium. In 2002 and 2004 I received a Diploma for Excellence in Research from the Dean of the Faculty of Electronics and Telecommunications.

I was reviewer for the following journals:

- 2006 IEEE Trans. on Information Forensics and Security,
- 2007-2008, 2011-2012 IEEE Trans. on Multimedia,
- 2009-2010 IEEE Trans. on Signal Processing,
- 2010-2011, 2013 IEEE Trans. Image Processing
- 2007-2008 EURASIP Journal on Information Security,
- 2007-2010 IET Information Security,
- 2008 Research Letters in Electronics, Elsevier
- 2008 Journal of Systems and Software Elsevier,
- 2008-2013 Signal Processing Elsevier
- 2013 IET Radar, Sonar & Navigation
- 2013 Physical Communication
- Acta Technica Napocensis

I was a TPC member and reviewer for the following conferences:

- 22nd European Signal Processing Conference,EUSIPCO 2014,September 1-5, 2014,Lisbon, Portugal
- 21st European Signal Processing Conference, EUSIPCO 2013, Marrakech, Morocco, 9-13 September 2013

- 20th European Signal Processing Conference, EUSIPCO 2012, Bucharest, Romania, 27-31 August 2012
- 18th EUNICE Conference on Information and Communications Technologies EUNICE 2012, 29-31 August 2012, Budapest, Hungary
- 4th IEEE International Workshop on Information Forensics and Security, WIFS 2012, Tenerife, Spain, December 2-5, 2012

I was a reviewer for the following conferences:

- ICASSP 2014, IEEE International Conference on Acoustics, Speech, and Signal Processing,May 4-9, 2014 - Florence, Italy
- ISCAS 2014 IEEE International Symposium on Circuits and Systems, 1-5 june 2014, Melbourne, Australia
- 21st European Signal Processing Conference, EUSIPCO 2013, Marrakech, Morocco, 9-13 September 2013,
- 11-th International Symposium on Signals, Circuits and Systems, July 11-12, 2013, Iasi, Romania.
- 13th International Conference on Optimization of Electrical and Electronic Equipment OPTIM 2012, May 24-26, 2012, Brasov, Romania,
- 2nd IEEE International Conference on Information Science and Technology, ICIST 2012, 23- 25 May 2012, Wuhan, China
- IEEE International Symposium on Electronics and Telecommunications, Timisoara, November 15-16, 2012, ISETC 2012
- Statistical Signal Processing Workshop, 28-30 June 2011, Nice, France, SSP 2011
- IEEE International Symposium on Electronics and Telecommunications, November 11-12, 2010, Timisoara, ISETC 2010,
- 8-th International Symposium on Signals, Circuitsand Systems, ISSCS 2007, Iasi, July 12-13,2007

Grants (director):

- 2011-2012 - bilateral program Brancusi EGIDE/ANCS, Romanian Director, "Classification de textures fondée sur la théorie des ondelettes hyper-analytiques et les copules", French Director: Prof. Yannick Berthoumieu grant no. 510/31.03.2011, period 2011-2012, partners UPT, IPB-ENSEIRB MATMECA, funded by ANCS-UEFISCDI and EGIDE
- 2004-2006 – national grant TD, CNCSIS code 47, Digital watermarking for still images in the transform domain funding by CNCSIS

Grants (member):

- 2014- ongoing, Quality of Services Improvement for GNSS Localisation in Constraint Environment by Image Fusing Techniques (IMFUSING), Contract with European Space Agency, ESA, nr. 4000111852/14/NL/Cbi, contractor UPT, subcontractor Thales Alenia (2014)
- 2014- ongoing, SEOM SY4Sci Synergy - Ocean Virtual Laboratory (OVL), Contract with European Space Agency, ESA, nr. 4000112389/14/I-NB, contractor OceanDataLab, subcontractor UPT
- 2011-2014 – FP7 EU program, Advanced Radar Tracking and Classification for Enhanced Road Safety ARTRAC
- 2013-2014 – PC7 EU program, Advanced Radar Tracking and Classification for Enhanced Road Safety ARTRAC, funded by UEFISCDI
- 2009-2011 – national grant – The use of wavelet theory for decision making, funded by CNCSIS, ID 930, 2009-2011
- 2007-2009 – national grant, Improvement of research & development basis in the field of communications at the Faculty of Electronics and Telecommunications, Politehnica

Univ. of Timisoara, funded by ANCS, CAPACITATI PN II, 2007-2009, 77/CP/II/13.09.2007
- 2005-2007 – national grant, Performance increase of digital receptors using wavelet theory, funded by CNCSIS, code 637/A/CNCSIS
- 2004-2006 – national grant, Modern methods for image analysis and image processing, 2004-2006, funded by CNCSIS
- 2011-2012 – member of target group Doctoral School in support of research in the European context ("Scoala doctorala in sprijinul cercetarii in context european"), POSDRU program 21/1.5/G/13798 2010-2012

Scholarships:
- Oct. 2009 -EGIDE scholarship for research, LAPS, Bordeaux, France
- Sep. 2005-ECRYPT scholarship, Summer School for Multimedia Security, University of Salzburg, Austria, 21-24 Sept. 2005

Awards:
- 2012: Nominated for the Information Forensics and Security Technical Committee IEEE

1.2 Rezumat

Am primit titlul de doctor în Electronică şi Telecomunicaţii în 2008, de la Universitatea Tehnică din Cluj-Napoca, Romania. Din 2003, sunt încadrată ca şi cadru didactic şi de cercetare la Departamentul de Comunicaţii din cadrul Univ. Politehnica Timisoara, unde sunt în prezent Conferenţiar (din 2013). Activitatea mea se desfăşoară în cadrul Centrului de Cercetare de Prelucrarea Inteligentă a Semnalelor Adelaida Mateescu din cadrul aceleasi instituţii. Preocupările mele includ, dar nu sunt limitate la: prelucrarea semnalelor şi a imaginilor, prelucrarea statistică a semnalelor, securitatea multimedia, watermarking (marcare transparentă), wavelete (undişoare), prelucrarea semnalelor radar.

Prin urmare, aceasta teză cuprinde activitatea mea de cercetare publicată în lucrări, cărţi şi capitole de cărţi din perioada 2008-2014, efectuate după teza de doctorat.

Mi-am scris teza de doctorat sub îndrumarea **d-nei Profesoare Monica Borda** (de la Universitatea Tehnică din Cluj-Napoca) şi a **d-lui Profesor Alexandru Isar** (de la Universitatea Politehnica Timişoara). Aceasta a avut subiectul *Contribuţii la marcarea transparentă a imaginilor în domeniul transformatei wavelet*. Eforturile mele de cercetare în acest domeniu, al **marcării transparente a imaginilor** au continuat în mod natural şi după teză, de exemplu, am propus folosirea domeniul transformatei wavelet hiperanalitice pentru inserarea marcajului, sau folosirea turbocodurilor, pentru creşterea robusteţii marcajului.

Sunt autor şi co-autor al unor lucrări ştiinţifice în domeniul **eliminării zgomotului din imagini** folosind transformata mai sus menţionată, transformata wavelet hiperanalitică, în colaborare cu dl. Profesor Alexandru Isar, dr. Ioana Firoiu, d-na Profesor Dorina Isar şi dl. Profesor Jean-Marc Boucher (Telecom Bretagne, Brest, France).

Sunt co-autor al unei lucrări care prezintă implementarea unei noi transformate wavelet 2D complexe, şi anume **transformata wavelet, (HWT)**; aceasta a fost folosită cu succes în marcarea transparenta şi eliminarea zgomotului în imagini, cu performanţă superioară comparativ cu alte transformate complexe cvasi-invariante la translaţii. O preocupare de cercetare a fost de asemenea **analiza statistică a transformatelor wavelet 2D** incluzand transformata wavelet discreta bidimensională (DWT) precum şi HWT.

Am propus **îmbunătăţirea selectivităţii directionale** a transformarii HWT folosind transformata **Hyperanalytic Wavelet Packets Transform** (HWPT). Pentru a distinge intre direcţii preferenţiale în imagini anisotropice, am propus folosirea HWPT, şi pe fiecare direcţie se estimează regularitatea (netezimea) folosind **exponentul Hurst**.

În continuare, am imbunătăţit tehnicile de **estimare a exponentului Hurst**, aplicând o tehnică de regularizare bazată pe **LASSO** în domeniul wavelet şi am aplicat această metodă de estimare pentru rezolvarea unei probleme de eliminare a zgomotului din imagini, unde regularitatea variază pe porţiuni.

Am considerat coeficienţii HWT ca fiind distribuiţi circular conform cu distribuţia complexă Gaussiană generalizată. Am calculat o formă explicită pentru **divergenţa Kullback-Leibler în cazul distribuţiei complexe Gaussiene generalizate (CGGD)**.

Am propus o noua metodă de **clasificare a texturilor** bazată pe distribuţia baricentrică pentru fiecare grup sau cluster. Aceste activităţi s-au desfăşurat în cadrul grantului internaţional de cercetare Brâncusi, finanţat de UEFISCDI şi EGIDE, la care am fost director pe partea Română. Directorul de grant pe partea Franceză a fost d-l. Profesor Yannick Berthoumieu, ENSEIRB MATMECA, Bordeaux, Franţa.

Îmbunătăţirea contrastului în imagini a fost făcută pentru imagini expuse la iluminare neuniformă, folosind o transformată wavelet complexă, şi un model bivariat pentru coeficienţi. Metoda implică folosirea a două tehnici deodată şi anume, îmbunătăţirea contrastului precum şi eliminarea zgomotului în domeniul transformatei wavelet complexe cu arbore dublu (DTCWT).

Recent, în cadrul unui grant European de tip FP7 (FP7-ARTRAC), am lucrat în domeniul **prelucrării semnalelor radar**, şi am propus folosirea tehnicii de denoising pentru a îmbunătăţi probabilitatea de detecţie a detectorului de anvelopă; de asemenea am propus o metodă de construire a matricii distanţă-Doppler pentru ţinte multiple în domeniul automotiv.

Alte preocupări au fost prelucrarea semnalelor biomedicale (electrocardiograme şi magnetocardiograme), cum ar fi eliminarea zgomotului, compresie şi corecţie a abaterii liniei de bază (liniei izoelectrice). În telecomunicaţii am propus metode de reducere a raportului Peak-to-Average Power Ratio (PAPR) al semnalului transmis folosind OFDM (multiplexare cu diviziune în frecvenţă şi subpurtătoare ortogonale).

Sunt membru IEEE din 2003, recenzor la mai multe reviste, membru în comitetul tehnic (TPC) al unor conferinţe internaţionale foarte prestigioase. În perioada Aprilie-Iunie 2011, am fost invitată ca şi cercetător la Laboratorul Intégration du Matériau au Système, ENSEIRB Bordeaux iar în perioada Sept-Oct. 2009 am fost Profesor Invitat la "Lab. Intégration du Matériau au Système", Universite Bordeaux I, unde mi s-a acordat o bursă de cercetare EGIDE (Oct. 2009).

Sunt secretar ştiinţific al Buletinului Stiinţific al Universitaţii "Politehnica" din Timisoara, Seria Electronica şi Telecomunicaţii (2006-) şi am fost Publication chair pentru Simpozionul desfăsurat la Timisoara, IEEE International Symposium of Electronics and Telecommunications, ediţiile 2014, 2012 şi 2010, respectiv membru în comitetul de organizare pentru ediţiile 2004, 2006 şi 2008. În 2012 şi 2014 am fost de asemenea Session Chair la simpozionul ISETC. In 2002 şi 2004 am primit Diploma de Excelenţă în Cercetare de la Decanul Facultaţii de Electronică şi Telecomunicaţii.

Am fost recenzor pentru următoarele reviste:

- 2006 IEEE Trans. on Information Forensics and Security,
- 2007-2008, 2011-2012 IEEE Trans. on Multimedia,
- 2009-2010 IEEE Trans. on Signal Processing,
- 2010-2011, 2013 IEEE Trans. Image Processing
- 2007-2008 EURASIP Journal on Information Security,
- 2007-2010 IET Information Security,
- 2008 Research Letters in Electronics, Elsevier
- 2008 Journal of Systems and Software Elsevier,
- 2008-2013 Signal Processing Elsevier
- 2013 IET Radar, Sonar & Navigation
- 2013 Physical Communication
- Acta Technica Napocensis

Am fost membru în comitetul tehnic şi recenzor pentru următoarele conferinţe:

- 22nd European Signal Processing Conference,EUSIPCO 2014,September 1-5, 2014,Lisbon, Portugal
- 21st European Signal Processing Conference, EUSIPCO 2013, Marrakech, Morocco, 9-13 September 2013
- 20th European Signal Processing Conference, EUSIPCO 2012, Bucharest, Romania, 27-31 August 2012
- 18th EUNICE Conference on Information and Communications Technologies EUNICE 2012, 29-31 August 2012, Budapest, Hungary
- 4th IEEE International Workshop on Information Forensics and Security, WIFS 2012, Tenerife, Spain, December 2-5, 2012

Am fost recenzor pentru următoarele conferinţe:

- ICASSP 2014, IEEE International Conference on Acoustics, Speech, and Signal Processing,May 4-9, 2014 - Florence, Italy
- ISCAS 2014 IEEE International Symposium on Circuits and Systems, 1-5 june 2014, Melbourne, Australia
- 21st European Signal Processing Conference, EUSIPCO 2013, Marrakech, Morocco, 9-13 September 2013,
- 11-th International Symposium on Signals, Circuits and Systems, July 11-12, 2013, Iasi, Romania.
- 13th International Conference on Optimization of Electrical and Electronic Equipment OPTIM 2012, May 24-26, 2012, Brasov, Romania,
- 2nd IEEE International Conference on Information Science and Technology, ICIST 2012, 23- 25 May 2012, Wuhan, China
- IEEE International Symposium on Electronics and Telecommunications, Timisoara, November 15-16, 2012, ISETC 2012
- Statistical Signal Processing Workshop, 28-30 June 2011, Nice, France, SSP 2011
- IEEE International Symposium on Electronics and Telecommunications, November 11-12, 2010, Timisoara, ISETC 2010,
- 8-th International Symposium on Signals, Circuitsand Systems, ISSCS 2007, Iasi, July 12-13,2007

Granturi (director):

- 2011-2012 - program bilateral Brancusi EGIDE/ANCS, Director pe partea Română, "Classification de textures fondée sur la théorie des ondelettes hyper-analytiques et les copules", Director pe partea Franceză: Prof. Yannick Berthoumieu grant no. 510/31.03.2011, period 2011-2012, parteneri UPT, IPB-ENSEIRB MATMECA, finantat de ANCS-UEFISCDI şi EGIDE

- 2004-2006 – national grant TD, CNCSIS code 47, Digital watermarking for still images in the transform domain funding by CNCSIS

Granturi (membru):

- 2014- în curs, Quality of Services Improvement for GNSS Localisation in Constraint Environment by Image Fusing Techniques (IMFUSING), Contract cu Agentia Spatiala Europeana, ESA, nr. 4000111852/14/NL/Cbi, contractor UPT, subcontractor Thales Alenia (2014)
- 2014- în curs, SEOM SY4Sci Synergy - Ocean Virtual Laboratory (OVL), Contract cu Agentia Spatiala Europeana, ESA, nr. 4000112389/14/I-NB, contractor OceanDataLab, subcontractor UPT
- 2011-2014 – FP7 EU program, Advanced Radar Tracking and Classification for Enhanced Road Safety ARTRAC finanţat de Uniunea Europeana
- 2013-2014 – PC7 EU program, Advanced Radar Tracking and Classification for Enhanced Road Safety ARTRAC, finanţat de UEFISCDI
- 2009-2011 – grant naţional– The use of wavelet theory for decision making, finanţat de CNCSIS, ID 930, 2009-2011
- 2007-2009 – grant naţional, Improvement of research & development basis in the field of communications at the Faculty of Electronics and Telecommunications, Politehnica Univ. of Timisoara, finanţat de ANCS, CAPACITATI PN II, 2007-2009, 77/CP/II/13.09.2007
- 2005-2007 – grant naţional, Performance increase of digital receptors using wavelet theory, finanţat de CNCSIS, code 637/A/CNCSIS
- 2004-2006 – grant naţional, Modern methods for image analysis and image processing, 2004-2006, finanţat de CNCSIS
- 2011-2012 – membru al grupului ţintă “Şcoala doctorală în sprijinul cercetării în context european” (Doctoral School in support of research in the European context), program POSDRU 21/1.5/G/13798 2010-2012

Burse:

- Oct. 2009 - bursă EGIDE pentru cercetare, LAPS, Bordeaux, France
- Sep. 2005 – bursă ECRYPT, Summer School for Multimedia Security, University of Salzburg, Austria, 21-24 Sept. 2005

Premii:

- 2012: Nominalizata pentru comitetul IEEE, Information Forensics and Security Technical Committee IEEE

2. Contributions

2.1 Overview of contributions

My research interests include: statistical signal and image processing applied in communications, RADAR, medicine, multimedia security, watermarking, their mathematical bases (with a predilection for wavelets theory) and their software implementation.

My PhD thesis was written under the guidance of Professor Monica Borda, from Technical University of Cluj-Napoca, and Professor Alexandru Isar, from Politehnica University Timisoara, with the subject of *Contributions to Image watermarking in the wavelet domain*.

My first image processing subject was **watermarking**. **Wavelet based image watermarking** research was continued further in some of the papers I have published: [NafIsa11]; [NafIsaKov09]; [NafIsa09]; [NafIsa08]; [NafNafIsaBor08]; [NafFirBouIsa08].

My second image processing subject was **denoising**.

I have co-authored the paper [FirNafBouIsa09] that presents the implementation of a new complex 2D wavelet transform, namely the **Hyperanalytic wavelet transform, HWT**; this was used for watermarking and denoising with a better performance than other quasi shift-invariant complex transforms.

A research preoccupation was the **statistical analysis of 2D wavelet transforms** including the 2D DWT and the HWT. First, I have made second order statistical analysis: ([IsaNaf14], [NafBerNafIsa12]; [FirNafIsaBouIsa10]; [NafFirIsaBouIsa10a]; [NafFirIsaBouIsa10b]). Next, I established statistical models, [NafBerNafIsa12]. In [NafBerNafIsa12] we have considered the repartition of the HWT coefficients to be like circularly symmetric, with CGGD for the complex coefficients. We computed a closed form for the **Kullback-Leibler divergence for the CGGD distribution**.

The HWT has six preferential directions (three with positive orientations and three with negative orientations) and it is quasi-shift invariant. We suggested **improving the directional selectivity** of 2D wavelet transforms: using **hyperanalytic wavelet packets** [NafIsaNaf12] (any number of preferential directions) and for anisotropic images, to distinguish between directions we have proposed to use the HWPT, and on each direction the smoothness is estimated via the **Hurst exponent and HWPT** [NafIsa13]. I have improved further the Hurst exponent estimation techniques by applying a LASSO based regularization in the wavelet domain [NafIsaNel14] and I applied this estimation method to solve an image denoising problem, where regularity varies piecewise.

I have co-authored research papers in the field of **HWT based image denoising:** [IsaFirNafMog11]; [FirNafIsaIsa11]; [NafIsaIsa11]; [FirNafBouIsa10]; [FirNafBouIsa09] in collaboration with Professor Alexandru Isar, dr. Ioana Firoiu, Professor Dorina Isar and Professor Jean-Marc Boucher (Telecom Bretagne, Brest, France). This direction will be pursuited by the analysis of despecklization algorithms in the framework of the ESA contract SY4Sci Synergy - Ocean Virtual Laboratory (OVL).

My third image processing subject was **denoising based image contrast enhancement** [NafIsa14].

My fourth image processing processing preocupation was **texture analysis**. A new method for **texture clustering** based on the information-geometry tools (barycentric distribution for each cluster) is proposed in [SchBerTurNafIsa12].

My signal processing research activities were: biomedical signal processing (ECG and MCG signals), such as denoising, compression and wander baseline reduction; in communications we proposed methods for the reduction of the Peak-to-Average Power Ratio

(PAPR) of the transmitted signal (OFDM), RADAR signal processing such as detection or waveform generation and the generation of new mother wavelets based on the frames theory.

Recently, in the framework of an European Project (FP7-ARTRAC), I have worked in the field of **RADAR signal processing**, proposing denoising to improve probability of detection for the envelope detector; as well as a method to build the range-Doppler map for multiple targets in the automotive field [MacNafIsa14], [NafMacIsa14].

2.2 Image watermarking

Papers: [NafIsa11]; [NafIsaKov09]; [NafIsa09]; [NafIsa08]; [NafNafIsaBor08]; [NafFirBouIsa08]

Proliferation of multimedia data on the Internet and the ease of copying this data have brought an interest for copyright protection [CoxMilBlo02]. During transmission, data can be protected using encryption; however after decrypting it, it is no longer protected. As an alternative to encryption, watermarking has been proposed as a means of identifying the owner, by secretly embedding an imperceptible signal into the host signal [Cox05] – see Fig. 1.

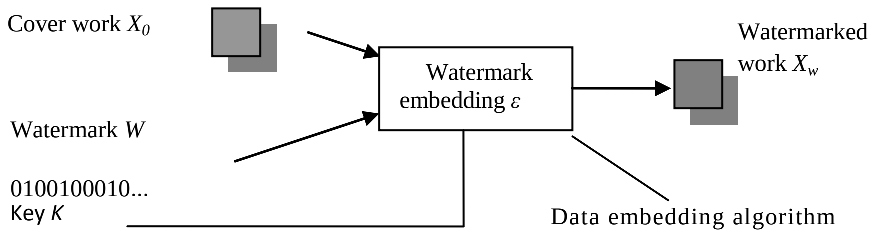

Fig. 1. Watermark embedding. The watermark is embedded using a secret or public key, making invisible changes to the cover work.

The main properties of a watermarking system are perceptual transparency, robustness, security, and data hiding capacity [CoxKilLeiSha97]. Some of the terms used in watermarking are [CoxMilBlo02]:

- The original data where the watermark is to be inserted is referred to as host or cover work.
- The hidden information is called payload.
- Visible watermarks are visual patterns (images, logos) inserted or overlaid on images/video. Visible watermarks are applied to photos publicly available on the web, to prevent commercial use of such images. One example of visible watermarking has been implemented by IBM for the Vatican library [BraMagMin96].
- Most watermarking systems involve making the watermark imperceptible.
- The key is required for embedding the watermark. If the same key is used for retrieving the watermark, the system is private, while if another key is used to retrieve it, the system is known as public.
- If the cover work is required at the detector, the system is informed (non-blind); if it’s not required at the detector, the system is blind.
- Watermarking systems are robust or fragile. Robust watermarks should resist any modifications and are designed for copyright protection. Fragile watermarks are designed to fail whenever the cover work is modified and to give some measure of the tampering. Fragile watermarks are used in authentication.

Most of existing watermarking systems proposed in the literature can be classified depending on the watermarking domain, where the embedding takes place: **spatial domain** techniques [NikPit98], where the pixels are directly modified, or **transform domain** techniques.

The majority of watermarking algorithms operate based on the spread spectrum (SS) communication principle. A pseudorandom sequence is added to the host signal in some critically sampled domain and the watermarked signal is obtained by inverse transforming the modified coefficients. Typical transform domains are the Discrete Wavelet Transform (DWT), the Discrete Cosine Transform (DCT) and the Discrete Fourier Transform (DFT). The DWT based algorithms usually produce watermarked images with the best balance between visual quality and robustness due to the absence of blocking artefacts [Naf08].

Watermarks can be robust or fragile, depending on the application. For copyright protection, robustness is required. This can be assured with encoding of the watermark using a repetition code or an error correcting code. Robustness is increased with the increase of the correction capacity of the code. Despite of their efficient use in telecommunications, turbo codes have been rarely used in watermarking [AbdGlaPan02], [SerAmbTomWad03], [BalPer01], [NafIsaKov09].

At the embedding side, the watermark can be added to coefficients of known robustness (large valued coefficients) or perceptually significant regions [Cox05], such as contours and textures of an image. This can be done empirically, selecting larger coefficients [CoxKilLeiSha97] or using a thresholding scheme in the transform domain [PodZen98], [NafIsaBor05]. Another approach is to insert the watermark in all coefficients of a transform, using a variable strength for each coefficient [BarBarPiv01]. Hybrid techniques, based on compression schemes, embed the watermark using a thresholding scheme and variable strength [PodZen98]. The performance of such a system depends on the quality of the wavelet transform.

In [NafIsa11]; [NafIsaKov09]; [NafIsa09]; [NafIsa08]; [NafNafIsaBor08]; [NafFirBouIsa08], were reported image watermarking method results that were obtained during and after the PhD thesis. We focused mostly on the application of the wavelet transforms in **robust blind watermarking** for static images (we do not require the original image at the detection side) [NafIsa11]; [NafIsa09]; [NafIsa08]; [NafNafIsaBor08]; [NafFirBouIsa08], except for [NafIsaKov09].

Classical techniques of watermarking such as the spread spectrum (SS) watermarking system, based on the DCT transform, proposed by Cox et al. [CoxKilLeiSha97] and those proposed in the wavelet domain are presented. Other wavelet transforms as the 2D DTCWT [SelBarKin05] or the HWT [NafFirBouIsa08], [FirNafBouIsa09] could also be considered. The advantages of such transforms compared to DWT are: quasi-shift invariance and enhanced directional selectivity. The data hiding capacity increases with the increase of redundancy (4x for DTCWT and HWT). We compare the efficiency of those wavelet transforms in watermarking.

Most techniques embed the watermark in a transform domain as mentioned before. Early techniques have used the Discrete Cosine Transform (DCT). One of the most influential watermarking works is a SS approach proposed in [CoxKilLeiSha97]. They argue that the watermark be placed explicitly in the perceptually most significant components of the data, and that the watermark be composed of random numbers drawn from a Gaussian distribution $\mathcal{N}(0,1)$, in order to make it invisible and robust to attacks:

$$v'(i) = v(i)\left(1+\alpha w(i)\right), \tag{1}$$

where *v*(*i*) is the DCT coefficient to be watermarked, *w*(*i*) is the watermark bit, α is the embedding strength and *v*'(*i*) is the watermarked coefficient. Detection is made using the similarity between the original W and extracted Ŵ watermarks:

$$\mathrm{sim}\left(W,\hat{W}\right)=\frac{\hat{W}\cdot W}{\sqrt{\hat{W}\cdot\hat{W}}}. \tag{2}$$

The fact that the transform is performed over the entire image increases the computation time. Other methods have been proposed that use the block-based DCT transform, just like in the JPEG compression (see for example [PodZen98]).

Other authors have proposed the use of the Discrete Fourier Transform (DFT) or its variant – the Fourier-Mellin transform. This is useful in order to perform phase modulation between the watermark and the original signal [RuaDowBol96]. The phase is more important than the amplitude; hence it will be difficult for an attacker to remove the watermark. Phase modulation often possesses superior noise immunity in comparison with amplitude modulation. Many watermarking techniques use DFT amplitude modulation because the watermark will be translation invariant. The DFT is more often used in its derived forms such as the Fourier-Mellin transform. This Fourier-Mellin transform approach has arisen out of the need for Rotation, Scale and Translation (RST)-invariant watermarking techniques. It involves creating a Log Polar map of the DFT amplitudes of the image, where the embedding takes place. This method is said to be extremely RST invariant and uses a RST invariant watermark [LinWuBlo01], [RuaPun98].

There are different approaches to embed the watermark in the **wavelet domain**. Almost all methods rely on masking in some way the watermark, either by selecting a few coefficients, or using adaptive embedding strength.

Podilchuk & Zeng [PodZen98] propose an image-adaptive (IA) approach. They use the just difference noticeable difference (JND) to determine the image dependent perceptual mask for the watermark. They applied this method in both DCT and wavelet domain:

$$I^{*}_{u,v}=\begin{cases} I_{u,v}+JND_{u,v}\times w_{u,v}, & \text{if } I_{u,v}>JND_{u,v} \\ I_{u,v}, & \text{otherwise} \end{cases}, \tag{3}$$

$I_{u,v}$ are the coefficients of the original image, $w_{u,v}$ are the watermark bits, and $JND_{u,v}$ are the JND values computed using visual models. In the case of DCT, they are computed using Watson's perceptual model; for the wavelet domain, the weight is computed for each frequency band based on typical viewing conditions. Detection is made using correlation between the image difference and the watermark sequence. This method is more robust than the spread-spectrum method in [CoxKilLeiSha97]. Although more robust than IA-DCT, the IA-W method does not take into account perceptual significant regions, so the watermark can be erased from perceptually insignificant coefficients. For example, low-pass filtering will affect the watermark inserted in high frequency components.

Xia et al. [XiaBonArc98] propose a watermarking algorithm using the Haar mother wavelet, and two levels of decomposition. A pseudo-random sequence is added to the highest coefficients not located in the lowest resolution:

$$f'(m,n)=f(m,n)+\alpha\cdot f(m,n)^{\beta}w_i, \tag{4}$$

where α is the watermark strength, and β is the amplification for large coefficients. This algorithm concentrates most of the energy in edges and textures, which are the coefficients in detail subbands. This increases the invisibility of the watermark, because human observers are less sensitive to change in edges and textures compared to changes in smooth areas of an image. More watermarks are inserted in each subband, and detection is done hierarchically, for each resolution level, using intercorrelation between original watermark and the difference of the two images. The method is robust to a series of distortions, but low-pass and median filtering affect the watermark.

Kundur & Hatzinakos [KunHat98] use the Daubechies wavelet family to compute the DWT on three levels of decomposition. The watermarking algorithm selects in a pseudo-random manner the embedding locations from the detail subbands. The authors state that the spread-spectrum technique is not appropriate for transmitting the watermark because the correlator used for watermark detection is not effective in the presence of fading. Hence, they use quantization for embedding the watermark bits. To increase robustness, they use a reference watermark in order to estimate if the watermark bit has been embedded [KunHat01].

2.2.1 Perceptual watermarks in the wavelet domain

A spread spectrum method in the wavelet domain is proposed in [BarBarPiv01]. The watermark is masked according to the characteristics of the human visual system (HVS), taking into account the texture and the luminance content of all the image subbands. The contours of the image are watermarked with a higher strength, textures with a medium strength and homogeneous regions (with high regularity) with a lower strength, in accordance with the analogy water-filling and watermarking [Kun00].

The image I, of size $2M \times 2N$, is decomposed into 4 levels using Daubechies-6 wavelet mother, where I_l^θ is the subband from level $l \in \{0, 1, 2, 3\}$, and orientation $\theta \in \{0, 1, 2, 3\}$ (horizontal, diagonal and vertical detail subbands, and approximation subband). A pseudorandom binary (± 1) sequence is casted into 2D binary watermarks, each of size $MN/4^l$, x_l^θ. The watermark is embedded in all coefficients from level $l=0$ by addition

$$\tilde{I}_l^\theta(i,j) = I_l^\theta(i,j) + \alpha w_l^\theta(i,j) x_l^\theta(i,j), \tag{5}$$

where α is the embedding strength and $w_l^\theta(i,j)$ is half of the quantization step:

$$q_l^\theta(i,j) = \Theta(l,\theta)\Lambda(l,i,j)\Xi(l,i,j)^{0.2}, \tag{6}$$

as it is presented in the following figure.

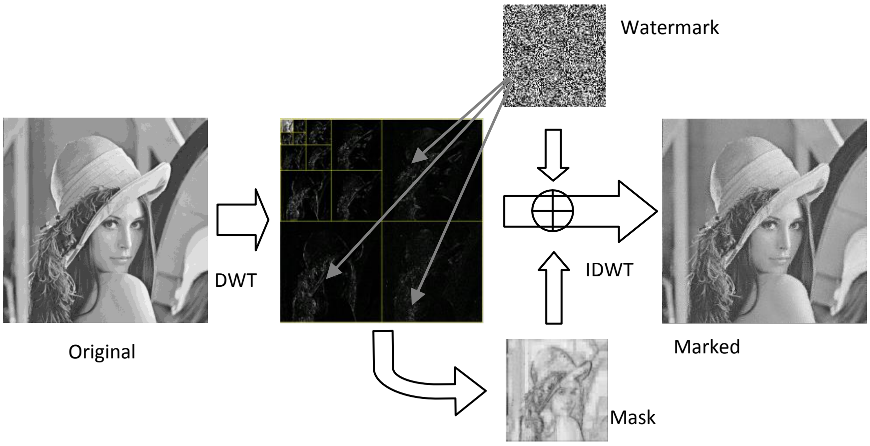

Fig. 2. Watermark embedding in the wavelet domain [BarBarPiv01]. The watermark is embedded in the first resolution level using a perceptual mask.

This is a product of three factors: sensitivity to noise Θ, local brightness Λ and texture activity around a pixel Ξ. They are computed as follows:

$$\Theta(l,\theta)=\begin{Bmatrix}\sqrt{2}, & \theta=1\\ 1 & \text{otherwise}\end{Bmatrix}\cdot\begin{Bmatrix}1.00 & l=0\\ 0.32 & l=1\\ 0.16 & l=2\\ 0.10 & l=3\end{Bmatrix}, \tag{7}$$

$$\Lambda(l,i,j)=1+L'(l,i,j), \tag{8}$$

$$L(l,i,j)=I_3^3\left(1+\left\lfloor i/2^{3-l}\right\rfloor,1+\left\lfloor j/2^{3-l}\right\rfloor\right)\Big/256, \tag{9}$$

$$\Xi(l,i,j)=\sum_{k=0}^{3-l}16^{-k}\sum_{\theta=0}^{2}\sum_{x,y=0}^{1}\left[I_{k+l}^{\theta}\left(y+i/2^k,x+j/2^k\right)\right]^2\cdot\mathrm{Var}\left\{I_3^3\left(1+y+\frac{i}{2^{3-l}},1+x+\frac{j}{2^{3-l}}\right)\right\}_{\substack{x=0,1\\ y=0,1}}. \tag{10}$$

The texture activity around a pixel is composed by the product of two contributions; the first is the local mean square value of the DWT coefficients in all detail subbands and the second is **the local variance** of the 4th level approximation image. Both are computed in a small 2×2 neighborhood corresponding to the location (*i*, *j*) of the pixel. The first contribution is the distance from the edges, and the second one is the texture. This local variance estimation is computed with a low resolution.

Detection is made using the correlation between the marked DWT coefficients and the watermarking sequence to be tested for presence (the original image is not needed):

$$\rho(l)=4^l\sum_{\theta=0}^{2}\sum_{i=0}^{M/2^l-1}\sum_{j=0}^{N/2^l-1}\tilde{I}_l^{\theta}(i,j)\,x_l^{\theta}(i,j)\Big/(3MN). \tag{11}$$

The correlation is compared to a threshold $T_\rho(l)$, computed to grant a given probability of false positive detection, using the Neyman-Pearson criterion. For example, for $P_f\le 10^{-8}$, the threshold is $T_{\rho(l)}=3.97\sqrt{2\sigma_{\rho(l)}^2}$, with $\sigma_{\rho(l)}^2$ the variance of the wavelet coefficients, if the image was watermarked with a code Y other than X,

$$\sigma_{\rho(l)}^2\approx\left(4^l/(3MN)\right)^2\sum_{\theta=0}^{2}\sum_{i=0}^{M/2^l-1}\sum_{j=0}^{N/2^l-1}\left(\tilde{I}_l^{\theta}(i,j)\right)^2. \tag{12}$$

Barni's method is quite robust against common signal processing techniques like filtering, compression, cropping and so on. However, because embedding is made only in the last resolution level, the watermark information can be easily erased by an attacker.

We proposed in [Naf08] a pixel-wise mask allowing insertion of the watermark **in lower resolution levels**. The third factor of the texture is estimated using the local standard deviation of the original image computed on a rectangular moving window *W*(*i,j*) of $W_S\times W_S$ pixels, centered on each pixel *I*(*i,j*). This criterion of segmentation finds its contours, textures and regions with high homogeneity. The local mean is:

$$\hat{\mu}(i,j)=W_S^{-2}\sum_{I(m,n)\in W(i,j)}I(m,n). \tag{13}$$

The local variance is given by:

$$\hat{\sigma}^2(i,j)=W_S^{-2}\sum_{I(m,n)\in W(i,j)}\left(I(m,n)-\hat{\mu}(i,j)\right)^2. \tag{14}$$

The local standard deviation is the square root of this local variance. The texture activity for a considered DWT coefficient is proportional with the local standard deviation of the corresponding pixel from the host image. We denote this local standard deviation image with *S*, and the local mean image with *U*. Embedding is made in the subband *s*, level *l*; the size of the texture matrix must agree with the size of the subband. Hence, the approximation image at the l^{th} decomposition level is used. This compression can be realized exploiting the separation properties of the DWT. To generate the mask required for the embedding into the detail subimages corresponding to the l^{th} decomposition level, the DWT of the local standard deviation image is computed (making l+1 iterations). The required mask will be the approximation subimage from level l, denoted S_l^3, normalized to the local mean, also compressed in the wavelet domain, U_l^3. This is illustrated in Fig. 3.

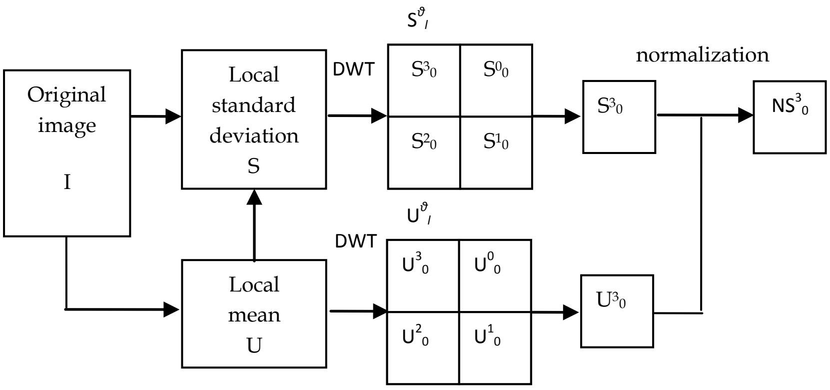

Fig. 3. Watermark embedding. The watermark is embedded using a secret or public key, making invisible changes to the cover work.

One difference between the watermarking method proposed by [Naf08] and the one proposed in [BarBarPiv01], is given by the computation of the local variance – the second term – in (10). To obtain the new values of the texture, the local variance of the image to be watermarked is computed, using the relations (13) and (14). The local standard deviation image is decomposed using one iteration wavelet transform, and only the approximation image is kept. Relation (10) is then replaced with:

$$\Xi(l,i,j)=\sum_{k=0}^{3-l}16^{-k}\sum_{\theta=0}^{2}\sum_{x,y=0}^{1}\left[I_{k+l}^{\theta}\left(y+i/2^k,x+j/2^k\right)\right]^2\cdot S_l^3(i,j)/U_l^3(i,j) \qquad (15)$$

The second difference is that the luminance mask is computed on the approximation image from level l, where the watermark is embedded. The DWT of the original image using l decomposition levels was computed and the approximation subimage corresponding at level l was separated, obtaining the image I_l^3. The luminance content is computed using:

$$L(l,i,j)=I_l^3(i,j)/256 \qquad (16)$$

Since both factors are more dependent on the resolution level in the method proposed by Barni, the noise sensitivity function becomes:

$$\Theta(l,\theta)=\begin{Bmatrix}\sqrt{2}, & \theta=1\\ 1, & \text{otherwise}\end{Bmatrix}\begin{Bmatrix}1.00 & l\in\{0,1\}\\ 0.66 & l=2\end{Bmatrix} \qquad (17)$$

It was considered the ratio between the correlation $\rho(l)$ in Eq. (11) and the image dependent threshold $T_\rho(l)$, hence the detector was viewed as a nonlinear function with a fixed threshold. In [Naf07a], three detectors are used, to take advantage of the wavelet hierarchical decomposition. The watermark presence is detected,

1) from all resolution levels, “all_levels”,

2) separately from each resolution level, considering the maximum detector response from each level, “max_level”,

3) separately from each subband, considering the maximum detector response from each subband, “max_subband”.

Evaluating the correlations separately per resolution level or subband can be sometimes advantageous. In the case of cropping attack, the watermark will be damaged more likely in the lower frequency than in the higher frequency, while lowpass filtering affects more the higher frequency than lower ones. Layers or subbands with lower detector response are discarded. This type of embedding combined with new detectors is more attack resilient to a possible erasure of the three subbands watermark. The detector “all_levels” evaluates the watermark’s presence on all resolution levels:

$$d_1 = \rho_{d1} / T_{d1} \, , \tag{18}$$

where the correlation ρ_{d1} is given by:

$$\rho_{d1} = \sum_{l=0}^{2} \sum_{\theta=0}^{2} \sum_{i=0}^{M/2^l-1} \sum_{j=0}^{N/2^l-1} \tilde{I}_l^{\theta}(i,j) x_l^{\theta}(i,j) \Big/ \left(3MN \sum_{l=0}^{2} 4^{-l} \right) . \tag{19}$$

The threshold for $P_f \leq 10^{-8}$ is $T_{\mathrm{d1}} = 3.97\sqrt{\sigma^2_{\rho\mathrm{d1}}}$, with:

$$\sigma^2_{\rho\mathrm{d1}} \approx \sum_{l=0}^{2} \sum_{\theta=0}^{2} \sum_{i=0}^{M/2^l-1} \sum_{j=0}^{N/2^l-1} \left(\tilde{I}_l^{\theta}(i,j) \right)^2 \Big/ \left(3MN \sum_{l=0}^{2} 4^{-l} \right)^2 . \tag{20}$$

The second detector “max_levels” considers the responses from different levels, as $d(l)=\rho(l)/T(l)$, with $l \in \{0, 1, 2\}$, and discards the detector responses with lower values:

$$d_2 = \max_{l} \{ d(l) \} . \tag{21}$$

The third detector considers the responses from different subbands and levels, as $d(l,\theta)$ the ratio $\rho(l,\theta)/T(l,\theta)$, with $l,\theta \in \{0, 1, 2\}$, and discards the detector responses with lower values,

$$d_3 = \max_{l,\theta} \{ d(l,\theta) \} . \tag{22}$$

The correlation and threshold are computed with the same rationale on one subband, indicated by its orientation and level.

Watermarking using the HWT. The 2D DWT is useful to embed the watermark because the visual quality of the images is very good. However, it has three main disadvantages [Kin01]: lack of shift invariance, lack of symmetry of the mother wavelets and poor directional selectivity. Caused by the lack of shift invariance of the DWT, small shifts in the input signal can produce important changes in the energy distribution of the wavelet coefficients. Due to the poor directional selectivity for diagonal features of the DWT the watermarking capacity is small. The most important parameters of a watermarking system are robustness and capacity. These parameters must be maximized. These disadvantages can be diminished using a complex wavelet transform as for example the 2D DTCWT [Kin00], [Kin01].

A very simple implementation of the HWT, recently proposed [FirNafBouIsa09] [AdaNafBouIsa07] has a high shift-invariance degree versus other quasi-shift-invariant wavelet transforms (WT) at same redundancy. It has also an enhanced directional selectivity. All the WTs have two parameters: the mother wavelets (MW) and the primary resolution (PR), (number of iterations). The importance of their selection is highlighted in [Nas02]. Another appealing particularity of those transforms, coming from their multiresolution capability, is the interscale dependency of the wavelet coefficients.

After the PhD thesis, we proposed to use our new implementation of the HWT transform [AdaNafBouIsa07] for image watermarking [NafFirBouIsa08]. The watermark capacity was studied in [MouMih02], where an information-theoretic model for image watermarking and data hiding is presented. Models for geometric attacks and distortion measures that are invariant to such attacks are also considered. The lack of shift invariance of the DWT and its poor directional selectivity are reasons to embed the watermark in the field of another WT. To maximize the robustness and the capacity, the role of the redundancy of the transform used must be highlighted first. An example of redundant WT is represented by the tight frame decomposition. In [HuaFow02] are analyzed the watermarking systems based on tight frame decompositions. The analysis indicates that a tight frame offers no inherent performance advantage over an orthonormal transform (DWT) in the watermark detection process despite the well-known ability of redundant transforms to accommodate greater amounts of added noise for a given distortion. The overcompleteness of the expansion, which aids the watermark insertion by accommodating greater watermark energy for a given distortion, actually hinders the correlation operator in watermark detection. As a result, the tight-frame expansion does not inherently offer greater spread-spectrum watermarking performance. This analytical observation should be tempered with the fact that spread-spectrum watermarking is often deployed in conjunction with an image-adaptive weighting mask to take into account the human visual model (HVM) and to improve perceptual performance. Another redundant WT, the DTCWT, was already used for watermarking [LooKin00]. The authors of this paper prove that the capacity of a watermarking system based on a complex wavelet transform is higher than the capacity of a similar system that embeds the watermark in the DWT domain. Many authors (e.g. [Dau80]) have suggested that the processing of visual data inside our visual cortex resembles filtering by an array of Gabor filters of different orientations and scales. The proposed implementation of HWT is efficient, has only a modest amount of redundancy, provides approximate shift invariance, has better directional selectivity than the 2D DWT and it can be observed that the corresponding basis functions closely approximate the Gabor functions. So, the spread spectrum watermarking based on the use of an image adaptive weighting mask applied in the HWT domain is potentially a robust solution that increases the capacity.

Adapting the strategy already described previously to the case of HWT, new methods were proposed in [NafFirBouIsa08]. The coefficients z are complex, with real z_r and imaginary part z_i. The HWT orientations or preferential directions are: atan(1/2), $\pi/4$, atan(2) (for $\theta = 0, 1, 2$), for the image z_+ and -atan(1/2), $-\pi/4$, -atan(2), ($\theta=0, 1, 2$) for the image z_- .

The first three wavelet decomposition levels are used and the watermark is embedded into the real coefficients with positive and negative orientations, z_{+r} and z_{-r}, respectively. The relations already described previously were used independently for each of these two images. The same message was embedded in both images, using the mask from [Naf07a].

At the detection side, we consider the pair of images (z_{+r}, z_{-r}), thus having twice as much coefficients than the standard approach, and θ takes all the possible values, ±atan(1/2), $\pm\pi/4$, ±atan(2).

We will compare in the following watermarking systems based on DWT with the ones based on complex WTs, namely the HWT.

Results for DWT based methods In [NafIsaBor06a], the system proposed by Barni et al. was modified, using the texture mask in (15). The image Barbara is watermarked with various values of the embedding strength α. The binary watermark is embedded in all the detail wavelet coefficients of the first resolution level. Watermarked Barbara for α=1.5 is shown in Fig. 4.

Fig. 5 shows results for JPEG compression attack, for different quality factors: the ratio ρ/T is plotted as a function of the peak signal-to-noise ratio (PSNR) between the marked (un-attacked) image and the original one, and respectively as a function of α. The probability of false positive detection is set to 10^{-8}.

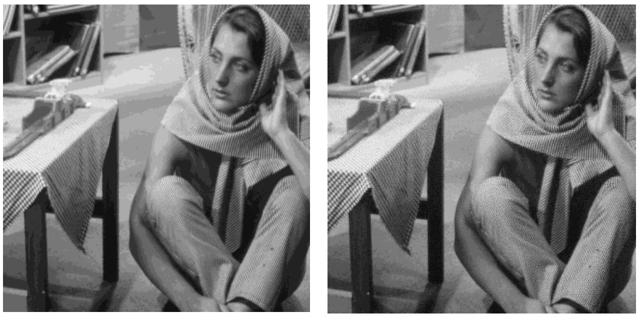

Fig. 4 Original and watermarked Barbara images with $\alpha = 1.5$.

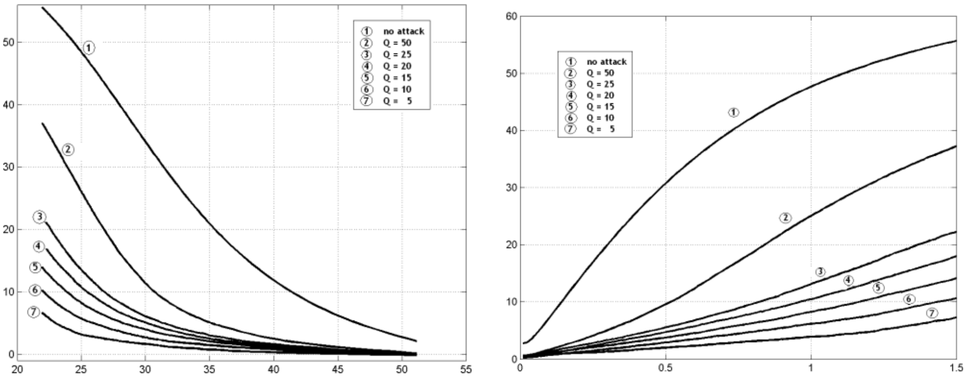

Fig. 5 Left: The ratio ρ/T as a function of the PSNR between the marked and the original images, for different quality factors, JPEG compression. Right: Ratio ρ/T as a function of embedding strength, for different quality factors, JPEG compression. P_f is set to 10^{-8}.

If this ratio is greater than 1 then the watermark is positively detected. Generally, for a PSNR higher than 30 dB, the original image and watermarked one are considered indistinguishable. For compression quality factors higher or equal than 25 the distortion introduced by JPEG compression is tolerable. For PSNR in the range of 30-35 dB, of practical interest, the watermark is detected for all significant compression quality factors. Increasing the embedding strength, the PSNR of the watermarked image decreases, and the ratio ρ/T increases. The watermark is still detectable even for very small values of α. For the quality factor Q=5 (or a compression ratio CR=32), the watermark is still detectable even for α=0.5.

Fig. 6 shows the detection of a true watermark for various quality factors, in the case of α=1.5; the threshold is well below the detector response.

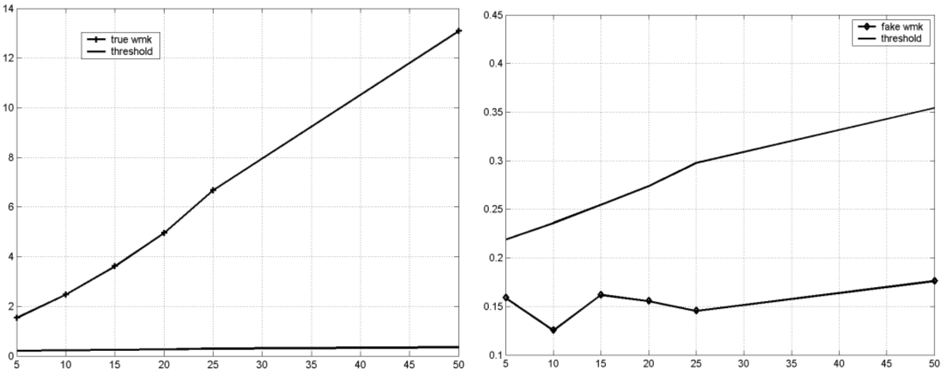

Fig. 6 Left: Detector response ρ, threshold T, as a function of different quality factors (JPEG compression). The watermark is successfully detected. P_f is set to 10^{-8}. Right: Highest detector response, ρ_2, corresponding to a fake watermark and threshold T. The threshold is above the detector response.

	[NafIsaBor06a]	[BarBarPiv01]
ρ	0.3199	0.038
T	0.0844	0.036
ρ_2	0.0516	0.010

Table 1. A comparison for JPEG compression with a compression ratio CR = 46. The detector response for the original embedded watermark ρ, the detection threshold T, and the second highest detector response ρ_2 are given. $P_f = 10^{-8}$ and 1000 marks were tested. The detector response is higher than in Barni's case.

Fig. 7 Original image Lena; mask from [NafIsaBor06b] and Barni's mask for level l=0. The masks are the complementary of the real ones.

In Table 1 we give a comparison between the two methods, for the Lena image, α=1.5 in the case of JPEG compression with a quality factor of 5 (compression ratio of 46).

In [NafIsaBor06b], Barni's method is modified, using the texture mask in (15), as well as the luminance factor in (16). The masks obtained are shown in Fig. 7. The improvement is clearly visible around edges and contours. The method is applied in two cases, when the watermark is inserted in level 0 only and when it's inserted in level 1 only. JPEG compression is again considered. The image Lena is watermarked at level l=0 and respectively at level l=1 with α ranging from 1.5 to 5. The binary watermark is embedded in all the detail wavelet coefficients of the resolution level, l as previously described. For α=1.5, the watermarked images, in level 0 and level 1, as well as the image watermarked using Barni's mask, are shown in Fig. 8. Obviously the quality of the watermarked images are preserved using the new pixel-wise mask. The PSNR values are 38 dB (level 0) and 43 dB (level 1), compared to Barni's method, with a PSNR of 20 dB.

Fig. 8 Watermarked images, α =1.5, for [NafIsaBor06b], level 0 (PSNR = 38 dB); level 1 (43 dB); for [BarBarPiv01], level 0 (20 dB).

The PSNR values are shown in Fig. 9(left) as a function of the embedding strength. The watermark is still invisible, even for high values of α.

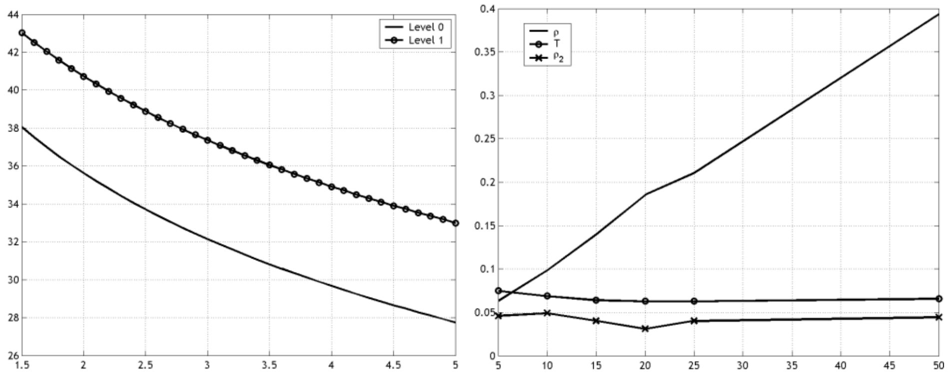

Fig. 9 Left: PSNR as a function of α. Embedding is made either in level 0 or in level 1. Right: Detector response ρ, threshold T, highest detector response, ρ_2, corresponding to a fake watermark, as a function of different quality factors (JPEG compression). The watermark is successfully detected. P_f is set to 10^{-8}. Embedding was made in level 0.

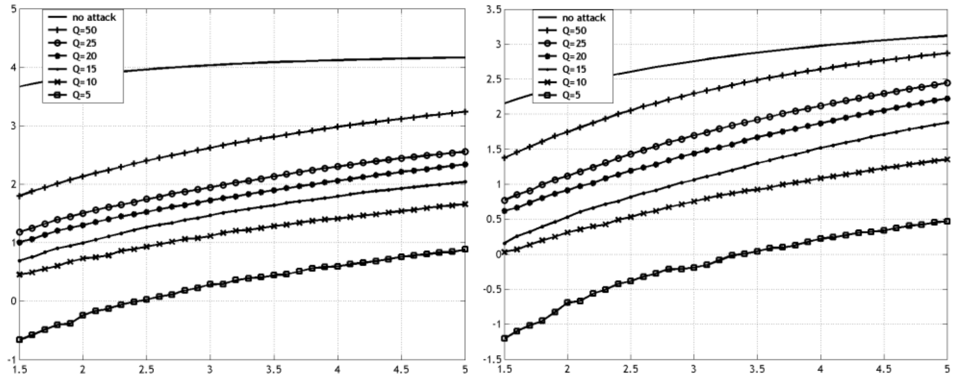

Fig. 10 Ratio ρ/T as a function of the embedding strength α. The watermarked image is JPEG compressed with different quality factors Q. P_f is set to 10^{-8}. Embedding was made in level 0 (left), and in level 1 (right).

Fig. 10 gives the results for JPEG compression. In all experiments, the probability of false positive detection is set to 10^{-8}. The watermark is successfully detected for a large interval of compression quality factors.For PSNR values higher than 30 dB, the watermarking is invisible. For quality factors Q≥10, the distortion introduced by JPEG compression is tolerable. For all values of α, the watermark is detected for all the significant quality factors (Q≥10). Increasing the embedding strength, the PSNR of the watermarked image decreases, and ρ/T increases. For the quality factor Q = 10 (or a compression ratio CR = 32), the watermark is still detectable even for low values of α.

Fig. 9 (right) shows the detection of a true watermark from level 0 for various quality factors, for α=1.5; the threshold is below the detector response. The selectivity of the watermark detector is also illustrated, when a number of 999 fake watermarks were tested: the second highest detector response is shown, for each quality factor. False positives are rejected.

In Table 2 a comparison between [NafIsaBor06b] and [BarBarPiv01], can be seen for JPEG compression with Q=10 (compression ratio of 32). The detector response for the original watermark ρ, the detection threshold T, and the second highest detector response ρ_2, when the watermark was inserted in level 0 are given. The detector response is higher than for Barni et al. The method in [Naf07a] allows embedding of the watermark in ***all resolution levels***, except the last one (low resolution). Three types of detectors are used, as described before.

Various images of size 512x512, have been watermarked at levels $l \in \{0, 1, 2\}$ using the new mask. The embedding strength is α=1.5. Based on human observation and the peak-signal-to-noise ratio, PSNR, the images are indistinguishable from the original ones. For Barni et al. method, a watermark is embedded in all the detail wavelet coefficients of the first resolution level, l=0, for α=0.2, that results in a similar image quality (see Fig.11). This has been concluded in [Naf07b], where by limiting the watermark strength such that the PSNR is 35 dB and in average the percentage of affected pixels is less than 25%, the quality of the images is greatly improved. Girod's model has been used for determining the location and number of affected pixels (Girod, 1989).

	[NafIsaBor06b]	[BarBarPiv01]
ρ	0.0750	0.062
T	0.0636	0.036
ρ_2	0.0461	0.011

Table 2. A comparison for JPEG compression with a compression ratio CR = 32.

Fig. 11 (left) Original image Lena, (middle) Watermarked images for [Naf07a], α=1.5, PSNR=36.86 dB, (right) [BarBarPiv01], α=0.2, PSNR=36.39 dB.

Detector response vs. attack	Method in [Naf07a]- DWT domain			Barni's method DWT domain
	1-All levels	2-Max level	3-Max subband	
JPEG Q=10	2.38	1.98	1.44	1.75
Median filt., M=5	1.32	1.12	1.46	0.25
Scaling, 50%	4.06	5.21	5.76	1.85
Cropping, 512x512 -> 32x32	0.68	0.98	1.73	1.48
Gamma corr., γ=2	20.32	29.19	28.06	32.54
Motion blur, L=31, θ=11	1.98	5.48	8.04	6.14

Table 3. Resistance to different attacks, for the method proposed in [Naf07a]. The detector response is a mean value of different responses.

For instance, in Barni's case, the watermarked image with α=0.2 has a PSNR of 36.39 dB, 11.84% affected pixels, compared to the one watermarked with α=1.5 has a PSNR of 20 dB, and all pixels are affected. What are kept constant for comparison are the 2D watermarks embedded in the first level, and the image quality. The method [Naf07a] cannot be compared with the one in [BarBarPiv01] when the watermark is embedded in all resolution levels, simply because their mask isn't suited for embedding in other levels than the highest resolution level. Results for some of the standard images from the USC SIPI Image Database are given.

Table 3 includes PSNR values for the two cases. For the first detector, an estimate of the false positive probability is shown for the image Lena, before and after JPEG compression attack, with quality factor Q=10, as a function of the detection thresholds, $T_{\rho 1}$. The threshold values have been computed using as estimate the variance of the ρ_1 obtained from experiments. The mean PSNR for the twelve images is 34.16 dB for the proposed method [Naf07a] and 34.06 dB for Barni's method.

Tests were made for JPEG compression, median filtering, cropping, resizing, gamma correction and blurring. Table 3 shows the mean values of the detector responses for each attack. A particular attack parameter is chosen where the watermark is still detectable by at least one detector. For compression, the method in [Naf07a] successfully detects the watermark at Q=10. The 1st detector is better in all cases. This new method has better results than Barni's technique. The watermark of both methods survived in all images for median filtering with kernel sizes up to 3. For kernel size 5, the watermark of [Naf07a] using the first and third detector is detectable; Barni's method fails to detect the watermark. In the case of scaling to 50%, the watermark was successfully detectable in both cases, with better results for [Naf07a]. The third detector has the best performance in detecting the mark. The watermark of [Naf07a] was successfully detected in the cropped image of 32x32, only with the third detector, which proves its efficiency. Barni's method detects the watermark with similar detector responses as in the case of the third detector. As expected for normalized correlation detection, both methods are practically insensitive to gamma correction adjustment. For the motion blur attack, both methods have successfully detected the watermark in all cases. Detector 3 has slightly better results than the others.

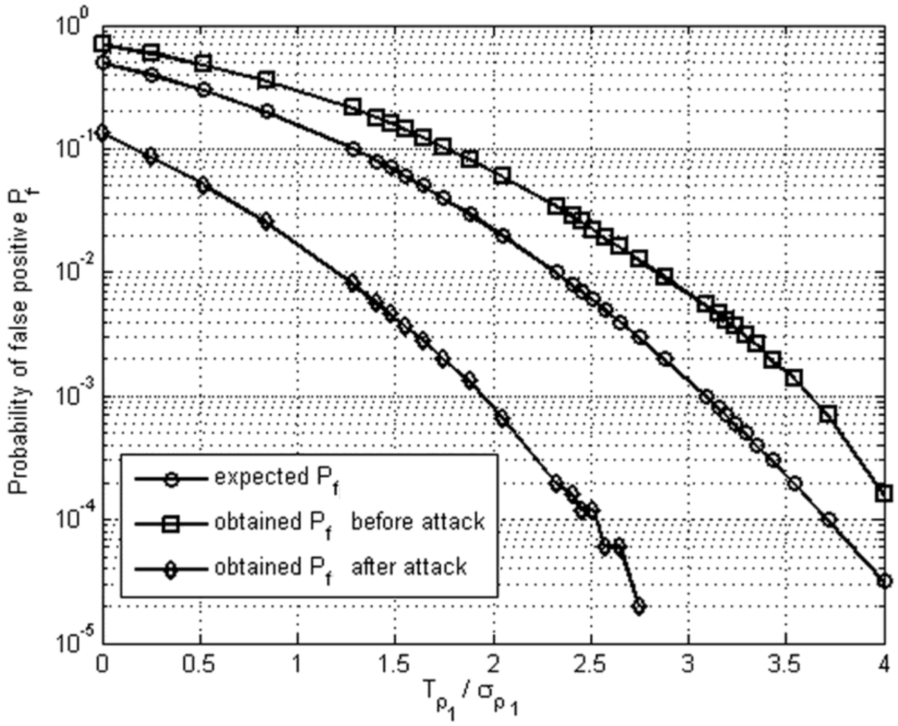

Fig. 12. Experimentally evaluated probability of false positive P_f vs. $T_{\rho 1}/\sigma_{\rho 1}$, the ratio between the detection threshold and standard deviation of the correlations in the case where an incorrect watermark was embedded. The theoretical trend is also shown ('o' marker). Tests were made on Lena, before and after JPEG compression with quality factor 10, using 5×10^4 different watermarks.

For the first detector, the probability of false positive was estimated by searching many different watermarks into one watermarked image, Lena. Each threshold $T_{\rho 1}$ was set in such a way to grant a given value of P_f. The trial was repeated for values of P_f ranging from 10^{-1} through 10^{-4}. In total $5x10^4$ watermarks per image have been tested. The estimation has been done before any type of manipulation and after JPEG compression, with quality factor 10. The estimated P_f is plotted in Fig. 12 versus the ratio $T_{\rho 1}/\sigma_{\rho 1}$ between the detection thresholds and standard deviations of correlations for the case corresponding to certain estimates of this probability of false positive. This case corresponds to the situation where the image is watermarked with a code Y other than X.

Surprisingly, the estimated false alarm P_f, is lower in the case of compression than in the case of no attack, for the same detection threshold. This can be explained by the fact that before compression, the empirical pdf of the correlations in the case for an incorrect watermark is embedded, was not Gaussian. Although the two empirical pdf's are closer after the attack, they are still very good separated and the empirical pdf for an incorrect watermark has the mean below zero, compared to the equivalent one before – which is centered on zero. Thus setting a particular threshold can indeed result in a lower false alarm after attack. Similar results were obtained for Barbara, and for the same attack.

For the first detector, the obtained probability of false positive is close to the expected one. The assumption that the wavelet coefficients from different levels and subbands are i.i.d. is thus reasonable and the detector has a good performance.

Results for methods based on the Hyperanalytic Wavelet transform In [NafFirBouIsa08] the watermark is embedded in the HWT domain, in all levels (0, 1 and 2) and all orientations (positive and negative). The test image is Lena, of size 512x512. For α=1.5, the watermarked image has a PSNR of 35.63 dB. The original image, the corresponding watermarked image and the difference image are presented in Fig. 13.

Fig. 13. Original and watermarked images with method ([NafFirBouIsa08]), for α=1.5, PSNR=35.63 dB; Difference image, amplified 8 times.

Measure of invisibility vs. methods	DWT	Barni's method	HWT
PSNR	36.86 dB	36.39 dB	35.60 dB
Weighted PSNR	53.20 dB	33.20 dB	52.00 dB

Table 4. Comparison of invisibility.

The watermarked images have been exposed at some common attacks: JPEG compression with different quality factors (Q), shifting, median filtering with different window sizes M, resizing with different scale factors, cropping with different areas remaining, gamma correction with different values of γ, blurring with a specified point spread function (PSF) and perturbation with AWGN with different variances. Resistance to unintentional attacks, for watermarked image Lena, can be compared to the results obtained using the watermarking methods in [BarBarPiv01] and [Naf07a] analyzing Table 4. For the method in [Naf07a], the same watermark strength, 1.5 is used and the watermark is embedded in all three wavelet decomposition levels, resulting in a PSNR of 36.86 dB. For the method in [BarBarPiv01], the watermark strength 0.2 is used and the embedding is made only in the first resolution level, resulting in a similar quality of the images (PSNR=36.39 dB).

Attacks vs. detector response	DWT-[Naf07a], $\alpha=1.5$			DWT-[BarBarPiv01], $\alpha=0.2$	HWT-[NafFirBouIsa08], $\alpha=1.5$		
	all levels	max level	max subband		all levels	max level	max subband
Before attack	21.57	39.12	33.60	**44.31**	24.78	43.18	26.30
JPEG, Q=50	5.45	6.76	5.02	6.22	6.25	**7.87**	4.85
JPEG, Q=25	3.02	3.67	2.60	3.03	3.23	**4.19**	2.62
JPEG, Q=20	2.55	3.08	2.09	2.38	2.72	**3.58**	2.33
Median filter, M=3	4.29	4.58	4.87	1.57	4.59	**5.42**	4.37
Median filter, M=5	**1.66**	1.24	2.27	0.59	1.61	1.64	1.49
Resizing, 0.75	9.53	15.86	15.64	14.09	10.93	**19.34**	14.67
Resizing, 0.50	4.21	5.72	5.75	2.31	4.56	6.14	**8.71**
Cropping, 256x256	7.40	12.14	17.10	**18.08**	8.68	15.20	13.82
Cropping, 128x128	3.11	4.66	**8.31**	8.01	3.53	6.04	6.86
Cropping, 64x64	1.10	1.72	**4.45**	3.92	1.32	2.47	3.71
Gamma corr., $\gamma=1.5$	22.18	39.76	33.74	43.04	25.31	**43.61**	26.45
Gamma corr., $\gamma=2$	22.59	39.70	32.98	42.43	25.62	**43.24**	25.88
Blur, L=31, $\beta=11$	2.69	7.81	**9.56**	9.05	3.05	9.18	7.55
LPCD, N=5,L=6	9.99	16.13	15.33	**24.84**	12.23	19.58	12.34

Table 5. Resistance to different attacks, for HWT based method compared to DWT based methods.

We have submitted the watermarked images to a local desynchronization attack (DA): local permutation with cancellation and duplication (LPCD) DAs [AngBarMer08], [NafIsa08]. The parameters used in the attack were the ones that visually damage the image less indicated by the authors, N=5 and L=6. The watermark is successfully detected each time, for each method. An example for the attack corresponding at the last line in table 5 is presented in Fig. 14.

From the results, it is clear that embedding in the real parts of the HWT transform yields in a higher capacity at the same visual impact and robustness. In fact the results obtained in [NafFirBouIsa08] are slightly better than the results obtained with the DWT-based methods for JPEG compression, median filtering with window size M=3, resizing and gamma correction. For the other attacks the results obtained are similar with the results of the watermarking methods based on DWT.

Fig. 14a: (left): Watermarked image in the DWT domain, having a PSNR=36.86 dB and a weighted PSNR=53.20 dB compared to the original Lena, (middle): Distorted watermarked with the LPCD attack N=5 and L=6 with PSNR=29.20 dB, weighted PSNR=38.41 dB. (right): Difference between the two images, magnified 100 times.

Fig. 14b: (left): Watermarked image in the HWT domain, having a PSNR=35.60 dB and a weighted PSNR=52 dB compared to the original Lena, (middle): Distorted watermarked with the LPCD attack N=5 and L=6 with PSNR=28.16 dB, weighted PSNR=37.87 dB, (right): Difference between the two images, magnified 100 times.

In conclusion, for a watermarking system, robustness evaluation should be made if invisibility criteria are satisfied. For this purpose, perceptual watermarks are being used to overcome the issue of robustness against invisibility. In the literature, there was proposed a blind spread spectrum technique that uses a perceptual mask in the wavelet domain, taking into account the noise sensitivity, texture and the luminance content of all image subbands. We described new techniques proposed, based on the modifications of this perceptual mask, in order to increase robustness, while still maintaining imperceptibility. Moreover, using the new mask, information is successfully hidden in the *lower frequency* levels, thus increasing the capacity and making the watermark more robust to common attacks that affect both high frequencies and low frequencies of the image. A good balance between robustness and invisibility of the watermark is achieved when embedding is made in all detail subbands for all resolution levels, except the coarsest level; this can be particularly useful against erasure of high frequency subbands containing the watermark in Barni’s system.

A nonlinear detector with fixed threshold – as ratio between correlation and the image dependent ratio – has been used; three watermark detectors were proposed in [Naf07a] that take advantage of the hierarchical wavelet decomposition: 1) from all resolution levels, 2) separately from each level, considering the maximum detector response for each level and 3) separately from each subband, considering the maximum detector response for each subband. This has been advantageous for cropping, scaling and median filtering where the 3rd detector shows improved performance. We tested our methods against different attacks, and found out that it is better than Barni’s method. The behavior of our methods can be explained by the fact that we have used a better estimate of the mask and we took advantage of the diversity of the wavelet decomposition. The effectiveness of the new perceptual mask is appreciated by comparison with Barni’s method.

The HWT is a very modern WT and a very simple implementation of this transform has been used, which permits the exploitation of the mathematical results and of the algorithms previously obtained in the evolution of wavelets theory. It does not require the construction of any special wavelet filter. It has a very flexible structure, as we can use any orthogonal or bi-orthogonal real mother wavelets for the computation of the HWT. The presented implementation leads to both a high degree of shift-invariance and to an enhanced directional selectivity in the 2D case. An ideal Hilbert transformer was considered. A new type of pixel-wise masking for robust image watermarking in the HWT domain has been presented [NafFirBouIsa08]. Modifications were made to two existing watermarking technique proposed in [BarBarPiv01] and [Naf07a], based on DWT. These techniques were selected for their good robustness against the usual attacks. The method is based on the method in [BarBarPiv01], with some modifications. The first modification is in computing the estimate of the variance, which gives a better measure of the texture activity. An improvement is also owed to the use of a better luminance mask. The third improvement is to embed the watermark in the detail coefficients at all resolutions, except the coarsest level, making the watermark more attack resilient. The HWT embedding exploits the coefficients z_{+r} and z_{-r}.

The simulation results illustrate the effectiveness of the proposed algorithms. The methods were tested against different attacks (in terms of robustness). The HWT based watermarking method is similar and in some cases outperforms the DWT based methods, but it has a superior capacity than the DWT based methods.

Other embedding mechanisms can also be conceived. it can be observed that the coefficients z_{+i} and z_{-i} are not exploited yet. So, the redundancy of the embedding can be increased exploiting the quaternions $(z_{+r}, z_{-r}, z_{+i}, z_{-i})$. Another embedding mechanism can use complex images of the form $z_{+} = z_{+r} + jz_{+i}$ or $z_{-} = z_{-r} + jz_{-i}$. The watermark can be embedded in the absolute value or in the phase of those images. We have already tried the embedding in the absolute values, [NafFirIsaBou08], obtaining similar results with those presented. The observation that most of the information contained into a complex image is carried by its phase component can be taken into account in the future. Another future research direction is the use of the statistical properties of the HWT to improve the watermark detection.

2.2.2 Best mother wavelet for perceptual watermarks

In the paper [NafIsa09] we investigated ***the choice of the best mother wavelet*** for perceptual data hiding [Naf08, NafNafIsaBor08] in the wavelet domain. The watermarked images are submitted to a series of attacks based on normal image processing techniques. Simulations show that regardless of the content of the images (contours, textures, homogeneous zones), the best mother wavelets are the ones used in the JPEG2000 standard.

Initially, the proposed technique was fine-tuned on the DWT with the mother wavelet Daubechies-6. The question was however if this mother wavelet gives the best results in terms of detection, in the case of attacks based on normal processing techniques. We investigate the choice on the best mother wavelet for optimization before and after attacks based on normal processing techniques on various watermarked images.

Various images [USC09], [Pic09] have been watermarked at level l=0 with embedding strengths α=1.5 [NafIsaBor06] and α=0.2 [BarBarPiv01] resulting in a similar image quality. From those images we present results for Lena, Texmos1.p512, Baboon [USC09] and Picasso [Pic09], a less known image, but nevertheless also interesting for its content.

Generally, images contain three types of regions: homogeneous zones, textures and contours. We have identified these regions for the test images using the normalized local standard deviation, *nlv*, of the original image. Pixels with *nlv*>0.35 are from contours, pixels with 0.045<*nlv*<0.35 are from textures and pixels with 0.045>*nlv* are from homogeneous zones. We chose three categories of test images, containing mostly contours (class 3, Texmos1.p512), textures (class 2, Lena and Baboon) respectively homogeneous zones (class 1, Picasso); see Table 2, second column.

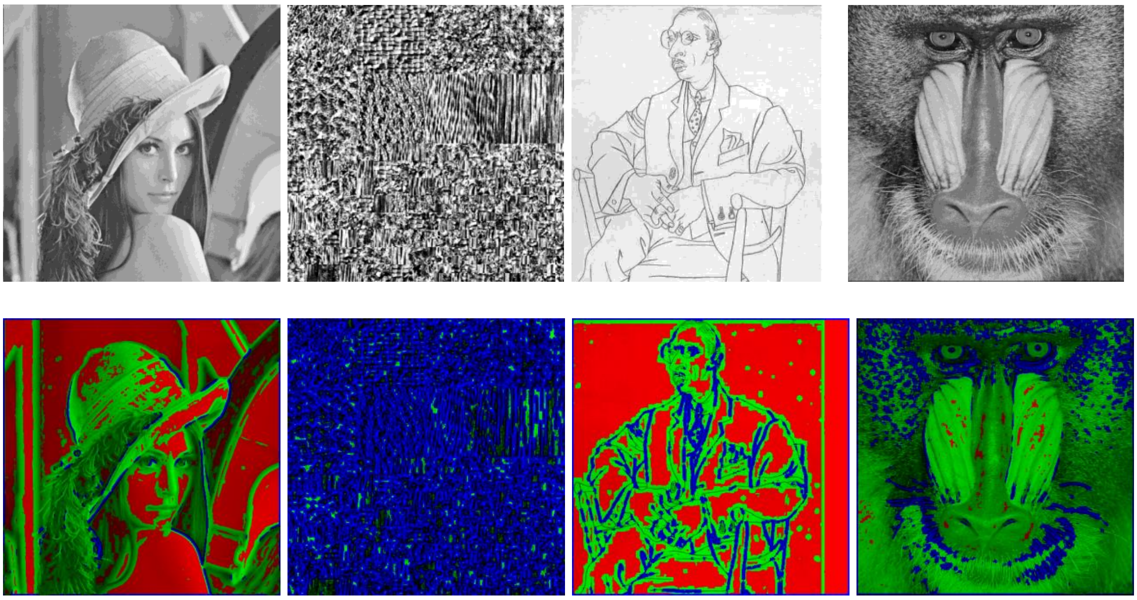

Fig 15. Top: Images used in experiments; Bottom: Segmentation in three types of regions, criterion normalized local standard deviation. Regions: red=1/Homogeneous 0→0.045; green=2/Textures 0.045→ 0.35; blue=3/Contours 0.35→1

	PSNR (dB)								
Image vs. Mother wavelet	***db2***	***db3***	***db4***	***db5***	***db6***	***db7***	***bior4.4***	***bior2.2***	***Barni***
Lena	37.92	38.16	38.28	38.33	***38.35***	**38.41**	38.26	35.97	36.39
Picasso	33.97	34.04	34.15	34.25	***34.27***	**34.35**	34.02	32.07	35.95
Texmos1p.512	28.09	28.21	28.28	28.26	***28.29***	**28.33**	28.28	26.08	**29.04**
Baboon	33.30	33.39	33.40	33.43	***33.46***	**33.47**	33.30	31.32	33.33

Table 6. Comparison of invisibility

Image	**Predominant class /Percentage**	**Best mother wavelet**	**Observations**		
			1/Homogeneous zones	***2/Textures***	***3/Contours***
Lena	2/48.50	bior2.2, db7	46.61%	**48.50%**	4.89%
Picasso	1/56.28	bior2.2, bior4.4	**56.28**%	30.19%	13.54%
Texmos1	3/92.15	bior2.2, bior4.4	0.00%	7.85%	**92.15%**
Baboon	2/76.28	bior2.2, db6	1.21%	**76.28%**	22.51%

Table 7. Image content classification based on the local standard deviation; best mother wavelet for watermarking for each image.

For the watermarking method [NafIsaBor06], we choose a different mother wavelet for each experiment, having *n* vanishing moments, with *n* ranging from 2 to 7: db2, db3, and so on, as well as the biorthogonal mother wavelets used in the JPEG2000 standard: Daubechies 9/7 (bior4.4) and the 5/3 LeGall wavelet (bior2.2). We chose them because they are extremely short, symmetric, hence avoiding boundary artifacts, with a maximum number of vanishing moments and minimum support [UnsBlu03].

A binary watermark is embedded in all the detail wavelet coefficients of the first resolution level, l=0, as previously described. The peak signal-to-noise ratio values are given in Table 6. The highest PSNR values are obtained for the mother wavelet db7, followed by the ones with db6, while the smallest PSNR values are obtained for bior2.2.

The watermarked images were tested against attacks based on normal signal processing techniques: JPEG and JPEG2000 compression, median filtering, cropping, resizing and gamma correction, for different parameters. For each attacked image, the ratio correlation per threshold ρ/T_ρ is computed for $P_f=10^{-8}$. Results obtained for Lena are presented in Table 8.

The highest results are marked with bold characters, while the second highest results are marked with bold italic characters. Counting the number of "best" detector response (highest and second highest) for each mother wavelet, the best mother wavelets for the image Lena are: bior2.2, db7, db6, bior4.4, as seen in the third column of Table 7.

Repeating the above procedure, we obtain similar results for the other test images; see Table 9-12. Practically, we can see that regardless the content of the image, the best mother wavelet that optimizes the detection for the method in [NafIsaBor06] is also the one proposed in the standard JPEG2000 (bior2.2 followed closely by bior4.4). Unfortunately, this also leads to smallest PSNR values between the original and watermarked images.

	Detection response for DWT based method [NafIsaBor06] using different mother wavelets vs. Barni's method [BarBarPiv01]								
Attack vs. Mother wavelet	***db2 (3)***	***db3 (0)***	***db4 (2)***	***db5 (1)***	***db6 (4)***	***db7 (4)***	***bior4.4 (3)***	***bior2.2 (11)***	***Barni (6/14)***
Before	37.61	39.08	39.29	40.88	40.92	***41.01***	40.79	**42.76**	**44.31**
JPEG,Q=50	6.08	6.05	4.92	***6.15***	5.53	5.06	6.12	**7.47**	6.46
JPEG,Q=20	***2.90***	2.79	1.90	2.89	2.34	1.99	2.66	**3.29**	2.47
Median filt., 3×3	***3.65***	3.45	3.48	2.91	3.00	2.83	**3.80**	3.50	1.06
Median filt., 5×5	1.65	1.57	1.63	1.11	1.40	1.15	***1.70***	**1.74**	0.49
Resizing, ¾	14.69	16.24	15.58	17.17	16.81	16.55	***17.38***	**17.83**	14.35
Resizing, ½	***8.19***	1.09	0.56	6.90	0.26	4.42	7.80	**9.04**	2.35
Cropping, 256×256	11.71	11.76	**15.94**	12.25	13.07	15.14	13.35	***15.12***	**17.20**
Cropping, 64×64	1.98	1.91	**3.15**	1.93	2.18	***2.72***	2.22	2.60	**3.34**
Gamma corr., γ=0.5	36.06	37.35	37.62	39.09	39.07	***39.25***	38.95	**40.87**	**44.51**
Gamma corr., γ=2	38.18	39.71	39.81	41.35	***41.49***	41.46	41.25	**43.01**	42.66
Blurring, L=31, θ=31	6.95	8.20	8.92	9.30	***9.56***	**9.82**	9.66	9.28	8.86
JPEG2000, CR=20	20.90	24.69	22.80	24.48	**25.47**	23.09	22.02	***24.81***	**28.91**
JPEG2000, CR=12.5	30.53	33.62	32.43	34.53	***35.01***	33.46	33.05	**35.24**	**38.56**

Table 8. Robustness in the case of different types of attacks, for the image Lena.

	Detection response for DWT based method [NafIsaBor06] using different mother wavelets vs. Barni's method [BarBarPiv01]								
Attack vs. Mother wavelet	***db2 (2)***	***db3 (2)***	***db4 (1)***	***db5 (1)***	***db6 (0)***	***db7 (1)***	***bior4.4 (7)***	***bior2.2 (12)***	***Barni (0/14)***
Before	22.15	22.90	22.70	24.07	24.05	23.57	***24.41***	**26.60**	18.81
JPEG,Q=50	2.89	2.96	2.24	2.78	2.37	1.86	***3.01***	**4.47**	1.51
JPEG,Q=20	1.50	***1.66***	0.83	1.54	1.10	0.60	1.58	**2.04**	0.70
Median filt., 3×3	**2.01**	***1.70***	1.46	1.51	1.19	0.57	1.35	1.36	0.47
Median filt., 5×5	-0.01	-0.18	-0.28	-0.28	-0.56	-0.76	-0.22	0.05	0.39
Resizing, ¾	8.23	9.15	8.84	9.55	9.28	9.03	***9.72***	**10.16**	5.00
Resizing, ½	***5.11***	0.68	0.42	4.22	-0.14	3.17	4.83	**5.83**	1.20
Cropping, 256×256	8.94	9.68	**10.97**	9.78	10.32	10.95	10.54	**11.79**	8.96
Cropping, 64×64	1.50	2.19	2.56	1.93	1.95	**2.95**	2.59	***2.94***	1.97
Gamma corr., γ=0.5	20.17	20.89	20.62	21.80	21.72	21.29	***22.19***	**24.14**	21.42
Gamma corr., γ=2	25.06	25.83	25.73	27.33	27.46	26.90	***27.44***	**29.84**	17.26
Blurring, L=31, θ=31	3.78	3.48	3.58	**4.16**	4.11	4.01	4.01	**4.26**	2.81
JPEG2000, CR=20	14.09	15.72	14.54	15.50	15.71	14.04	***15.92***	**17.56**	11.81
JPEG2000, CR=12.5	18.26	19.45	18.84	19.94	20.06	19.15	***20.37***	**22.31**	15.90

Table 9. Robustness in the case of different types of attacks, for the image Picasso.

	Detection response for DWT based method [NafIsaBor06] using different mother wavelets vs. Barni's method [BarBarPiv01]								
Attack vs. Mother wavelet	***db2 (0)***	***db3 (0)***	***db4 (0)***	***db5 (0)***	***db6 (3)***	***db7 (1)***	***bior4.4 (9)***	***bior2.2 (13)***	***Barni (0/14)***
Before	22.34	23.46	24.57	23.67	24.47	24.77	***24.84***	**27.10**	21.87
JPEG,Q=50	13.62	14.34	14.86	14.21	14.77	14.75	***14. 92***	**17.24**	12.74
JPEG,Q=20	6.91	7.35	7.38	7.16	7.61	7.01	***7.74***	**8.84**	6.09
Median filt., 3×3	2.62	2.76	2.22	2.46	2.45	2.21	***2.67***	**2.90**	0.25
Median filt., 5×5	0.36	0.08	-0.08	-0.30	0.03	-0. 44	-0.17	0.08	0.02
Resizing, ¾	8.18	9.70	9.53	9.57	9.92	9.92	***10.32***	**10.94**	6.27
Resizing, ½	4.92	0.91	0.25	4.16	0.11	3.50	***5.41***	**6.57**	1.18
Cropping, 256×256	10.75	11.61	12.16	11.71	12.08	12.10	***12.41***	**13.54**	10.55
Cropping, 64×64	2.74	2.46	2.91	2.88	***2.94***	2.64	2.74	**3.04**	2.48
Gamma	24.46	26.09	27.19	26.24	27.05	***27.61***	27.07	**29.15**	20.05

	Detection response for DWT based method [NafIsaBor06] using different mother wavelets vs. Barni's method [BarBarPiv01]								
Attack vs. Mother wavelet	***db2 (0)***	***db3 (0)***	***db4 (0)***	***db5 (0)***	***db6 (3)***	***db7 (1)***	***bior4.4 (9)***	***bior2.2 (13)***	***Barni (0/14)***
corr., γ=0.5									
Gamma corr., γ=2	21.32	21.57	22.55	21.86	22.52	22.47	***23.44***	**25.48**	24.54
Blurring, L=31, θ=31	3.23	3.54	3.85	3.86	3.84	4.14	***4.15***	**4.43**	3.23
JPEG2000, CR=20	8.79	10.61	9.99	9.39	***10.65***	9.71	9.69	**10.74**	9.53
JPEG2000, CR=12.5	14.85	16.89	16.78	15.90	***17.33***	16.73	16.59	**17.93**	15.55

Table 10. Robustness in the case of different types of attacks, for the image texmos1.p512.

	Detection response for DWT based method [NafIsaBor06] using different mother wavelets vs. Barni's method [BarBarPiv01]								
Attack vs. Mother wavelet	***db2 (2)***	***db3 (4)***	***db4 (1)***	***db5 (0)***	***db6 (5)***	***db7 (2)***	***bior4.4 (2)***	***bior2.2 (10)***	***Barni (2/14)***
Before	24.23	24.97	24.85	24.91	25.30	25.06	***25.34***	**27.38**	25.16
JPEG,Q=50	9.62	***9.78***	9.25	9.59	9.51	9.20	9.76	**11.14**	9.56
JPEG,Q=20	5.03	***5.08***	4.17	4.91	4.67	4.20	4.89	**5.81**	4.50
Median filt., 3×3	**1.52**	1.33	0.95	0.95	0.79	0.72	1.09	***1.44***	0.25
Median filt., 5×5	-0.16	-0.40	-0.54	-0.51	-0.83	-0.64	-0.47	-0.17	-0.01
Resizing, ¾	9.09	**11.28**	10.49	10.10	***11.24***	10.48	10.34	11.00	8.81
Resizing, ½	***6.05***	0.80	0.20	4.96	0.06	3.79	6.02	**7.33**	1.95
Cropping, 256×256	12.56	12.86	15.00	13.14	13.68	***14.84***	13.88	**15.27**	15.24
Cropping, 64×64	1.79	1.77	**2.74**	1.77	2.00	***2.41***	2.08	2.36	**3.03**
Gamma corr., γ=0.5	23.34	24.56	24.20	24.14	***24.86***	24.34	24.37	**26.40**	24.92
Gamma corr., γ=2	24.53	24.90	24.94	25.04	***25.22***	25.15	25.63	**27.56**	24.85
Blurring, L=31, θ=31	2.92	3.03	3.09	3.10	3.18	3.15	***3.30***	**3.66**	2.69
JPEG2000, CR=20	12.24	**14.28**	13.06	12.99	**14.15**	12.75	12.56	13.78	**14.11**
JPEG2000, CR=12.5	17.69	19.46	18.52	18.62	***19.53***	18.39	18.31	**20.00**	19.57

Table 11. Robustness in the case of different types of attacks, for the image Baboon.

Wavelets have two important properties: the magnitudes of the wavelet coefficients are strongly correlated across scales and the wavelet coefficients of a piecewise smooth image fall into two categories: large amplitude coefficients located near edges, and the smaller ones, located in smooth regions [UnsBlu03]. The JPEG2000 algorithm takes into account these properties. In fact, it uses the filters LeGall 5/3 for lossless compression; these are used to construct the mother wavelet bior2.2 which has a more compact support, and is suitable for edges from an image.

The perceptual masking embeds the watermark with a higher strength in high wavelet coefficients which means the watermarking method in [NafIsaBor06] can be optimized on the criterion of the choice of the best mother wavelet, in the same manner as the image compression method recommended in the JPEG2000 standard [UnsBlu03]. Moreover, the two image processing methods are optimized using the same mother wavelet.

The best mother wavelet for the method proposed in [NafIsaBor06], regardless of the content of the host image, is bior2.2, as seen from the results. The mother wavelet bior2.2 leads to better detection results than the ones obtained in [BarBarPiv01] for all the host images tested here. For highly textured images, there are attacks where Barni's method is better (6 out of 14 cases for Lena and 2 out of 14 cases for Baboon). For images with contours or homogeneous zones, for all attacks, the method in [NafIsaBor06] using bior2.2 works better than the method in [BarBarPiv01]. This is in accordance with [UnsBlu03]: the approximation properties of the LeGall 5/3 are much better than those of the Daubechies4 filter of the same order.

2.2.3 Watermarking using turbocodes

Watermarking robustness can be also assured by using some sort of encoding of the watermark, usually a repetition code or an error correcting code [Naf08]. The association between watermarking and turbo codes is effective in the wavelet domain [SerAmbTomWad03], [AbdGlaPan02], [BalPer01].

In [NafIsaKov09] we proposed a watermarking system that uses the biorthogonal discrete wavelet transform, DWT and the message is encoded before embedding. The method is very simple, implying four steps: turbo coding of the watermark message, embedding the turbo coded watermark into the host image using a perceptual mask, extraction of the turbo coded watermark from the watermarked, possibly corrupted image, and turbo decoding of the watermark. The encoded watermark is masked using the same mask described previously.

The orthogonal DWT permits the analysis in the wavelet domain. The analyzed signal can be exactly reconstructed using the inverse DWT (IDWT). The same scaling function and mother wavelets are used in the analysis and in the reconstruction stages. The biorthogonal DWT was proposed by Feauveau [Fea92]. This is a more flexible DWT. Sacrificing the perfect reconstruction (a delayed variant of the analyzed signal is reconstructed) different couples of scaling functions and mother wavelets can be used for analysis and for reconstruction. In fact, our system embeds the watermark in the biorthogonal DWT domain.

The image I, of size $2M \times 2N$, is decomposed into 4 levels of the DWT, where I_l^θ is the subband from level $l \in \{0,1,2,3\}$, and orientation $\theta \in \{0,1,2,3\}$ (horizontal, diagonal and vertical detail subbands, and approximation subband). A binary watermark message m is turbo coded and the result is casted on subbands on different levels of resolutions, $x_l^\theta(i,j)$. The turbo coded watermark $x_l^\theta(i,j)$ is embedded in the wavelet coefficients of the l^{th} level, having the magnitude higher than a threshold T:

$$\tilde{I}_l^\theta(i,j) = I_l^\theta(i,j) + \alpha w_l^\theta(i,j) x_l^\theta(i,j), \text{ if } \left|I_l^\theta(i,j)\right| > T, \tag{23}$$

where α is the embedding strength, $w_l^\theta(i,j)$ is a weighing function, which is a half of the quantization step $q_l^\theta(i,j)$. The quantization step of each coefficient is computed as in

[NafNafIsaBor08] and the embedding takes place in all resolution levels, $l \in \{0,1,2\}$, except the coarsest resolution level.

The detection requires the original watermark and the original image, or some significant vector extracted from its wavelet transform, specifically in this case, the detail coefficients with an absolute value above the threshold T. The watermark bit is obtained from the wavelet coefficient $\hat{I}_l^\theta(i,j)$ of the possibly distorted image $\hat{I}^w$, and the original coefficient $I_l^\theta(i,j)$:

$$\hat{x}_l^\theta(i,j)=\frac{\hat{I}_l^\theta(i,j)-I_l^\theta(i,j)}{\alpha w_l^\theta(i,j)},\ \text{if } \left|I_l^\theta(i,j)\right|>T\,. \tag{24}$$

The estimate of the encoded message is decoded and the watermark message $\hat{m}$ is obtained. We compute at the output the bit error rate between the original watermark message m and the received watermark message $\hat{m}$:

$$BER=\frac{\text{number of erroneous bits}}{\text{number of bits}}, \tag{25}$$

which gives a measure of the performance. In the following, we explain the architecture of the chosen turbo code.

Turbo codes [BerGlaThi93] [BerGla96] are characterized by their powerful error correcting capability while maintaining reasonable complexity and flexibility in terms of coding rates. Douillard and Berrou have proposed a new family of turbo codes with multiple inputs [DouBer05]. Particularly, they show that a parallel concatenation of two binary recursive systematic convolutional (RSC) codes based on multiple-input (*r*-inputs) linear feedback shift registers (LFSRs) provides a better overall performance than turbo codes with single input over AWGN channel. Multi-binary turbo codes (MBTC) have been adopted in the digital video broadcasting (DVB) standards for return channel via satellite (DVB-RCS) and the terrestrial distribution system (DVB-RCT), and also in the 802.16 standard for local and metropolitan area networks.

A parallel concatenation of two identical *r*-ary RSC encoders with an interleaver (ilv) is shown in Fig. 16 [KovBalNaf06], where *u*, c^1 and c^2 represent the encoder outputs. The scheme of the 8-state duo-binary RSC encoder, with polynomials 15 (feedback) and 13 (redundancy) in octal form, is shown in Fig. 17, where S_1, S_2 and S_3 denote the encoder states. We consider here the particular case of MBTC, namely, the duo-binary turbo codes (DBTC). The trellis of the first encoder is closed to 0 and the trellis of the second encoder is unclosed. The rate of the DBTC is ½.

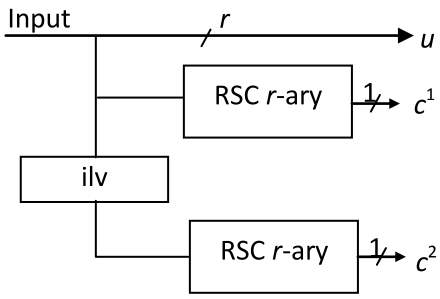

Fig. 16. The *r*-ary turbo-encoder

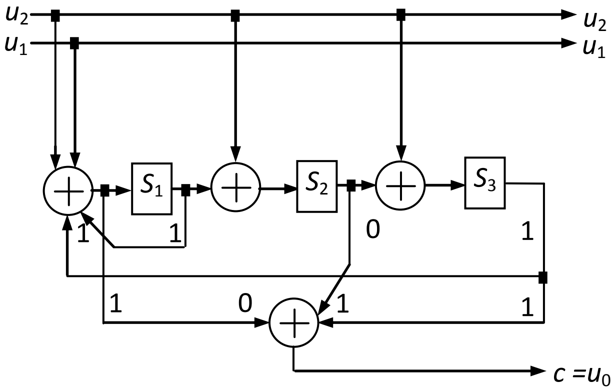

Fig. 17. Scheme of the 8-state duo binary RSC encoder with the rate 2/3. Encoder polynomials: 15 (feedback) and 13 (redundancy) in octal form (DVB-RCS constituent encoder for *r*=2).

We consider an *S*-interleaver [Cro00], which is semi-random and exhibits excellent performance since it has very high minimum distances even for moderate block sizes. For the block size of 768 bits, the *S*-interleavers designed in [DolDiv95] [KovBalNaf05] yields minimum distances of 20. The minimum distance can be further increased [Cro00]. The design of the interleaver is based on a random selection with the following constraint:

$$d(i,j)=\left|\pi(i)-\pi(j)\right|+\left|i-j\right|\geq S\,, \tag{26}$$

where π is the fully random permutation function and $d(i,j)$ represents the interleaving distance between the positions i and j, $i,j=1,\ldots,n$. Here, n denotes the codeword size. Based on this design method, the interleaver used has a minimum distance of 28 for a block size of 768 bits. The length of the coded sequence is 2×768=1536 bits. For decoding we used the Max-Log-MAP algorithm [VogFin00]. This suboptimal version is preferred in practice due to its low computational complexity while keeping near-optimal performance [DouBer05]. The scaling factor of the extrinsic information is equal with 0.75 [KovBalBayNaf07]. We assume at the decoder a number of 15 iterations with a stopping criterion.

In Fig. 18 a) and b), bit error rate (BER) and frame error rate (FER) performance of the uncoded case and of the DBTC are plotted for rate ½. In our simulations we considered the AWGN channel. For a SNR=1.6 dB the bit error rate is BER=$1.5\cdot 10^{-6}$. For a FER=$2\cdot 10^{-4}$, DBTC performs as close as 0.8 dB from the Shannon limit.

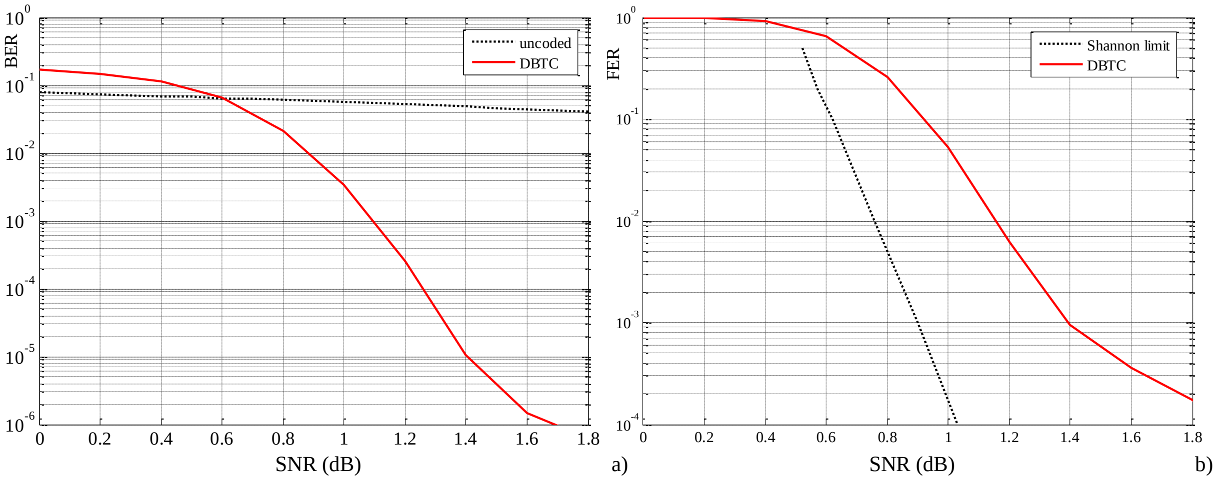

Fig. 18. Bit Error Rate and Frame Error Rate performance for uncoded case and 1/2 rate Duo-Binary Turbo Coded (DBTC) transmission over AWGN channel as function of SNR.

The image Lena (512×512) is decomposed into a four level decomposition with a biorthogonal mother wavelet. As shown in [NafIsa09], the biorthogonal mother wavelets used in the JPEG2000 standard are most suitable. In experiments, we use the mother wavelet Biorthogonal 2.2 (bior2.2). A pseudo-random binary message m with values $\{-1,1\}$ is turbo coded using a DBTC, resulting in a coded watermark message. The block size is 768 bits and the number of blocks for the image Lena is 7. The coded watermark is embedded into each subband in coefficients with the magnitude greater than a threshold T, for levels 0, 1 and 2, using eq. (23). In all simulations, this threshold was experimentally set to the value 10. The embedding strength is set to $\alpha=9$, resulting in a watermarked image with the peak signal-to-noise ratio PSNR=29.95 dB. Two attack experiments were performed: addition of white Gaussian noise (AWGN) and JPEG compression.

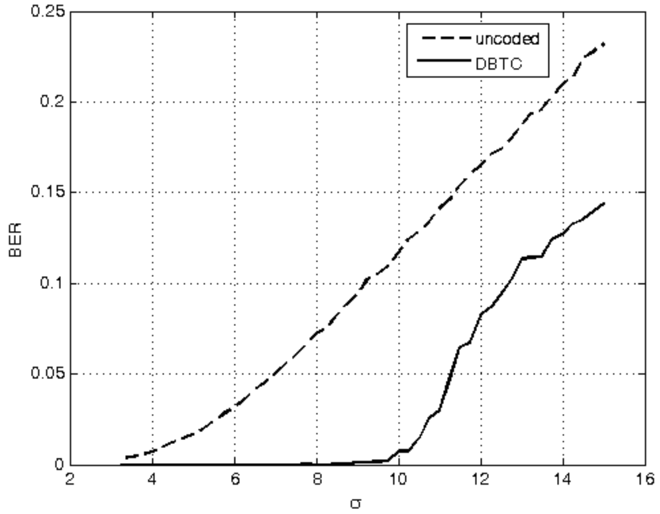

Fig. 19. BER versus noise standard deviation obtained without coding the watermark and using a DBTC for the AWGN attack.

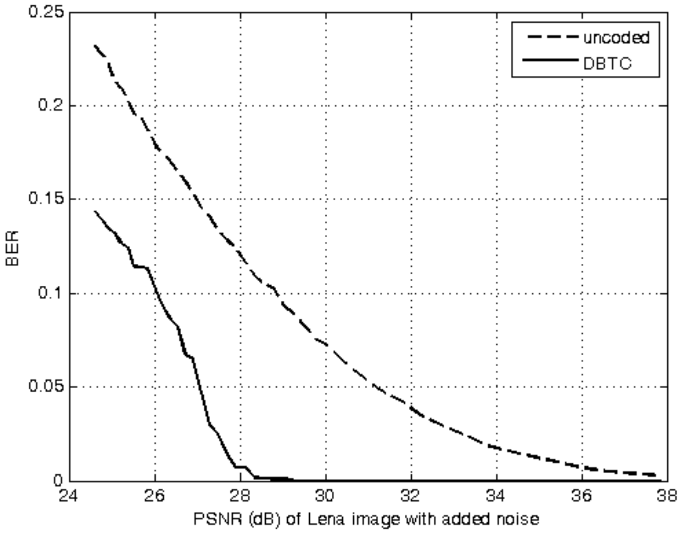

Fig.20. BER versus the PSNR obtained without coding the watermark and using a DBTC for the AWGN attack.

In the first experiment, we added noise with mean 0 and variance σ^2 to the watermarked image. We repeated the experiment for σ ranging from 3.25 to 15 with step 0.25; we plotted BER, without coding the watermark, and with a DBTC. Fig. 19 presents the values of the BER computed for different values of σ, while Fig. 20 presents BER as a function of the PSNR between the attacked image and the watermarked image, for the uncoded sequence as well the coded sequence. For values of σ inferior to 8, the noise addition doesn't degrade the image too much and the PSNR value is still high. For a PSNR superior to 29 dB, the watermark is reconstructed without error, using turbo decoding. For PSNR values inferior to 29 dB, the attacked images are visually impaired by the noise addition, making the attacked images useless.

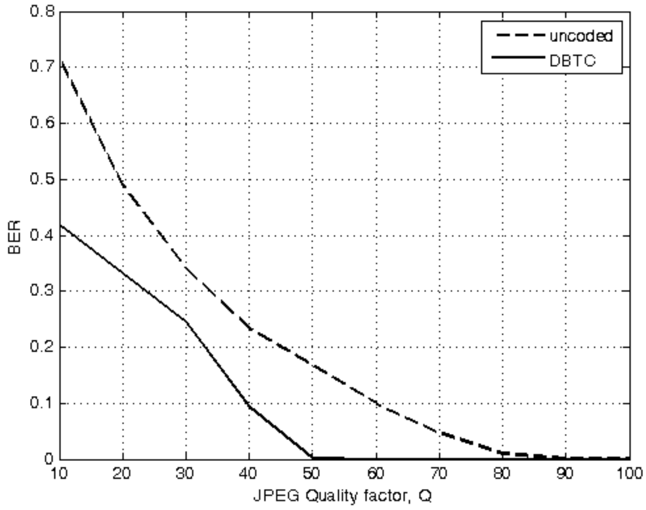

Fig. 21. BER versus quality factor obtained without coding the watermark and using a DBTC for JPEG compression.

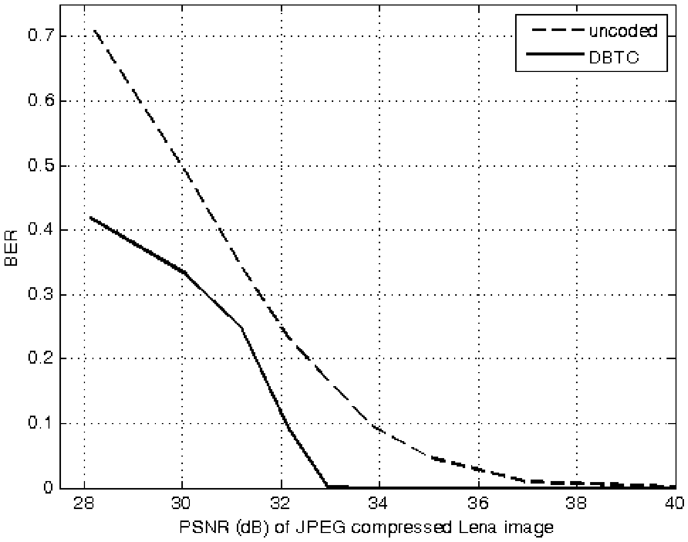

Fig. 22. BER versus PSNR obtained without coding the watermark and using a DBTC for JPEG compression.

Next we studied the robustness of the watermark using the JPEG compression attack. We have compressed the watermarked image using different quality factors, Q from 100 to 10, and we have plotted the BER with and without turbo coding the watermark. Fig. 21 presents the values of the BER computed for different values of the quality factors, for the uncoded sequence as well the coded sequence. For a quality factor higher than 50, the reconstruction of the watermark is almost perfect. Fig. 22 presents BER as a function of the PSNR between the attacked image and the watermarked image.

Attack vs. BER	BER	
	Uncoded	DBTC
JPEG compression, Q=50, PSNR=32.94 dB	0.167132	0.001488
AWGN, σ=8, PSNR=29.29 dB	0.0885	$3.25 \cdot 10^{-4}$

Table 12. A BER based comparison of the coded and uncoded approach.

Table 12 shows numerical values of the BER for the uncoded and for the coded case for each attack. We can see the performance of turbo coding in watermarking in the decrease of the bit error rate. For less severe attacks, the watermark is perfectly reconstructed. This is the case when the attack on the watermarked image can be modeled like an AWGN transmission channel, with a high value of the SNR. It is to be noted that the coding gain brought by the use of the DBTC is superior to 2 dB.

Analyzing the simulation results the advantages of the use of turbo coding in data embedding are obvious. The simulation results presented illustrate the decrease of the bit error rate of the message extracted from the watermarked image attacked with two types of attacks. For less severe attacks, the watermark is perfectly reconstructed if turbo codes are used. This is the case when the attack on the watermarked image can be modeled like an AWGN channel, with a high value of the SNR, needed for a successful decoding for the Max-Log-MAP algorithm. For severe attacks, the images obtained are visually impaired, making them useless. It is to be noted that the coding gain brought by the use of the DBTC is higher than 2 dB.

2.3 Image Denoising

Papers: [IsaFirNafMog11]; [FirNafIsaIsa11]; [NafIsaIsa11]; [FirNafBouIsa10]; [FirNafBouIsa09]

2.3.1 Images affected by AWGN

Shift-invariance associated with good directional selectivity is important for the use of a wavelet transform, (WT), in many fields of image processing. Generally, complex wavelet transforms, e.g. the Double Tree Complex Wavelet Transform, (DT-CWT), have these useful properties. In [FirNafBouIsa09] we proposed the use of an implementation of such a WT, namely the Hyperanalytic Wavelet Transform, (HWT) [AdaNafBouIsa07], in association with filtering techniques already used with the Discrete Wavelet Transform, (DWT). The result is a very simple and fast image denoising algorithm. Some simulation results and comparisons prove the performance obtained using the new method.

During acquisition and transmission, images are often corrupted by additive noise. The aim of an image denoising algorithm is then to reduce the noise level, while preserving the image features. There is a big diversity of estimators used as denoising systems. One may classify these systems in two categories: those directly applied to the signal and those who use a wavelet transform before processing. In fact, David Donoho introduced the word denoising in association with the wavelet theory [DonJoh94]. From the first category, we must mention the denoising systems proposed in [FoiKatEgi07] and [WalDat00]. The first one is based on the shape-adaptive DCT (SA-DCT) transform that can be computed on a support of arbitrary shape. The second one is a maximum a posteriori (MAP) filter that acts in the spatial domain.

The multi-resolution analysis performed by the WT has been shown to be a powerful tool to achieve good denoising. In the wavelet domain, the noise is uniformly spread throughout the coefficients, while most of the image information is concentrated in the few largest ones (sparsity of the wavelet representation) [FouBenBou01], [SenSel02], [PizPhi06], [AchKur05], [GleDat06], [LuiBluUns07], [Shu05], [ZhoShu07], [Olh06]. The corresponding denoising methods consist of three steps [DonJoh94]:

1) the computation of the forward WT,
2) the filtering of the wavelet coefficients,
3) the computation of the IWT of the result obtained.

Consequently, there are two tools to be chosen: the WT and the filter. In what concerns the first choice, we proposed in [FirNafBouIsa09] the new implementation of the HWT. In [FouBenBou01], [PizPhi06] was used the UDWT, in [SenSel02], [AchKur05], [Shu05] the DTCWT, and in [GleDat06], [LuiBluUns07] the DWT. Concerning the second choice, numerous non-linear filter types can be used in the WT domain. A possible classification is based on the nature of the noise-free component of the image to be processed. Basically, there are two categories of filters: those built assuming only the knowledge of noise statistics (a non-parametric approach), and those based on the knowledge of both signal and noise statistics (a parametric approach). From the first category we can mention: the hard-thresholding filter, [DonJoh94], the soft-thresholding filter (soft) [DonJoh94], [Mal99], that minimizes the Min-Max estimation error and the Efficient SURE-Based Inter-scales Point-wise Thresholding Filter [LuiBluUns07], that minimizes the Mean Square Error (MSE). To the second category belong filters obtained by minimizing a Bayesian risk under a cost function, typically a delta cost function (MAP estimation [FouBenBou01], [SenSel02], [AchKur05]) or the minimum mean squared error (MMSE estimation [PizPhi06]). The denoising algorithms proposed in [SenSel02], [PizPhi06], [AchKur05], [GleDat06], [LuiBluUns07] exploit the inter-scale dependence of wavelet coefficients. The method proposed in [PizPhi06] takes into account the intra-scale dependence of wavelet coefficients as well. The statistical distribution of the wavelet coefficients changes from scale to scale. The coefficients for the first iterations of the WT have a heavy tailed distribution. To deal with this mobility, there are two solutions. The first one assumes the use of a fixed simple model, risking a decrease of accuracy across the scales. This way, there is a chance to obtain a closed form input-output relation for the MAP filter. Such an input-output relationship has two advantages: it simplifies the implementation of the filter and it allows the sensitivity analysis. The second solution assumes the use of a generalized model, defining a family of distributions and the identification of the best fitting element of this family to the distribution of the wavelet coefficients at a given scale (e.g. the family of Pearson's distributions in [FouBenBou01], the family of $S\alpha S$ distributions in [AchKur05] and the model of Gauss–Markov random field in [GleDat06]). The use of a generalized model makes the treatment more accurate but requires implicit solutions for the MAP filter equation, which can often be solved only numerically. The MAP estimation of u, based on the observation $z = u + n$, (where n represents the WT of the noise and u the WT of the useful component of the input image) is given by the MAP filter equation: $\hat{u}(z) = \arg\max_u \left\{ \ln\left(p_n(z-u)\, p_u(u) \right) \right\}$, where p_a represents the probability density function (pdf) of a. If the pdfs p_u and p_n do not take into account the inter-scale dependency of the wavelet coefficients the obtained filter is called marginal. For the MAP filters that take into account the inter-scale dependency, the pdfs are multivariate functions. In the following, we consider a univariate Gaussian distribution for the noise coefficients (p_n) and a univariate Laplacian distribution for the useful signal coefficients (p_u). The noise coefficients have zero mean and variance σ_n^2.

The solution of the MAP filter equation Consequently, we take:

$$p_u(u) = \frac{1}{\sqrt{2}\sigma_u} \exp\left(-\frac{\sqrt{2}}{\sigma_u} |u| \right). \qquad (27)$$

Under the considered hypothesis, the MAP filter equation becomes:

$$\frac{(z - \hat{u})}{\sigma_n^2} - \frac{\sqrt{2}}{\sigma_u} \operatorname{sgn} \hat{u} = 0 . \qquad (28)$$

Finally, the solution corresponding to the proposed marginal MAP filter (pmMAPf) can be expressed as:

$$\hat{u} = \operatorname{sgn}(z)\left(|z| - \frac{\sqrt{2}\sigma_n^2}{\sigma_u}\right)_+ , \tag{29}$$

where $(X)_+ = X$ for $X > 0$ and 0 otherwise. In the equation (29) σ_n^2 is the noise variance and σ_u is the standard deviation of the useful image coefficients. The relation (29) reduces to a soft-thresholding of the noisy coefficients with a variable threshold. In the non-parametric approach this threshold has a constant value, proportional to the noise standard deviation, [DonJoh94]. As an alternative, we use a denoising method based on the association of the DWT with a soft, where the already mentioned constant of proportionality equals 2, called adaptive soft. In practice, the statistical parameters in (29) are not known and therefore we use their estimates. To estimate σ_n from the noisy wavelet coefficients, a robust median estimator is applied to the finest scale wavelet coefficients corresponding to each of the four DWTs:

$$\hat{\sigma}_n = \frac{\operatorname{median}(|z_i|)}{0.6745}, \quad z_i \in \text{subband HH}. \tag{30}$$

The marginal variance of the k 'th coefficient is estimated using neighboring coefficients in the region $N(k)$, a window centered at the k 'th coefficient. To make this estimation, one gets $\sigma_z^2 = \sigma_u^2 + \sigma_n^2$ where σ_z^2 is the marginal variance of noisy observations, y. For the estimation of σ_z^2 the following relationship is used:

$$\hat{\sigma}_z^2 = \frac{1}{M} \sum_{z_i \in N(k)} z_i^2 , \tag{31}$$

where M is the size of the neighborhood $N(k)$. Then σ_u can be estimated as:

$$\hat{\sigma}_u = \left(\hat{\sigma}_z^2 - \hat{\sigma}_n^2\right)_+^{1/2} . \tag{32}$$

This estimation is not very accurate. In addition, after computing the sensitivities of that MAP filter with the noise and the clean image standard deviations (given in (30) and (32)), it can be observed that the absolute values of those sensitivities increase with the increase of $\hat{\sigma}_n$ and with the decrease of $\hat{\sigma}_u$ respectively. These behaviors must be counteracted. A solution is the use of a denoising algorithm in two stages [Shu05].

Directional windows in the wavelets domain In [SenSel02] the regions $N(k)$ were rectangular of size 7×7. The energy clusters in different subbands are mainly distributed along the corresponding preferential directions. For this reason, the estimator using a squared window often leads to downward-biased estimates within and around energy clusters, which is disadvantageous for the preservation of edges and textures in images. In [Shu05], the elliptic directional windows are introduced to estimate the signal variances in each oriented subband. We generalized here this idea for the proposed implementation of the 2D-HWT associated with pmMAPf, using constant array elliptic estimation windows with their main axes oriented following the directions: ±atan(1/2), ±π/4 and ±atan(2).

The proposed denoising method in [FirNafBouIsa09] **First stage**: After applying the pmMAPf in the HWT domain, using elliptic estimation windows, a first partial result, $\hat{u}_l^{\text{HWT-MAP}}$ is obtained. The local standard deviation of each pixel is computed into a rectangular window of size 7×7, obtaining an image, *stdev*, that will lead the entire algorithm. To further enhance the denoising process, the image *stdev* is used as follows. The maximum local standard deviation, $stdev_{\max}$ is extracted and used to segment this image. Two classes are obtained, with elements separated by a threshold equal to 0.1 $stdev_{\max}$. These classes are used as masks. The second class, containing the higher values of the local standard deviations, is associated with the first partial result. Pixels, having the same coordinates as those belonging to the second class, are transferred into an intermediate result:

$$inres_l(i,j)=\begin{cases}\hat{u}_l^{\text{HWT-MAP}}(i,j), & \text{if } stdev(i,j)>0.1stdev_{\max}\\ 0, & \text{otherwise}\end{cases}, \tag{33a}$$

where l=2…10 vanishing moments.

Second stage: The adaptive soft is applied in the DWT domain for the same input image (using the same mother wavelets), obtaining a second partial result, $\hat{u}_l^{\text{DWT-soft}}$. The intermediate result will be completed with the pixels of the second partial result having the same coordinates as those belonging to the first class of the *stdev* image:

$$inres_l(i,j)=\begin{cases}\hat{u}_l^{\text{HWT-MAP}}(i,j), & \text{if } stdev(i,j)>0.1stdev_{\max}\\ \hat{u}_l^{\text{DWT-soft}}(i,j), & \text{otherwise}\end{cases}, \tag{33b}$$

where l=2…10 vanishing moments.

Third stage: A way to reduce the sensitivity of the denoising results with respect to the mother wavelets selection is *the diversity enhancement*. The first two stages are repeated for each of the nine mother wavelets from the family proposed by Ingrid Daubechies (having a number of vanishing moments between 2 and 10), obtaining nine intermediate results. The final result is obtained by computing their mean:

$$fires(i,j)=(1/9)\sum_{l=2}^{10} inres_l(i,j). \tag{34}$$

Simulation results obtained using the image Lena (size 512×512) perturbed with additive white Gaussian noise (AWGN) are presented. Three types of results were considered. The association of the first and third stages:

$$\hat{u}^{\text{HWT-pmMAPf}}(i,j)=(1/9)\sum_{l=2}^{10}\hat{u}_l^{\text{HWT-MAP}}(i,j), \tag{35a}$$

is denoted by HWT-pmMAPf in Tables 13-15. DWT-adaptive stf refers to the combination of the second and third stages:

$$\hat{u}^{\text{DWT-adaptive soft}}(i,j)=(1/9)\sum_{l=2}^{10}\hat{u}_l^{\text{DWT-soft}}(i,j). \tag{35b}$$

The complete denoising method based on the association of all of the three stages produces the *fires* and is named in the following Hybrid.

We consider two types of simulations. The first one refers to the visual aspect of the image while the latter focuses on the peak signal-to-noise ratio (PSNR) enhancement.

Generally, an image contains three types of regions: contours, textures and homogeneous areas. We propose new measures of the contours and homogeneous region degradations due to denoising. First, the contours of the useful component of the input image and of the denoising results were detected and the absolute values of the sums of contour approximation errors were computed. A small value of the sum indicates a good quality treatment (the denoising preserves the contours). The results obtained are presented in Table 13. The best results are obtained using the mono-wavelet parametric method (Best parametric) when the mother wavelets Dau8 (l=8) is used, followed by the results obtained using the Hybrid method. The quality of a homogeneous region denoising can be measured by computing the ratio of the square of its mean and its variance, *R*. The corresponding simulation results can be found in Table 14. The best method is the mono-wavelet non-parametric one (Best non-parametric), when the mother wavelets Dau6 is used, followed very close by the method named DWT-adaptive soft and the method Hybrid.

The second set of simulations is presented in Table 15 and it refers to the PSNR enhancement. Let s and $\hat{s}$ be the noise-free (original) and the denoised images. The root mean square of the approximation error is given by: $\varepsilon=((1/N)\Sigma_q(s_q-\hat{s}_q)^2)^{1/2}$ where N is the number of pixels. The PSNR in dB is: $\text{PSNR}=20\log_{10}(255/\varepsilon)$. The best results are obtained using HWT-pmMAPf, that outperforms the results reported in [Shu05] and [Olh06], proving the efficiency of the proposed MAP system. These results are followed by the results of the Hybrid method. In fact these results are comparable (slightly better) with the results obtained using another WT with enhanced directionality, the contourlet transform associated with a filtering method using directional estimation windows, reported in [ZhoShu07]. From the PSNR enhancement point of view the denoising methods proposed are slightly inferior to the best results obtained in [SenSel02], [PizPhi06], [AchKur05]. The images corresponding to σ_n=35 are presented in Fig. 23. The visual aspects of the results obtained are satisfactory: the noise was completely eliminated, the contours are highlighted and the homogeneous regions are uniform.

It is also interesting to evaluate the various denoising methods by the computation time. In this respect, the three proposed denoising methods are classified in the following order: DWT-adaptive soft, HWT-pmMAPf and Hybrid.

σ_n	Noisy	l=8		HWT-pmMAPf	DWT-adaptive soft	Hybrid
		Best parametric	Best non-parametric			
10	3418	348	1018	615	1397	443
25	6458	921	1484	1544	2296	1373
35	7019	1360	1695	1882	2497	1806

Table 13. A comparison of the contour treatment of the proposed denoising method and its components [FirNafBouIsa09].

σ_n	Noisy	l=6		HWT-pmMAPf	DWT-adaptive soft	Hybrid
		Best parametric	Best non-parametric			
10	63	208	256	202	211	211
25	14	173	212	187	194	194
35	7	148	196	153	175	167

Table 14. A comparison of the homogeneous regions treatment of the proposed denoising method and of its components (R).

The HWT is a modern WT as it has been formalized recently [OlhMet06]. We used a simple implementation of this transform, which permits the exploitation of the mathematical results and of the algorithms previously obtained in the evolution of wavelets theory. This implementation has a very flexible structure, as we can use any orthogonal or bi-orthogonal real mother wavelets for the computation of the HWT. We preferred a denoising strategy based on diversity enhancement, on a simple MAP filter and on the estimation of the local standard deviation using directional windows. The simulation results in Table 16 illustrate the effectiveness of the proposed association HWT-pmMAPf.

To appreciate the contribution of the new implementation of the HWT and of the proposed MAP filter, Table 15 compares the method HWT-pmMAPf with the denoising association DWT-Wiener filter based on the genuine use of directional estimation windows [Shu05]. Our results are slightly better.

Fig. 23 Noisy image for $\sigma_n = 35$; Denoising result (hybrid)

σ_n	Noisy	[Shu05]	[ZhoShu07]	[Olh06]	*l*=10		HWT-pmMAPf	DWT-adaptive soft	Hybrid
					Best par.	Best non-par.			
10	28.18	*34.7*	-	-	34.06	31.6	**34.92**	31.4	34.54
20	22.16	*31.5*	-	31.58	**-**	**-**	**31.6**	28.56	31.42
25	20.20	*30.4*	-	-	29.67	27.85	**30.55**	27.63	30.37
30	18.62	-	28.77	-	**-**	**-**	**29.61**	26.91	*29.45*
35	17.29	-	-	-	28.01	26.44	**28.83**	26.28	*28.65*
40	16.53	-	27.47	27.74	**-**	**-**	**28.13**	25.75	*27.93*
50	14.18	-	26.46	-	**-**	**-**	**26.96**	24.84	*26.63*

Table 15. A comparison of the PSNRs obtained using different denoising methods reported in the references indicated (in dB).

Two new ideas were proposed. The first one refers to the diversity enhancement. Its useful effect is the increasing with 0.6 dB of the output PSNR of Prop with respect to the best mono-wavelet intermediate result. The drawback of the diversity enhancement is a slight degradation of the visual aspect quality. The second new idea proposed is the cooperation between a parametric and a non-parametric denoising technique. Despite the small output PSNR reduction, the hybrid approach enhances the visual aspect of the HWT-pmMAPf. A future research direction will be the speed optimization of our codes. Another research direction will be the segmentation threshold selection optimization (the value 0.1*stdev* was empirically chosen). Finally, we will find better solutions for the intermediate results synthesis. The comparisons made suggest that the new image denoising results are competitive with some of the best wavelet-based results reported in literature, despite the inaccuracy of the statistical model used.

In [FirNafBouIsa10] ***denoising of images affected by additive white Gaussian noise*** (AWGN) is done in the ***HWT domain***, but this time, the maximum a posteriori (MAP) filter, named ***bishrink***, is used [SenSel02]. The best results are obtained with the biorthogonal mother wavelets Daubechies 9/7.

We compared the performance of the denoising method in terms of output SNRs for Lena and Barbara, size 512 × 512 pixels and four wavelets families: the family of orthogonal wavelets with compact support having the higher number of vanishing moments for the considered support length, Daubechies, the family of Symmlets, the family of Coiflets and the family of biorthogonal wavelets [Dau92].

The Daubechies family contains 44 elements (first being denoted by Dau_4). The family Symmlets contains 17 elements (first one being denoted by Sym_4). The family Coiflets contains 5 members, the first one being denoted by Coif_1. We have also tested 17 pair of biorthogonal wavelets. In each case we have used AWGN with different standard deviations (10, 15, 20, 25, 30 and 35) obtaining different values for the input PSNR (PSNRi) and we have estimated the output PSNRs.

The results are presented in Table 16. On the first column are given the values of PSNRi. On second to last colums, we give the output PSNR result for each wavelet family, indexed by the respective parameter. The Daubechies family is indexed by the length of the corresponding quadrature mirror filter.

On the third column are given the PSNRs obtained using the best mother wavelets from the Biort family. On the fourth column are presented the PSNRs obtained using the best Coiflet. These functions are indexed by their ordering number in the family. Finally, on the last column are highlighted the output PSNRs obtained using the best mother wavelets from the Symm family. They are also indexed by their ordering number in the family.

Lena

$PSNR_i$	**Dau 6**	**Biort9/7**	**Coif 2**	**Sym 4**
28.17	*35.04*	**35.08**	34.97	35.01
24.66	*33.27*	**33.30**	33.22	33.24
22.13	32.00	**32.04**	31.95	*32.02*
20.23	*31.01*	**31.03**	30.91	30.95
18.61	*30.22*	**30.23**	30.12	30.21
17.30	*29.5*	**29.58**	29.38	*29.50*

Barbara

$PSNR_i$	**Dau 14**	**Biort9/7**	**Coif 3**	**Sym 6**
28.17	*33.2*	**33.32**	33.17	33.19
24.66	30.93	**31.06**	30.92	*30.94*
22.13	29.32	**29.51**	29.32	*29.33*
20.23	*28.09*	**28.28**	28.09	28.08
18.61	27.09	**27.36**	27.09	*27.10*
17.30	*26.28*	**26.44**	26.24	26.25

Table 16 PSNR results for the denoising method in [FirNafBouIsa10] , for different wavelet mother used in the HWT transform.

The best results are obtained with the biorthogonal pair of mother wavelets Daubechies 9/7. This is one of the pair recommended by the JPEG-2000 image compression standard as well. For the other families, different best mother wavelets are obtained for the treatment of the two different images considered here. The corresponding PSNRs are slightly smaller in comparison with the values obtained using the mother wavelets Daubechies 9/7. To compare the proposed variant of HWT with the 2D DWT, we applied the same denoising procedure based on both WTs in similar conditions (input image, mother wavelets) obtaining the results in following figure.

Fig. 24 represents a zoom on a leg with a regular texture from Barbara image. This illustrates that, compared with 2D DWT, the HWT leads to better visual results. Fig. 24(left) corresponding to the 2D DWT is strongly blurred. It clearly appears that the texture with an apparent angle of -π/4 is heavily corrupted by patterns in the opposite direction, due to the mixing in the “diagonal” subband produced in the 2D DWT case. Details are better preserved in the HWT case, [Fig. 2(b)]. There is much less directional mixture in the HWT case.

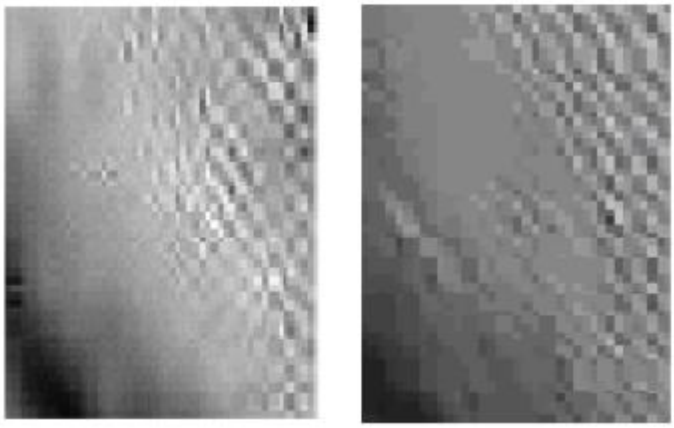

Fig. 24 A comparison of the directional selectivity of 2D DWT (left) and HWT (right).

The simulation results are better than the results presented in [FirNafBouIsa09] proving that the bishrink filter is one of the best MAP filters. The proposed variant of HWT outperforms the 2D DWT in denoising applications, due to its quasi shift-invariance and better directional selectivity. The results are inferior with 0.3 dB in comparison with the results reported in [SenSel02], where the 2D DTCWT was associated with the bishrink filter. But the HWT architecture is simpler than the one of the 2D DTCWT, and our algorithm is faster. The superiority of 2D DTCWT versus the HWT in denoising applications, already mentioned, disappears when the noise is multiplicative as in the case of despecklisation systems.

As we will see below, both the 2D DTCWT and the HWT can be considered equivalent in despecklisation applications. The blurring effect introduced by the HWT can be reduced by substituting the 2D DWTs in the HWT architecture, by other 2D WTs with better frequency localization like for example the 2D Wavelet Packets Transform or the 2D M-band WT. The HWT can be regarded as a Gabor’s filter bank [LajHus09]. We have searched here the best mother wavelets following a classical approach based on trials. We have found results compatible with the whole noiseless image. This strategy could be applied for other image processing methods as well.

2.3.2. SONAR images affected by speckle

The proliferation of SONAR images produced by different equipments: multibeam echo sounders, side scan sonar, forward looking imaging SONAR etc. [Lur02] created the necessity of expert systems for assisting the decision making. An example is the SonarScope expert system. The basic functionality of such an expert system is the representation and the analysis of sonar data, organized as a "multilayer" structure defined by its various attributes (bathymetry, image, angles, and data from auxiliary sensors …). These data can be represented and processed using various techniques either classical (signal or image processing) or specific to SONAR.

The goal of an expert system for SONAR images is to achieve Quality Control, Data Processing and Data Interpretation [IsaFirNafMog11]. Signal processing methods used in an expert system for SONAR images are: *image conditioning methods* and *intelligent image processing* techniques (segmentation, textures analysis, classification, etc.).

Conditioning methods are:

- echoes acquisition, meaning the acquisition of: depth, across and along-track distance, the received beam angle, the numbers of the transmitted and received beam, or the two-way travel time of the acoustic pulse.
- correction of acquired data to complete the missing data and techniques for the correction of the differences between the directivity characteristics of the sensors.
- data organization: SONAR data are arranged as a set of arrows called pings (swath), which correspond to all the soundings acquired in a ping cycle. At the beginning of the ping cycle, each sensor's value is logged: gyro, pitch, roll, positions, etc.
- the formation of SONAR images: a SONAR image is linked with the sensor's time series, pertaining to that given dataset and in synchronization with each ping. The time series can be plotted as curves, displayed in conjunction with the image. There are few geometric formats for the SONAR images: PingBeam, LatLong, PingSamples and PingSwat.
- assembling of few neighboring individual images. This could be a technique to produce mosaics or digital terrain models (DTM).
- angular correction and despecklisation of SONAR images. The SONAR images are perturbed by speckle. The aim is the despecklisation of SONAR images. It is of multiplicative nature. The aim of a *denoising algorithm* is to reduce the noise level, while preserving the image features. The noisy image is:

$$f = s \cdot v, \tag{36}$$

where s is the noise-free input image and v the speckle noise.

The most frequently used despecklisation techniques are: i) the classical (Lee, Kuan and Frost filters) ii) the pure statistical despecklisation method [WalDat00] to arrive at iii) the most modern which act in the wavelet domain.

The field of natural images denoising methods is very large. A lot of articles dedicated to denoising methods were already written, most of them treating the case of additive noise. There are two ways of reducing the speckle to an additive noise:

$$f = s + s \cdot (v - 1), \tag{37}$$

or:

$$\ln f = \ln s + \ln v. \tag{38}$$

Assuming that usually f is not stationary, in the first approach the additive noise is not stationary as well [ArgBiaScaAlp09].

Denoising can be done either in the spatial domain or in a transform domain. They can be parametric or nonparametric.

Denoising based on differential equations with partial derivatives. These methods do not take into account a priori information about the image to be processed, being *non parametric*. The aim of those methods is to conceive the denoising like a decomposition of the acquired image into two components, the noiseless part and the noise. This decomposition can be realized by the projection of the acquired image on two very different vector spaces. The projection can be done by the minimization of a cost function. The result corresponds to the solution of the system of equations which is obtained imposing the zero value to the partial derivatives of the cost function. This is a system of partial differential equations. The simpler projection on the noiseless space is realized by the averaging of the acquired image. The corresponding denoising method works well for the homogeneous regions of the acquired image if the noise is of zero mean. Taking into account the fact that the averager is a low-pass filter, this method distorts the edges and some of the textured regions by oversmoothing.

Denoising by non-local averaging Another very modern non parametric denoising method is based on non-local (NL) averaging [Bua07]. The NL-means algorithm tries to take advantage of the high degree of redundancy of any natural image. Every small window in a natural image has many similar windows in the same image. In a very general sense, one can define as „neighborhood of a pixel *i*" any set of pixels *j* in the image so that a window around *j* looks like a window around *i*. All pixels in that neighborhood can be used for predicting the value at *i*. Given a discrete noisy image $x=\{x(i)|i\in I\}$, the estimated value $NL_x(i)$ is computed as a weighted average of all the pixels in the image, $NL_x(i)=\sum_{j\in I}\beta(i,j)x(j)$, where the weights $\{\beta(i,j)\}_j$ depend on the similarity between the pixels *i* and *j* and satisfy the usual conditions $0\le\beta(i,j)\le 1$ and $\sum_j \beta(i,j)=1$. The non-locality of the average prevents for oversmoothing.

Parametric denoising methods take into account statistical models for the noiseless component of the acquired image and for the noise. One of the best parametric denoising methods uses maximum a posteriori (MAP) filters. The MAP estimation of *w*, based on the observation *y*=*w*+*n*, (where *n* represents the additive noise) is given by the MAP filter equation:

$$\hat{w}(y)=\underset{w}{\operatorname{argmax}}\left\{\ln\left(p_{\mathbf{n}}(y-w)p_{\mathbf{w}}(w)\right)\right\}, \tag{39}$$

where p_a represents the probability density function (pdf) of *a*.

Some classical filters are proposed by Kuan, Lee, and Frost. Kuan considered a multiplicative speckle model [KuaSawStr87] and designed a linear filter based on the minimum mean square error (MMSE) criterion, optimal when both the scene and the detected intensities are Gaussian distributed. The Lee filter [Lee81] is a particular case of the Kuan filter, the Frost filter [FroStiShaHol82] is a Wiener filter adapted to multiplicative noise. The parameters of the Kuan, Lee and Frost filters are: the size of the rectangular windows used for the estimation of the local standard deviation of the useful component of the acquired image and its number of looks.

Denoising in the wavelet domain. These methods, for additive noise, assume: i) the computation of a wavelet transform (WT); ii) the filtering of the detail wavelet coefficients; iii) the computation of the corresponding inverse WT (IWT). The usefulness of the filtering in the wavelet domain comes from the sparseness of the WTs. Only few wavelet coefficients have high magnitude, concentrating almost of the energy of the noiseless component of the input image, the other wavelet coefficients have small magnitude and can be considered as noise, an can be discarded without producing high distortions.

A category of denoising methods applied in the wavelets domain is based on *non-parametric techniques using the hard or the soft thresholding filters: i)* MAP filters in the wavelet domain, ii) Adaptive Soft-Thresholding filter (soft). D. Donoho, [DonJoh94], wanted to estimate the noiseless component of the acquired image by the minimization of the min-max approximation error. He studied the case of the Discrete Wavelet Transform (DWT). Other wavelet transforms used for images denoising are: the Undecimated Discrete Wavelet Transform (UDWT), the Double Tree Complex Wavelet Transform (DTCWT) and the Hyperanalytic Wavelet Transform (HWT).

The bishrink is a local bivariate MAP filter. Its performance depends on the quality of the estimation of a parameter, the local variance of the noiseless component of the acquired image. The quality of this estimate depends on the shape and the size of the estimation window. These estimation windows have different shapes in subbands with different preferential orientations highlighting the better directional selectivity of DTCWT and HWT versus the DWT.

Despeckling SONAR Images

Since SONAR images are perturbed by speckle noise, which is of multiplicative nature, in [FirNafIsaIsa11] we presented a new denoising method in the wavelet domain, which tends to reduce the speckle, preserving the structural features and textural information of the scene. We used the Hyperanalytic Wavelet Transform (HWT) in association with a Maximum A Posteriori (MAP) filter named bishrink. The algorithm is simple and fast.

The aim of a denoising algorithm is to reduce the noise level, while preserving the image features. One may classify the denoising systems in two categories: those directly applied to the signal [AubAuj08] and those which use a wavelet transform before processing [DonJoh94].

Classical despecklization systems, proposed by Lee, Kuan and Frost, belong to the first category [AubAuj08]. The denoising solution proposed in [AubAuj08] is based on variational techniques. Its implementation was optimized in [DenTupDarSig09].

The good performance of the methods in the second category is explained by the fact that the multi-resolution analysis performed by the WT is a powerful tool to achieve good denoising. In the wavelet domain, the noise is uniformly spread throughout the coefficients, while most of the useful information is concentrated in the few largest ones due to the sparsity of the wavelet representation.

A particularity of SONAR images is the high directional diversity of their content. The multiplicative speckle noise that disturbs the SONAR images can be transformed into an additive noise with the aid of a logarithm computation block. To obtain the denoising result, the logarithm inversion is performed at the end of the additive noise denoising process. A potential architecture for a SONAR denoising system is presented in Fig. 25. The block named Sensitivity reduction corrects the drawbaks of the additive noise denoising kernel. The despecklization system also contains a bias correction block composed by two mean computation systems. The first one computes the expectation of the acquired image which is equal with the mean of its noise-free component because the speckle noise has unitary expectation. The second one computes the expectation of the image at the output of the Sensitivity reduction block. This value is extracted and the mean of the acquired image is added. In this way the undesirable bias introduced by the homomorphic method is corrected. The first goal is the additive noise denoising kernel in fig. 25.

We use the HWT [FirNafBouIsa09], to take into account the high directional diversity of SONAR images and to have a high flexibility for the selection of mother wavelets. In [FouBenBou01] was used a very redundant WT, namely the 2D Undecimated Wavelet Transform (2D UWT) and in [SenSel02] the 2D Double Tree Complex Wavelet Transform (2D DTCWT) which has a lower flexibility for the selection of mother wavelets.

There are two categories of estimators: non-parametric and parametric. From the first category can be mentioned: the hard-thresholding filter and the soft thresholding [DonJoh94], which are generalized in [AntFan96] for the case of non-uniform sampling. To the second category belong filters obtained by minimizing a Bayesian risk under a cost function, typically a delta cost function (MAP estimation [FouBenBou01], [SenSel02]) or the minimum mean squared error (MMSE estimation).

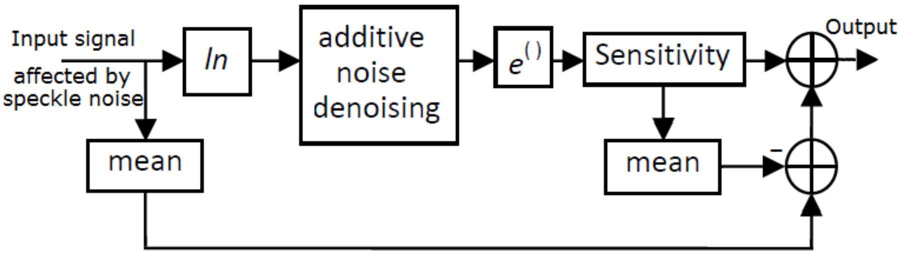

Fig. 25. Proposed denoising system. There exists a mean correction mechanism and additive noise denoising kernel.

We have already associated the proposed implementation of HWT with a marginal MAP filter in [FirNafBouIsa09]. The aim is to improve the results in [FirNafBouIsa09] by the substitution of the marginal MAP filter with the bishrink filter [SenSel02]. The MAP estimation of w, based on the observation $y=w+n$, (where n represents the WT of the noise and w the WT of the useful component of the input image) is given by the MAP filter:

$$\hat{w}(y)=\underset{w}{\arg\max}\{\ln(p_n(y-w)p_w(w))\}, \tag{39}$$

where p_a represents the probability density function (pdf) of a. In the case of the bishrink filter [SenSel02] the noise is assumed i.i.d. Gaussian,

$$p_{\mathbf{n}}(\mathbf{n})=\frac{1}{2\pi\sigma_n^2}\cdot\exp\left(-\frac{n_1^2+n_2^2}{2\sigma_n^2}\right). \tag{40}$$

The model of the noise-free image in [SenSel02] is a heavy tailed distribution:

$$p_{\mathbf{w}}(\mathbf{w})=\frac{3}{2\pi\sigma^2}\cdot\exp\left(-\frac{\sqrt{3}}{\sigma}\sqrt{w_1^2+w_2^2}\right). \tag{41}$$

Each of the vectors $\mathbf{w}=(w_1,w_2)$ and $\mathbf{n}=(n_1,n_2)$ contain two components representing the wavelet coefficients of the noiseless image f and of the noise n at the current decomposition level (child coefficients) and of the wavelet coefficients localized at the same geometrical positions at the next decomposition level (parent coefficients). Substituting these two pdfs in the equation of the MAP filter, the input-output relation of the bishrink filter is:

$${}^{1}\hat{w}_1=\frac{\left(\sqrt{y_1^2+y_2^2}-\sqrt{3}\sigma_n^2/\sigma\right)_+}{\sqrt{y_1^2+y_2^2}}\,y_1. \tag{42}$$

This estimator requires prior knowledge of the noise variance and of the marginal variance of the clean image for each wavelet coefficient. To estimate the noise standard deviation from the noisy wavelet coefficients, a robust median estimator from the finest scale wavelet coefficients is used [DonJoh94]:

$$\hat{\sigma}_n=\frac{\text{median}(|y_i|)}{0.6745},\quad y_i\in\text{subband HH}. \tag{43}$$

In [SenSel02], the marginal variance of the k^{th} coefficient is estimated using neighboring coefficients in the region $N(k)$, a squared shaped window centered on this coefficient with size 7×7. To make this estimation one gets $\sigma_y^2=\sigma^2+\sigma_n^2$ where σ_y^2 represents the marginal variances of noisy observations y_1 and y_2. For the estimation of the marginal variance of noisy observations, in [SenSel02] is proposed the following relation:

$$\hat{\sigma}_y^2=\frac{1}{M}\sum_{y_i\in N(k)}y_i^2, \tag{44}$$

where M is the size of the neighborhood $N(k)$. Then σ can be estimated as:

$$\hat{\sigma}=\sqrt{\left(\hat{\sigma}_y^2-\hat{\sigma}_n^2\right)_+}. \tag{45}$$

A very important parameter of the bishrink filter is the local estimation of the marginal variance of the noise-free image $\hat{\sigma}$. The sensitivity of the estimation $\hat{w}_1$ with $\hat{\sigma}$ is given by:

$$S_{\hat{w}_1}^{\hat{\sigma}}=\begin{cases}\dfrac{\sqrt{3}\hat{\sigma}_n^2}{\hat{\sigma}\sqrt{y_1^2+y_2^2}-\sqrt{3}\hat{\sigma}_n^2}, & \text{if } \sqrt{y_1^2+y_2^2}>\dfrac{\sqrt{3}\hat{\sigma}_n^2}{\hat{\sigma}}\\ 0, & \text{otherwise}\end{cases}. \tag{46}$$

This is a decreasing function of $\hat{\sigma}$. The precision of the estimation based on the use of the bishrink filter decreases with the decreasing of $\hat{\sigma}$. To reduce this drawback, the system with the name Sensitivity reduction was included in the architecture in Fig. 25-an averager for the pixels with small local variances.

We present two types of simulation results: for synthesized speckle noise and for real SONAR images. In all cases the proposed denoising method was implemented using the same mother wavelets, nammely Daubechies 9/7 (which will be denoted in the following by B9.7). The best values in the following tables are represented by bold characters and the values from the second place by italic characters.

Synthesized speckle noise For the first experiment the noise is generated following a Rayleigh distribution with unitary mean. It is obtained computing the square root of a sum of squares of two white Gaussian noises having the same variance. The first image of Fig. 26 contains a normalized representation of the pdf in equation (37) particularized for the variance of the noise in the first experiment. The second image of fig. 26 represents the normalized bivariate histogram of the HWT coefficients **of the logarithm of the noise.** It was obtained considering the HWT coefficients z_{+r} corresponding to horizontal details from the first two decomposition levels. The similarity of the surfaces from the two images in figure 26 proves the validity of the bivariate noise statistical model used for the construction of the bishrink filter and the possibility to use this filter in despecklisation applications.

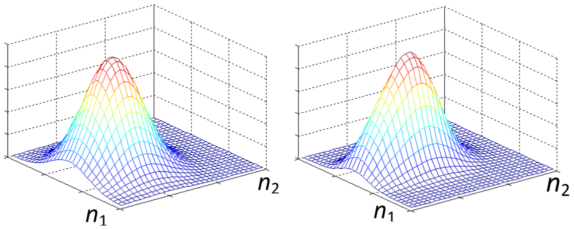

Fig. 26. The representation of the pdf in eq. (37) (left) and the corresponding bivariate histogram (right).

A comparison of the proposed method with the classical speckle removing methods proposed by: Lee, Frost and Kuan and with the wavelets based method from [IsaMogIsa09], is presented in Table 17.

Noisy	Lee	Frost	Kuan	[IsaMogIsa09]	Hybrid
21.4	27.2	27.0	28.1	*31.4*	**31.7**

Table 17. The PSNR of different speckle denoising methods (in dB).

In the case of the classical speckle removing methods, rectangular estimation windows with size 7×7 were used. The method in [IsaMogIsa09] uses a system with architecture similar with that from Fig. 25, but the structure of the additive noise denoising kernel is different. It is based on an association of a different WT, namely the DTCWT, with a bishrink filter. The sensitivity reduction is realized by diversification followed by non local averaging. From the PSNR point of view our method has the best performance among those compared in Table 17. The aim of the second experiment is to compare the proposed denoising method with another despecklisation method based on MAP filtering in the wavelets domain [ArgBiaAlp06]. The proposed method can be considered equivalent with the SAR denoising method proposed in [ArgBiaAlp06]. The two denoising algorithms proposed in [ArgBiaAlp06] use the UWT. It is computed either with the aid of the Daubechies mother wavelets with four vanishing moments db8 or with B9.7. The first denoising algorithm proposed in [ArgBiaAlp06] performs a local linear minimum mean square error (LLMMSE) filtering in the UWT domain. The second one uses a MAP filter constructed supposing that the noise-free wavelet coefficients and the wavelet coefficients of the noise are distributed according to Generalized Gaussian

Distributions. The four parameters of those pdfs are estimated for each pixel of the input image. The corresponding MAP filter equation is solved with the aid of numerical methods. A comparison of the PSNRs obtained processing the image Lena with the proposed denoising method and the methods proposed in [ArgBiaAlp06] is presented in table 18.

(A)	(B)	(C)		(D)		(E)	(F)	
		db8	B9.7	db8	B9.7		db8	B9.7
1	12.1	24.2	24.2	26.0	*26.2*	**26.4**	26	26
4	17.8	28.2	28.3	29.4	29.6	29.9	**30.2**	**30.2**
16	23.7	32.2	32.4	32.9	*33.0*	32.2	*33.0*	**33.1**

Table 18 A comparison between the speckle reduction methods described in [ArgBiaAlp06], [IsaMogIsa09] and proposed method; (A)-The number of looks of the acquired image, (B)-PSNR of raw image, (C)- PSNR results obtained using LLMSE-UWT, (D)-PSNR results obtained using MAP-UWT, (E) Method in [IsaMogIsa09] and (F) Hybrid method from [FirNafIsaIsa09].

This time, the speckle was generated using the method proposed in [ArgBiaAlp06]. The method proposed is better than the LLMSE-UWT method for all the noise levels. It is comparable with the MAP-UWT method and with the method proposed in [IsaMogIsa09]. For high input PSNRs, the results obtained using the DTCWT and the HWT are better than the results reported in [ArgBiaAlp06] because the UWT has a poorer directional selectivity. The proposed denoising method is the less sensitive with the selection of the mother wavelets. In Fig. 27 is presented a comparison of the results corresponding to the last line of table 18. The first image in figure 27 represents a region of the noisy image. In the second and third images are presented the denoising results of the same region obtained applying the method proposed in [ArgBiaAlp06] with the MAP filter and the mother wavelet B9.7 and the proposed method. Comparing the last two images in figure 27 it can be observed the better directional selectivity and the better contrast preservation of the proposed method (proving the superiority of the HWT versus the UWT). Analyzing the two regions marked in the last two images it can be observed the incapacity of the UWT to separate the orientations corresponding to orthogonal directions.

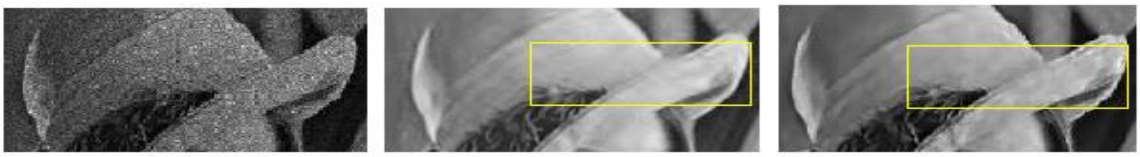

Fig. 27. Acquired image (left); result from [ArgBiaAlp06] (middle); result of the hybrid method (right).

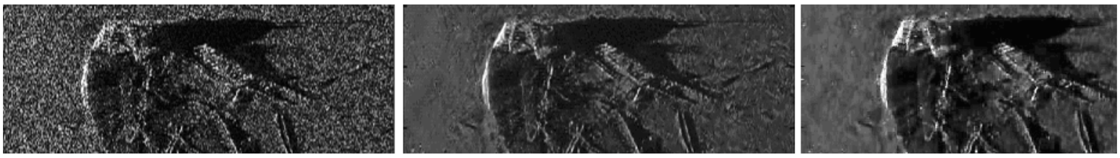

Fig. 28. Speckle removal for the sea-bed SONAR Swansea image (we are thankful to GESMA for providing this image); a region of the acquired image (ENL=3) (left); result in [IsaMogIsa09] (ENL=102) (middle), result of the proposed method (ENL=150) (right).

Real SONAR Images Fig. 28 shows the original SONAR image “Swansea” and the results obtained with the method in [IsaMogIsa09] and with the proposed method. The visual analysis of the filtered images proves the correctness of our assumptions. Indeed, the result of the proposed method has a better visual aspect. An objective measure of the homogeneity degree of a region is the enhancement of the Equivalent Number of Looks (ENL). It is defined by the ratio of the square mean and the variance of the pixels situated in the considered region:

$$ENL = \left(\frac{\text{mean}}{\text{standard deviation}} \right)^2 . \tag{47}$$

The enhancement of the ENL of a denoising method in a homogeneous region is defined by the ratio of the ENLs of the considered region computed before and after the application of the method. The performance of the proposed denoising method is certificated by the important enhancement of the ENL obtained considering a homogeneous region of 200×1000 pixels. The gain in performance can be explained by the superiority of HWT versus DTCWT in despecklization applications.

In [FirNafIsaIsa11] we presented an effective image denoising algorithm for SONAR images. Despite the actual proliferation of this type of images, there are not numerous publications dealing with their denoising. The proposed algorithm is based on a new additive noise denoising kernel. It uses one of the best WTs, the HWT, and a very good MAP filter which can be associated for despecklization purposes in a homomorphic framework as can be seen in figure 24. We have proved by simulation that the HWT is a better choice than the UWT or the DTCWT for SONAR images despecklization. The proposed denoising metod outperforms other denoising methods from the visual aspect, the PSNR enhancement and the enhancement of ENL points of view. It is faster than the methods proposed in [IsaMogIsa09] and [ArgBiaAlp06] and its results have a better visual aspect.

2.4 2D wavelet transforms

Papers: [IsaNaf14], [NafBerNafIsa12]; [FirNafIsaBouIsa10]; [NafFirIsaBouIsa10a]; [NafFirIsaBouIsa10b]

2.4.1 The Hyperanalytic Wavelet Transform (HWT)

Shift-invariance associated with good directional selectivity is important for the use of a wavelet transform, (WT), in many fields of image processing. Generally, complex wavelet transforms, e.g. the Double Tree Complex Wavelet Transform, (DT-CWT), have these useful properties. In [FirNafBouIsa09] we proposed the use of an implementation of such a WT, namely the Hyperanalytic Wavelet Transform, (HWT) [AdaNafBouIsa07], in association with filtering techniques already used with the Discrete Wavelet Transform, (DWT). The result is a very simple and fast image denoising algorithm. Throughout recent years many WTs were used in image processing such as denoising. The first one was the DWT [DonJoh94]. It has three main disadvantages [Kin01]: lack of shift invariance, lack of symmetry of the mother wavelets and poor directional selectivity. These disadvantages can be diminished using a complex wavelet transform [Kin01], [Kin00]. Over twenty years ago, Grossman and Morlet [GroMor84] developed the Continuous Wavelet Transform (CWT) [SelBarKin05]. A revival of interest in later years has occurred in both signal processing and statistics for the use of complex wavelets [BarNas04], and complex analytic wavelets, in particular [Kin99], [Sel02], [Sel01]. It may be linked to the development of complex-valued discrete wavelet filters [LinMay95] and the clever dual filter bank [Kin99], [SelBarKin05]. The complex wavelet transform has been shown to provide a powerful tool in signal and image analysis [Mal99]. In [OlhMet06] were derived large classes of wavelets generalizing the concept of the one-dimensional local complex-valued analytic decomposition introducing two-dimensional vector-valued hyperanalytic decompositions. We proposed the use of a very simple implementation of the HWT, recently proposed [AdaNafBouIsa07].

The shift-sensitivity of the DWT is generated by the down-samplers used for its computation. In [Mal99], [LanGuoOdeBur96] is presented the undecimated DWT (UDWT), which is a WT without down-samplers. Although the UDWT is shift-insensitive, it has high redundancy, 2^J (where J represents the number of iterations of the WT). In [CoiDon95] was proposed a new shift-invariant but very redundant WT, named Shift Invariant Discrete Wavelet Transform (SIDWT). It is based on an algorithm called Cycle Spinning (CS) and it was conceived to suppress the artifacts in the neighborhood of discontinuities introduced by the DWT in denoising applications. For a range of delays, data is shifted, its DWT is computed, and then the result is un-shifted. Averaging the several obtained results, a quasi shift-invariant DWT is implemented. In [Abr94], it is demonstrated that approximate shiftability is possible for the DWT with a small fixed amount of transform redundancy. In this reference a pair of real mother wavelets is designed such that one is approximately the Hilbert transform of the other. In the following we will give the mathematical basis for this approach. In [Hig84] the author provides a way to build new complete orthonormal sets of the Hilbert space of finite energy band-limited functions with bandwidth π, named the Paley-Wiener space (PW). He proved the following proposition:

P1. Let χ denote the characteristic function of the interval $[-\pi,\pi]$ and let $\mu(x)$ be real valued and piecewise continuous there. Then the integer translations of the inverse Fourier transform of $\chi e^{j\mu}$ constitute a complete orthonormal set in PW.

Following this proposition, some new orthonormal complete sets of integer translations of a generating function can be constructed in the PW space. The scaling function and the mother wavelets of the standard multi-resolution analysis of PW generate by integer shifts such complete orthonormal sets. The proposition P1 was generalized in [Isa93] to give a new mechanism of mother wavelets construction. In [FirNafBouIsa09] the following two propositions were formulated:

P2. If $A_m = \{\alpha_{m,n}(t)\}\big|_{n\in\mathbb{Z}}$ is a complete orthonormal set generating a Hilbert space H_m then the set $\hat{A}_m = \left\{(1/(2\pi))^{1/2}\cdot\hat{\alpha}_{m,n}(\omega)\right\}\Big|_{n\in\mathbb{Z}}$ is a complete orthonormal set of $\hat{H}_m$ (the Hilbert space composed by the Fourier transforms of the elements of the space H_m) and reciprocally;

P3. If $\mu(\omega)$ is a real valued and piecewise continuous function and $\hat{A}_m = \left\{(1/(2\pi))^{1/2}\cdot\hat{\alpha}_{m,n}(\omega)\right\}\Big|_{n\in\mathbb{Z}}$ is a complete orthonormal set of $\hat{H}_m$ then ${}_{\mu}\hat{A}_m = \left\{(1/(2\pi))^{1/2}\exp(i\mu(\omega))\cdot\hat{\alpha}_{m,n}(\omega)\right\}\Big|_{n\in\mathbb{Z}}$ is another complete orthonormal set of the same space.

These two propositions can be used to build new mother wavelets if we identify the sub-spaces of an orthogonal decomposition of the Hilbert space $L^2(\mathbb{R})$, W_m, $m\in\mathbb{Z}$ with the Hilbert spaces $\hat{H}_m$. With respect to this, the function $\mu(\omega)$ must satisfy the following constraint: $\mu(\omega)=\mu(2^m\omega)$, $\forall m\in\mathbb{Z}$.

An example of function that satisfies this constraint is: $\mu(\omega) = (\pi/2)(\operatorname{sgn}\omega + 1)$. In this case: $\exp(i\mu(\omega)) = \operatorname{sgn}(\omega)$. So, the function generating the set ${}_{\mu}A_m$ (that corresponds to the new mother wavelets) is obtained by applying the Hilbert transform to the function generating the set A_m (that corresponds to the initial mother wavelets) multiplied by i. In consequence if the function ψ is a mother wavelets then the functions $i\mathcal{H}\{\psi\}$ and $\psi_a = \psi + i\mathcal{H}\{\psi\}$ are also mother wavelets. This wavelets pair $(\psi, i\mathcal{H}\{\psi\})$ defines a complex discrete wavelet transform (CDWT), presented in Fig. 29a). A complex wavelet coefficient is obtained by interpreting the wavelet coefficient from one DWT tree as being its real part, whereas the corresponding coefficient from the other tree is considered to form its imaginary part.
In [Kin01], the DTCWT, which is a quadrature pair of DWT trees similar to the CDWT, is developed. The DTCWT coefficients may be interpreted as arising from the DWT associated with a quasi-analytic wavelet. Both DTCWT and CDWT are invertible and quasi shift-invariant.

The implementation of the HWT is presented in Fig. 29b). First, we apply a Hilbert transform to the data. The real wavelet transform is then applied to the analytical signal associated to the input data, obtaining complex coefficients. The two implementations presented in Fig. 29 are equivalent because:

$$\begin{aligned} d_{DTCWT}[m,n] &= \left\langle x(t), \psi_{m,n}(t) + i\mathcal{H}\{\psi_{m,n}(t)\}\right\rangle = \left\langle x(t), \psi_{m,n}(t)\right\rangle - i\left\langle x(t), \mathcal{H}\{\psi_{m,n}(t)\}\right\rangle \\ &= \left\langle x(t), \psi_{m,n}(t)\right\rangle + i\left\langle \mathcal{H}\{x(t)\}, \psi_{m,n}(t)\right\rangle = \left\langle x(t) + i\mathcal{H}\{x(t)\}, \psi_{m,n}(t)\right\rangle = d_{HWT}[m,n] \end{aligned} \tag{48}$$

While the DTCWT requires special mother wavelets, the implementation of the HWT proposed in Fig. 29b) can be done using classical mother wavelets like those introduced by Daubechies. These two transforms have a redundancy of 2 in the 1D case. In [FerSpaBur00] a two-stage mapping-based complex wavelet transform (MBCWT) that consists of a mapping onto a complex function space followed by a DWT of the complex mapping computation is proposed. The authors observed that DTCWT coefficients may be interpreted as the coefficients of a DWT applied to a complex signal associated with the input signal. The complex signal is defined as the Hardy-space image of the input signal. As the Hardy-space mapping of a discrete signal cannot be computed, they defined a new function space called the Softy-space, which is an approximation of the Hardy-space. In [SimFreAdeHee92], a new measure of the shift-invariance is defined, called “shiftability”. We introduced a new criterion: the degree of shift invariance, *d*. It requires the computation of the values of the energy of every set of detail coefficients (at different decomposition levels) and of the approximation coefficients, corresponding to a certain delay (shift) of the input signal samples. This way, we obtain a sequence of energy values at each decomposition level, each sample of this sequence corresponding to a different shift. Then using the mean *m* and the standard deviation *sd* of every energy sequence, the degree of shift invariance is:

$$d = 1 - sd/m. \tag{49}$$

It can be increased if the absolute values of the wavelet coefficients are considered. In Fig. 30, the dependence of the degree of shift invariance of the new implementation is shown with respect to the regularity of the mother wavelets used for its computation, when the absolute values of the wavelet coefficients are considered. The procedure followed in this simulation is described in [AdaNafBouIsa07]. The Daubechies family was investigated, each element being indexed by its number of vanishing moments. As the curve illustrated in Fig. 29 indicates it, the degree of shift-invariance increases with the degree of regularity of the mother wavelets used.

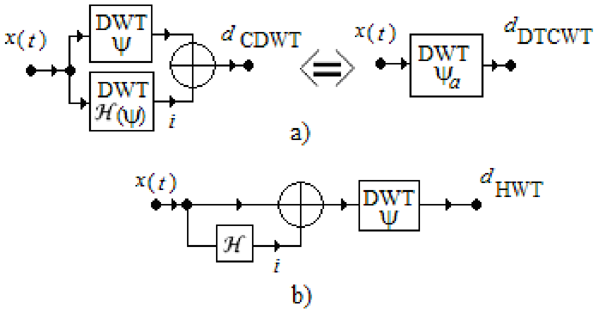

Fig. 29. The implementation of the DTCWT a) and of the HWT b) are equivalent.

An analytical 1D DWT of a real signal can be computed by applying a real 1D DWT to the analytical signal associated to the input signal. In the following we will summarize the construction based on the notion of hypercomplex signal. Its definition is not unique. Hyperanalytic mother wavelets have four components, each one localized in a different quadrant of their 2D spectrum. The construction of the hyperanalytic mother wavelets requires algebra whose elements are sets of four numbers. Choosing different algebras, different definitions of the hyperanalytic signal are obtained. In [OlhMet06] was chosen the algebra of quaternions. We have preferred the 4-D **commutative hypercomplex algebra** proposed in [Dav14] because the multiplication is not commutative in the algebra of quaternions. An element of the hypercomplex algebra and its conjugate can be expressed as:

$$Z = 1x + iy + jz + ku$$

$$Z^{*} = 1x - iy - jz + ku$$

$$Z = \left[(x-u) + i(y+z)\right]\left(\frac{1-k}{2}\right) + \left[(x+u) + i(y-z)\right]\left(\frac{1+k}{2}\right)$$

The generalization of the analyticity concept in 2D is not obvious, as there are multiple definitions of the Hilbert transform in this case. We use the definition leading to the so-called hyper-complex signal. The hyper-complex mother wavelet associated to $\psi(x,y)$ is defined as:

$$\psi_a(x,y) = \psi(x,y) + i\mathcal{H}_x\{\psi(x,y)\} + j\mathcal{H}_y\{\psi(x,y)\} + k\mathcal{H}_x\{\mathcal{H}_y\{\psi(x,y)\}\} \tag{50}$$

where: $i^2=j^2=-k^2=-1$ and $ij=ji=k$, [Dav14]. The HWT of the image $f(x,y)$ is:

$$HWT\{f(x,y)\} = \langle f(x,y), \psi_a(x,y)\rangle. \tag{51}$$

Taking into account relation (50) it can be written:

$$\begin{aligned} HWT\{f(x,y)\} &= DWT\{f(x,y)\} + iDWT\{\mathcal{H}_x\{f(x,y)\}\} + \\ &\quad + jDWT\{\mathcal{H}_y\{f(x,y)\}\} + kDWT\{\mathcal{H}_y\{\mathcal{H}_x\{f(x,y)\}\}\} \\ &= \langle f_a(x,y), \psi(x,y)\rangle = DWT\{f_a(x,y)\}. \end{aligned} \tag{52}$$

So, the 2D-HWT of the image $f(x,y)$ can be computed with the aid of the 2D-DWT of its associated hyper-complex image. The new HWT implementation [AdaNafBouIsa07], [AdaNafBouIsa07b], presented in fig. 31, uses four trees, each one implementing a 2D-DWT. The first tree is applied to the input image. The second and the third trees are applied to 1D discrete Hilbert transforms computed across the lines ($\mathcal{H}_x$) or columns ($\mathcal{H}_y$) of the input image. The fourth tree is applied to the result obtained after the computation of the two 1D discrete Hilbert transforms of the input image. The enhancement of the directional selectivity of the 2D-HWT is made as in the case of the 2D-DTCWT [Kin00], [SelBarKin05], by linear combinations of detail coefficients belonging to each subband of each of the four 2D-DWTs. This technique is explained, based on an example, in [AdaNafBouIsa07b].

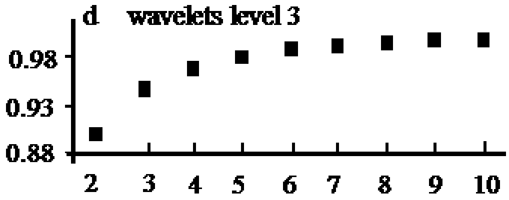

Fig. 30. Degree of shift-invariance of HWT as a function of the regularity of the mother wavelet used for its computation.

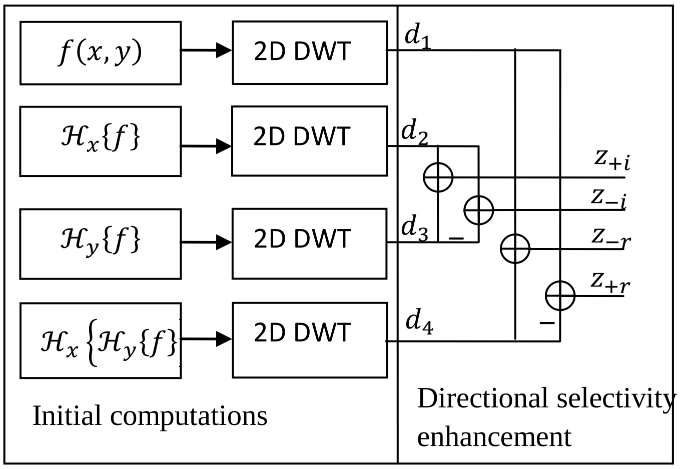

Fig. 31. HWT architecture, [FirNafBouIsa09].

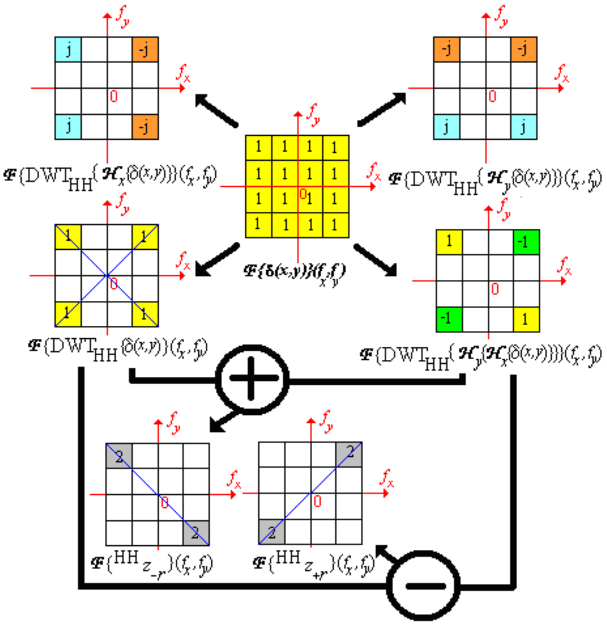

Fig. 32. The strategy of directional selectivity enhancement in the HH subband. The frequency responses of the systems that transform the input image *f* into the output diagonal detail coefficient sub-images z_{-r} and z_{+r} represented in figure 30. [IsaFirNafMog11]

2.4.2. Hyperanalytic Wavelet Packets (HWPT) – a solution to increase the directional selectivity in image analysis

We proposed [NafIsaNaf12] a solution to increase the directional selectivity in image analysis based on wavelets theory. The classical two-dimensional Discrete Wavelet Transform (2d-DWT) has a poor directional selectivity, separating only three directions: 0° or 180°, ±45° and ±90°. The directional selectivity can be improved by using 2d Discrete Wavelet Packets Transform (2d-DWPT). Neither one of these transforms is able to separate directions with opposite orientations. This separation can be done by using a complex wavelet or wavelet packets transform, such as the Hyperanalytic Wavelet Packets Transform (HWPT). We analyze the directional selectivity of the HWPT and we propose an algorithm for the detection of the principal directions in a given image.

The discrete wavelet transform and the discrete wavelet packets transform are shift-variant. In the two-dimensional case, both 2d-DWT and 2d-DWPT are not able to separate the orientations with opposite directions (orientations ±45°). To reduce the shift-variance, several solutions can be used. In [CohRazMal97], the shift invariant wavelet packets transform (SIWPT) is proposed. Another solution consists in the use of the Undecimated Discrete Wavelet Packets Transform (UDWPT), [PesKriCar96]. There are two drawbacks: an increased redundancy and a reduced directional selectivity in the case of image processing. For this reason, the Complex Wavelet Packets Transforms (CWPT) were studied. We highlighted in [NafIsaNaf12] the improved directional selectivity of a particular CWPT, namely the HWPT.

The 2d-CWT [Kin98] is build using a quad-tree algorithm, with 4 trees *A*, *B*, *C* and *D*, with a half-sample shift between the trees to achieve the approximate shift invariance. Different filter lengths are used for each tree. Complex coefficients are obtained by combining the different trees together. If the subbands are indexed by *k*, the detail subbands $d^{j,k}$ of the parallel trees *A*, *B*, *C* and *D* are combined to form complex subbands $z_{+}^{j,k}$ and $z_{-}^{j,k}$, by the linear transforms:

$$\begin{aligned} z_{+}^{j,k} &= \left(d_{A}^{j,k} - d_{D}^{j,k}\right) + i\left(d_{B}^{j,k} + d_{C}^{j,k}\right) \\ z_{-}^{j,k} &= \left(d_{A}^{j,k} + d_{D}^{j,k}\right) + i\left(d_{B}^{j,k} - d_{C}^{j,k}\right) \end{aligned}, \tag{53}$$

where $i^2=-1$. This 2d-CWT is generalized to a corresponding 2d-CWPT [JalBlaZer03]. This transform is quasi shift-invariant. Also, compared to the original 2d-CWT, which only separates 6 directions, the directional selectivity is highly improved. With the tree chosen in [JalBlaZer03], up to 26 directions can be separated. The CWPT's disadvantage is the lack of analyticity, [BaySel08]. Analytic transforms have improved frequency localization. This disadvantage is solved in [BaySel08], where the Dual Tree Complex Wavelet Packet Transform (DTCWPT) is proposed, representing the generalization of the Dual Tree Complex Wavelet Transform (DTCWT) [Kin01]. DTCWPT is quasi shift-invariant, quasi-analytic and the two-dimensional DTCWPT (2d-DTCWPT), also introduced in [BaySel08], has a good directional selectivity. The frequency resolution of DTCWPT and 2d-DTCWPT can be further improved if M Band DTCWPT is used, as described in [BaySel08]. A generalization of the Hyperanalytic Wavelet Transform (HWT) is proposed in [FirIsaBouIsa09].

The HWT implementation [AdaNafBouIsa07b] supposes four trees, each one implementing a 2d-DWT. The first tree is applied to the input image producing the detail wavelet coefficients d_A. The second and the third trees are applied to one dimensional (1D) discrete Hilbert transforms computed across rows ($\mathcal{H}_x$) or columns ($\mathcal{H}_y$) of the input image and produce the detail wavelet coefficients d_B and d_C. The fourth tree is applied to the result obtained after the computation of the two 1D discrete Hilbert transforms of the input image ($\mathcal{H}_x$ and $\mathcal{H}_y$) and generates the detail wavelet coefficients d_D. The directional selectivity is enhanced using linear transformations from equation (53). HWPT was obtained from HWT in

[FirIsaBouIsa09], by replacing the four trees computing the 2d-DWT with trees that compute 2d-DWPTs. There are several similarities between the HWPT and the complex wavelet packets transforms previously mentioned. As the CWPT and the DTCWPT, HWPT uses four trees. Its quasi-analyticity comes from (52). The quasi shift-invariance, highlighted in [FirIsaBouIsa09], is inherited from the HWT. The HWPT improves the frequency resolution of HWT in the same way the DWPT improves the frequency resolution of DWT. At last, HWPT and DTCWPT, have an increased directional selectivity in comparison with the 2d-DWPT. This is so because the same mechanism of improving the directional selectivity as in the case of DTCWT (based on the linear transformation from equation (53)) was used for the HWT implementation.

HWPT Directional Selectivity In the case of the 2d-DWT three preferential directions are defined: horizontal, vertical and diagonal. 2d-DWPT has an increased directional selectivity, compared to 2d-DWT due to supplementary splitting of the high-pass filters outputs denoted by g. In the following the example given in [FirIsaBouIsa09] and highlighted in Fig. 33 will be considered. This example is based on two hypotheses: the spectrum of the input image is considered constant and the lowpass and highpass filters (h and g) are considered ideal.

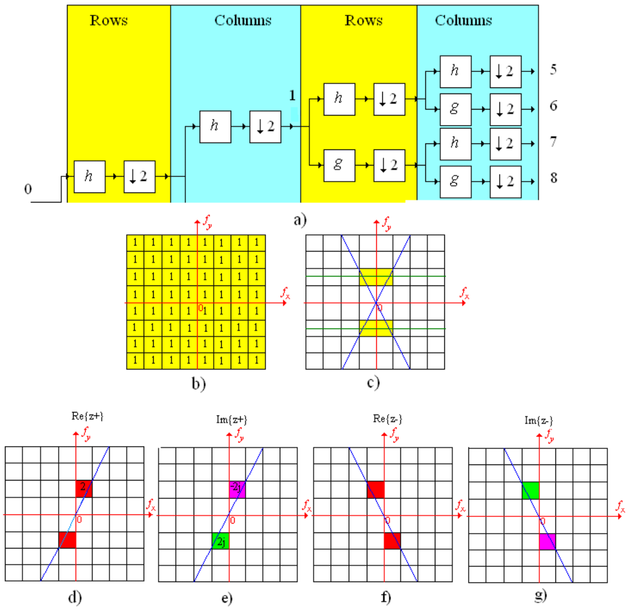

Fig 33 A comparison of the directional selectivities of 2d DWPT and HWPT. a) The selected path is 0→6. b) The spectrum of the input image is supposed to be constant. c) Directional selectivity of 2d DWPT. Directional slectivity of HWPT: d) real part of coefficients z_+, e) imaginary part of coefficients z_+, f) real part of coefficients z_-, g) imaginary part of coefficients z_-.

A part of the 2d-DWPT computation scheme, with two iterations, and the spectrum of the input image are shown in Fig.33a and b, respectively. The spectrum of the image obtained at the output 6 is shown in Fig. 33c. It has two preferential orientations: ±atan(2). Consequently, the directional selectivity of the 2d-DWPT is higher than that of the 2d-DWT. As shown in [AdaNafBouIsa07b], HWT is capable to separate six preferential orientations. We consider the same path (0→6) for the four 2d-DWPTs that implement the HWPT as in Fig. 33a and we apply eq. (53). The four images with the spectra represented in Fig. 33d-g are obtained.

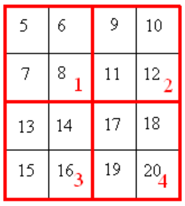

Fig.34 The rule used for indexing the sub-images which represent the results of the HWPT with two decomposition levels.

Taking into account its increased directional selectivity, we propose a possible application of HWPT for the identification of the principal orientations contained in an image. A solution for this problem was proposed in [AndKinFau05]. It implies the utilization of the 2d-DTCWT and is based on a new concept, namely the Inter-Coefficient Product (ICP). Contrary to [AndKinFau05], the method proposed in the following is based on the energy of each subband. We identify the principal orientations from the image Lena. Applying the HWPT with two decomposition levels, we obtain the sub-images z_+ and z_-, which are indexed as in Fig. 34.

Sub-image index	***Direction***	***Sub-image index***	***Direction***
2	± atan(2)	8, 17, 20	± atan(1)
3	± atan(1/2)	9, 13	± atan(1/5)
4	± atan(1)	10, 14	± atan(3/5)
6	± atan(3)	11, 15	± atan(1/7)
7	± atan(1/3)	12,16	± atan(3/7)
18	± atan(7/5)	19	± atan(5/7)

Table 19 Principal orientations of detail sub-images for HWPT with two decomposition levels.

Sub-image	**Energy**	**Order**
z_{+6}	3.8471e+007	**1**
z_{-6}	3.4375e+007	**2**
z_{+7}	1.5123e+007	**3**
z_{+8}	1.0834e+007	**4**

Table 20 The energies of the sub-images which correspond to the principal directions contained in image Lena.

The principal directions of those sub-images are presented in Table 19. Computing the normalized energies of each detail sub-image obtained applying the HWPT with two decomposition levels to the image Lena, we can identify the principal orientations contained in this image as the preferential orientations of the sub-images which contain the highest values of normalized energy. We have normalized the energies of the detail wavelet coefficients with respect to the subband bandwidth in order to make objective the comparison of the energies computed at different decomposition levels. These values are presented in Table 20. The normalized energies values reflect two types of information, about the principal orientations contained in the input image and about the frequency content of the image features which correspond to those orientations. In general the simple computation of the normalized energies does not permit the separation of those two types of information. The information about the principal orientations contained in the input image can be accurately separated from the values of normalized energies only for flat spectrum input images. We have marked the principal orientations contained in the image Lena (which does not have a flat spectrum), as are they classified in Table 20, in Fig. 35. We observe by visual inspection that the orientations detected by the proposed algorithm are dominant for the image Lena despite the fact that its spectrum is not flat. Orientation 1 is observed in the left part of the contour of the hat, orientation 2 corresponds to the right part of the same contour, orientation 3 is observed in the region of feathers and orientation 4 corresponds to the brim heat. We used in this experiment the HWPT with two decomposition levels computed with the aid of the mother wavelet Daubechies-20 (having ten vanishing moments).

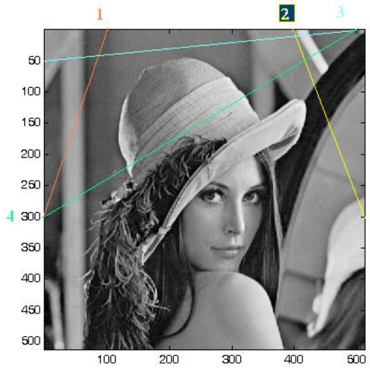

Fig. 35 Main directions contained in the image Lena.

We reviewed several methods for the enhancement of the directional selectivity in image analysis highlighting the role of Hyperanalytic Wavelet Packets. It was shown that the directional selectivity of the HWPT depends on the number of decomposition levels of the transform. For two decomposition levels, the HWPT can separate eighteen orientations, as can be seen in Table 19. The degree of separation depends on the MW used, being proportional with the number of vanishing moments of the MW. The HWPT can be seen as a Gabor FB inheriting all the applications of that structure as for example the segmentation of SONAR images [KarFabBou08]. We have proposed as new application of the HWPT, the detection of the principal directions contained in an image. The corresponding algorithm consists in the computation of the normalized energies of the HWPT sub-images. The preferential orientations of the sub-images with the highest normalized energies represent the principal directions contained in the image analyzed if its spectrum is flat. The constraint of flatness can be avoided using the concept of ICP but the corresponding algorithm [AndKinFau05] is more complex. We have exemplified the proposed algorithm with the aid of the image Lena, which does not have a flat spectrum. The results obtained have good visual quality, showing that the proposed method is promising for images without flat spectrum as well. Principal direction of a texture is a parameter, which can be used for the retrieval of a particular image from a database. The proposed detection algorithm could be used in the same way as a Gabor FB [KarFabBou08]. In the case of content-based image retrieval application, the separation of the two types of information contained in the values of the normalized energies could be not necessary.

2.4.3 A second order statistical analysis of the 2D Discrete Wavelet Transform

In [IsaNaf14], we presented a second order statistical analysis of the 2D Discrete Wavelet Transform (2D DWT) coefficients. This continues the analysis from [NafBerNafIsa12]; [FirNafIsaBouIsa10]; [NafFirIsaBouIsa10a]; [NafFirIsaBouIsa10b].

The input images are considered as wide sense bivariate random processes. We derived closed form expressions for the wavelet coefficients’ correlation functions in all possible scenarios: inter-scale and inter-band, inter-scale and intra-band, intra-scale and inter-band and intra-scale and intra-band. The particularization of the input process to the White Gaussian Noise (WGN) case is considered as well. A special attention was given to the asymptotical analysis obtained by considering an infinite number of decomposition levels. Simulation results are also reported, confirming the theoretical results obtained. The equations derived, and especially the inter-scale and intra-band dependency of the 2D DWT coefficients, are useful for the design of different signal processing systems as for example image denoising algorithms. We showed how to apply our theoretical results for designing state of the art denoising systems which exploit the 2D DWT.

A great number of Wavelet Transforms (WT) as for example: 2D Discrete WT (2D DWT) [Mal99], 2D Undecimated DWT (2D UDWT) [StaFadMur07], 2D Double Tree Complex WT (2D DTCWT) [SelBarKin05], etc., can be used for image processing, because most of the image information is concentrated in few large wavelet coefficients, property known as sparsity of the wavelet representation. This simplifies and accelerates the image processing algorithm considered and is a consequence of the 2D WT decorrelation properties. The first results about the decorrelation effect of WT were obtained for 1D transforms. For example the covariance of coefficients obtained by wavelet decomposition of random processes can be computed recursively based on an algorithm described in [VanCor99]. This algorithm has an interesting link to the 2D DWT, which makes computations faster. A statistical analysis of 1D DWT was reported in [CraPer05] and it was generalized in [AttPasIsa07] to the wavelet packets case. Some results of statistical analysis of 2D WT can also be found. In [LiuMou01] is treated the case of 2D DWT, highlighting the inter-scale and inter-band dependencies of wavelet coefficients, with the aid of the mutual information concept, but closed form expressions for the correlation functions are missing. A statistical analysis of 2D UDWT is presented in [FouBenBou01] and a second order statistical analysis of 2D DTCWT is presented in [ChaPesDuv07].

All the WT are characterized by two features: the mother wavelets (MW) and the primary resolution (PR), or the number of decomposition levels. The importance of their selection is highlighted in [Nas02]. An appealing particularity of 2D DWT is the inter-scale dependency of the wavelet coefficients [LiuMou01]. The goal of the present paper is a complete second order statistical analysis of the 2D DWT, establishing closed form expressions for the correlation functions in all four possible scenarios. We also highlight the influences of the 2D DWT features on those correlation functions.

We study the statistical decorrelation of the 2D DWT coefficients when the image is a wide sense stationary bivariate random process, developing the results presented in [NafFirIsaBouIsa10b]. Starting from the implementation of this transform, we highlight the four possible scenarios: inter-scale and inter-band, inter-scale and intra-band, intra-scale and inter-band and intra-scale and intra-band dependencies. We treat the case of the 2D DWT coefficients of a bivariate white Gaussian noise (WGN) as well. The most important theoretical results obtained were verified by simulation. The object is a discussion of the results presented, oriented toward images denoising.

The main advantage of 2D DWT versus other 2D WT, as for example the 2D DTCWT, is its computational flexibility, as it inherits some of the classes of MW developed in the framework of the 1D DWT, like the Daubechies, Symmlet or Coiflet families [Dau92]. This non-redundant transform can be implemented using the very fast Mallat's algorithm [Mal99]. The drawbacks of the 2D DWT are lack of translation invariance and poor directional selectivity. The perfect translation invariance can be reached using the 2D UDWT. Quasi translation invariance can be obtained using Complex WT (CWT) as for example the 2D DTCWT or the Hyperanalytic Wavelet Transform (HWT) [FirNafIsaIsa11]. It represents a generalization of the 2D DWT, which is conceived for real images, for hyperanalytic images. The HWT implementation supposes the computation of 2D DWT of four different images, representing the components of the hyperanalytic input image. The lack of translation invariance of 2D DWT can be corrected in denoising application [BluLui07]. Both CWT also have better directional selectivity than 2D DWT.

Each of the iterations of the Mallat's algorithm implies several operations [Mal99]. The rows of the input image, obtained at the end of the previous iteration, are passed through two different filters: a low-pass filter - L with the impulse response m_0 and a high-pass filter - H with the impulse response m_1, resulting in two different sub-images. The rows of the two sub-images obtained at the output of the two filters are decimated with a factor of two. Next, the columns of the two images obtained are filtered with m_0 and m_1. The columns of those four sub-images are also decimated with a factor of two. Four new sub-images, representing the result of the current iteration (which corresponds to the current decomposition level – or scale), are obtained. These sub-images are called subbands. The first sub-image, obtained after two low-pass filtering (LL), is named approximation sub-image (or LL subband). The other three are named detail sub-images: LH, HL and HH. The LL subband represents the input for the next iteration. In the following, the coefficients of 2D DWT will be denoted by d_m^k, where m represents the current scale and k is the subband and it is $k = 1$ – for LH, $k = 2$ – for HL, $k = 3$ – for HH and $k = 4$ – for LL. These coefficients are computed using the following scalar products:

$$d_m^k[n,p] = \langle f(\tau_1,\tau_2), \psi_{m,n,p}^k(\tau_1,\tau_2)\rangle, \tau_1 \in \mathbb{R}, \tau_2 \in \mathbb{R}, \tag{54}$$

where f represents the image whose DWT is computed (considered as a bivariate random process) and the wavelets are real functions and can be factorized as:

$$\psi_{m,n,p}^k(\tau_1,\tau_2) = \alpha_{m,n}^k(\tau_1) \cdot \beta_{m,p}^k(\tau_2), \tag{55}$$

and the two factors can be computed using the scaling function $\varphi(\tau)$ and the MW $\psi(\tau)$ with:

$$\alpha_{m,n}^k(\tau) = \begin{cases} \varphi_{m,n}(\tau), & \text{for } k = 1,4 \\ \psi_{m,n}(\tau), & \text{for } k = 2,3 \end{cases} \tag{56}$$

$$\beta_{m,p}^k(\tau) = \begin{cases} \varphi_{m,p}(\tau), & \text{for } k = 2,4 \\ \psi_{m,p}(\tau), & \text{for } k = 1,3 \end{cases} \tag{57}$$

where:

$$\varphi_{m,n}(\tau) = 2^{-\frac{m}{2}}\varphi(2^{-m}\tau - n) \text{ and } \psi_{m,n}(\tau) = 2^{-\frac{m}{2}}\psi(2^{-m}\tau - n). \tag{58}$$

Taking into account Eqs. (56)-(58), it can be written:

$$\psi_{m,n,p}^k(\tau_1,\tau_2) = 2^{-m}\psi^k(2^{-m}\tau_1 - n, 2^{-m}\tau_2 - p) \text{ where } \psi^k(\tau_1,\tau_2) = \psi_{0,0,0}^k(\tau_1,\tau_2). \tag{59}$$

The expectation of the wavelet coefficients: We begin the second order statistical analysis by computing the statistical mean of the wavelet coefficients:

$$\mu_{d_m^k} = E\{d_m^k\} = E\{\langle f(\tau_1,\tau_2), \psi_{m,n,p}^k(\tau_1,\tau_2)\rangle\}, \quad \mu_{d_m^k} = E\left\{\iint_{-\infty}^{\infty} f(\tau_1,\tau_2)\psi_{m,n,p}^{k*}(\tau_1,\tau_2)d\tau_1 d\tau_2\right\}. \tag{60}$$

Applying Fubini's theorem and taking into account the fact that the random process f is wide sense stationary, we obtain:

$$\mu_{d_m^k} = \iint_{-\infty}^{\infty} E\{f(\tau_1,\tau_2)\}\psi_{m,n,p}^{k*}(\tau_1,\tau_2)d\tau_1 d\tau_2 = \mu_f \iint_{-\infty}^{\infty} \psi_{m,n,p}^{k*}(\tau_1,\tau_2)d\tau_1 d\tau_2 = \mu_f \mathcal{F}^*\{\psi_{m,n,p}^k(\tau_1,\tau_2)\}(0,0). \tag{61}$$

The Fourier transform was denoted by $\mathcal{F}$ and the expectation of the input image by μ_f in Eq. (61). Because the spectrum of the wavelet can be expressed as,

$$\mathcal{F}\{\psi_{m,n,p}^k\}(\tau_1,\tau_2) = 2^m e^{-j2^m(\xi_1 n + \xi_2 p)}\mathcal{F}\{\psi^k\}(2^m\xi_1, 2^m\xi_2), \tag{62}$$

the last equation becomes:

$$\mu_{d_m^k} = 0, \text{ for } k = 1,2,3 \text{ and } \mu_{d_m^k} = 2^m \mu_f \text{ , for } k = 4. \tag{63}$$

Consequently, the expectations of the detail wavelet coefficients are null. Only the expectations of the fourth subband (approximation sub-image) are not null but are dependent on the scale and on the expectation of the original image μ_f.

The correlation of the wavelet coefficients. The pyramid corresponding to the computation of the 2D DWT is presented in Fig. 36, where four types of coefficients dependencies are exemplified: inter-scale and inter-band, inter-scale and intra-band, intra-scale and inter-band and intra-scale and intra-band. In the inter-scale and inter-band case, the coefficients are located in different scales and subbands ($m = 1$, $k = 4$ and $m = 3$, $k = 3$, for example). In the inter-scale and intra-band case, coefficients are located in different scales, but same subband ($m = 1$, $k = 1$ and $m = 2$, $k = 1$ for example). The coefficients belonging to the sets indexed by $m = 3$, $k = 4$ and $m = 3$, $k = 2$ in Fig. 36, have an intra-scale and inter-band dependency. Finally, the coefficients belonging to same decomposition level and same subband have an intra-scale and intra-band dependency. The coefficients having same geometrical coordinates at consecutive decomposition levels are named parents (for the last decomposition level), children (for previous decomposition level) and nephews (for previous decomposition level).

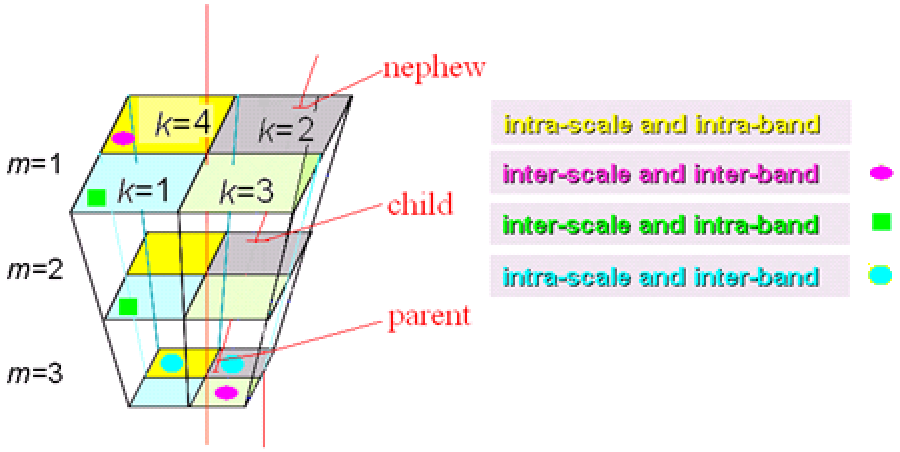

Fig. 36. 2D DWT pyramid, three decomposition levels, subbands and examples of coefficients dependencies.

In the following we analyzed the four types of correlation.

The inter-scale and inter-band case We consider that the input image f is a bivariate second order random process. The cross-correlation of two wavelet coefficients, located in the subbands k_1 and k_2 at the scales m_1 and $m_2 = m_1 + q$, where $q \in \mathbb{N}^+$, and of geometrical coordinates (n_1, p_1) and (n_2, p_2) respectively, can be computed using the following equation:

$$R_{d_{m_1}^{k_1} d_{m_2}^{k_2}}(2^q n_1' - n_2, 2^q p_1' - p_2) = 2^{2m_1+q} R_f\left(2^{m_1+q}(n_2 - n_1'), 2^{m_1+q}(p_2 - p_1')\right) * R_{\psi^{k_2}\psi^{k_1}}(n_2 - n_1', p_2 - p_1'), \tag{64}$$

where the effect of decimators (used at each iteration of 2D DWT) was considered by putting $n_1 = 2^q n_1'$ and $p_1 = 2^q p_1'$. As one can observe, the inter-scale ($q \neq 0$) and inter-band ($k_1 \neq k_2$) dependency of the wavelet coefficients is function of the autocorrelation of the input image, R_f and of the cross-correlation of the MW which generate the considered subbands, $R_{\psi^{k_2}\psi^{k_1}}$. If the input image is stationary, then the image formed by the coefficients is also stationary. A simplified version of (64) is obtained, if we suppose that the input signal is a bivariate independent and identically distributed (i.i.d.) WGN with variance σ_n^2 and zero mean, $f(\tau_1, \tau_2) = w(\tau_1, \tau_2)$:

$$\begin{aligned} R_{d^{k_1}_{m_1} d^{k_2}_{m_2}} & \left(2^q n'_1 - n_2, 2^q p'_1 - p_2\right) \\ & = 2^{2m_1+q}\left(\sigma_n^2 \delta * R_{\psi^{k_2}\psi^{k_1}}\right)\left(n_2 - n'_1, p_2 - p'_1\right) \\ & = 2^{2m_1+q}\sigma_n^2 R_{\psi^{k_2}\psi^{k_1}}\left(n_2 - n'_1, p_2 - p'_1\right). \end{aligned} \tag{65}$$

In this case, the inter-scale and inter-band dependency is function on the cross-correlation of the MW generating the considered subbands only. Generally speaking, **the 2D DWT correlates the input signal.**

The inter-scale and intra-band case. For $k_1 = k_2 = k$, the cross-correlation of the wavelet coefficients expressed by (11) becomes an inter-scale and intra-band dependency:

$$R_{d^k_{m_1} d^k_{m_2}}(2^q n'_1 - n_2, 2^q p'_1 - p_2) = 2^{2m_1+q} R_f\left(2^{m_1+q}(n_2 - n'_1), 2^{m_1+q}(p_2 - p'_1)\right) * R_{\psi^k}(n_2 - n'_1, p_2 - p'_1). \tag{66}$$

In this case, the cross-correlation of MW ψ^{k_2} and ψ^{k_1} (from Eq. (64)) is substituted by the autocorrelation of the MW, ψ^k. If it generates by translations and dilations an **orthogonal** basis of $L^2(\mathbb{R}^2)$, then its autocorrelation has the following property:

$$R_{\psi^k}(n,p) = \delta(n,p), \tag{67}$$

which can be proved by direct computation. In the following, the MW which satisfy condition (67) will be called orthogonal MW. The expression of the inter-scale and intra-band dependency of the coefficients cross-correlation becomes:

$$R_{d^k_{m_1} d^k_{m_2}}(2^q n'_1 - n_2, 2^q p'_1 - p_2) = 2^{2m_1+q} R_f\left(2^{m_1+q}(n_2 - n'_1), 2^{m_1+q}(p_2 - p'_1)\right). \tag{68}$$

This cross-correlation is function of the autocorrelation of the input image only. The wavelet coefficients are still correlated. If the input is a bivariate i.i.d. WGN with variance σ_n^2 and zero mean, $f(\tau_1, \tau_2) = w(\tau_1, \tau_2)$, then:

$$R_{d^k_{m_1} d^k_{m_2}}(2^q n'_1 - n_2, 2^q p'_1 - p_2) = 2^{2m_1+q}\sigma_n^2 \delta\left(2^{m_1+q}(n_2 - n'_1), 2^{m_1+q}(p_2 - p'_1)\right). \tag{69}$$

The right hand side of the last equation equals zero almost everywhere because the conditions $n_2 = n'_1$ and $p_2 = p'_1$ can not be fulfilled, as referring to indexes of coefficients belonging to different decomposition levels separated by decimators. We conclude from the equation above that the wavelet coefficients of a WGN, at different decomposition levels, are not correlated inside a subband for orthogonal MW.

The intra-scale and inter-band case. For $m_1 = m_2 = m$ and $k_1 \neq k_2$, the cross-correlation in Eq. (64) becomes:

$$R_{d^{k_1}_m d^{k_2}_m}(n'_1 - n_2, p'_1 - p_2) = 2^{2m} R_f\left(2^m(n_2 - n'_1), 2^m(p_2 - p'_1)\right) * R_{\psi^{k_2}\psi^{k_1}}(n_2 - n'_1, p_2 - p'_1). \tag{70}$$

If the input image is a zero mean bivariate i.i.d. WGN random process with variance σ_n^2, then the last equation can be written in the following form:

$$R_{d^{k_1}_m d^{k_2}_m}(n'_1 - n_2, p'_1 - p_2) = 2^{2m}\sigma_n^2 R_{\psi^{k_2}\psi^{k_1}}(n_2 - n'_1, p_2 - p'_1). \tag{71}$$

The wavelet coefficients are still correlated.

The intra-scale and intra-band case. For $m_1 = m_2 = m$, the cross-correlation of the wavelet coefficients given in Eq. (68) becomes an autocorrelation, expressing an intra-scale and intra-band dependency:

$$R_{d^k_m}(n_1 - n_2, p_1 - p_2) = 2^{2m} R_f\left(2^m(n_2 - n_1), 2^m(p_2 - p_1)\right).. \tag{72}$$

The autocorrelation of the wavelet coefficients depends only on the autocorrelation of the input image. The last equation can be put in the equivalent form:

$$R_{d_m^k}(n_1-n_2,p_1-p_2) = \frac{1}{4\pi^2}\iint_{-\infty}^{\infty} S_f\left(2^{-m}\omega_1,2^{-m}\omega_2\right)e^{-j[\omega_1(n_2-n_1)+\omega_2(p_2-p_1)]}d\omega_1 d\omega_2. \quad (73)$$

At the limit $m \to \infty$, we obtain:

$$R_{d_\infty^k}(n_1-n_2,p_1-p_2) = S_f(0,0)\delta(n_2-n_1,p_2-p_1). \quad (74)$$

We can say that, asymptotically, the 2D DWT transforms the colored noise into a white one. Hence this transform can be regarded as a **whitening system in an intra-band and intra-scale scenario.**

A stronger result can be obtained if the input is a bivariate i.i.d. WGN with variance $\sigma_n^2$and zero mean, $f(\tau_1,\tau_2) = w(\tau_1,\tau_2)$. In this case, Eq. (73) becomes:

$$R_{d_m^k}(n_1-n_2,p_1-p_2) = \sigma_n^2\delta(n_2-n_1,p_2-p_1). \quad (75)$$

The dependence of the autocorrelation of the wavelet coefficients on m disappeared. The wavelet coefficients of a zero mean white noise image with variance σ_n^2 are organized in zero mean white noise sub-images of same variance at any decomposition level. We can state that, **in the same subband and at the same scale, the 2D DWT does not correlate the i.i.d. bivariate WGN random process for orthogonal MW.** This is a surprising conclusion, taking into account the fact that the implementation of 2D DWT is based on filters which correlate the WGN. The result in Eq. (75) is more significant than the result presented in Eq. (21) because it is verified at each decomposition level (the result in Eq. (75) is not of asymptotical nature).

Experimental results. We carried out experimental tests, where the random process at the input of the 2D DWT is wide sense stationary, to confirm the theoretical results. Two types of results were established; concerning the comportment of the 2D DWT in the presence of a WGN input process, highlighted in Eqs: (65), (69), (71) and (75); and concerning the asymptotical behavior described in Eq. (74). For the first case, we have used a zero mean bivariate WGN random process w. To confirm the result concerning the asymptotical regime of 2D DWT, we have used for simulations another wide sense stationary random process, obtained by filtering the process w with a bivariate running averager having a rectangular sliding window with size 10×10, which will be denoted in the following by f. The random variables W_{n_1,n_2}, $1 \leq n_1 \leq N_1, 1 \leq n_2 \leq N_2$, are Gaussian independent and identically distributed with zero mean and unitary standard deviation. The autocorrelation of the bivariate WGN process w is presented in Fig. 37 and the autocorrelation of the process f is presented in Fig. 38.

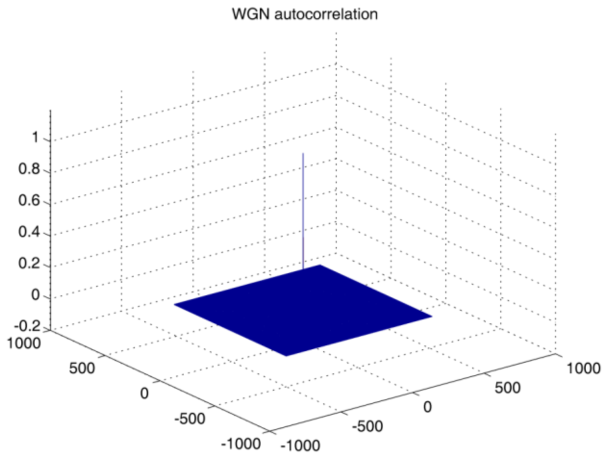

Fig. 37. The normalized autocorrelation of the WGN process.

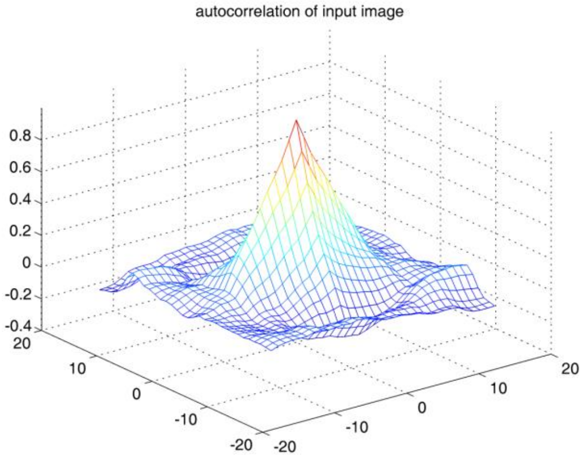

Fig. 38. Normalized autocorrelation of a group of 256 pixels belonging to a realization of the process f.

The experimental results [IsaNaf14] show that, for the random processes considered above, the theoretical results can actually be attained with reasonable values for the decomposition level m using MW with 10 vanishing moments, with the shorter support, proposed by Ingrid Daubechies [Dau92]. These experimental results have been obtained by achieving full 2D DWT decompositions of the input random process specified above. In some cases, 10 realizations of this input random process were considered and the corresponding results given hereafter are average values over these 10 realizations.

The average empirical cross-correlation functions of the 2D DWT coefficients are calculated on the basis of 256 coefficients per subband. The values N_1 and N_2 were selected in each experiment, to make possible the computation of those average empirical cross-correlation functions in each subband for every decomposition level.

The first experiment refers to Eq. (69), by computing the cross-correlation between the coefficients belonging to same subband at two successive decomposition levels, for a bivariate WGN input process. In this experiment, we have used the values $N_1 = N_2 = 2048$. The group of pixels considered was obtained by cropping a region from the input image with size 32×32. We have selected the following parameters:

- decomposition levels: $m = 1$ and $m = 2$,
- subbands: $k = 1$ and $k = 2$.

The corresponding cross-correlations are represented in Fig. 39. The empirical cross-correlation functions were obtained by averaging the corresponding cross-correlations obtained for 10 different realizations of the input process w. It can be observed that the values of the cross-correlations are small enough to consider that the corresponding 2D DWT coefficients are decorrelated.

The second experiment for a WGN input refers to Eq. (73). In the following, we illustrate Eq. (75) to show that the 2D DWT does not correlate the input bivariate WGN process in an intra-scale and intra-band scenario. In this experiment we have used the values $N_1 = N_2 = 512$ and the following parameters:

- decomposition levels: $m = 1$ and $m = 2$,
- subbands: $k = 1, 2$ and 3.

The corresponding autocorrelations are represented in Fig. 40.

The autocorrelations of the wavelet coefficients represented in Fig. 40 are similar with the autocorrelation of the input image for any decomposition level and any subband, showing that the 2D DWT does not correlate the input bivariate WGN. Finally, the third experiment refers to the 2D DWT coefficients of a colored bivariate noise process. More specifically, we deal with the Eq. (74). In this experiment we have used the values $N_1 = N_2 = 2048$ and we have considered as input image the random process f.

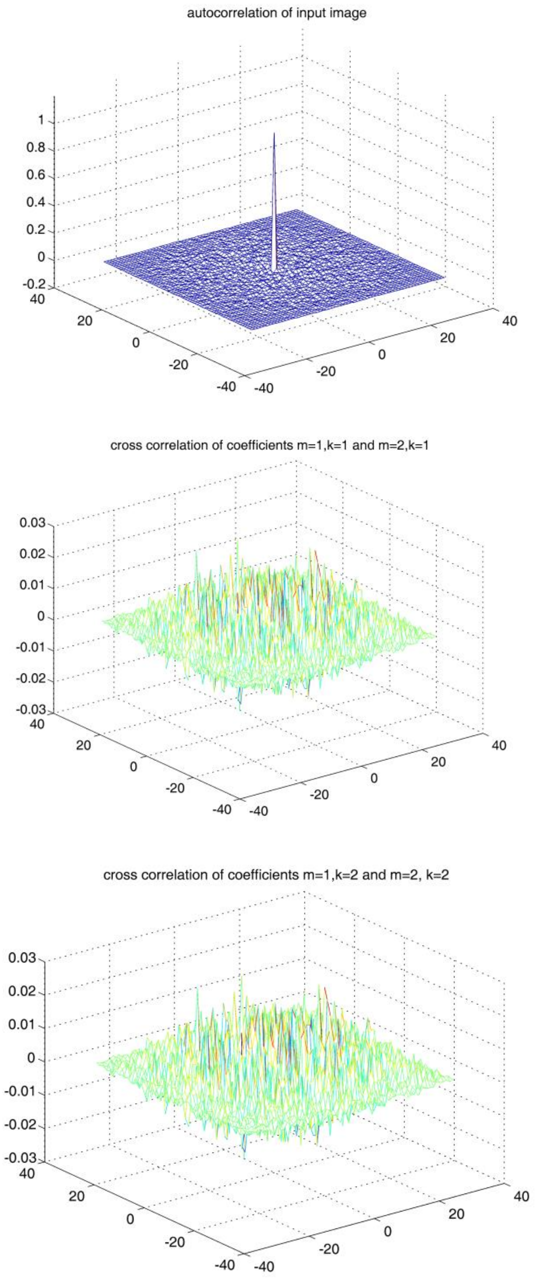

Fig. 39. Autocorrelation of input image (up) and cross-correlation between the coefficients belonging to subbands ($k = 1$-middle) and subbands ($k = 2$-bottom) situated at successive decomposition levels ($m = 1$ and $m = 2$) of 2D DWT of a bivariate WGN (inter-scale and intra-band scenario). The correlations are normalized to the maximum of the autocorrelation of input image.

We have selected the following parameters:

- decomposition levels: $m = 1$ or 5,
- subbands: $k = 1$ or 2.

The corresponding autocorrelations are represented in Fig. 41. Analyzing the results, it can be noticed that with the increasing of the number of decomposition levels, the resemblance of the shapes of those correlations with the shape of the autocorrelation of the process from Fig. 37, which corresponds to a bivariate WGN random signal, increases. The results in Fig. 41 were obtained on a single realization of the input process. The shapes of the autocorrelations could be even closer to the shape of the autocorrelation of a WGN random process if multiple realizations of the input random process would be used.

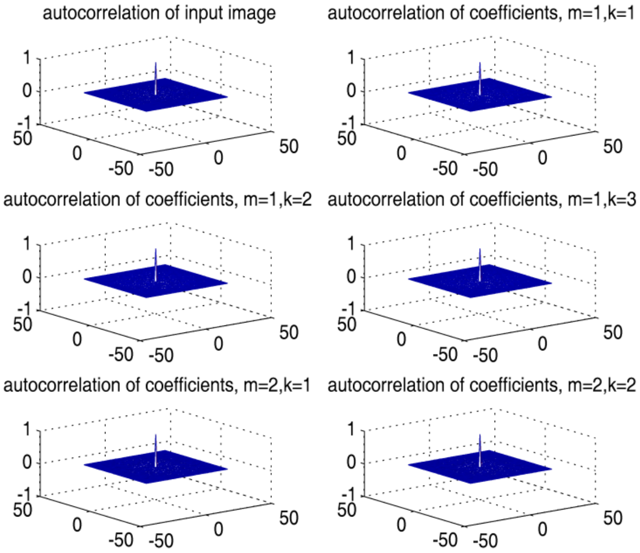

Fig. 40. Autocorrelations of 2D DWT coefficients of a bivariate WGN process in an intra-scale and intra-band scenario. From left to right and top to bottom are represented the autocorrelations of input image, and of the wavelet coefficients from the decomposition level *m*=1 and the subbands *k*=1, 2, or 3; and from the decomposition level *m*=2 and the subbands *k*=1 and 2.

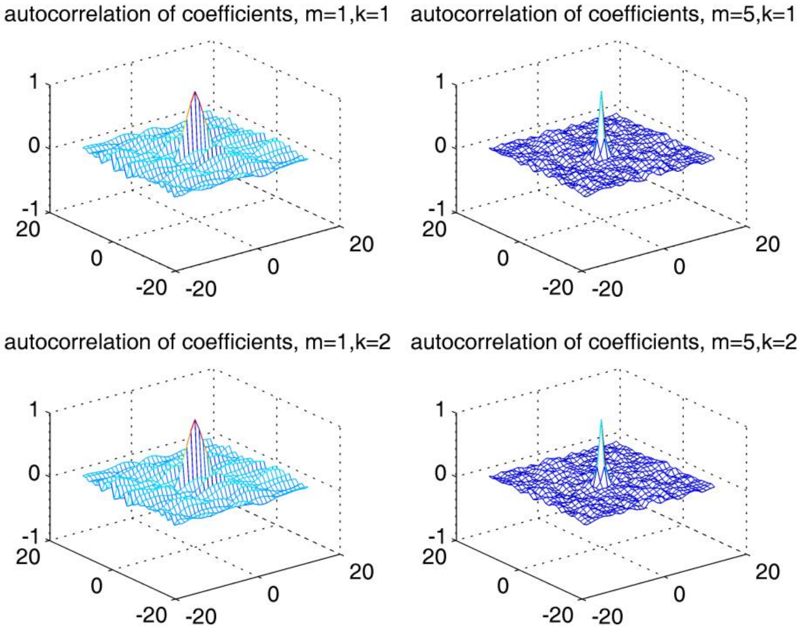

Fig. 41. Autocorrelations of 2D DWT detail coefficients of a bivariate correlated random process at the first decomposition level (left column) and fifth decomposition level (right column). First line ($k = 1$ subband) and second line ($k = 2$ subband).

The experimental results show that, for the random process considered above, the asymptotic decorrelation stated by Eq. (74) can actually be attained with reasonable values for the decomposition level $(m_1 = m_2 \geq 7)$. It must be observed that the random process f used for the illustration of the asymptotical decorrelation effect of the 2D DWT coefficients, represented in Fig. 39, is highly correlated. For input random processes less correlated, the number of decomposition levels required to obtain the decorrelation could be smaller $(m < 6)$.

The results highlighted are useful for the design of different image processing methods: compression (JPEG-2000), denoising [FirNafIsaIsa11], watermarking [NafIsa11] or classification systems. The principal difficulty arising in the design of those systems, with statistical tools, lies in the nonstationary nature of the bivariate random process which model natural images. As suggested in [Pes99], the approach for the statistical analysis of WT of nonstationary random processes is based on higher order statistics. In [AttBer12] is shown that the Wavelet Packet Transform realizes a kind of stationnarisation by reducing the higher order dependencies of nonstationary input signal. During acquisition and transmission, images are often corrupted by additive noise. The aim of an image denoising algorithm is then to reduce the noise level, while preserving the image features.

In case of additive noise, the acquired image is expressed as:

$$f = s + r, \tag{76}$$

where s represents the noiseless component of input image and r is noise. Computing the 2D DWT of both members of the last equation we obtain:

$$h = u + v \Leftrightarrow \ {}_{h}d_{m}^{k} = \ {}_{u}d_{m}^{k} + \ {}_{v}d_{m}^{k}, \tag{77}$$

where: h=2D DWT$\{f\}$, u=2D DWT$\{s\}$ and v=2D DWT$\{r\}$. If the input noise r is WGN, $r = w$, then $v = w$, because the 2D DWT of WGN is also WGN (as it is shown in Eq. (75) and in Fig. 40).

In the case of multiplicative noise (for example speckle noise), Eq. (76) becomes:

$$f_m = s \times r. \tag{78}$$

The multiplicative noise can be reduced to additive noise by homomorphic treatment: $f = \log f_m$.

We will consider in the following the denoising scenario which correspond to additive WGN (AWGN) only. Every image denoising method has three steps: acquired signal’s WT computation; filtering in wavelets domain; computation of Inverse WT (IWT). A huge number of denoising methods were developed in the last years, by associating different WT with different filters (requested in the second step of the denoising method). In the following, we present a possible classification of denoising methods, highlighting each class with examples based on 2D DWT. A first category of denoising methods is composed by non-parametric techniques. These are denoising methods which not take into account any model of the components of the acquired signal [DonJoh94]. A second category of denoising methods is composed by parametric techniques, [FirNafIsaIsa11], [GleDat06], [FirNafBouIsa09], which consider statistical models for both components of the acquired image. Finally, there are some denoising methods, which lie at the border of parametric and non-parametric techniques, named semi-parametric techniques [BluLui07], [LuiBluUns07], [LuiBluUns11], [LuiBluWol12]. These consider models only for the noise component of the input image. The denoising methods belonging to the second and third category, already mentioned, exploit some of the consequences of the second order statistical analysis reported in [IsaNaf14]. The results of our statistical analysis can be directly applied in denoising to characterize the noise detail coefficients by ignoring the term u in Eq. (77).

The use of orthogonal 2D DWT, denoted in the following as 2D DOWT, has some consequences in denoising:

1. **The noise remains white and Gaussian with same statistics (mean, variance) see Eq. (75) and Fig. 40, in wavelet domain**. The detail 2D DOWT coefficients of noise, ${}_{w}d_{m}^{k}$, belonging to different subbands, $(k_1 \neq k_2)$ from the same scale (m) or from different scales $(m_1 \neq m_2)$ are not correlated. So, the most important dependency in case of AWGN scenario is the intra-scale and intra-band dependence. **This allows applying a new denoising function independently in every detail subband**, which means that the solution obtained is subband-adaptive **[SelBarKin05], [BluLui07], [GleDat06], [LuiBluUns07], [LuiBluUns11], [LuiBluWol12].**
2. **The cross-correlation of detail wavelet coefficients of noise in inter-scale and intra-band case equals zero almost everywhere (Eq. (69), Fig. 39).** Hence, the inter-scale dependency of noise detail coefficients is not important in this case. The right hand side of Eq. (68), which consists of the autocorrelation of the input image, R_f, equals the autocorrelation of the noiseless component of the input image, R_s (Eq. (76)). We can estimate scaled versions of the autocorrelation of the noiseless component of input image s, by computing the cross-correlation of wavelet coefficients of the acquired image. **The integration of interscale information in denoising algorithms has been shown to improve their quality, both visually and in terms of PSNR [FirNafIsaIsa11, [BluLui07], [GleDat06], [LuiBluUns07], [LuiBluUns11], [LuiBluWol12].**

The design of filters in the second step of denoising methods proposed in **[BluLui07], [GleDat06], [LuiBluUns07]** were clever enough to compensate the first drawback of 2D DOWT. The absence of translation invariance is caused by the potentially non-integer – shifts introduced by the filters m_0 and m_1, which produce contours denoising errors as consequence of Gibbs phenomena in the neighborhood of discontinuities.

In conjunction with the expansion of new wavelet estimators, some researchers have worked on improving the wavelet transform itself. Since the early – non-redundant – 2D DOWT, substantial improvements have been reached in denoising by using shift-invariant transformations, as the 2D UDWT [FouBenBou01], [PizPhi06], or quasi shift-invariant WT with better directional selectivity, as for example the 2D DTCWT [SelBarKin05], [SenSel02], [AchKur05], [MilKin08], the steerable pyramid [PorStrWaiSim03], the Dual-Tree *M*–band WT (DTMBWT) [ChaDuvBenPes08], [ChaDuvPes06] or the HWT [FirNafIsaIsa11]. The new properties resulting from the use of often highly redundant transforms (as for example the 2D UDWT) have been obtained at the expense of the loss of orthogonality, a substantially more intensive memory usage and a higher computational cost than that of the 2D DOWT. The latter point becomes a major concern in image volume denoising and more generally in multichannel image denoising, in particular when the number of channels is large. For instance, even though the usual color image representations require no more than 3–4 channels (RGB, HSV, YUV, or CMYK descriptions), the computational cost is already quite large when shift-invariant (i.e., un-decimated) transforms are involved. Recently, it was proposed a general methodology, the “SURE-LET” paradigm [BluLui07], for building (using a linear expansion of thresholds: “LET” parameterization) and optimizing (using Stein’s unbiased risk estimate: SURE principle) denoising algorithms adapted to any kind of linear transforms, including 2D DOWT. The originality of this approach lies in the hypothesis that the noiseless component of the input image is deterministic. This is the reason why, we have considered the SURE-LET approach as semi-parametric.

Taking into account the drawback of redundancy already mentioned, in [LuiBluUns07] was considered only the case of the association of 2D DOWT with the SURE-LET estimator for multichannel image denoising. The SURE-LET estimator considers the inter-scale and intra-band dependency of the noiseless detail wavelet coefficients as is explained in the following. The parent detail wavelet coefficients of the noiseless component from different subbands of the same decomposition level are large together in the neighborhood of image discontinuities. The corresponding child coefficients are also large, as a consequence of the aforementioned inter-scale and intra-band dependency. So, the position of large wavelet coefficients out of parents at lower decomposition levels (which represent detail wavelet coefficients of noise) can be detected with reasonably good accuracy. The detection of the positions of the large detail wavelet coefficients of noise can be realized by segmentation of subband images. Two classes of detail wavelet coefficients are obtained as result of segmentation: large coefficients and small coefficients. In the case of 2D DOWT, the parent subband is half the size of the child subband. The usual way of putting the two subbands in correspondence is simply to expand the parent by a factor of two. Unfortunately, this approach requires translation invariance. In [BluLui07] is, thus, proposed a solution, which corrects the absence of translation invariance of 2D DOWT and ensures the alignment of image features between the child and its parent. The idea proposed in [BluLui07] comes from the following observation: Let LH_m and LL_m be, respectively, band-pass and low-pass outputs at iteration m of the filterbank. Then, if the group delay between the band-pass and the low-pass filters are equal, no shift between the features of LH_m and LL_m will occur. When the group delays differ—which is the general case—in [BluLui07] is proposed to filter the low-pass subband LL_m in order to compensate for the group delay difference with LH_m. Because the filters considered are separable (see Eq. (55)), only 1-D group delay compensation (GDC) must be considered. After GDC, the features of LH_m and LL_m are aligned, next these sub-images are segmented and the corresponding two classes are compared. As result, the positions of large noise coefficients can be detected and these coefficients can be discarded. In [LuiBluUns07], the association of the 2D DODWT with SURE-LET, already explained, compared favorably with the association of Prob-Shrink algorithm with 2D UDWT (which is translation invariant) [PizPhi06] and with the famous association of the BLS-GSM algorithm with the steerable pyramid transform (which has better directional selectivity than 2D DOWT) [PorStrWaiSim03]. The idea of SURE-LET estimator was further developed in [LuiBluUns11], [LuiBluWol12].

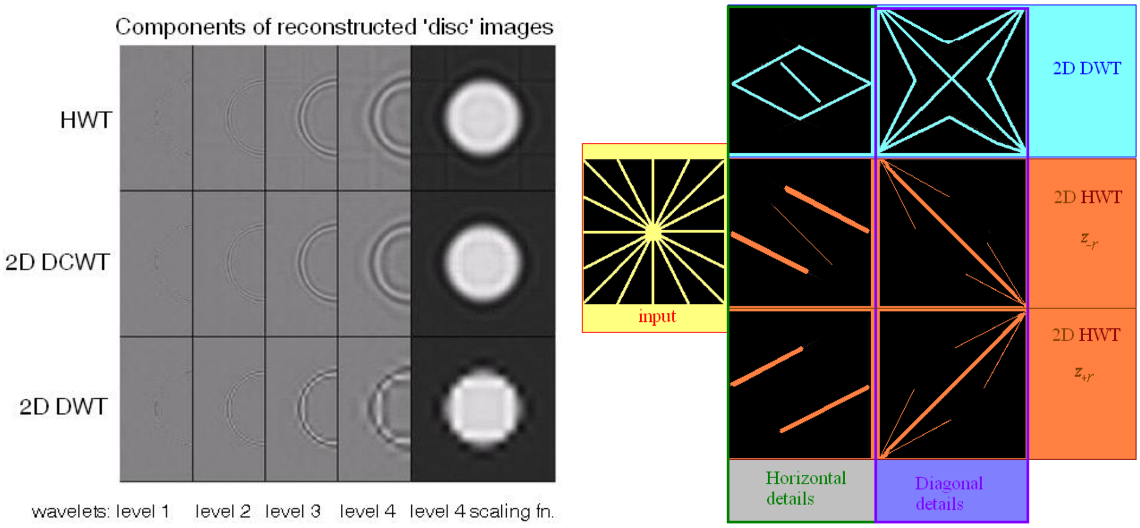

Fig. 42 a) A comparison of HWT (up), 2D DTCWT (middle) and 2D DWT (bottom) of a disc image, which shows that 2D DTCWT and HWT are quasi-shift invariant and that 2D DWT is shift variant. Fig. 42 b) The absolute values of the spectra of horizontal and diagonal detail sub-images obtained after the first iterations of 2D DWT and HWT. In the HWT case, the real and imaginary parts of complex coefficients are separated.

The second drawback of 2D DWT refers to its poor directional selectivity and its effects can be reduced by generalizing this transform to HWT [FirNafBouIsa09].

The hyperanalytic image, associated to the input image f, is composed by four components: f, the 1D discrete Hilbert transform computed across the lines of f, $\mathcal{H}_x\{f\}$, the 1D discrete Hilbert transform computed across the columns of f, $\mathcal{H}_y\{f\}$ and $\mathcal{H}_x\left\{\mathcal{H}_y\{f\}\right\}$. The architecture of HWT is composed by two parts. The first part implements the 2D DWT of the hyperanalytic image associated to the input image f in the initial computations block. The second part realizes the directional selectivity enhancement, using the same solution based on complex linear combinations of detail wavelet coefficients from every type of subband as in case of 2D DTCWT [SelBarKin05]:

$$z_{\pm} = z_{\pm r} + j z_{\pm i} = \left({}_{f}d_m^{1,2,3} \mp {}_{\mathcal{H}_y\{\mathcal{H}_x\{f\}\}}d_m^{1,2,3} \right) + j\left({}_{\mathcal{H}_x}d_m^{1,2,3} \pm {}_{\mathcal{H}_y}d_m^{1,2,3} \right). \tag{79}$$

The HWT coefficients, $z_{\pm}$, are complex and can have positive or negative orientations: ±atan(1/2); ±π/4 and ±atan(2).

The HWT is quasi-shift invariant, as can be seen in Fig. 42a.

A comparison between HWT and 2D DWT is depicted in Fig. 42b. The spectrum of the input image has several preferential orientations: 0, ±atan(1/2), ±π/4, ±atan(2) and π. The better directional selectivity of HWT versus the 2D DWT can be easily observed, comparing the corresponding detail sub-images in Fig. 42b. For the diagonal detail sub-images, for example, the imaginary part of the HWT rejects the directions: -atan(1/2), -π /4 and -atan (2), whereas the 2D DWT conserves these directions. Exploiting the results of the present second order statistical analysis, on the basis of the HWT architecture, we have reported in [NafFirIsaBouIsa10a] results of a complete second order analysis of HWT, which have similar consequences for denoising:

-the AWGN noise remains white and Gaussian in HWT domain,

-the inter-scale and intra-band cross-correlation of detail wavelet coefficients depends only on the autocorrelation of the noiseless component of the input image s.

We have compared in [FirNafIsaIsa11] the method based on the association: 2D DTCWT – bishrink filter, proposed in [SenSel02]; and the method which associates HWT with bishrink filter, respectively, for the case of SONAR images denoising. The HWT outperforms 2D DTCWT, producing a higher PSNR enhancement in case of synthesized images and a higher Equivalent Number of Looks (ENL) in case of real SONAR images.

We have made a complete second order statistical analysis of the 2D DWT of wide-sense stationary random processes, considering all the four possible scenarios: inter-scale and inter-band, inter-scale and intra-band, intra-scale and inter-band and intra-scale and intra-band, giving explicit formulae for the correlation functions in each case. We have shown the importance of orthogonal wavelets and of the number of decomposition levels. We have proved the practical importance of the asymptotic analysis of the autocorrelation of 2D DOWT detail coefficients by simulations, evaluating the speed of convergence towards the unitary impulse.

We have shown how the results of the second order statistical analysis proposed can be used for the design of denoising systems based on 2D DOWT for images affected by AWGN. A different denoising function can be applied independently for every detail subband and decomposition level. We have highlighted the importance of inter-scale and intra-band dependency of detail wavelet coefficients in denoising images affected by AWGN. We have compared three denoising approaches: non-parametric, parametric and semi-parametric, showing the advantages of models based on the hypothesis that the noiseless component of the image to be denoised is deterministic and the noise is a random process.

These results on the second order statistical analysis of 2D DWT have been generalized to HWT in [NafFirIsaBouIsa10a].

A possible continuation is to compare the actual results and the results obtained for HWT with the results of the second order statistical analysis of 2D DTCWT [ChaPesDuv07].

2.4.4 A second order statistical analysis of the Hyperanalytic Wavelet Transform

Wavelet Transforms (WT) are used to process images in many applications in communications. The 2D Discrete WT, 2D DWT has disadvantages [Kin01], [Kin00]: lack of shift invariance and poor directional selectivity, which can be diminished by a complex wavelet transform [Kin00], [AdaNafBouIsa07].

In the papers [FirNafIsaBouIsa10], [NafFirIsaBouIsa10a]. [NafIsa12], we present a second order statistical analysis of the HWT. We applied it in denoising and watermarking but we have not fully exploited its statistical properties. A particularity of HWT is the interscale dependency of coefficients. Similar to the DWT analysis, we derive closed form expressions for the wavelet coefficients' correlation functions in all possible scenarios:

- inter-scale and inter-band (different scale/different subband),
- inter-scale and intra-band (different scale/same subband),
- intra-scale and inter-band (same scale/different subband)
- intra-scale and intra-band (same scale/subband).

In the following, *f* will denote the input image (considered as a stationary bivariate random process), *m* will represent the current scale and *k* = 1 - for the sub-band LH, *k* = 2 - for HL, *k* = 3 - for HH (detail coefficients) and *k* = 4 - for LL (approximation coefficients). The detail coefficients are computed as scalar products of f and the wavelets $\psi^{k}_{m,n,p}$ where *n* and *p* represent horizontal and vertical translations in the expression of the bivariate mother wavelets [Mal99]. We will consider in the following the case of orthogonal wavelets.

The HWT of the image $f(x,y)$ is computed with the aid of the 2D DWT of its associated hypercomplex image, composed by two sequences of complex coefficients, one containing three subbands with positive angle orientations $\operatorname{atan}(1/2)$, $\pi/4$ and $\operatorname{atan}(2)$:

$$z_{+} = z_{+r} + jz_{+i} = \left({}_{f}D_{m}^{1,2,3} - {}_{\mathcal{H}_y\{\mathcal{H}_x\{f\}\}}D_{m}^{1,2,3} \right) + j\left({}_{\mathcal{H}_x}D_{m}^{1,2,3} + {}_{\mathcal{H}_y}D_{m}^{1,2,3} \right),$$

and one containing three subbands with negative angle orientations $-\operatorname{atan}(1/2)$, $-\pi/4$ and $-\operatorname{atan}(2)$:

$$z_{-} = z_{-r} + jz_{-i} = \left({}_{f}D_{m}^{1,2,3} + {}_{\mathcal{H}_y\{\mathcal{H}_x\{f\}\}}D_{m}^{1,2,3} \right) + j\left({}_{\mathcal{H}_x}D_{m}^{1,2,3} - {}_{\mathcal{H}_y}D_{m}^{1,2,3} \right).$$

The expectation of coefficients z_+ and z_- is:

$$E\{z_+\} = E\left\{ {}_{f}D^{1,2,3} \right\} - E\left\{ {}_{\mathcal{H}y\{\mathcal{H}x\{f\}\}}D^{1,2,3} \right\} + jE\left\{ {}_{\mathcal{H}x}D^{1,2,3} \right\} + jE\left\{ {}_{\mathcal{H}y}D^{1,2,3} \right\} = 0 = E\{z_-\}. \quad (80)$$

1) Inter-scale and inter-band case

The intercorrelation between real and imaginary parts of the coefficients in subbands with same type of orientation (positive or negative)

Applying the definition of the statistical correlation for the real and imaginary parts of the coefficients z_+ we obtain a sum of correlations of 2D DWT coefficients:

$$\begin{aligned} &R_{z_{+r}z_{+i}}\left[m_1,m_2,k_1,k_2,n_1,n_2,p_1,p_2\right]=R_{D_f D_{\mathcal{H}x}}\left(m_1,m_2,k_1,k_2,n_1-n_2,p_1-p_2\right)-\\ &-R_{D_{\mathcal{H}y\{\mathcal{H}x\}}D_{\mathcal{H}x}}\left(m_1,m_2,k_1,k_2,n_1-n_2,p_1-p_2\right)+R_{D_f D_{\mathcal{H}y}}\left(m_1,m_2,k_1,k_2,n_1-n_2,p_1-p_2\right)-\\ &-R_{D_{\mathcal{H}y\{\mathcal{H}x\}}D_{\mathcal{H}y}}\left(m_1,m_2,k_1,k_2,n_1-n_2,p_1-p_2\right). \end{aligned} \tag{81}$$

Each term in (81) can be computed using (8) from [FirNafIsaBouIsa10]. S_f is substituted with the power spectral densities and interspectra: $S_{f\mathcal{H}x}$, $S_{\mathcal{H}y\{\mathcal{H}x\}\mathcal{H}x}$, $S_{f\mathcal{H}y}$ and $S_{\mathcal{H}y\{\mathcal{H}x\}\mathcal{H}y}$:

$$\begin{aligned} &S_{f\mathcal{H}x}\left(\xi_1,\xi_2\right)=j\operatorname{sgn}\xi_1 S_f\left(\xi_1,\xi_2\right),\\ &S_{\mathcal{H}y\{\mathcal{H}x\}\mathcal{H}x}\left(\xi_1,\xi_2\right)=-j\operatorname{sgn}^2\xi_1\operatorname{sgn}\xi_2 S_f\\ &S_{f\mathcal{H}y}\left(\xi_1,\xi_2\right)=j\operatorname{sgn}\xi_2 S_f\left(\xi_1,\xi_2\right),\\ &S_{\mathcal{H}y\{\mathcal{H}x\}\mathcal{H}y}\left(\xi_1,\xi_2\right)=-j\operatorname{sgn}\xi_1\operatorname{sgn}^2\xi_2 S_f. \end{aligned} \tag{82}$$

So we have:

$$\begin{aligned} &R_{z_{+r}z_{+i}}\left[m_1,m_2,k_1,k_2,n_1,n_2,p_1,p_2\right]=j/(4\pi^2)\int_{-\infty}^{\infty}\int_{-\infty}^{\infty}\Big[\operatorname{sgn}\left(2^{-m_1}2^{-q}\nu_1\right)+\operatorname{sgn}^2\left(2^{-m_1}2^{-q}\nu_1\right)\cdot\\ &\cdot\operatorname{sgn}\left(2^{-m_1}2^{-q}\nu_2\right)+\operatorname{sgn}\left(2^{-m_1}2^{-q}\nu_2\right)+\operatorname{sgn}\left(2^{-m_1}2^{-q}\nu_1\right)\cdot\\ &\cdot\operatorname{sgn}^2\left(2^{-m_1}2^{-q}\nu_2\right)\Big]\cdot\cdot S_f\left(2^{-m_1}2^{-q}\nu_1,2^{-m_1}2^{-q}\nu_2\right)\cdot\\ &\cdot 2^{-q}\cdot e^{-j\left(\nu_1\left(n_2-2^{-q}n_1\right)+\nu_2\left(p_2-2^{-q}p_1\right)\right)}\cdot\mathcal{F}\left\{\psi^{k_2}\right\}\left(\nu_1,\nu_2\right)\cdot\mathcal{F}^*\left\{\psi^{k_1}\right\}\left(\nu_1,\nu_2\right)d\nu_1 d\nu_2. \end{aligned} \tag{83}$$

The intercorrelation of real and imaginary parts of z_- is given in equation (84). Taking the limit for m_1 infinity in equations (83) and (84) we obtain the result in equation (85) because sgn(0)=0. This result proves that real and imaginary parts of z_+ and z_- are asymptotically decorrelated in an inter-band context.

$$\begin{aligned} &R_{z_{-r}z_{-i}}\left[m_1,m_2,k_1,k_2,n_1,n_2,p_1,p_2\right]=j/(4\pi^2)\int_{-\infty}^{\infty}\int_{-\infty}^{\infty}\Big[\operatorname{sgn}\left(2^{-m_1}2^{-q}\nu_1\right)-\operatorname{sgn}^2\left(2^{-m_1}2^{-q}\nu_1\right)\\ &\cdot\operatorname{sgn}\left(2^{-m_1}2^{-q}\nu_2\right)-\operatorname{sgn}\left(2^{-m_1}2^{-q}\nu_2\right)+\operatorname{sgn}\left(2^{-m_1}2^{-q}\nu_1\right)\cdot\\ &\cdot\operatorname{sgn}^2\left(2^{-m_1}2^{-q}\nu_2\right)\Big]\cdot S_f\left(2^{-m_1}2^{-q}\nu_1,2^{-m_1}2^{-q}\nu_2\right)\\ &2^{-q}\cdot e^{-j\left(\nu_1\left(n_2-2^{-q}n_1\right)+\nu_2\left(p_2-2^{-q}p_1\right)\right)}\cdot\mathcal{F}\left\{\psi^{k_2}\right\}\left(\nu_1,\nu_2\right)\cdot\mathcal{F}^*\left\{\psi^{k_1}\right\}\left(\nu_1,\nu_2\right)d\nu_1 d\nu_2. \end{aligned} \tag{84}$$

$$\lim_{m_1\to\infty}R_{z_{\pm r}z_{\pm i}}\left[m_1,m_2,k_1,k_2,n_1,n_2,p_1,p_2\right]=0. \tag{85}$$

Correlation of real parts and of imaginary parts of coefficients in subbands with same type of orientation. We identify inter-band and inter-scale dependencies of the real and respectively of the imaginary parts of z_+ and z_-:

$$\begin{aligned} &R_{z_{+i}z_{+i}}\left[m_1,m_2,k_1,k_2,n_1,n_2,p_1,p_2\right]=\\ &=R_{D_{\mathcal{H}x}D_{\mathcal{H}x}}\left(m_1,m_2,k_1,k_2,n_1-n_2,p_1-p_2\right)+R_{D_{\mathcal{H}x}D_{\mathcal{H}y}}\left(m_1,m_2,k_1,k_2,n_1-n_2,p_1-p_2\right)+\\ &+R_{D_{\mathcal{H}y}D_{\mathcal{H}x}}\left(m_1,m_2,k_1,k_2,n_1-n_2,p_1-p_2\right)+R_{D_{\mathcal{H}y}D_{\mathcal{H}y}}\left(m_1,m_2,k_1,k_2,n_1-n_2,p_1-p_2\right). \end{aligned} \tag{86}$$

Each term in the right hand side can be computed using (8) from [FirNafIsaBouIsa10], but instead of S_f we must substitute with $S_{\mathcal{H}x}$, $S_{\mathcal{H}x\mathcal{H}y}$, $S_{\mathcal{H}y\mathcal{H}x}$ and $S_{\mathcal{H}y}$. We have similar relations for other orientations, for real part of z_+ and z_-. The equation (86) becomes:

$$
\begin{aligned}
&R_{z_{+i}z_{+i}}\left[m_1,m_2,k_1,k_2,n_1,n_2,p_1,p_2\right]=1/(4\pi^2)\cdot\int_{-\infty}^{\infty}\int_{-\infty}^{\infty}\Big[\mathrm{sgn}^2\left(2^{-m_1}2^{-q}\nu_1\right)+2\,\mathrm{sgn}\left(2^{-m_1}2^{-q}\nu_1\right)\\
&\cdot\mathrm{sgn}\left(2^{-m_1}2^{-q}\nu_2\right)+\mathrm{sgn}^2\left(2^{-m_1}2^{-q}\nu_2\right)\Big]\cdot 2^{-q}\cdot e^{-j\left(\nu_1\left(n_2-2^{-q}n_1\right)+\nu_2\left(p_2-2^{-q}p_1\right)\right)}\cdot\\
&\cdot\mathcal{F}\left\{\psi^{k_2}\right\}(\nu_1,\nu_2)\cdot\mathcal{F}^*\left\{\psi^{k_1}\right\}(\nu_1,\nu_2)\,d\nu_1 d\nu_2
\end{aligned}
\tag{87}
$$

Taking the limit for m_1 tending to infinity, the right hand side of the last equation becomes equal with zero because sgn(0)=0. The imaginary parts of the coefficients z_+ are asymptotically decorrelated [FirNafIsaBouIsa10].

Intercorrelation of coefficients in subbands with opposite type of orientation. The HWT subbands are positive oriented for z_+ and negative orientated for z_-. The intercorrelation between the imaginary parts of the coefficients z_+ and z_- can be expressed as:

$$
\begin{aligned}
&R_{z_{+i}z_{-i}}\left[m_1,m_2,k_1,k_2,n_1,n_2,p_1,p_2\right]\\
&=R_{D\mathcal{H}xD\mathcal{H}x}\left(m_1,m_2,k_1,k_2,n_1-n_2,p_1-p_2\right)-R_{D\mathcal{H}xD\mathcal{H}y}\left(m_1,m_2,k_1,k_2,n_1-n_2,p_1-p_2\right)+\\
&+R_{D\mathcal{H}yD\mathcal{H}x}\left(m_1,m_2,k_1,k_2,n_1-n_2,p_1-p_2\right)-R_{D\mathcal{H}yD\mathcal{H}y}\left(m_1,m_2,k_1,k_2,n_1-n_2,p_1-p_2\right).
\end{aligned}
\tag{88}
$$

We obtain:

$$
\begin{aligned}
&R_{z_{+i}z_{-i}}\left[m_1,m_2,k_1,k_2,n_1,n_2,p_1,p_2\right]=1/(4\pi^2)\cdot\int_{-\infty}^{\infty}\int_{-\infty}^{\infty}\left[\left|\mathrm{sgn}\left(2^{-m_1}2^{-q}\nu_1\right)\right|^2-\left|\mathrm{sgn}\left(2^{-m_1}2^{-q}\nu_2\right)\right|^2\right]\cdot\\
&S_f\left(2^{-m_1}2^{-q}\nu_1,2^{-m_1}2^{-q}\nu_2\right)\cdot 2^{-q}\cdot e^{-j\left(\nu_1\left(n_2-2^{-q}n_1\right)+\nu_2\left(p_2-2^{-q}p_1\right)\right)}\cdot\\
&\cdot\mathcal{F}\left\{\psi^{k_2}\right\}(\nu_1,\nu_2)\cdot\mathcal{F}^*\left\{\psi^{k_1}\right\}(\nu_1,\nu_2)\,d\nu_1 d\nu_2
\end{aligned}
\tag{89}
$$

The first factor under the integral from the right hand side of the last equation equals zero for any pair of not nulls real numbers (ν_1,ν_2), reason for which it can be written:

$$
R_{z_{+i}z_{-i}}\left[m_1,m_2,k_1,k_2,n_1,n_2,p_1,p_2\right]=0\ \text{a.e.w},\forall\nu_{1,2}\neq 0. \tag{90}
$$

Imaginary parts of positively oriented subbands are not correlated with imaginary parts of the negatively oriented subbands for any finite values m_1 and m_2. This is a more general result than former ones which are of asymptotical nature only. The same value is obtained for intercorrelation between real parts of z_- and imaginary parts of z_+, or for intercorrelation between real parts of z_+ and z_-:

$$
R_{z_{\mp r}z_{\pm i}}\left[m_1,m_2,k_1,k_2,n_1,n_2,p_1,p_2\right]=0\ \text{a.e.w}. \tag{91}
$$

2) Inter-scale and Intra-band Dependencies

For $k_1=k_2=k$, if the mother wavelet ψ^k generates by translations and dilations an orthogonal basis of $L^2(R^2)$ then:

$$
\begin{aligned}
&R_{z_{+i}z_{+i}}\left[m_1,m_2,k,2^q n_1'-n_2,2^q p_1'-p_2\right]=\\
&=2^{2m_1+q}\Big\{R_{\mathrm{Hx}\mathrm{Hx}}\left(2^{m_1+q}(n_2-n_1'),2^{m_1+q}(p_2-p_1')\right)+R_{\mathrm{Hx}\mathrm{Hy}}\left(2^{m_1+q}(n_2-n_1'),2^{m_1+q}(p_2-p_1')\right)+\\
&R_{\mathrm{Hy}\mathrm{Hx}}\left(2^{m_1+q}(n_2-n_1'),2^{m_1+q}(p_2-p_1')\right)+R_{\mathrm{Hy}\mathrm{Hy}}\left(2^{m_1+q}(n_2-n_1'),2^{m_1+q}(p_2-p_1')\right)\Big\}.
\end{aligned}
\tag{92}
$$

Similar results are obtained for $R_{z_{+r}z_{+r}}$, $R_{z_{-i}z_{-i}}$ and $R_{z_{-r}z_{-r}}$. In an inter-scale and intra-band context, correlation functions of the HWT coefficients depend solely on the correlations of the four input images f, $\mathcal{H}_x\{f\}$, $\mathcal{H}_y\{f\}$, $\mathcal{H}_y\{\mathcal{H}_x\{f\}\}$, if orthogonal wavelets are used.

3) Intra-scale and Intra-band Dependencies. For $m_1 = m_2 = m$ we have:

$$R_{z_{+i}z_{+i}}\left[m,k,n_1'-n_2,p_1'-p_2\right]=$$
$$=2^{2m}\left\{R_{\mathrm{H}x\mathrm{H}x}\left(2^m\left(n_2-n_1'\right),2^m\left(p_2-p_1'\right)\right)+R_{\mathrm{H}x\mathrm{H}y}\left(2^m\left(n_2-n_1'\right),2^m\left(p_2-p_1'\right)\right)+\right. \tag{93}$$
$$\left.+R_{\mathrm{H}y\mathrm{H}x}\left(2^m\left(n_2-n_1'\right),2^m\left(p_2-p_1'\right)\right)+R_{\mathrm{H}y\mathrm{H}y}\left(2^m\left(n_2-n_1'\right),2^m\left(p_2-p_1'\right)\right)\right\}.$$

Using Wiener-Hincin theorem we obtain equation (94). At the limit for $m\to\infty$, the equation (94) becomes (95) which represent the autocorrelation of a white noise. Similar asymptotic results are obtained for the subbands z_{+r}, z_{-i} and z_{-r}. HWT can also be seen as a whitening system in an intra-scale and intra-band scenario, just like the 2D DWT.

$$R_{z_{+i}z_{+i}}\left[m,k,n_1-n_2,p_1-p_2\right]=\frac{1}{4\pi^2}\int_{-\infty}^{\infty}\int_{-\infty}^{\infty}\left[S_{\mathcal{H}x\mathcal{H}x}\left(2^{-m}\xi_1,2^{-m}\xi_2\right)+S_{\mathcal{H}x\mathcal{H}y}\left(2^{-m}\xi_1,2^{-m}\xi_2\right)+\right.$$
$$\left.+S_{\mathcal{H}y\mathcal{H}x}\left(2^{-m}\xi_1,2^{-m}\xi_2\right)+S_{\mathcal{H}y\mathcal{H}y}\left(2^{-m}\xi_1,2^{-m}\xi_2\right)\right]\cdot \tag{94}$$
$$\cdot\exp\left\{-j\left[\xi_1\left(n_2-n_1\right)+\xi_2\left(p_2-p_1\right)\right]\right\}d\xi_1 d\xi_2$$

$$R_{z_{+i}z_{+i}}\left[\infty,k,n_1-n_2,p_1-p_2\right]=\left(S_{\mathcal{H}x\mathcal{H}x}\left(0,0\right)+S_{\mathcal{H}x\mathcal{H}y}\left(0,0\right)\right.$$
$$\left.+S_{\mathcal{H}y\mathcal{H}x}\left(0,0\right)+S_{\mathcal{H}y\mathcal{H}y}\left(0,0\right)\right)\cdot\delta\left[n_2-n_1,p_2-p_1\right] \tag{95}$$

4) The intra-scale and inter-band scenario is the most general one and supposes the computation of the cross-correlation of the HWT coefficients belonging to the decomposition levels indexed by m_1 and m_2 and to the subbands indexed by k_1 and k_2. These cross-correlation functions are computed in [NafFirIsaBouIsa10a]. For example, the cross-correlation of the imaginary parts of coefficients z_+ and z_- is expressed in the equation (90). For $m_1 = m_2 = m$, the equations (90) and (91) become intra-scale and inter-band dependencies. So, there are categories of HWT coefficients, as for example those belonging to subbands with opposite type of orientations, which are decorrelated a. e., in the intra-scale and inter-band scenario. It can be proved, following the strategy proposed in [NafFirIsaBouIsa10a], that the HWT coefficients belonging to the other categories are asymptotically decorrelated in the intra-scale and inter-band scenario.

The results of the HWT second order statistical analysis reported are resumed in the following table. These results refer to different categories of HWT coefficients: real and/or imaginary parts of complex numbers *z* belonging to subbands with same type of orientation (++ or --) or to subbands with opposite type of orientation (+- or -+). All these coefficients have zero statistical mean (in conformity with the first column of the table).

Expectation	Correlation			
	Inter-scale & inter-band	Inter-scale & intra-band	Intra-scale & intra-band	intra-scale & inter-band
0, for *k*=1, 2, 3	Asymptotically decorrelated	Correlated	Asymptotically decorrelated	Asymptotically decorrelated

Table 21. Results.

There are two types of results which concern the correlation functions: non asymptotically and asymptotically (which are obtained as limits for *m* approaching infinity). Generally, the results of first type indicate that the HWT coefficients are correlated (as it is indicated on the third column of the table). Still, there are categories of HWT coefficients, as for example those belonging to subbands with opposite type of orientations, which are decorrelated almost everywhere (a. e.) in the inter-scale and inter-band scenario, see equations (26) and (27) in [NafFirIsaBouIsa10a]. The HWT coefficients are asymptotically decorrelated in the inter-scale and inter-band (see second column of Table 21) and in the intra-scale and intra-band scenarios (see fourth column of Table 21).

We carried out experimental tests where the random process f at the input of the HWT is stationary [NafIsa12]. This process is obtained by filtering a zero mean bivariate White Gaussian Noise (WGN) random process w with a bivariate running averager having a rectangular sliding window with size 10×10. The random variables $W(n_1,n_2)$, $1 \leq n_1 \leq N_1$, $1 \leq n_2 \leq N_2$, are Gaussian, independent and identically distributed with zero-mean and unitary standard-deviation. We have used the MWs with 10 vanishing moments and shorter support proposed by Ingrid Daubechies. These experimental results have been obtained by achieving full HWT decompositions of the input random process specified above. In some cases, 10 realizations of this input random process were considered and the corresponding results given hereafter are average values over these 10 realizations. The average empirical cross-correlation functions of the HWT coefficients are calculated on the basis of 256 coefficients per subband. We have selected the values N_1 and N_2 in each experiment to make possible the computation of those average empirical cross-correlation functions in each subband for every decomposition level and for each preferential orientation considered below.

The first experiment refers to the cross-correlation between the real and imaginary parts of the coefficients belonging to subbands with same type of orientation in an ***inter-scale and inter-band scenario (#4)***. In Fig. 43 is presented the normalized auto-correlation of a group of 256 pixels of a realization of the input process f. In this experiment we have used the values $N_1=N_2=2048$. The group of pixels considered was obtained by cropping a region from the input image with size 16×16. We have selected the following parameters:
- decomposition levels: $m_1=6$ and $m_2=7$,
- orientation: negative,
- subbands: $k_1=1$ and $k_2=2$.

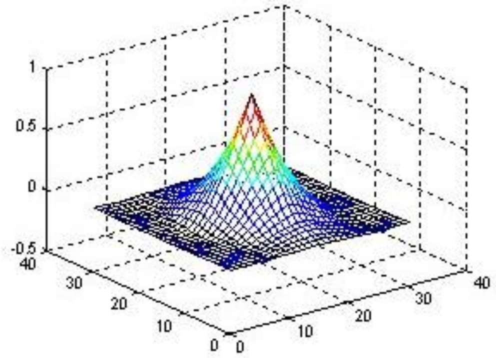

Fig. 43. Normalized auto-correlation of a group of 256 pixels belonging to a realization of the process f.

The corresponding cross-correlation is represented in Fig. 44. It was obtained by averaging the cross-correlation of the real and imaginary parts of the coefficients z_- obtained for 10 different realizations of the input process f. It can be observed, analyzing comparatively Fig. 43 and Fig. 44, that the values of the cross-correlation in Fig. 44 are small enough to consider that the corresponding HWT coefficients are quasi-decorrelated. The experimental result detailed below shows that, for the random process considered above, the asymptotic decorrelation (obtained for $m_1 \rightarrow \infty$) can actually be attained with reasonable values for the resolution level ($m_1 \geq 6$, $m_2 > m_1$).

The second experiment refers to the cross-correlation of the real parts of the coefficients belonging to subbands with opposite type of orientation in ***an intra-scale and inter-band scenario***. In this experiment we have used the values N_1=N_2=256. We have selected the following parameters:
- decomposition levels: m_1= m_2=1,
- orientations: negative, positive,
- subbands: k_1 =k_2=2.

The corresponding cross-correlation is represented in Fig. 45 and it equals zero almost everywhere. So, the HWT coefficients belonging to subbands with opposite type of orientations are decorrelated in an intra-scale and inter-band scenario. The ***intra-scale and intra-band scenario***, considered in the following experiment, is the most frequently used in applications.

The third experiment refers to the asymptotic decorrelation of the real parts of the coefficients belonging to the same subband and same decomposition level. In this experiment we have used the values N_1=N_2=2048. We have selected the following parameters:
- decomposition levels: m_1= m_2=7,
- orientation: negative,
- subbands: k_1 =k_2=1, k_1 =k_2=2, k_1 =k_2=3.

The corresponding auto-correlations are represented in Fig. 46.

They were obtained by averaging the auto-correlations of real parts of coefficients z_- obtained for 10 different realizations of the input process *f*. Analyzing Fig. 46, it can be observed that the form of the auto-correlations is similar with the form of the auto-correlation of a WN process. So we can consider that the corresponding HWT coefficients are quasi-decorrelated.

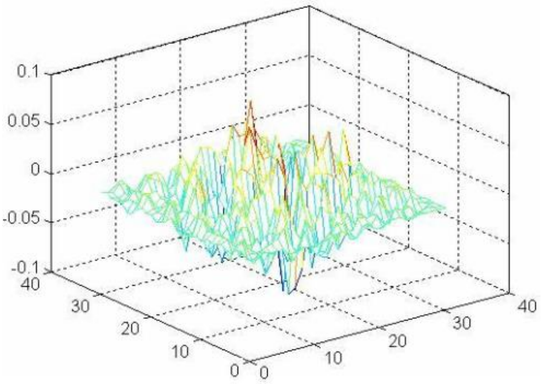

Fig. 44. Normalized cross-correlation between the real and imaginary parts of the coefficients belonging to subbands with same type of orientation in an inter-scale and inter-band scenario.

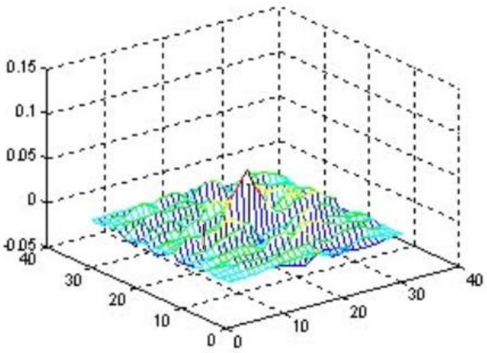

Fig. 45. Normalized cross-correlation between real parts of coefficients belonging to subbands with opposite type of orientations situated at the same decomposition level.

We generalized the second order statistical analysis of 2D DWT from [NafFirIsaBouIsa10b] for HWT. This WT seems more complicated than 2D DWT, because of the greater number of subbands and complex coefficients. HWT coefficients have strong inter-scale and inter-band dependencies. Real and imaginary parts of coefficients in subbands with same type of orientation are asymptotically decorrelated. In an inter-band and inter-scale context, real and respectively imaginary parts of z_+ and z_- are asymptotically decorrelated. We analyzed coefficients in subbands with opposite type of orientation. Intercorrelations are zero a.e.w. even for finite number of scales. This allows parallel processing of the HWT coefficients in subbands with opposite type of orientation [FirNafBouIsa09]. HWT coefficients correlations are independent of the mother wavelets in an inter-scale and intra-band context, depending on correlations of the four input images f, $\mathcal{H}_x\{f\}$, $\mathcal{H}_y\{f\}$, $\mathcal{H}_y\{\mathcal{H}_x\{f\}\}$ only, if orthogonal wavelets are used. HWT is a whitening system in an intra-scale and intra-band scenario, similarly to 2D DWT. We analyzed the two WTs in only three scenarios: inter-scale and inter-band, inter-scale and intra-band and intra-scale and inter-band. The 2D DWT and the HWT have similar statistical behaviors in inter-scale scenarios. Asymptotically, HWT has higher decorrelation strength in intra-band scenarios.

Despite its superior complexity, the HWT inherits the good statistical properties of 2D DWT and outperforms it in several cases as for example for the subbands of opposite type of orientations (when the decorrelation is even not asymptotically).

The experimental results confirm the theoretical findings showing that, for the random processes considered above, the asymptotic theoretical results (obtained for $m_{1,2}\rightarrow\infty$) can actually be attained with reasonable finite values for the resolution level ($m_1\geq 6$, $m_2> m_1$ for the first experiment and $m_1= m_2\geq 7$ for the third experiment).

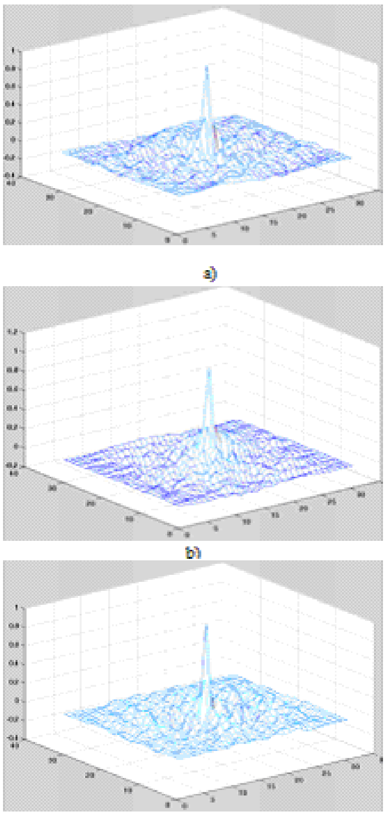
a)

b)

c)

Fig. 46. Normalized auto-correlations of real parts of coefficients with preferential direction negative at the seventh decomposition level in subband: a) k=1, b) k=2 and c) k=3.

2.5 Kullback-Leibler divergence between complex generalized Gaussian distributions

Papers: [NafBerNafIsa12]

In texture classification, feature extraction can be made in a transform domain. A possibility to preserve the translation invariance is to use a complex transform like the Hyperanalytic Wavelet transform. It exhibits a circularly symmetric density function for subband coefficients so it can be modeled by a particular form of the complex generalized Gaussian (CGGD) distribution function. The Kullback-Leibler (KL) divergence, or distance, can be used to measure the similarity between subbands density function. We derived in [NafBerNafIsa12] a closed-form expression for the KL divergence between two complex generalized Gaussian distributions. In probability and information theory, the Kullback–Leibler (KL) divergence is a non-symmetric measure of the difference between two probability density functions (pdf), *p* and *q*. This is defined as [KulLei51]:

$$D_{KL}\left(p\|q\right)=\int_{-\infty}^{\infty}\int_{-\infty}^{\infty}p\left(x,y\right)\log\frac{p\left(x,y\right)}{q\left(x,y\right)}dxdy. \tag{96}$$

If the two pdfs are the same (*p*=*q*), the divergence is null. The KL distance is used as a similarity measure between textures, which makes it useful for texture classification [DoVet02]. In [DoVet02], the authors deal with computation of KL divergence for statistics of real wavelet subband coefficients. A wavelet subband is modeled using the generalized Gaussian distribution (GGD). Based on this model, hyperparameters of the coefficients pdf from each subband are estimated. The KL divergence is computed between the pdf of subbands for two compared textures.

If this classification is made using a complex wavelet transform, we need a complex model and the closed-form for the KL divergence.

The generalization for the GGD model in the complex case was proposed by Novey and Adali which approximates the pdf based on a histogram [NovAdaRoy10]. The computation problem for the distance between two pdf for complex variables was also discussed by Verdoolaege [VerBacSch08]. He established equations for geodesics in probability space. Unfortunately, these relations are not usable at this moment.

Because the hyperanalytic wavelet transform (HWT) produces complex coefficients with a circular distribution we have studied the simpler problem of KL divergence for such distributions [FirNafBouIsa09]. We derived a closed-form for the KL divergence of pairs of CGGD random variables and we studied its sensitivity with the shape parameter.

In the following, we give the definition of HWT and its main statistical properties; we then briefly presents the CGGD [NovAdaRoy10] and we explain why we chose this model for HWT. We give the closed-form of the KL divergence of two CGGD. The sensitivity of this KL divergence with the parameters of the CGGDs is analyzed as well.

In [FirNafBouIsa09] a new complex wavelet transform was proposed, the HWT , which identifies six orientations, 3 positive and 3 negative, ±atan(1/2), ±π/4 and ±atan(2):

$$z_{\pm}=z_{\pm R}+jz_{\pm I}.$$

A problem of interest is the statistical modeling of the HWT coefficients. For input random processes, random variables as *Z*, can be associated to the HWT coefficients z.

The coefficients have zero mean, the cross-correlation between their real and imaginary parts is zero and the variances of their real and imaginary parts are estimated to be the same, $\sigma_R^2=\sigma_I^2=\sigma^2/2$, for any second order stationary bivariate input random process [NafFirIsaBouIsa10a]. Therefore, we considered the repartitions of the random variables $Z_{\pm}$ corresponding to the HWT coefficients $z_{\pm}$ to be like circularly symmetric. The cross-correlation matrix is:

$$\mathbf{C}_b = E\left\{\mathbf{Z}_b\mathbf{Z}_b^T\right\} = \begin{bmatrix} \sigma^2/2 & 0 \\ 0 & \sigma^2/2 \end{bmatrix}, \tag{97}$$

where $\mathbf{Z}_b=[Z_R ,Z_I]^T$ is the bivariate vector of the real and imaginary parts of the HWT coefficients. The augmented form: $\mathbf{Z}_a=[Z , Z^*]^T$ [NovAdaRoy10] can also be used.

CGGD. For a complex generalized Gaussian distribution, CGGD, where the bivariate random vector is $\mathbf{z}_b$ and the augmented vector is $\mathbf{z}_a$ [NovAdaRoy10], the general form of the bivariate covariance matrix is:

$$\mathbf{C}_b = E\left\{\mathbf{Z}_b\mathbf{Z}_b^T\right\} = \begin{bmatrix} \sigma_R^2 & \rho \\ \rho & \sigma_I^2 \end{bmatrix}, \tag{98}$$

where $\rho = E\left\{Z_R Z_I\right\}$ is the cross-correlation between the real and imaginary part. The augmented covariance matrix is established by Novey and Adali as:

$$\mathbf{C}_a = E\left\{\mathbf{Z}_a\mathbf{Z}_a^H\right\} = \begin{bmatrix} \sigma_R^2+\sigma_I^2 & (\sigma_R^2-\sigma_I^2)+2j\rho \\ (\sigma_R^2-\sigma_I^2)-2j\rho & \sigma_R^2+\sigma_I^2 \end{bmatrix}. \tag{99}$$

The probability density function generalizes the GGD family of densities,

$$p_{\mathrm{X}}\left(x;\sigma,c\right) = \frac{c}{2\sigma\Gamma\left(\frac{1}{c}\right)}\exp\left\{-\left(\frac{|x|}{\sigma}\right)^c\right\}, \tag{100}$$

where $\Gamma(\bullet)$ is the gamma function, σ is the scale parameter, and c is the shape parameter. The generalized probability density function for the augmented vector is:

$$p_{\mathrm{V}a}\left(\mathbf{v}_a\right) = \frac{\beta(c)}{\sqrt{\left|\mathbf{C}_a\right|}}\exp\left\{-\left[\eta(c)\left(\mathbf{v}_a^H\mathbf{C}_a^{-1}\mathbf{v}_a\right)\right]^c\right\}, \tag{101}$$

where $\mathbf{v}_a = \dfrac{\mathbf{z}_a}{\sqrt{\Gamma(2/c)/\Gamma(1/c)}}$, $\beta(c) = \dfrac{c\Gamma(2/c)}{\pi\Gamma^2(1/c)}$ and $\eta(c) = \dfrac{\Gamma(2/c)}{2\Gamma(1/c)}$. In [NovAdaRoy10] a Matlab program is presented which gives the ML estimation for the vector $\boldsymbol{\phi} = \left[\sigma_R^2,\sigma_I^2,\rho,c\right]^T$. This means we can have the ML estimation for the shape parameter c and the matrices $\mathbf{C}_b$ and $\mathbf{C}_a$. We show in the following the importance of the quality of this estimation.

In the case of circular vectors, with $\sigma_R^2=\sigma_I^2=\sigma^2/2$ and $\rho=0$, which corresponds to the HWT coefficients of any bivariate stationary random process [NafFirIsaBouIsa10a], starting from the augmented pdf in (10), the bivariate pdf is:

$$p(x,y) = \frac{\beta(c)}{\sigma^2}\exp\left\{-\left(\frac{\Gamma(2/c)}{\Gamma(1/c)}\right)^c\left(\frac{x^2+y^2}{\sigma^2}\right)^c\right\}. \tag{102}$$

For the pdf having the shape parameters c_1, c_2 and the variances $\sigma_1^2=\sigma_2^2$ using relationship (11) and the definition in (1) we obtain the Kullback-Leibler distance:

$$\begin{aligned} D_{KL}\left(p_1 \| p_2\right) = {} & \ln\left(\frac{c_1}{c_2}\frac{\sigma_2^2}{\sigma_1^2}\frac{\Gamma(2/c_1)\Gamma^2(1/c_2)}{\Gamma(2/c_2)\Gamma^2(1/c_1)}\right) - \frac{1}{c_1} \\ & + \frac{1}{\Gamma(1/c_1)}\left(\frac{\sigma_1^2}{\sigma_2^2}\frac{\Gamma(2/c_1)\Gamma(1/c_2)}{\Gamma(1/c_1)\Gamma(2/c_2)}\right)^{c_2}\Gamma\left(\frac{1}{c_1}+\frac{c_2}{c_1}\right) \end{aligned}. \tag{103}$$

The proof of this relation can be found in the Paragraph 2.5.1.

We plot the KL distance between p_1 and p_2, for $\sigma_1 = \sigma_2$. In Fig.47, the shape parameter for p_2, that is c_2, is fixed, with values 0.3, 0.5, 1, 1.5 and 2. The shape parameter for p_1, that is c_1, varies from 0.2 to 2. In Fig.48, the shape parameter for p_1, c_1 is fixed, with values 0.3, 0.5, 1, 1.5 and 2. The shape parameter for p_2, that is c_2, varies from 0.2 to 2.

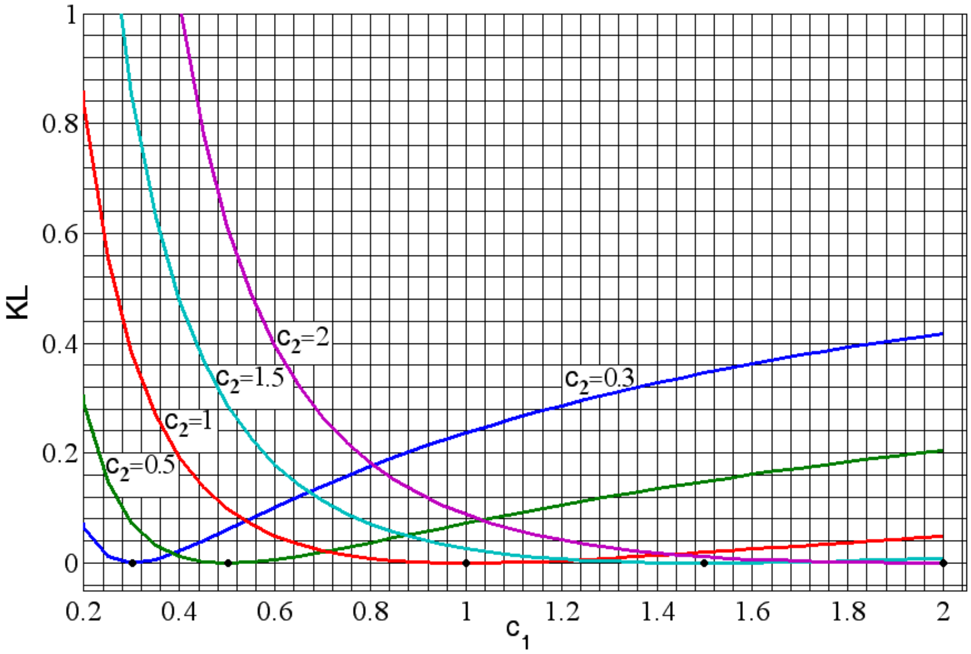

Fig. 47. KL distance between p_1 and p_2 ($\sigma_1 = \sigma_2$). The shape parameter for p_2, c_2 is fixed, with values 0.3, 0.5, 1, 1.5 and 2. The shape parameter for p_1, that is c_1, varies from 0.2 to 2.

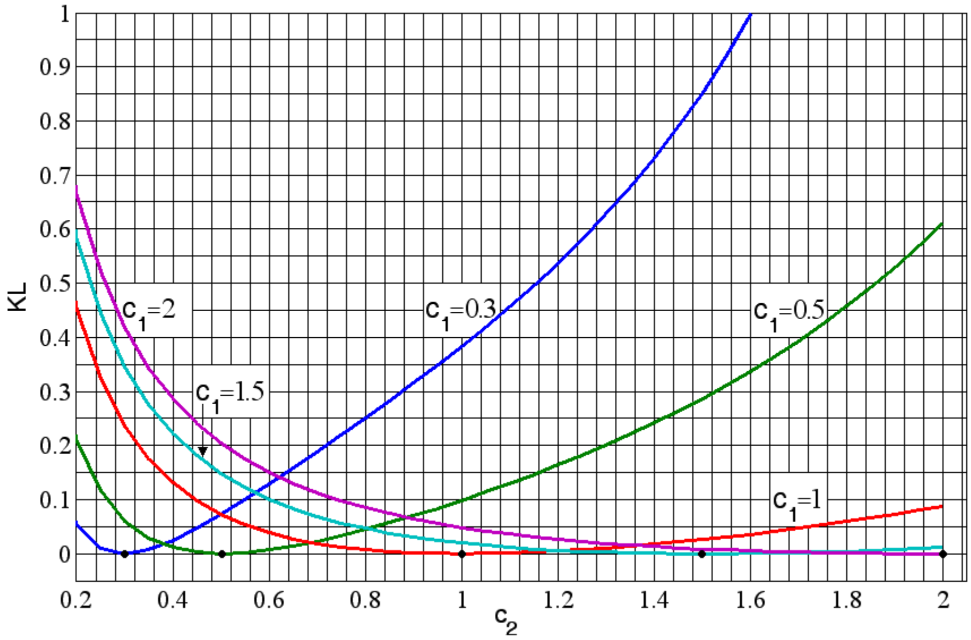

Fig. 48. KL distance between p_1 and p_2 ($\sigma_1 = \sigma_2$). The shape parameter for p_1, c_1 is fixed, with values 0.3, 0.5, 1, 1.5 and 2. The shape parameter for p_2, that is c_2, varies from 0.2 to 2.

It is essential for any classification that the distance between the two pdf to be as discriminant as possible. In other words, if c_1 and c_2 are very close then KL should be close to zero, and if they have different values, this distance should be as high as possible.

It can be observed, analyzing Fig. 47 and Fig. 48 that the KL becomes zero if $c_1=c_2$ and $\sigma_1=\sigma_2$. These parameters are not a priori known in textures classification applications and they must be estimated. The success of the classification depends on the quality of the estimators used. For an efficient classification, it is necessary that the speed of variation of the curves in Fig. 47 and Fig. 48 around their intersections with the line expressed by the equation $D_{KL}=0$, to be as high as possible.

For the VisTex database [VisTex02], using 40 images subdivided in 16 subimages each, resulting in 640 smaller images, we have repeated the estimation of the shape parameter c and of the covariance matrix $\mathbf{C}_a$, using the programs presented in [NovAdaRoy10]. This was done in the HWT domain, using one decomposition level and Daubechies-3 mother wavelet. We have noticed that the shape parameter varies in the range 0.1÷5 but its values around 0.5 appear more frequently.

From Fig.47 it is easily noticeable that the KL distance varies only slightly for values of c_1 between 0.8 and 1.2. It is interesting that it responds better around the value $c_1=0.25$. The KL distance is more sensitive for the plot $c_2=0.3$ than for Gaussian case ($c_2=1$).

For Fig.48, where we plotted KL distance with c_1 fixed, the best case is for $c_1=0.3$, as opposed to the case of $c_1=1$ (Gaussian case). The KL distance varies only slightly for example in the range c_2 of 0.5÷1.5. As expected, the KL distance is non-symmetric with respect to c_1 and c_2.

In texture classification, when using a complex transform such as the HWT, modeled by the CGGD distribution, the KL distance can be used to measure the similarity between subband density functions. This is not always satisfactory because there are intervals where KL distance varies only slightly despite the fact that the two pdfs are very different. It would be useful in the future to study more measures for texture classification.

2.5.1 Derivation of KL distance

We compute the KL distance for the CGGD model, in the circular case. The probability density function is:

$$p(x,y)=\frac{\beta(c)}{\sigma^2}\exp\left\{-\left(\frac{\Gamma(2/c)}{\Gamma(1/c)}\right)^c\left(\frac{x^2+y^2}{\sigma^2}\right)^c\right\}=A\exp\left\{-\left(\frac{x^2+y^2}{B^2}\right)^c\right\}, \qquad \text{(A.1)}$$

where x and y are the real and imaginary components, and

$$A=\frac{c\Gamma\left(\frac{2}{c}\right)}{\pi\Gamma^2\left(\frac{1}{c}\right)\sigma^2} \quad \text{and} \quad B^2=\frac{\sigma^2\Gamma\left(\frac{1}{c}\right)}{\Gamma\left(\frac{2}{c}\right)}. \qquad \text{(A.2)}$$

We compare two pdf:

$$p_1=A_1\exp\left\{-\left(\frac{x^2+y^2}{B_1^2}\right)^{c_1}\right\} \text{and } p_2=A_2\exp\left\{-\left(\frac{x^2+y^2}{B_2^2}\right)^{c_2}\right\}. \qquad \text{(A.3,4)}$$

We start from the KL distance definition:

$$D_{KL}\left(p_1\|p_2\right)=\int_{-\infty}^{\infty}\int_{-\infty}^{\infty}p_1(x,y)\log\frac{p_1(x,y)}{p_2(x,y)}dxdy. \qquad \text{(A.5)}$$

First we have:

$$\ln\frac{p_1}{p_2}=\ln\frac{A_1}{A_2}-\left(\frac{x^2+y^2}{B_1^2}\right)^{c_1}+\left(\frac{x^2+y^2}{B_2^2}\right)^{c_2}. \tag{A.6}$$

The integrand is then:

$$p_1\ln\frac{p_1}{p_2}=A_1\exp\left\{-\left(\frac{x^2+y^2}{B_1^2}\right)^{c_1}\right\}\cdot\left\{\ln\frac{A_1}{A_2}-\left(\frac{x^2+y^2}{B_1^2}\right)^{c_1}+\left(\frac{x^2+y^2}{B_2^2}\right)^{c_2}\right\}. \tag{A.7}$$

The KL distance can be written as a sum of three terms, I_1, I_2 and I_3:

$$D_{KL}\left(p_1\| p_2\right)=I_1+I_2-I_3. \tag{A.8}$$

The first term is:

$$\begin{aligned}I_1&=A_1\int_{-\infty}^{\infty}\int\exp\left\{-\left(\frac{x^2+y^2}{B_1^2}\right)^{c_1}\right\}\ln\frac{A_1}{A_2}dxdy=A_1\int_0^{2\pi}\int_0^{\infty}\exp\left\{-\left(\frac{r^2}{B_1^2}\right)^{c_1}\right\}\ln\frac{A_1}{A_2}rdrd\varphi\\&=2\pi A_1\ln\frac{A_1}{A_2}\int_0^{\infty}\exp\left\{-\left(\frac{r^2}{B_1^2}\right)^{c_1}\right\}rdr\end{aligned}. \tag{A.9}$$

Because:

$$\frac{r^2}{B_1^2}=t^{\frac{1}{c_1}}\quad\Rightarrow\quad 2rdr=\frac{B_1^2}{c_1}t^{\frac{1}{c_1}-1}dt, \tag{A.10}$$

we obtain:

$$I_1=\pi A_1\ln\frac{A_1}{A_2}\frac{B_1^2}{c_1}\int_0^{\infty}t^{\frac{1}{c_1}-1}e^{-t}dt=\pi A_1\left(\ln\frac{A_1}{A_2}\right)\frac{B_1^2}{c_1}\Gamma\left(\frac{1}{c_1}\right). \tag{A.11}$$

In the same manner, we have:

$$\begin{aligned}I_2&=-A_1\iint_{\mathbb{R}}\left(\frac{x^2+y^2}{B_1^2}\right)^{c_1}\exp\left\{-\left(\frac{x^2+y^2}{B_1^2}\right)^{c_1}\right\}dxdy=-2\pi A_1\int_0^{\infty}\left(\frac{r^2}{B_1^2}\right)^{c_1}\exp\left\{-\left(\frac{r^2}{B_1^2}\right)^{c_1}\right\}rdr\\&=-\pi A_1\frac{B_1^2}{c_1}\Gamma\left(1+\frac{1}{c_1}\right)\end{aligned} \tag{A.12}$$

and

$$\begin{aligned}I_3&=A_1\iint_{\mathbb{R}}\left(\frac{x^2+y^2}{B_2^2}\right)^{c_2}\exp\left\{-\left(\frac{x^2+y^2}{B_1^2}\right)^{c_1}\right\}dxdy=2\pi A_1\int_0^{\infty}\left(\frac{r^2}{B_2^2}\right)^{c_2}\exp\left\{-\left(\frac{r^2}{B_1^2}\right)^{c_1}\right\}rdr\\I_3&=\pi A_1\int_0^{\infty}t^{\frac{c_2}{c_1}}\left(\frac{B_1^2}{B_2^2}\right)^{c_2}e^{-t}\frac{B_1^2}{c_1}t^{\frac{1}{c_1}-1}dt=\pi A_1\left(\frac{B_1^2}{B_2^2}\right)^{c_2}\frac{B_1^2}{c_1}\int_0^{\infty}t^{\frac{c_2}{c_1}+\frac{1}{c_1}-1}e^{-t}tdt\\&=\pi A_1\left(\frac{B_1^2}{B_2^2}\right)^{c_2}\frac{B_1^2}{c_1}\Gamma\left(\frac{1+c_2}{c_1}\right)\end{aligned} \tag{A.13}$$

The distance becomes:

$$\begin{aligned}D_{KL}\left(p_1\| p_2\right)&=\pi A_1\left(\ln\frac{A_1}{A_2}\right)\frac{B_1^2}{c_1}\Gamma\left(\frac{1}{c_1}\right)-\pi A_1\frac{B_1^2}{c_1}\Gamma\left(1+\frac{1}{c_1}\right)\\&+\pi A_1\left(\frac{B_1^2}{B_2^2}\right)^{c_2}\frac{B_1^2}{c_1}\Gamma\left(\frac{1+c_2}{c_1}\right)\end{aligned}, \tag{A.14}$$

where:

$$A_i = \frac{c_i \Gamma\left(\frac{2}{c_i}\right)}{\pi \Gamma^2\left(\frac{1}{c_i}\right)\sigma_i^2}; \quad B_i^2 = \frac{\sigma_i^2 \Gamma\left(\frac{1}{c_i}\right)}{\Gamma\left(\frac{2}{c_i}\right)} \quad i = 1, 2 . \tag{A.15}$$

It results that:

$$\begin{aligned} D_{KL}\left(p_1 \| p_2\right) &= \ln\left(\frac{c_1}{c_2}\frac{\sigma_2^2}{\sigma_1^2}\frac{\Gamma(2/c_1)\Gamma^2(1/c_2)}{\Gamma(2/c_2)\Gamma^2(1/c_1)}\right) - \frac{1}{c_1} \\ &+ \frac{1}{\Gamma(1/c_1)}\left(\frac{\sigma_1^2}{\sigma_2^2}\frac{\Gamma(2/c_1)\Gamma(1/c_2)}{\Gamma(1/c_1)\Gamma(2/c_2)}\right)^{c_2} \Gamma\left(\frac{1}{c_1} + \frac{c_2}{c_1}\right) \end{aligned} . \tag{A.16}$$

We took into account that:

$$\Gamma\left(1 + \frac{1}{c_1}\right) = \frac{1}{c_1}\Gamma\left(\frac{1}{c_1}\right). \tag{A.17}$$

We verify that the distance is correct, for

$$c = c_1 = c_2; \qquad \sigma = \sigma_1 = \sigma_2 ,$$

it should be zero:

$$\begin{aligned} D_{KL}\left(p \| p\right) &= \ln\left(\frac{c}{c}\frac{\sigma^2}{\sigma^2}\frac{\Gamma(2/c)\Gamma^2(1/c)}{\Gamma(2/c)\Gamma^2(1/c)}\right) - \frac{1}{c} \\ &+ \frac{1}{\Gamma(1/c)}\left(\frac{\sigma^2}{\sigma^2}\frac{\Gamma(2/c)\Gamma(1/c)}{\Gamma(1/c)\Gamma(2/c)}\right)^{c} \Gamma\left(\frac{1}{c} + \frac{c}{c}\right) \quad . \\ &= -\frac{1}{c} + \frac{1}{\Gamma(1/c)}\frac{1}{c}\Gamma\left(\frac{1}{c}\right) = 0 \end{aligned} \tag{A.18}$$

2.6 Texture classification/clustering

Papers: [SchBerTurNafIsa12]

A new method for texture clustering was proposed in [SchBerTurNafIsa12] based on the information-geometry tools. Considering textured images as a collection of heavy-tailed prior probability distributions related to some space/scale decomposition, an average of distributions (a barycentric distribution) is used to characterize each cluster. The Jeffrey divergence is used of as a dissimilarity measure for the clustering of images. Taking into account the geometry of the probabilistic manifold associated to the prior family, we provide the steepest descent method used to estimate the barycentric distribution. The descent exploits the Fisher information matrix, which is the expected value of the Hessian matrix and the local metric to the manifold. The experimental results on well-known texture databases show that the Fisher information matrix approach provides a convergence speed significantly higher than the convergence speed of conventional methods of steepest descent.

Texture analysis is important for various issues such as classification, segmentation or indexing image databases. Many methods use jointly scale-space approaches and stochastic modeling to characterize the textural content [DoVet02], [MatSkaBr02], [WouSchDyc99], [KwiUhl08], [MalHasLasBer10], [LasBer10]. The stochastic modeling consists in fitting the empirical marginal probability density function (pdf) with a given prior parametric function for each set of sub-band coefficients. In the context of classification/segmentation, clustering approaches have known an increased interest providing efficient and tractable algorithms for various domains. The general purpose of a clustering algorithm consists in partitioning the data set into *k* homogeneous groups (clusters), represented by the most centrally located object in a cluster, that is the barycenter. Estimating the mean value of the objects in the cluster implies to define adapted measure to determine the similarity/dissimilarity. The clustering can be developed in different frameworks ranging from unsupervised context [HuZha09], for which any information is available, to the supervised case for which the barycenter of the cluster can be estimated from training data [ChoTon07]. However for all these frameworks, the common issue that one may encounter is the estimation of the barycenter associated to each cluster. In [SchBerTurNafIsa12] we provided efficient methods for texture clustering considering the supervised case. In the context of the probabilistic modeling devoted to texture analysis, we proposed a clustering approach which takes advantage of information-geometry theory and parametric point-of-view. The first proposal is related to the selection of the measure of similarity to intra-cluster comparison. We promote the symmetrized Jeffrey divergence in opposition to the Euclidean distance widely used for texture clustering. The main advantage of this dissimilarity corresponds to a closedform of the measure in terms of parameter prior distribution. The second proposal is exploited in the procedure to estimate the barycenter of each cluster which is also a distribution. The proposed estimator is based on steepest descent procedure [ComPes09]. The estimator exploits the Riemannian geometry [AmaNag07] of the parameter space of the prior statistical models to adapt to the local manifold geometry, with the Fisher information matrix [AmaDou98].

The main purpose of textured image analysis for classification, segmentation or indexing issues consists in providing a relevant and tractable measure of dissimilarity associated to a representative and compact parametric modeling of the textural content. In the following, dissimilarity and parametric pdf family are presented in order to introduce the concept of barycentric law.

In the framework of Bayesian parametric approach, the conditional pdf *p* is modeled by a family of prior pdf denoted by $p(t\,;\boldsymbol{\lambda}_{test})$ where $\boldsymbol{\lambda}_{test} \in M$ is a d-dimensional parameter vector and *M* is a parametric model family. The index *t* references an instance of the parametric vector within the space associated to *M* . The estimated class $\hat{c}(t)$ of the sample *t* is defined as [DoVet02]:

$$\hat{c}(t) = \underset{c\in\left[1,\dots,N_c\right]}{\arg}\left[m\left(p\left(t;\boldsymbol{\lambda}_t\right), p\left(t;\boldsymbol{\lambda}_c\right)\right)\right],$$

where $\boldsymbol{\lambda}_{test}$ is the d-dimensional parameter vector which maximizes the likelihood of $\boldsymbol{\lambda}_{test}$ given the outcome *t* and where *m* is a dissimilarity measure devoted to probabilistic context. Taking into account information-geometry theory [AmaNag07], the measure *m* can be specified as Jeffrey divergence (J) or Euclidean distance (E). Thanks for the availability of a closed form in terms of parameters for J, we define:

$$J\left(p\left(t;\boldsymbol{\lambda}_{test}\right), p\left(t;\boldsymbol{\lambda}_c\right)\right) = J\left(\boldsymbol{\lambda}_{test}, \boldsymbol{\lambda}_c\right). \tag{104}$$

Let *Ti* be a texture image decomposed by a linear operator *D* into N_s sub-bands [DoVet02] $\left\{D(T_i,s), s=1,\dots,N_s\right\}$. In texture analysis, usually empirical marginal densities of decomposed sub-band coefficients are approximated by parametric laws [DoVet02], [MatSkaBr02], [WouSchDyc99], [KwiUhl08], [MalHasLasBer10], [LasBer10]. Considering the parametric pdf family *M* , the stochastic model of T_i is then defined as $\left\{p\left(D(T_i,s);\boldsymbol{\lambda}_{i,s}\right), s\right\}$. The stochastic model of T_i is denoted as:

$$T_i = \left\{\boldsymbol{\lambda}_{i,s}, s=1,\dots,N_s\right\}, \tag{105}$$

where $\lambda i, s$ is the d-dimensional parameter vector that maximizes the likelihood of $D(Ti , s)$. Where the sub-band coefficients are independent, the separability of Jeffrey divergence allows us to define the dissimilarity between two texture images T_1 and T_2 :

$$J\left(T_1,T_2\right)=\sum_{s=1}^{N_s} J\left(\boldsymbol{\lambda}_{1,s},\boldsymbol{\lambda}_{2,s}\right). \tag{106}$$

Generally in the framework of texture analysis, the parametric model exibits heavy-tailed behavior which can be represented by the centred generalized Gaussian distribution [DoVet02].

The supervised framework starts from a set of *Nc* classes of textured images. For each class, *N* image samples are available. The clustering principle aims to estimate from the *N* samples a “barycentric texture” to each class noted *c* and which we define as follows:

$$\bar{T}_c=\left\{\bar{\boldsymbol{\lambda}}_{c,s}, s=1,\dots,N_s\right\}, \tag{107}$$

where $\bar{\boldsymbol{\lambda}}_{c,s}$ is the “barycentric distribution” for the sub-band *s*. Fig. 49 shows the parameter vector estimated from the samples of three class of textured images for the third subband, s=3.

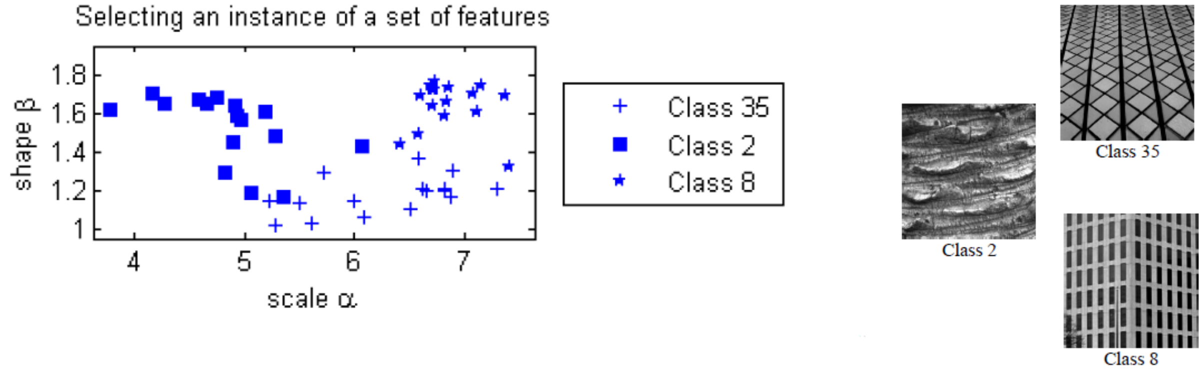

Fig. 49. For the sub-band s=3, display the parametrized vectors estimated on image samples from three different classes of Vistex database Class 8.

A. Cost Function and Barycentric Distribution

Let $\boldsymbol{\Lambda}=\left(\boldsymbol{\lambda}_n\right)_{n=1}^{N}$ be a collection of parameter vectors corresponding to the modeling *M* estimated from the *N* samples. The main issue is focused on the inference of the barycentric distribution based on the following cost function:

$$\boldsymbol{\lambda}=\arg\min_{\boldsymbol{\lambda}} l_{J,\Lambda}\left(\boldsymbol{\lambda}\right) \text{ s.t. } \boldsymbol{\lambda}\in\left(\mathbb{R}^{+}\right)^{d} \tag{108}$$

$$l_{J,\Lambda}\left(\boldsymbol{\lambda}\right)=\frac{1}{N}\sum_{n=1}^{N} J\left(\boldsymbol{\lambda}_n,\boldsymbol{\lambda}\right) \tag{109}$$

Knowing that $J\,(.\,,\,.)$ has a closed-form in terms of $\boldsymbol{\lambda}$ [DoVet02], the cost function $l_{J,\Lambda}\left(\boldsymbol{\lambda}\right)$ is a convex function in terms of λ and has a closed-form. The barycentric distribution $\bar{\boldsymbol{\lambda}}$ is a stationary point of J: $\boldsymbol{\lambda}=\left(\lambda_i\right)_{i=1}^{d}$

$$\nabla l_{J,\Lambda}\left(\boldsymbol{\lambda}\right)=\left[\frac{\partial}{\partial\lambda_i} l_{J,\Lambda}\left(\boldsymbol{\lambda}\right)\right]_{i=1}^{d}=0$$

But stationary points of J have no closed-form and need to be numerically estimated. We thus investigated different procedures in order to estimate $\bar{\boldsymbol{\lambda}}$.

B. Projected Gradient-Descent Algorithm

Obtaining the barycentric distribution by the minimization of (108), requires the use of the projected Gradient-descent algorithm i.e. proximal one, also called steepest descent algorithm. Let $\left(\boldsymbol{\lambda}_k\right)_{k=1}^{+\infty}$ be a sequence of parameter vectors defined as:

$$\boldsymbol{\lambda}_{k+1} = P\left(\boldsymbol{\lambda}_k - \xi_k \boldsymbol{K}^{-1} \nabla l_{J,\Lambda}\left(\boldsymbol{\lambda}_k\right)\right). \tag{110}$$

The sequence converges toward $\bar{\boldsymbol{\lambda}}$ which minimizes eq. (108). Proximal methods [ComPes09] conduct us to use the projection P on the closed space within $\left(\mathbb{R}^+\right)^d$. In eq. (110) $\boldsymbol{K}$ is the identity matrix of dimension d, and ξ_k is a step that decreases when the stationary point approaches $\bar{\boldsymbol{\lambda}}$.

C. Improved Projected Steepest-Descent Method

Thanks to the prior family chosen, each prior distribution is uniquely defined by its parameter vector. The parameter space $\left(\mathbb{R}^+\right)^d$ is called manifold. The curvature of the manifold of parameter vectors is obtained by the Hessian matrix $Hl_{J,\Lambda}$ of $l_{J,\Lambda}$ *lJ* ,Λ as follows:

$$\boldsymbol{\lambda} = \left(\lambda_i\right)_{i=1}^{d} \text{ and } Hl_{J,\Lambda}\left(\boldsymbol{\lambda}\right) = \left[\frac{\partial^2}{\partial\lambda_i \partial\lambda_j} l_{J,\Lambda}\left(\boldsymbol{\lambda}\right)\right]_{i,j}.$$

The definition of a Hessian-based algorithm consists in using the Hessian matrix inside the steepest-descent by replacing ***K***=*H l J* ,Λ(λ*k*) .

The geometry of the manifold is also locally defined by the tensor which is the Fisher information matrix:

$$\boldsymbol{\lambda} = \left(\lambda_i\right)_{i=1}^{d} \text{ and } \mathbf{G}\left(\boldsymbol{\lambda}\right) = \left(g_{i,j}\left(\boldsymbol{\lambda}\right)\right)_{i,j=1}^{d} = \left[\frac{-\partial^2}{\partial\lambda_i \partial\lambda_j} \log p\left(t;\boldsymbol{\lambda}\right)\right].$$

The Fisher information matrix for the GGD is writed as:

$$g_{1,1}\left(\boldsymbol{\lambda}\right) = \frac{\beta}{\alpha^2}$$

$$g_{1,2}\left(\boldsymbol{\lambda}\right) = g_{2,1}\left(\boldsymbol{\lambda}\right) = \frac{-\beta + 1 + \psi\left(1/\beta\right)}{\alpha\beta}$$

$$g_{2,2}\left(\boldsymbol{\lambda}\right) = \frac{\beta+1}{\beta^4}\psi'\left(\frac{1}{\beta}\right) + \frac{1}{\beta^3}\psi^2\left(\frac{1}{\beta}\right) + 2\frac{\beta+1}{\beta}\psi\left(\frac{1}{\beta}\right) + \frac{1}{\beta^2}.$$

$$\psi\left(z\right) = \frac{\Gamma'\left(z\right)}{\Gamma\left(z\right)};\ \Gamma\left(z\right) = \int_0^{+\infty} t^{z-1} e^{-t} dt, \quad z > 0$$

$$\alpha, \beta > 0$$

We proposed a generalized steepest-descent based on the expected value of the Hessian matrix: the Fisher information matrix ***K***=−***G***(λ*k*).

Experimental results. The texture clustering requires a barycentric texture computed with a proximal method (110). The three optimization methods obtained are compared in terms of performance and complexity.

The supervised clustering test on a texture image database consists in splitting the database into two parts: the training and the testing sets. The training set is composed by a random selection of N_{Tr} samples from the N_{Sa} samples of each texture class. The remaining samples define the "test" samples. Based on a training set, a barycentric distribution is estimated for each parametric model in the stochastic model which defines the signature of the texture class. The divergence between a test sample and the signature of each class that is minimum defines the estimated class for this test sample. The performance of the algorithm is illustrated by the percentage of tests samples accurately classified to the class among the tests samples from this class.

The supervised clustering test requires a texture image database. A texture image database consist in a set of high quality textures images. The three texture image databases are:

1. the VisTex database which is a conventional texture image database. Each of the 40 images is split in 16 non overlapping sub-images of size 128x128 pixels (N_{Sa}=16);
2. the Brodatz database proposed by Choy and Tong [ComPes09] contain 20 texture classes. Each textured image is split in N_{Sa}=16 non overlapping sub-images (128x128 pixels);
3. the VisTex complete database. Each of the 167 images is split in 16 non overlapping sub-images of size 128x128 pixels (N_{Sa}=16);
4. the Brodatz database contain 13 texture classes. Each textured image is split in $N\ Sa$=16 non overlapping sub-images (128x128 pixels).

The clustering algorithm is launched one hundred times with random training samples to evaluate its performance. In addition, the mean computing time value and the mean number of loops are recorded. The computing time value is the time in seconds needed to obtain one barycentric distribution and the number of loops corresponds to the complexity of the optimization method.

The supervised clustering test with the Jeffrey divergence is apportioned in three optimization methods: the Gradient descent algorithm ∇, the Hessian method H, and the Fisher information matrix approach G. A clustering test is done with the Euclidean distance E between the parameter vectors inside $(\mathbb{R}+)d$. The clustering with the Euclidean distance consists on the computation of a barycentric distribution as an arithmetic mean of parameter vectors.

N_{Tr} /N_{Sa}	**2/16**	**3/16**	**4/16**	**5/16**	**6/16**	**Time**	**Loops**
E, GGD	65%	66%	66%	68%	69%	80 µs	1
∇, GGD	82%	82%	82%	82%	84%	603 ms	159
H, GGD	81%	81%	80%	81%	83%	99 ms	36
G, GGD	84%	83%	83%	83%	84%	16 ms	7

Table 22. Performance and complexity on the VisTex database

N_{Tr} /N_{Sa}	**2/16**	**3/16**	**4/16**	**5/16**	**6/16**	**Time**	**Loops**
E, GGD	79%	80%	80%	80%	79%	78 µs	1
∇, GGD	90%	88%	87%	90%	89%	571 ms	173
H, GGD	90%	89%	86%	88%	89%	102 ms	37
G, GGD	90%	88%	88%	88%	89%	11 ms	5

Table 23. Performance and complexity on the Brodatz Choy database

N_{Tr} /N_{Sa}	**2/16**	**3/16**	**4/16**	**5/16**	**6/16**	**Time**	**Loops**
E, GGD	36%	35%	36%	35%	35%	80 µs	1
∇, GGD	51%	51%	52%	52%	51%	661 ms	190
H, GGD	51%	50%	51%	51%	50%	113 ms	39
G, GGD	52%	53%	53%	53%	52%	31 ms	12

Table 24. Performance and complexity on the VisTex complete database

N_{Tr} / N_{Sa}	**2/16**	**3/16**	**4/16**	**5/16**	**6/16**	**Time**	**Loops**
E, GGD	81%	82%	81%	80%	81%	80 μs	1
∇, GGD	84%	86%	86%	85%	85%	561 ms	161
H, GGD	83%	85%	85%	84%	85%	93 ms	34
G, GGD	84%	84%	84%	83%	82%	24 ms	9

Table 25. Performance and complexity on the Brodatz database

Tables 22-25 shows the clustering results with the centered generalized Gaussian distribution (GGD) assumption. The time needed to compute the barycentric distribution with the Euclidean distance is lower than the time needed to compute a barycentric distribution with an optimization method. The supervised clustering tests with the Jeffrey divergence have a gain of seven points against the supervised clustering test with the Euclidean distance.

The three optimization methods based on the projected steepest-descend method provide similar performance, the three methods converge globally towards the same stationary point of the cost function. Among the three methods, the Fisher information matrix-based method is preferred due to its low computing complexity. In addition, the Jeffrey divergence provides a gain of 2 points again the performance obtained by the method proposed by Choy and Tong [ChoTon07]. In their paper, authors proposed a simple implementation of the steepest descent without geometrical point of view.

It was introduced in [SchBerTurNafIsa12] the information-geometry tools in the clustering of textured images. Our parametric modeling of textured images defines the barycentric distribution. We estimate the barycentric distribution using a projected steepestdescent method geometrically conditioned by the Fisher information matrix The Fisher information matrix provides performance similar to other steepest-descent methods with a lower convergence speed. We obtain respectively a gain of fifteen and seven points on the mean retrieval rate on the Euclidean distance on the VisTex and Brodatz database.

2.7 Image contrast enhancement

In [NafIsa14] we have presented a fast and simple contrast enhancement technique, that uses the Dual-Tree Complex Wavelet transform (DT-CWT), coupled with the bivariate Laplace model for local adaptive contrast improvement. In order to overcome the noise amplification that results from nonlinear operations especially in the homogeneous areas of the image, denoising using bishrink filter in the DTCWT domain is used.

Digital images (photographs, medical images) can be affected by variable light intensity and non-uniform exposure, resulting in low-contrast images. To improve the visual quality of such an image, we have to modify its intensity values and to enhance its contrast. Contrast enhancement (CE) methods are non-linear transformations [Pel90] [BegNeg89] [GonWoo08], histogram-based techniques [PizJohEriYanMul904], [PisZonHem98], [TsaYeh08], contrast-tone optimization [Zha10], frequency domain methods [IsaFirNafMog11, LozBulHilAch13]. Typically some of these methods may result in noisier homogeneous areas; this is why in [LozBulHilAch13] it is proposed to use denoising in the complex wavelet domain.

The algorithm in [LozBulHilAch13] is an adaptive CE method estimating the statistics of the wavelet coefficients locally; the amplification of the noise in the homogeneous areas in the image is avoided by denoising it using the same statistical model.

In [NafIsa14] is presented a fast and simple CE algorithm, inspired by [LozBulHilAch13], which uses likewise the Dual Tree Wavelet Complex transform (DT-CWT) [Kin99], for both local adaptive contrast adjustment and denoising. Instead of using the

SαS model, we used the bivariate Laplace distribution and bishrink filter [SenSel02]. To evaluate the results, we use several quality measures, as well as visual observation. The major contribution of [NafIsa14] is the selection of the statistical model of wavelet coefficients, in contrast with [LozBulHilAch13], increasing the speed of the method. The performance of the method is compared with the well-known CLAHE technique [PizJohEriYanMul90].

For low-dynamic range images, the aim is to increase their contrast, therefore low and middle intensity pixels should be increased, but high intensity pixels should be left unchanged. When this nonlinear amplification occurs, noise can be more visible in less textured areas of the images. Color images are represented in the Red-Green-Blue space (RGB), but we may choose to work in the Hue-Saturation-Value (HSV) space, and more specifically, only on the V channel, similar to [LozBulHilAch13], reducing the computational cost.

The second step is to normalize the V channel values in order to use the entire [0,1] range:

$$L_1 = \frac{L^i \text{ - } \min\left\{L^i\right\}}{\max\left\{L^i \text{ - } \min\left\{L^i\right\}\right\}}. \tag{111}$$

We use for the local contrast enhancement and denoising steps, the Dual-Tree complex wavelet transform, which has six orientations and is quasi-shift invariant. Its directional selectivity is also improved as opposed to the discrete wavelet transform (DWT) being able to distinguish between positive and negative orientations. We use the AntonB filter to decompose the L_1 normalized image with J=6 decomposition levels. In the complex wavelet domain, we perform two operations, namely, denoising and local contrast enhancement. As mentioned before, denoising prevents the local contrast enhancement to amplify the noise in highly homogeneous areas.

Denoising in the DT-CWT domain: It is assumed the image is corrupted by additive white Gaussian noise, so the noisy wavelet coefficients x_j at level j, are:

$$x_j = w_j + n_j, \text{ with } n \sim \mathcal{N}\left(0, \sigma_n^2\right)$$

The coefficient and its parent are modeled by a Laplacian bivariate probability distribution function [NafFirIsaBouIsa10b], to take into account the interscale dependencies:

$$p_{\mathbf{w}}(w_j,\ w_{j+1}) = \frac{3}{2\pi\sigma^2}\exp\left(-\frac{\sqrt{3}}{\sigma}\sqrt{w_j^2 + w_{j+1}^2}\right),$$

where w_j is the wavelet coefficient at decomposition level j, and w_{j+1} is the parent wavelet coefficient, at the same location, but coarser level, j+1, respectively. The marginal variance σ^2 for each wavelet coefficient for the useful (noiseless) image needs to be known and it is estimated locally in a moving window of size NxN. The noise is modeled by

$$p_{\mathbf{n}}(n_j,\ n_{j+1}) = \frac{3}{2\pi\sigma_n^2}\exp\left(-\frac{n_j^2 + n_{j+1}^2}{2\sigma_n^2}\right),$$

where n_j is the wavelet coefficient of the noise at level j, and n_{j+1} is the parent wavelet coefficient of the noise, same location, coarser level, j+1.

The wavelet coefficients are denoised using Maximum a Posteriori (MAP) estimators $\hat{w}_j$ of noisy wavelet coefficients x_j. The MAP estimate is obtained as the bishrink filter [SenSel02]:

$$\hat{w}_j = \frac{\left(\sqrt{x_j^2 + x_{j+1}^2} - \sqrt{3}\sigma_n^2/\sigma\right)_+}{\sqrt{x_j^2 + x_{j+1}^2}} x_j.$$

A robust median estimator is used to compute the noise standard deviation, σ_n, from the noisy wavelet coefficients, at the finest level of decomposition:

$$\hat{\sigma}_n = \frac{\operatorname{median}\left(\left|x_i\right|\right)}{0.6745}, x_i \in \text{subband HH}.$$

Local Contrast Enhancement in the DT-CWT domain: We use the contrast measure proposed in [LozBulHilAch13], suitable for wavelet domain, defined as the ratio between the maximum of the marginal standard deviation and the standard deviation itself, σ:

$$C\left(x_j\right) = \frac{\max\left\{\sigma\left(x_j\right)\right\}}{\sigma\left(x_j\right)}. \tag{112}$$

The marginal variance is estimated in a similar manner as in the case of denoising, in a moving window of size *M*x*M*, where *M* may be different than *N*. This measure is supposed to be a reference value for the desired contrast. The local contrast values are used to adjust the corresponding wavelet coefficients using an exponential contrast enhancement function A_c

$$A_c\left(x_j\right) = \exp\left(-\frac{1}{C\left(x_j\right)}\right) + A_0, \tag{113}$$

where $A_0=1-\exp(-1)$ is a normalization constant. Basically the coefficients are denoised and their contrast improved at the same time. So we can write that the obtained value channel L_2 is

$$\hat{w}_j = A_c\left(x_j\right) bishrink\left(x_j\right) x_j, \tag{114}$$

where A_c is the enhancement function and the bishrink is the denoising filter given before.

The image resulted after denoising and local CE is then further post-processed, by scaling its levels logarithmically. This compresses the dynamic range [GonWoo08]:

$$L^o = \frac{\max\left\{L_2\right\}}{\log\left(\max\left\{L_2\right\}+1\right)} \log\left(L_2+1\right). \tag{115}$$

To obtain the color processed image, the V channel is replaced and we convert from HSV back to RGB. To summarize, the steps of the method are: 1-RGB – HSV conversion; 2-extracting the input V channel, denoted by L^i; 3-normalizing V channel, from L^i, we obtain L_1; 4-denoising and local contrast enhancement in the DT-CWT domain, using bishrink filter for the denoising and A_c for CE; we obtain L_2. 5-postprocessing to obtain L^o; 6-finally conversion back to RGB format.

For **the experiments**, we use two image sets, Memorial and Greenwich, for which there are so called reference images (in reality we would not have such a reference) [Deb14] [Dul14]. We compare our results with the adaptive histogram equalization (CLAHE) method.

For the DT-CWT transform, we use J=6 decomposition levels and AntonB filter. It is to be noted that for step 4, for the denoising part, we have to give an estimate of the marginal variance, σ^2 for the useful signal. This is done in a moving window of size 7x7, just as it is indicated in [SenSel02] (N=7). For the local contrast enhancement, the variance is computed using a square window of size: 3x3, 5x5 and 7x7 (M=3, 5 or 7).

For CE window size= 3*3 the method is noted with (1); for CE window size= 5*5 with (2), and CE window size= 7*7 with (3) in the following tables.

We evaluate the obtained images subjectively, using a human observer, as well as computing some objective measures. For the contrast enhancement, we use the same adapted measure as in [LozBulHilAch13], the Structural SIMilarity Image Quality Index (SSIM), between two images A and B, defined as:

$$SSIM(A,B)=\left(\frac{2\mu_A\mu_B}{\mu_A^2+\mu_B^2}\right)^{0.25}\left(\frac{2\sigma_A\sigma_B}{\sigma_A^2+\sigma_B^2}\right)^{0.5}\left(\frac{\sigma_{AB}}{\sigma_A\sigma_B}\right)^{0.25}, \tag{116}$$

where μ_A and μ_B are the sample means of A and B, σ_A and σ_B are sample standard deviations of A and B and σ_{AB} is the sample covariance of A and B:

$$\sigma_{AB}=\frac{1}{L-1}\sum_{l=1}^{L}\left(A_l-\mu_A\right)\left(B_l-\mu_B\right) \tag{117}$$

We also give the entropy of the images, which is a statistical measure of randomness used to characterize the texture. The entropy H of a grey level image, with G discrete grey levels with probabilities p_m is:

$$H=-\sum_{m=1}^{G}p_m\log_2 p_m\,. \tag{118}$$

Low entropy images have very little contrast, so we are interested in images with higher entropy after the contrast enhancement processing.

To see the effect of the denoising in step 4 (processing the V channel), we estimate the sample noise standard deviation before and after processing. We also estimate the sample noise standard deviation for L^o to compare it with the one of L^i.

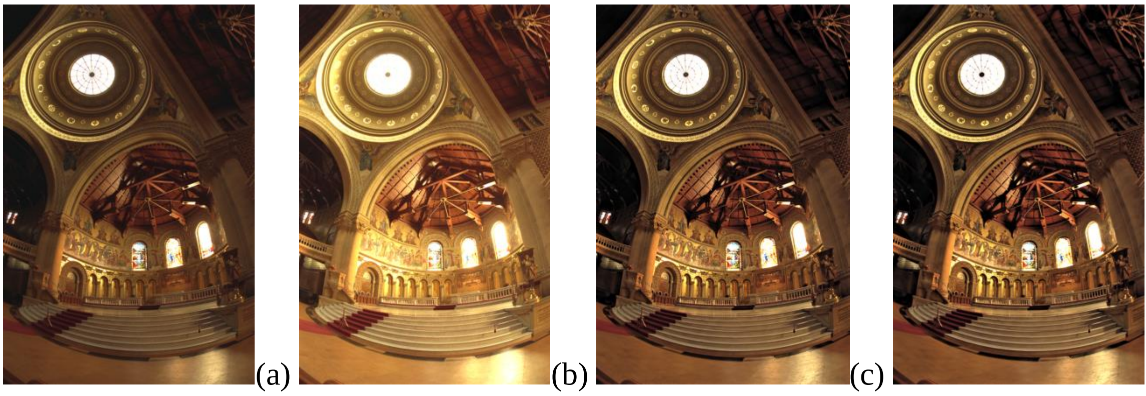

(a) (b) (c) (d)

Fig 50. Memorial image: original, reference, corrected image, proposed method with window size 7*7 (SSIM=97,08 %), corrected image for CLAHE (SSIM = 94,23%).

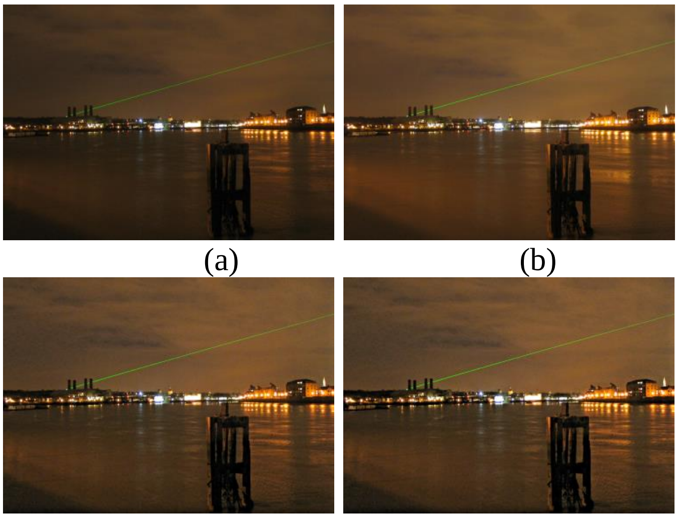

(a) (b)

(c) (d)

Fig. 51. Greenwich image, top to bottom, left to right: original (image #2), reference (image #3), corrected image for window size 7*7 (SSIM=97,22 %), corrected image for CLAHE (SSIM=93,27%).

For Memorial, the original low-contrast and reference images are shown in Fig. 50a)-b), where we used as original memorial0065 and as reference memorial0063 from the HDR image series for the Stanford Memorial Church. The result of the proposed contrast enhancement method is shown in Fig. 50c) and the result for the CLAHE method is shown in Fig 50d).

For the Greenwich images, the original and reference images are shown in Fig. 51a)-b). The result of the proposed method is shown in Fig. 51c) and CLAHE result is shown in Fig 51d). It can be observed visually that both methods are efficient, correcting the contrast of the original. The SSIM values, shown in Table 26 are higher for the proposed method in both cases, than for the CLAHE, indicating our method outperforms CLAHE. The highest value is obtained when both windows to estimate the local variance are of the same size, 7x7, for both denoising and local contrast enhancement. The output noise standard deviation σ_n^o values from Table 27 show the values for the proposed method are half of the values for CLAHE.

Image	**SSIM (%)**			
	[NafIsa14] 1	***[NafIsa14] 2***	***[NafIsa14] 3***	***CLAHE***
Memorial	97,03	97,08	**97,08**	94,23
Greenwich	96,99	97,13	**97,22**	93,27

Table 26 SSIM results.

Image, input noise standard deviation σ_n^i	**Output noise standard deviation σ_n^o**			
	[NafIsa14] 1	***[NafIsa14] 2***	***[NafIsa14] 3***	***CLAHE***
Memorial, 0,0125	0,0136	0,0133	**0,0131**	0,0249
Greenwich, 0,0045	0,0051	0,0051	**0,0050**	0,0097

Table 27 Noise standard deviation results.

Table 28 shows the denoising and contrast enhancement step greatly reduces the noise standard deviation. The entropy is higher for our method than for the CLAHE method, indicating the contrast is enhanced (Table 29). It is also increased when compared to the input image entropy. In Fig. 52 we are showing the corrected V channels for each step.

Image, input noise standard deviation σ_n^i	**Output noise standard deviation σ_n^o after step 4**		
	[NafIsa14] 1	***[NafIsa14] 2***	***[NafIsa14] 3***
Memorial, 0,0133	0,0049	0,0048	**0,0047**
Greenwich 0,0045	0,0007	0,0007	**0,0007**

Table 28 Noise Standard Deviation results for step 4, proposed.

Image, input entropy	**Output entropy**			
	[NafIsa14] 1	***[NafIsa14] 2***	***[NafIsa14] 3***	***CLAHE***
Memorial 7,27	7,61	7,61	**7,61**	7,52
Greenwich 6,68	7,00	7,00	**7,00**	6,63

Table 29 Entropy results.

We have proposed in [NafIsa14] a variant of the wavelet based contrast enhancement method in [LozBulHilAch13], which has similar performance but is faster. The reason is that we have used a simpler statistical model for the wavelet coefficients that simplifies the denoising procedure, requiring the estimation of a reduced number of parameters, and simpler estimation methods. We found this method works really well when the image is not very dark. Future work may involve correcting this.

Fig. 52 Memorial images-V channel, left to right: reference, original, preprocessed, after denoising+local CE, postprocessed (proposed), V channel for CLAHE.

2.8 Contributions to Hurst parameter estimation

Papers: [NafIsaNel14], [NafIsa13]

2.8.1Hurst estimation using HWPT

Anisotropic images have different smoothness degree values on the preferential orientations. To distinguish between preferential directions from such an image, we can use a complex wavelet transform with enhanced directional selectivity, such as the DTCWT ([NelKin10b]). In the paper [NafIsa13] we have proposed to use the Hyperanalytic Wavelet Packet Transform (HWPT) for the identification of the preferential orientations, and on each direction the smoothness is estimated via the Hurst exponent.

The smoothness of a signal is an important characteristics, and it can be used to optimize its treatment. For example, a treatment based on wavelets can be optimized by selecting mother wavelets (MW) with same smoothness as the signal to be treated [Rio93]. A fractional Brownian motion (fBm) random processes is a continuous-time Gaussian process depending on the Hurst exponent H, $0<H<1$. It generalizes the ordinary Brownian motion corresponding to $H = 0.5$, whose derivative is the white noise [AbrVei98]. A signal with a Hurst exponent of $H = 0.9$ is smoother than a signal which has a $H = 0.1$.

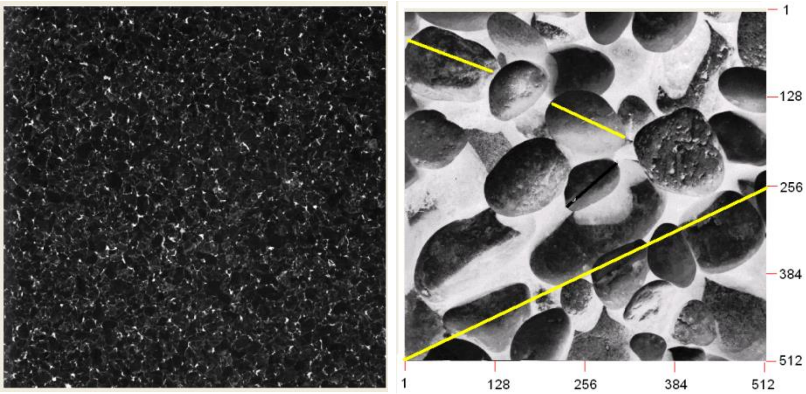

Fig. 53. Left: Image D33(Brodatz database) with a global mean Hurst exponent of 0.3926; right: Image D31, global mean Hurst exponent of 0.4645

The utilization of Hurst exponent for smoothness estimation can be generalized to images [NelKin10b]. The smoothness of the image D33 can be appreciated globally because it is isotropic. Despite the very different informational content of images D33 and D31, their global mean Hurst exponents are close. In the case of anisotropic images, as for example the image D31, the estimation of the global Hurst exponent is no longer sufficient, because they contain preferential orientations (some of them are marked on the image D31).

Different values of anisotropic Hurst exponent can be estimated considering each of these orientations, obtaining estimations of directional smoothness of the image. Vidakovic et al. [VidNicGar07] estimated anisotropic Fractal Distance (FD) in the horizontal, vertical and diagonal directions, using 2d-Discrete Wavelet Transform (2d-DWT). Nelson et al. [NelKin10b] used the 2d Dual-Tree Complex Wavelet Transform (2d-DTCWT) to increase the number of directions at six in which are estimated the anisotropic Hurst exponents. We have increased the number of orientations for which anisotropic Hurst exponents can be estimated, using the Hyperanalytic Wavelet Packets Transform (HWPT).

The number of directions selected by the HWPT depends on the number of iterations of the four DWPT used in its implementation. If we apply, for example, two iterations [NafIsaNaf12], we obtain the sub-images z_+ and z_-, which are indexed as in Fig. 34. The twenty two preferential directions of these sub-images are presented in Table 19. This number can be further increased, by increasing the number of iterations of the DWPT. We notice that there are directions associated with multiple subbands, as for example the directions ±atan(1). These two directions are associated with the subbands indexed by 4, 8, 17 and 20. Even if they have the same preferential orientations, these subbands differ by their frequency content (central frequency and bandwidth). The HWPT represents a tool useful for the estimation of the anisotropic smoothness of an image because it separates in subbands the details corresponding to different directions.

Hurst parameter estimation: The Hurst parameter is a measure of the degree of correlation of a signal. For a White Gaussian Noise process, the value of Hurst exponent is 0 and its samples are not correlated. There are several methods for estimating the Hurst exponent both for fBm and for multifractional Brownian motion processes (mfBm). In [NelKin10b], the authors measure the global H for the entire image using the 2d-DTCWT decomposition. However, in [NafIsa13], we computed for each subband the Hurst parameter, so we have used a simple and fast estimator based on local oscillation, implemented in FracLab [Frac14].

Subband	***H_{real}***	***Orientation***	***Subband***	***$H_{imaginary}$***
-2	0.59	-atan(2)	+2	0.59
-3	0.60	-atan(1/2)	+3	0.57
-4	**0.55**	-atan(1)	+4	**0.54**
-6	0.60	-atan(3)	+6	0.58
-7	0.54	-atan(1/3)	+7	0.55
-8	0.55	-atan(1)	+8	0.48
-9	**0.71**	-atan(1/5)	+9	**0.62**
-10	**0.75**	-atan(3/5)	+10	**0.68**
-11	0.60	-atan(1/7)	+11	0.68
-12	0.64	-atan(3/7)	+12	0.59
-13	0.60	-atan(1/5)	+13	0.54
-14	0.59	-atan(3/5)	+14	0.63
-15	0.64	-atan(1/7)	+15	0.68
-16	0.61	-atan(3/7)	+16	0.66
-17	0.57	-atan(1)	+17	0.52
-18	0.54	-atan(7/5)	+18	0.64
-19	**0.65**	-atan(5/7)	+19	**0.61**
-20	**0.65**	-atan(1)	+20	**0.58**

Table 30. Anisotropic Hurst exponents for the image D31

Experimental results: We have estimated, using FracLab, the anisotropic Hurst exponents corresponding to the twenty two directions, for the image D31, using the HWPT with two iterations, obtaining the results in Table 30. For each subband, we have obtained a matrix of local Hurst exponents, proving that the considered image is multi-fractal. The values are obtained by averaging the elements of each subband matrix.

Because the detail HWPT coefficients are complex, we have estimated separately the anisotropic Hurst exponents of the real and imaginary parts of those subbands, obtaining close results.

The highest difference between H_{real} and $H_{imaginary}$ is 0.12 and is observed in subbands z_{18} and z_{20} while the smallest difference equals 0.01 and is observed in subbands z_3 and z_{14}.

For the subbands z_{-3} and z_{+14}, in the directions −atan(1/2) and +atan(3/5), we have obtained the Hurst exponents: 0.60 and 0.63, relatively close, meaning that the test image has same smoothness on both directions.

Comparing the values from the second column of Table 30, we observe that the direction with the highest Hurst exponent, 0.75, is –atan(3/5) (subband z_{-10}) corresponding at the smoothest direction in Fig. 54. The minimum value corresponds to the directions ±atan(1) (subband $z_{\pm4}$) which represent the less smooth directions in Fig. 54. These directions are indicated in Fig. 54.

The contours of objects represent rapid transitions, reducing the smoothness. The number of contours intersected by the line corresponding to the smoothest direction in Fig. 3 is lower than the number of contours intersected by the line corresponding to the less smooth directions. The results in Table 30 are in agreement with the visual content of the image in Fig. 54.

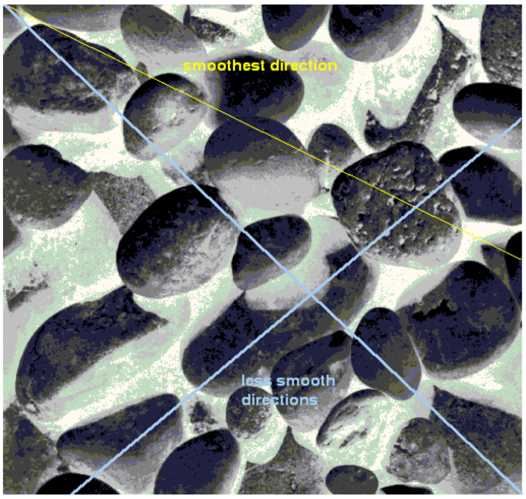

Fig 54. The smoothest and the less smooth directions, identified in the image D31, are marked with colored lines.

We compared the method proposed with the same method applied this time in the 2d-DTCWT domain. We have used the same test image, and again, two levels of decomposition. Obviously this time, the number of orientations is limited at six.The values for the Hurst exponent are very close for the real and imaginary coefficients. The lowest difference is for the orientation 15°, for both levels of decompositions. The highest difference is at orientation 135°, second level of decomposition.

Comparing Table 30 and Table 31, we notice the similar values obtained for the same direction. For example, for the direction 45°, the values obtained using HWPT are H_{real} =0.55 and $H_{imaginary}$=0.54 and the values obtained using 2d-DTCWT are H_{real} =0.55 and $H_{imaginary}$=0.53.

Scale	*Orientation*	H_{real}	$H_{imaginary}$
1	15°	0.56	0.56
	45°	0.55	0.53
	75°	0.48	0.45
	105°	0.57	0.56
	135°	0.52	0.55
	165°	**0.48**	**0.45**
2	15°	**0.65**	**0.65**
	45°	0.61	0.62
	75°	0.64	0.62
	105°	0.64	0.61
	135°	0.61	0.54
	165°	0.62	0.61

Table 31. Anisotropic Hurst exponents for the image D31 in the 2D-DTCWT domain.

From Table 31, we observe that the direction with the highest Hurst exponent, 0.65, is 15° (level 2). The highest value of the Hurst exponent from Table 30, 0.75, is missing in Table 31, because the 2d-DTCWT does not separate direction –atan(3/5), which corresponds at the smoothest direction in D31. The minimum value in Table 31, 0.45, corresponds to the direction 165° (level 1), which is not separated by HWPT implemented with two iterations.

The main contribution of [NafIsa13] consists in the substitution of the 2d-DTCWT, used in [NelKin10b], for the estimation of directional smoothness of images, with the HWPT. While the 2d-DTCWT has six preferential orientations; the HWPT could have any number of preferential orientations (for example 22 in Table 19). The HWPT, computed with an appropriate number of iterations, is able to detect all the directions present in a given image and to separate (in subbands) the corresponding details. By estimating the Hurst exponent of each subband, using an appropriate estimator, the image smoothness on the corresponding direction can be appreciated.

The method proposed has numerous applications in materials' science, geo-sciences or engineering, because it permits to appreciate the directional smoothness of an object based on one of its images. The great advantage of the proposed method is the absence of the direct contact. The method allows the search of a road using the SAR image of a forest, the detection of a scratch on the surface of a car or the identification of the portions of a road covered by snow or glace.

It has interesting theoretical consequences as well, facilitating the introduction of a new best MW searching criterion. Each of the smoothness values can be used for the selection of the MW (with same smoothness), which will generate the subband with same direction in a particular HWPT. So, that MW will be adapted to the image considered. Some image processing methods, as for example: denoising, compression or texture classification, based on wavelets, can be adapted in this way to the geometrical content of a given image. For example, Olivier Rioul used, in a limited context, the results of mother wavelets' smoothness estimation to find the most appropriate function for image compression [Rio93]. The adaptation of the MW to the geometrical content of a given image will represent a future research direction.

2.8.2 Regularised, semi-local Hurst estimation via generalised lasso and Dual-Tree Complex Wavelets

In accordance with my career development action plan presented at the Associate Professor competition (in sep.2013), I have proposed a paper in the field of **Hurst parameter**

estimation, to the most prestigious conference of Image Processing, IEEE International Conference on Image Processing (ICIP 2014), in collaboration with Professor Alexandru Isar and Senior Lecturer, Dr James Nelson (University College London, UK). This paper was accepted, presented and published, although the acceptance ratio was only 43%.

Strictly self-similar processes are invariant in distribution, up to a constant, under spatial (or temporal) scalings to a constant, under spatial (or temporal) scalings. These processes have long-range dependence behaviour which is encapsulated by regularity parameters : the Hurst exponent. These shape the spatial correlatory structure and determine the smoothness present in complex textures and natural phenomena. In a simple case, regularity is assumed constant throughout the data; but images typically comprise multiple textures and have multiple Hurst exponents throughout their spatial support.

We have considered a special case for this semi-local Hurst estimation for random fields, where the regularity varies in a piecewise manner, which is appropriate for segmentation/adaptive denoising and detrending where image is a disjoint union of textures.

The generalised lasso (Least Absolute Shrinkage and Selection Operator) is exploited to propose a spatially regularised Hurst estimator. Dual-tree complex wavelets are used to formulate the log-spectrum regression problem and an interlaced penalty matrix is constructed to form a 2-d fused lasso constraint on the double-indexed parameters.

We demonstrate with experiments that we have reasonably accurate pointwise estimates of the Hurst exponent and our lasso-based approach holds an advantage over the usual least-squares (or linear extensions thereof).

We extended a regularity-based denoising approach, of Echelard and Levy Vehel [EchLev08]. Moreover, our construction is such that this can easily be extended to the case where the Hurst exponent varies as a polynomial.

Weakly self-similar processes: If a self-similar process f satisfies some conditions (stochastic continuity and non-triviality) then there must exist an exponent H > 0 such that if $f(\lambda\,\cdot) = \lambda^H f(\cdot)$. In fact, we only here require a more general form of self-similarity, whereby the invariance property is satisfied over the first two orders of statistics.

Def.1 (Weak self-similar processes): Let $(\Omega, \mathcal{F}, \mathbb{P})$ probability space, $\lambda \in \mathbb{R}$, $H \in (0,1)$, $t \in \mathcal{T} \subset \mathbb{R}^2$. The stochastic field $f\colon \Omega \times \mathcal{T} \mapsto \mathbb{R}$ is weakly self-similar, $f \in WS_H$ if $\mathbb{E}f(\lambda\,\cdot) = \lambda^H \mathbb{E}f$ and $\mathbb{E}f(\lambda t)f(\lambda\,\cdot) = \lambda^{2H}\mathbb{E}f(t)f(\cdot)$

It immediately follows that weak self-similar processes are strictly self-similar, they contain the much studied Fractional Brownian surface, and have a power law spectrum.

Wavelets offer means to study self-similar processes, see Prop.2.

Proposition 2 (Nelson and Kingsbury [NelKin10a]).

Let $f \in WS_H$. Then $\mathbb{E}|(\mathcal{W}f)(\cdot;k,m)|^2 \propto 2^{2k(H+1)}$ where $\mathcal{W}$ denotes the wavelet transform operator, defined by , $(\mathcal{W}f)(t;k,m) \coloneqq 2^{-k}\langle f, \psi_m(2^{-k}\cdot - t)\rangle$ with some suitable wavelet ψ , defined over space *t*, orientation *m* and *k*th finest scale level.

The Hurst exponent describes the smoothness. Values close to one (zero) will be relatively smooth (rough). If *H* is fixed over the entire support, it can be estimated by taking the log of both sides of the proportionality in Prop. 2 and computing the slope of the regression via least squares. In general, regularity can vary with respect to space and direction and we have $H = H_m(t)$. In this case, the Hurst parameter can still be estimated by carrying out least squares over localised cones, and directional subbands, in the wavelet domain.

In practice $\mathbb{E}|\cdot|^2$ is approximated by the sample second moment E in the region δ_t, scale *k* and orientation *m*, namely

$$E_{km}(t) := |\delta_t|^{-1} \|(\mathcal{W}f)(\cdot;k,m)\|^2_{\ell_2(\delta_t)} \propto 2^{2k(H_m(t)+1)}. \tag{119}$$

When spatial localisation of Hurst is important, the pointwise estimate $|(\mathcal{W}f)(\cdot;k,m)|^2$ is used. The energy of the discrete wavelet coefficients, computed over a dyadic 2-d grid, can then be computed on the integer lattice (the original pixel locations) at each scale level by appropriate interpolation.

Estimation: In [NelKin10b] it was proposed to use the dual-tree complex wavelet estimator for the case where the Hurst exponent is anisotropic and piecewise locally varying. Nelson and Kingsbury showed that (shift-invariant) dual-tree wavelets provided Hurst estimates with greater accuracy and less variance than other, shift-variant, decimated wavelet transforms; a key reason for this is that the shift invariance of dualtree wavelets provides more stable energy estimates, especially near singularities or considerable oscillations [SelBarKin05].

Index the spatial domain as $t \in \mathcal{T} = \{t_i\}_{i=1}^{n}$. Since the same analysis can be applied in each direction as required, we drop m and let $y_k[i] := log E_{k,m}(t_i)$ denote the log sample second moment of the wavelet magnitudes about the location t_i and scale k. Throughout we will use dual-tree wavelets to compute the sample energy $E_{km}(t)$ but other wavelets or measures may be used to derive E without loss of generality.

Given the power law, the log sample second moments will ideally follow the simple linear model $y_k[i] = k\beta_2[i] + \beta_1[i]$, with slope $\beta_2[i] = 2(H_i + 1)$, where $H_i = H[t_i]$. In practice, the energies at some of the finest (low SNR) and coarsest (poorly localised) scale levels are excluded from the regression. The corresponding pointwise least squares problem takes the form:

$$\min_{\beta_i} \|\mathbf{y}_i - \mathbf{X}_0 \boldsymbol{\beta}_i\|_2 \text{ with } \mathbf{y}_i = [y_{k_-}[i] \quad \cdots \quad y_{k_+}[i]]^T,\ \mathbf{X}_0 = \begin{bmatrix} 1 & k_- \\ \vdots & \vdots \\ 1 & k_+ \end{bmatrix},\ \boldsymbol{\beta}_i = \begin{bmatrix} \beta_1[i] \\ \beta_2[i] \end{bmatrix}.$$

Here, the 1st $(k_- - 1)$ finest, and $(k_+ - 1)$ coarsest, scale levels are discarded. The Hurst estimate is then obtained from the slope estimate: $\widehat{H_i} = (\widehat{\beta_2}[i]/2 - 1)$.

The pointwise least-squares solver can be readily extended to the entire spatial domain: $\min_{\mathbf{B}} \|\mathbf{Y} - \mathbf{X}_0 \mathbf{B}\|_2$, where

$$\mathbf{Y} = [\mathbf{y}_1, \ldots, \mathbf{y}_n] \in \mathbb{R}^{K \times n},\ \ \mathbf{B} = [\boldsymbol{\beta}_1, \ldots, \boldsymbol{\beta}_n] \in \mathbb{R}^{2 \times n}.$$

As in the pointwise case, the solution $(\mathbf{X}_0^T \mathbf{X}_0)^{-1} \mathbf{X}_0^T \mathbf{Y}$ only involves the inversion of a two-by-two matrix.

Generalised LASSO formulation: The main drawback with the Hurst estimation, described above, is that the estimated regularity can vary quite markedly according to the behaviour at the finest, and usually noisier, scales. Ideally, we might want some spatial smoothing but only at those locations where the linear least squares solution was a poor fit to the log spectrum. This motivated us to propose the generalised lasso [TibTay10] as a means to spatially regularize the Hurst estimates. This non-linear smoother takes the form

$$argmin_{\boldsymbol{\beta}} \|\mathbf{y} - \mathbf{X}\boldsymbol{\beta}\|_2^2 + \lambda \|\mathbf{D}\boldsymbol{\beta}\|_1,$$

where $\mathbf{y}$ – is the response (data) vector, $\mathbf{X}$ – is a model matrix of predictor variables (the model), $\boldsymbol{\beta}$ – is a vector of model parameters, and $\mathbf{D}$ is a penalty matrix. This problem reduces to the so-termed 1-d fused lasso when $\mathbf{D}$ has a main diagonal of negative ones, an upper diagonal of positive ones, and is zero elsewhere.

Regularised Hurst estimation: The generalised lasso framework can accommodate a spatially regularised version of Hurst estimation as follows. We rearrange the least-squares problem as $\operatorname{argmin}_{\beta \in \mathbb{R}^{Kn}} \|\mathbf{y} - \mathbf{X}\boldsymbol{\beta}\|_2$ with $\mathbf{y} = [\mathbf{y}_1^T, \ldots, \mathbf{y}_n^T]^T \in \mathbb{R}^{Kn}$, $\boldsymbol{\beta} = [\boldsymbol{\beta}_1^T, \ldots, \boldsymbol{\beta}_n^T]^T \in \mathbb{R}^{2n}$ and

$$\mathbf{X} = \mathbf{I}_n \otimes \mathbf{X}_0 = \begin{bmatrix} \mathbf{X}_0 & & \mathbf{0} \\ & \ddots & \\ \mathbf{0} & & \mathbf{X}_0 \end{bmatrix} \in \mathbb{R}^{Kn \times 2n},$$

where $\otimes$ denotes the Kronecker product and $\mathbf{I}_n$ is the n-by-n identity matrix.

A modification of the so-called '2-d fused lasso' penalty is used to impose spatial regularisation on both parameters $\beta_1[i]$ and $\beta_2[i]$. For the case where we have defined as above, this is achieved by designing an interlaced version of the usual 2-d penalty, namely $\mathbf{D} = \left[\mathbf{D}_2^T, \mathbf{D}_{2n_0}^T\right]^T$ where $\mathbf{D}_2$ is the diagonal sub-matrix diag([1, 0,−1]) which performs the horizontal differences of the form $\beta_j[i] - \beta_j[i+1]$ and, likewise, $\mathbf{D}_{2n_0}$ is the diagonal sub-matrix which performs the vertical differences $\beta_j[i] - \beta_j[i + 2n_0]$, and where n_0 is the width of the image over which the β parameters are defined. The extra zeros between the +1 and −1 have the effect that the odd-numbered rows of the penalty matrix produce differences in the intercept parameter $\beta_1[i]$ and the even-numbered rows produce differences in the slope parameter $\beta_2[i]$; hence the term 'interlaced'.

Like the usual 2-d fusion penalty, it can easily be seen that the interlaced version also has a rank equal to the number of columns which is less than the number of rows. As such, we can follow similar arguments to that of Tibshirani [TibTay10] to conclude that our interlaced fusion penalty is 'generalised' in the sense that cannot be reduced to the standard lasso problem.

Two sets of **experiments** were carried out: Hurst estimation and spatially adaptive, regularity-based denoising. The incremental Fourier synthesis method [KapKuo96] favoured by the Fraclab toolbox [Frac14] was used to simulate fractional Brownian surfaces. These were furnished with piecewise Hurst parameters by stitching together surfaces generated with the same underlying white noise process but different spectral slopes in the same way as [NelKin10b]. This ensures that there were no 'artificial' artefacts caused by jumps from one piecewise region to the next. Four image types were designed and one hundred instances of each design were used for testing. The underlying Hurst parameters are depicted with respect to space in the first column of Fig. 56. These are referred to here as 'chequers', 'curves3', 'curves4', and 'curves5'. In keeping with the emphasis on the localised nature of our analysis all images were restricted in size to 64×64.

Three methods were used to estimate the Hurst parameter, namely:

(i) the usual least squares technique (OLS);

(ii) least squares followed by post-filtering (PS)—convolution of β_i by a 5×5 Gaussian filter; and

(iii) the proposed generalised lasso, mentioned above.

As well as Fraclab, we used Kingsbury's DTCWT Matlab toolbox and Tibshirani's genlasso R package. The finest and coarsest scale levels were discarded from the regression (scales $k_- = 2$, $k_+ = 5$) in all cases. Methods (ii) and (iii) require one parameter each to be set—the variance of the Gaussian filter and the 'λ' of the lasso. However, the results obtained here (cf. Fig. 55) suggest that the optimal settings are very stable across instances of the same image type and that both methods are superior to least squares over very large intervals of the parameter values.

To illustrate their realistic potential, we used three hold-out images to train the optimal parameter settings for each image type. Generally, if training data is not available, the smoothing parameters should set in accordance to how rapidly one expects, or wants, the Hurst parameter to vary.

Columns 2-4 in Fig. 56 illustrate the mean Hurst estimates of each method. The banding effect in the OLS method is due to the fact that, near the boundaries of the piecewise regions, the Hurst parameter estimation is disturbed by the conflicting statistics of the neighbouring regions. The PF method smooths these artefacts out but at the cost of spatial coherence. Only the lasso-based method appears, in the mean, to be able to convincingly cope with this effect. Furthermore, as Table 32 shows, lasso also obtains smaller error variance.

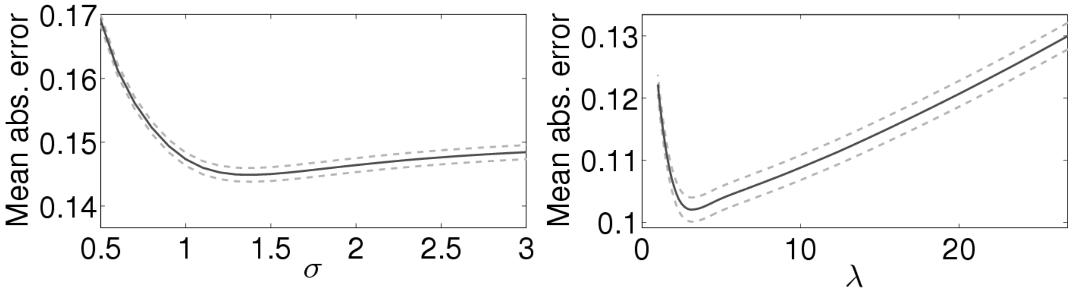

Fig. 55. Mean error of ‘curves4’, over all pixels and instances, and standard error (dotted lines), over the instances, with respect to smoothing parameter. Note the OLS error is 0.187.

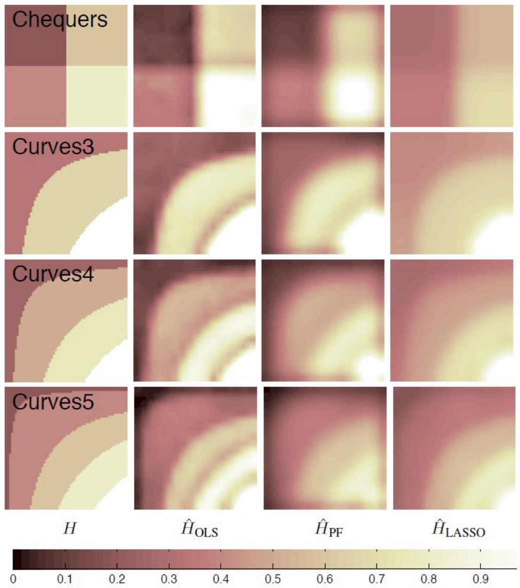

Fig. 56. True Hurst and mean Hurst estimates of four fractional Brownian surfaces (over 100 simulations each). 1st column: true Hurst; 2nd: OLS; 3rd: PF; 4th: LASSO. OLS: ***banding effect*** near boundaries; PF ***smooths*** these artefacts with cost of spatial coherence; LASSO convincingly ***copes*** with this effect.

Data	OLS	PF	Lasso
chequers	0.171 (0.045)	0.145 (0.030)	**0.125 (0.022)**
curves3	0.251 (0.183)	0.181 (0.065)	**0.118 (0.025)**
curves4	0.187 (0.070)	0.145 (0.028)	**0.111 (0.019)**
curves5	0.177 (0.481)	0.159 (0.029)	**0.125 (0.021)**

Table 32. Mean absolute error (error standard deviation) of Hurst estimators: OLS, PF, lasso.

Fig. 57 shows the absolute error histograms of the methods for the ‘curves5’ image. Although not shown here due to space restrictions, the OLS errors follow a very similar distribution over all data types. This is perhaps not too surprising since it is a more localised method than PF or lasso. The lasso’s errors are smaller than PF which is smaller than OLS. The advantage of the lasso as well as the PF becomes steadily weaker as the Hurst exponent varies more. This is to be expected since spatial smoothing has less significance when regularity varies more rapidly in space.

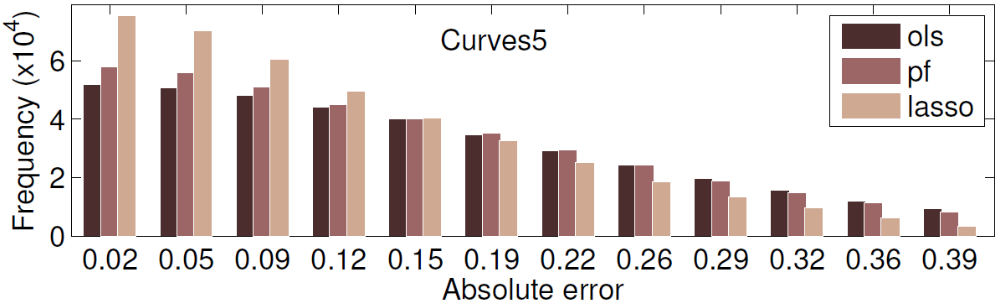

Fig. 57. Mean absolute error histograms of the OLS, PF, and lasso methods, for the 'curves5' data. OLS more localised than PF/lasso. Advantage of lasso/PF weaker as Hurst varies more (spatial smoothing less significant).

Denoising: Various strategies have been devised to exploit the Hurst or Hölder (regularity) exponent for denoising. The general idea assumes that the signal of interest follows a power law and uses shrinkage to mitigate any significant deviation from that model. Often, the regularity is known or assumed, as in [VidKatAlb00]. We follow, in spirit, the work of Echelard and Levy-Vehel [EchLev08] where the regularity is estimated and extend this by allowing the regularity to vary piecewise.

The four image types were simulated as before. High frequency Gaussian noise was then added (in the wavelet domain to the finer scale levels: $\sigma = 4$ at $k = 1$ and $\sigma = 2$ at $k = 2$). Then, scale levels $k = 3, \ldots, 5$ were used to estimate the Hurst parameter using OLS, PF, and lasso. Any (dual-tree) wavelet coefficients at levels $k = 1$ or $k = 2$ which had a magnitude above the estimated power law decay were shrunk to the expected value as defined by the power law model.

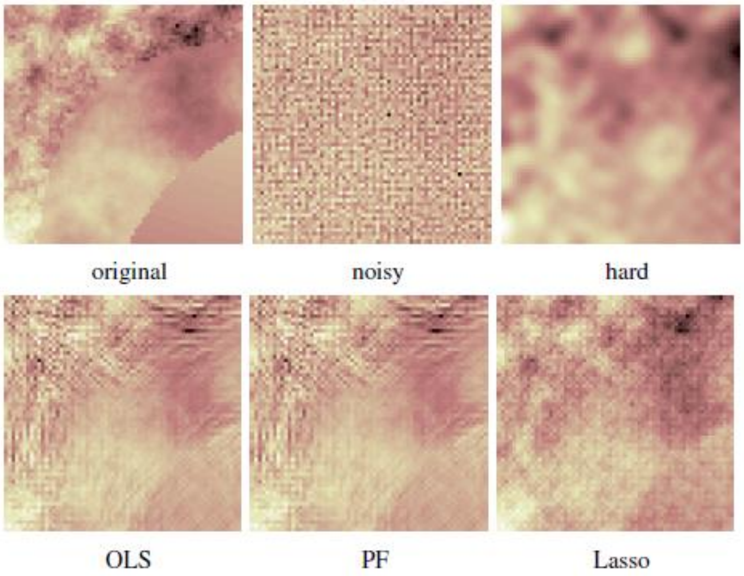

Fig. 58. Regularity-based denoising for 'curves3' subject to high frequency noise: hard thresholding; OLS; PF; LASSO.

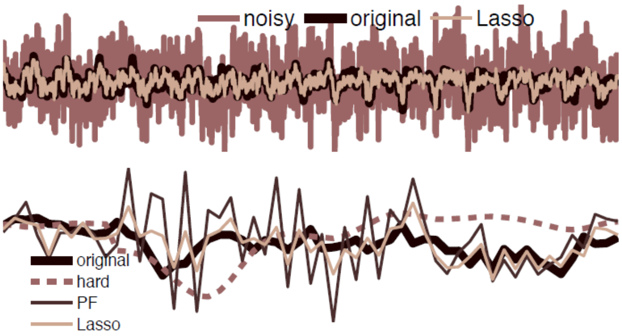

Fig. 59. Top: lasso-regularity-denoised example from ‘curves3’ image data, plotted wrt vectorised pixel index. Bottom: zoomed-in segment of top figure.

Figures 58 and 59 illustrate a typical example on the ‘curves3’ data. For comparison, in addition to the OLS, PF, and lasso regularity-based shrinkage methods, a non-adaptive hard thresholding was also implemented which simply shrunk all coefficients in the first two finest scale levels to zero (set all coefficients in $k = 1,2$ to zero). It can be seen that the hard shrinkage over smooths the data. The optimal variance parameter for the PF method was so small that it gave almost identical results to the OLS method. The PF and OLS did better than hard shrinkage but, because the Hurst estimation is not as good as the lasso-based method, they under- and over-shrunk various parts of the images. As suggested by Table 33 and confirmed by the error histogram in Fig. 60, this lead to many more large errors than the lasso. Some of these artefacts are clearly visible in Figs 58 and 59.

Data	OLS	PF	Lasso	Hard
chequers	0.200 (0.211)	0.200 (0.211)	**0.163 (0.151)**	0.373 (0.329)
curves3	0.169 (0.175)	0.169 (0.175)	**0.135 (0.118)**	0.354 (0.344)
curves4	0.190 (0.193)	0.190 (0.193)	**0.154 (0.137)**	0.523 (0.467)
curves5	0.189 (0.185)	0.189 (0.185)	**0.153 (0.135)**	0.356 (0.305)

Table 33. Mean absolute error (error standard deviation) of the regularity-based denoisers: OLS, PF, lasso, and hard thresholding.

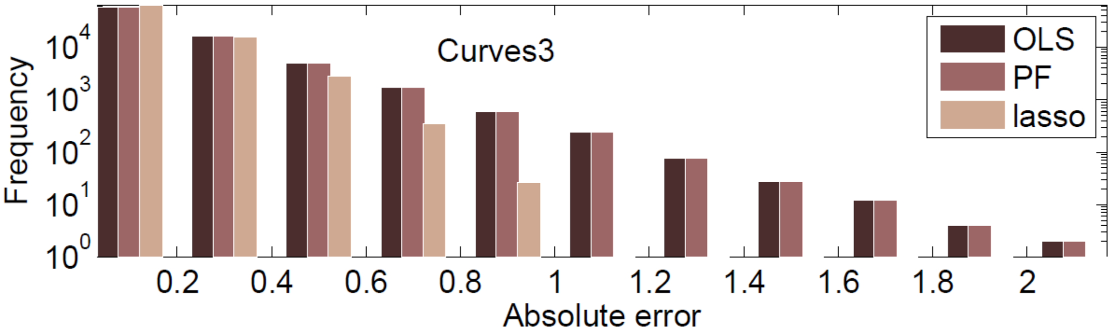

Fig. 60. Mean absolute error histograms,‘curves3’, of the regularity-based denoising methods, OLS, PF, and the lasso.

We have introduced a new spatially regularised Hurst estimation method which exploits situations where regularity is constant over unknown regions in an image. We have shown that, by framing the problem in terms of the generalised lasso, the solution can be obtained with powerful methodology from computational statistics. We have furthermore translated this idea to image reconstruction to arrive at a regularity-based denoising method which adapts to piecewise varying regularity. Much further work is possible: higher order differencers; anisotropic estimations and subsequent filtering; combination with data-driven methods; adaptive basis selection; establish and compare theoretical results on convergence and conditions thereof (cf. other local regularity-based denoising), empirical mode decomposition.

2.9 Radar signal processing: [MacNafIsa14]; [NafMacIsa14]

2.9.1 Envelope detector with denoising to improve the detection probability

In [NafMacIsa14] we proposed the use of soft-thresholding denoising to improve the signal-to-noise ratio in a simple envelope detector followed by a decision threshold block. Simulation results for a received useful signal perturbed by additive white Gaussian noise (AWGN) using the denoising systems, indicate that the probability of detection increases at the same probability of false alarm.

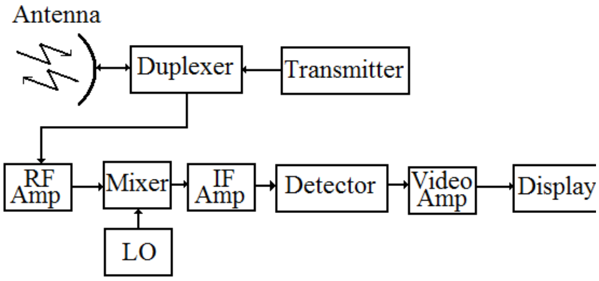

Fig.61 The architecture of a radar system.

The radar maximum detectable range R_{max} is determined by the radar equation as [EhaSasMor94], [Sko90]:

$$R_{\max}^4 = \frac{P_t G A_e \sigma_T}{(4\pi)^2 k T_0 B_n F_n (S_0/N_0)_{\min}}, \tag{120}$$

where P_t is the (peak) maximum transmit power, G the antenna gain, A_e the antenna effective aperture, σ_T the radar cross section of a target, k the Boltzmann constant, T_0 is the absolute temperature, B_n the receiver bandwidth, F_n the noise figure and $(S_0/N_0)_{\min}$ is the minimum intermediate frequency (IF) output signal-to-noise ratio (*SNR*) necessary for detection. A block scheme of the radar system is presented in Fig. 61. The minimum IF output SNR (*mIFoSNR*) is computed before the detector in Fig. 61. The factors P_t, G and A_e from (120) are determined by the radar system hardware. The increase of the detectable range requires the decreasing of the minimum IF SNR necessary for detection.

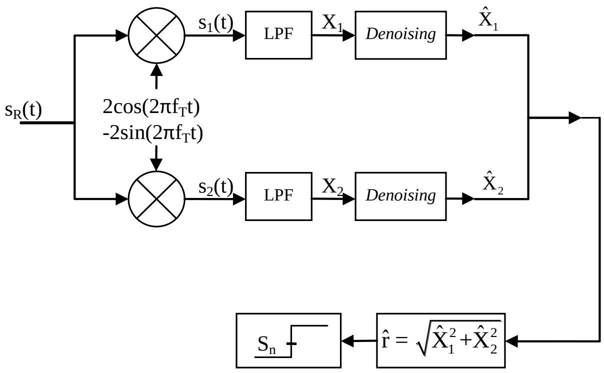

Fig. 62 The scheme of radar receiving system, using denoising systems and envelope detector.

The aim was to improve the IF SNR necessary in a simple envelope detector without supplementary phase errors. We refer to a simplified scheme of the radar receiver system that uses an envelope detector and a threshold decision. We propose to introduce denoising systems as seen in Fig. 62.

David Donoho introduced the term “denoising” for an additive white noise removing method which does not distort the useful component of the processed signal [DonJoh98]. His method, composed by three steps is based on the Discrete Wavelet Transform (DWT) [Mal99]. Starting from the input signal a_0, we obtain successively, the approximation sequences a_{-1}, …, a_{-m}, and the detail sequences d_{-1}, …, d_{-m}, at different resolutions. It is necessary that the length of the input signal a_0, (M) to be a power of two, for example $M = 2^J$. In this case, the maximal number of DWT decomposition levels is $m = J$.

The DWT of a deterministic signal is a sparse representation, containing a small number of large coefficients. The degree of sparsity depends on the selection of the features of the DWT: the mother wavelets and the number of decomposition levels. The DWT of a random noise signal is not sparse, the detail coefficients being small and uniformly distributed. Subsequently, the noise can be eliminated by thresholding the detail DWT coefficients (which is a nonlinear filtering).

Donoho proposed the two nonlinear filters having the input-output relations in Fig. 63, where s represents a threshold [DonJoh94], [Don95], [DonJohKerPic95]. Only the detail coefficients are filtered. One of the features of the denoising algorithm, denoted by L, indicates the number of decomposition levels where the soft-thresholding filter is not applied. Hence the soft-thresholding filter is applied on the detail coefficients belonging to the first $J–L+1$ decomposition levels of DWT. Ideally, L should be much smaller than J, but L should also be chosen in such a way that the useful component (if it is a bandlimited signal) is left unaffected.

We rephrase the denoising problem in terms of frequency analysis. Fig. 64 represents the subbands of the DWT for three decomposition levels ($M = 8$, $J = 3$, $L = 3$). The denoising system is presented in Fig. 65. We derive the statistical model of the signal $\hat{X}_i$.

We consider first noise only, $X_i = n_i$, a white Gaussian noise (WGN) with zero mean and variance N_0. In this case, the approximation (a_X) and detail (d_X) coefficients are zero mean WGN with variance N_0 as well. Hence, we suppose the detail coefficients, d_n, follow a Gaussian distribution law with zero mean and variance N_0 at each decomposition level l, with $l = 1,2,\ldots,J$, with the cumulative distribution function (CDF):

$$F_{d_n}(x) = \frac{1}{2}\left(1 + erf\,\frac{x}{\sqrt{2N_0}}\right), \tag{121}$$

where the error function is denoted by *erf*:

$$erf(x) = \frac{2}{\sqrt{\pi}}\int_0^x \exp\left(-t^2\right)dt\,. \tag{122}$$

The pdf of the approximation a_n and detail d_n coefficients is:

$$p_{a(d)}(x) = \frac{1}{\sqrt{2\pi N_0}}\exp(-\frac{x^2}{2N_0})\,. \tag{123}$$

Suppose that in Fig. 65 we have a soft thresholding filter having the input-output relation:

$$d_Y = \begin{cases} \operatorname{sgn}\{d_X\}(|d_X| - s), & \text{for } |d_X| > s \\ 0, & \text{elsewhere} \end{cases}. \tag{124}$$

The CDF of the detail coefficients at the output of the soft-thresholding filter is:

$$F_{d_Y}(y) = F_{d_X}(y-s)u(-y) + F_{d_X}(y+s)u(y)\,, \tag{125}$$

where u represents the unit step function.

The pdf of the detail wavelet coefficients, after thresholding, can be expressed now by differentiation in both members of (125):

$$p_{d_Y}(y) = p_{d_X}(y-s)u(-y) + (F_{d_X}(s) - F_{d_X}(-s))\delta(y) + p_{d_X}(y+s)u(y). \qquad (126)$$

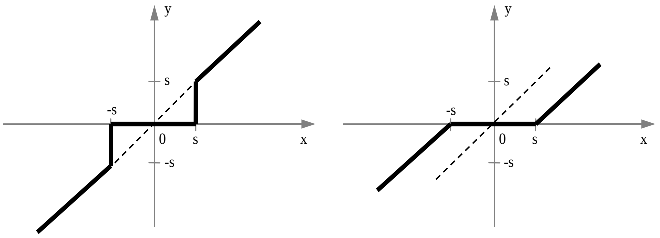

Fig. 63 Input-output characteristics of two non-linear filters which can be used in wavelet domain for denoising.

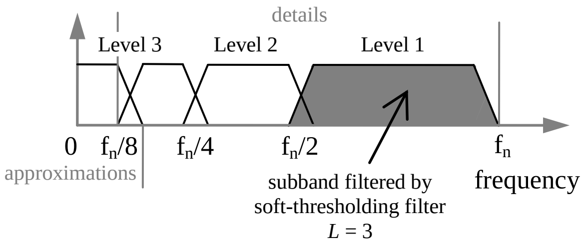

Fig. 64 The detail subband filtered by the soft-thresholding filter is the grey area. L=3 – three subbands are not filtered.

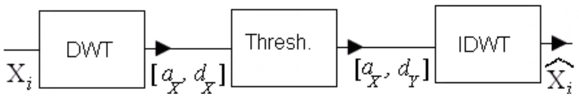

Fig. 65 The architecture of a denoising system.

So, the pdf of detail coefficients at the output of the soft-thresholding filter is composed by two branches of Gaussians which are symmetric around the ordinate (x = 0). The mean and the variance of the random variable d_Y are:

$$E\{d_Y\} = \int_{-\infty}^{\infty} y p_{d_Y}(y)\,dy = 0, \qquad (127)$$

$$\sigma_d^2 = s^2(1\text{-}F_{d_x}(s) + F_{d_x}(\text{-}s)) + 2N_0(1\text{-}F_{d_x}(s)\text{-}sp_{d_x}(s)). \qquad (128)$$

For high values of s, σ_d^2 is much smaller than N_0.

At the output of the soft-thresholding filter the approximation coefficients are identical with the approximation coefficients obtained after the DWT computation, a_X, concatenated with a sequence of detail wavelet coefficients d_Y having the pdf in (126).

Consider now the case of noiseless signal only $X_i = nc$ and suppose that nc is a low-pass bandlimited random signal with zero mean whose bandwidth is smaller than $f_n/2^Q$, where Q is a positive integer (see Fig. 64). Selecting an appropriate value for L, such that $Q < J - L + 1$, the noiseless component of the input signal will be perfectly reconstructed after denoising because its power spectral density is not affected by the filter.

Then, at any new iteration of the DWT (corresponding at the m^{th} decomposition level for example), the variance of the approximation (detail) coefficients of nc, denoted in the following by ${}_{nc}a(d)_{\mathrm{m}}$, doubles its value. Hence, the variance of the approximation (detail) coefficients of nc obtained after J decomposition levels can be expressed as:

$$\sigma^2_{a(d)_{{}_{nc}X_i}} = 2^J \sigma^2_{{}_{nc}a(d)_1}, \tag{129}$$

where we have denoted by $\sigma^2_{{}_{nc}a(d)_m}$ the variance of the approximation (detail) coefficients of *nc* at the m^{th} decomposition level.

Finally, we consider the case of noisy signal. Let us split the noiseless component in two parts: a low-pass bandlimited random signal with zero mean and bandwidth smaller than $f_n / 2^Q$, ${}^{bl}_{nc}X_i$ and a non-bandlimited random part ${}^{nbl}_{nc}X_i$, ${}_{nc}X_i = {}^{bl}_{nc}X_i + {}^{nbl}_{nc}X_i$, which are perturbed by a zero mean Gaussian random noise n_i.

Taking into account the linearity of DWT, the coefficients obtained at the output of the first block in Fig. 65 are:

$$\begin{aligned} a_{X_i} &= a_{{}_{nc}X_i} + a_{n_i}, \\ d_{X_i} &= {}_{ib}d_{{}_{nc}X_i} + {}_{ob}d_{{}_{nc}X_i} + n_i, \end{aligned} \tag{130}$$

where the approximation coefficients of the WGN n_i are denoted by a_{n_i}, the details of ${}^{nbl}_{nc}X_i$ by ${}_{ib}d_{{}_{nc}X_i}$ and the details of ${}^{bl}_{nc}X_i$ by ${}_{ob}d_{{}_{nc}X_i}$. The following approximation coefficients are obtained at the output of the second block in Fig. 65:

$$a_{Y_i} = a_{X_i}, \tag{131}$$

because the soft thresholding filter does not process the approximation coefficients.

The detail wavelet coefficients of the noise at the output of the second block in Fig. 65 have the pdf expressed in (126) with the mean in (127) and with the variance in (128). For the sake of simplicity, we consider in the following that these detail coefficients are modeled as a zero mean WGN with variance σ_d^2, $\hat{n}_i$. We will select for L a value smaller than $J - Q + 1$. This way, the soft thresholding filter will not affect the details of ${}^{bl}_{nc}X_i$.

The details of the non bandlimited noiseless component of the input signal, ${}_{ob}d_{{}_{nc}X_i}$ will be affected by the soft-thresholding filter, producing some distortions and the expression of the detail wavelet coefficients at the output of the soft thresholding filter will become:

$$d_{Y_i} = d_{{}_{nc}X_i} + d_{dist} + \hat{n}_i. \tag{132}$$

For input signals with bandlimited noiseless component, the second term in the right hand side disappears. Taking into account (129), it can be observed that the power of the first term of the right hand side of the first equation in (130) increases with the increasing of the number of decomposition levels of the DWT. The second term, a_{n_i}, represents the approximation coefficients of the noise component of the input signal and is a Gaussian random variable with zero mean and same variance, N_0, at any decomposition level. So, the weight of the power of the first term in the sum which represents the right hand side of the first equation in (130) increases with the increasing of the number of decomposition levels. In consequence, after a sufficient number of decomposition levels, the power of the signal which represents the second term in this sum becomes negligible in comparison with the power of the signal which represents the first term, and the first equation in (130) can be written in the equivalent form:

$$a_{Y_i} = a_{X_i} \approx a_{{}_{nc}X_i} + \hat{n}_i. \tag{133}$$

So, the approximation coefficients of the signal at the output of the second block in Fig. 65 represent the sum of the approximation coefficients of the noiseless component of the input signal and of the noise component $\hat{n}_i$.

Based on (133) and (132), we can view the concatenation of the coefficients a_{Y_i} and d_{Y_i}, denoted in the following by (a_{Yi}, d_{Yi}), as the DWT of the signal ${}_{nc}X_i + \mathit{distort} + \hat{n}_i$,

$$(a_{Y_i}, d_{Y_i}) = \mathrm{DWT}\{{}_{nc}X_i + distort + \hat{n}_i\}. \qquad (133')$$

Finally, the signal obtained at the output of the system in Fig. 65 can be expressed as:

$$\hat{X}_i = IDWT\{DWT\{{}_{nc}X_i + distort + \hat{n}_i\}\} = {}_{nc}X_i + distort + \hat{n}_i, \qquad (134)$$

because the DWT and the IDWT are inverse transforms.

Hence, at the output of the system in Fig. 65 we obtain a good approximation of the noiseless component of the input signal, ${}_{nc}X_i$, which is additively perturbed by small distortions and by the WGN $\hat{n}_i$ with zero mean and variance σ_d^2, many times smaller than the variance N_0 of noise component n_i of the signal X_i from the input of the system in Fig. 65. The input and output SNR of the system in Fig. 65 can be computed with the following equations:

$$\mathrm{SNR}_i = \frac{P_{{}_{nc}X_i}}{N_0}, \qquad (135)$$

$$\mathrm{SNR}_o = \frac{P_{{}_{nc}X_i}}{\sigma_d^2 + P_{distort}}, \qquad (136)$$

where we have denoted by $P_{{}_{nc}X_i}$ the power of the noiseless component of the input signal and by $P_{distort}$ the power of the distortion component. For input signals with bandlimited noiseless component, $P_{distort} = 0$.

The **envelope detector** has the structure in Fig. 62, where the denoising systems are considered as all pass systems ($\hat{X}_i = X_i, r = \hat{r} = \sqrt{X_1^2 + X_2^2}, i = 1,\ 2$ and $S_n = S$).

The signals X_1 and X_2 (in Fig. 62) could be seen as the real and imaginary parts of a complex signal X. The modulus of the signal X, denoted by r, represents the envelope of the input signal s_R. We will suppose in the following that $X_i = a_i + n_i$ where a_i the noiseless component is constant (the amplitude of the received sinusoid) and n_i the noise component is AWGN with zero mean and variance N_0 and i = 1, 2. Hence, the noiseless components are bandlimited.

In the case of noise only: $X_i = n_i$, we can establish the value of the detector threshold S which corresponds to a given probability of false alarm, P_{fa}. If this probability is constant for all the values of the SNR of s_R, then we are dealing with a Constant False Alarm Rate (CFAR) detector [Roh12]. In the case of noise only, the signal r is given by the absolute value of the complex noise n: $r = |n| = \sqrt{n_1^2 + n_2^2}$, which represents a random variable with Rayleigh distribution [Gal93-page 146, Eq. (1.789)], whose probability density function (pdf) is [Roh12]:

$$p_{|n|}(r) = \frac{r}{N_0}\exp\left(-\frac{r^2}{2N_0}\right), \quad \text{for } r \geq 0. \qquad (137)$$

For the threshold S, the probability of false alarm is [Roh12]:

$$P_{fa} = \int_S^{\infty} p_{|n|}(r)\,dr = -\int_S^{\infty} d\left(\exp\left(-\frac{r^2}{2N_0}\right)\right) = \exp\left(-\frac{S^2}{2N_0}\right). \qquad (138)$$

Based on (138) we can derive the expression of the detection threshold S:

$$-\frac{S^2}{2N_0} = \ln P_{fa} \Leftrightarrow S^2 = -2N_0 \ln P_{fa} \Rightarrow S = \sqrt{-2N_0 \ln P_{fa}}. \qquad (139)$$

To establish the value of the detection probability P_d, we will consider in the following the general case, where the useful signal is present as well (noisy signal). For $a_1 = a_2 = a$ and $a_1^2 + a_2^2 = A^2$, the expression of the signal r becomes:

$$r=\sqrt{X_1^2+X_2^2}=\sqrt{(a_1+n_1)^2+(a_2+n_2)^2}= \\ =\sqrt{A^2+|n|^2+2(a_1n_1+a_2n_2)}. \tag{140}$$

Taking into consideration the fact that the noiseless and noise components on both branches of the classical envelope detector in Fig. 2, a_i and n_i, are independent, the variance of the envelope becomes:

$$E\left\{r^2\right\}=E\left\{A^2+|n|^2+2(a_1n_1+a_2n_2)\right\}=E\left\{A^2\right\}+E\left\{|\mathrm{n}|^2\right\}+2a_1E\left\{n_1\right\}+2a_2E\left\{n_2\right\} \\ =E\left\{A^2\right\}+E\left\{|\mathrm{n}|^2\right\}\ , \tag{141}$$

where E denotes the statistical mean operator and the SNR at the input of the last block in Fig. 62 in case of classical envelope detector can be computed as:

$$SNR=10\log\frac{A^2}{2N_0}. \tag{142}$$

The detection probability, P_d, represents the area of the surface under the pdf of the noisy signal computed from S to infinity. No closed form exists for this integral which is called the Q function or the Marcum function, but it can be very accurately estimated by numerical methods [Gal93-page 150].

Envelope Detection with Denoising The architecture of the proposed system is presented in Fig. 62. We have used for the implementation of denoising the VisuShrink estimator: the soft-thresholding filter whose threshold is selected with the equation: $s=N_0\sqrt{2\ln M}$ and M is the length of the input sequences X_i, i = 1, 2, proposed in [DonJoh94].

As for the classical radar receiver, we have treated first the case of noise only, to choose the value of the decision threshold S_n, in accordance with the imposed probability of false alarm, P_{fa}. We deal once again with a complex noise whose real and imaginary parts are zero mean AWGN with variance N_0. The power (variance) of the random signals $\hat{X}_1^2$ and $\hat{X}_2^2$ is smaller now. Practically, the denoising systems in Fig. 62 transform the input WGN random variables with zero mean and variance N_0 into output WGN random variables with zero mean and variance σ_d^2, reducing the noise power.

Again, these signals represent the real and imaginary parts of a complex signal. Its absolute value is the output noise: $\hat{r}=|\hat{n}|=\sqrt{\hat{n}_1^2+\hat{n}_2^2}$, which has a Rayleigh distribution:

$$p_{|n|}(\hat{r})=\frac{\hat{r}}{\sigma_d}\exp\left(-\frac{\hat{r}^2}{2\sigma_d^2}\right),\quad \text{for } \hat{r}\geq 0\,, \tag{143}$$

because the signals $\hat{n}_i, i=1,2$ are WGN with zero mean and variance σ_d^2.

This has lead us to conclude that the threshold for the constant false alarm rate can be obtained using the same equation from the classical procedure, provided that the parameter σ_d of the distribution is estimated after denoising, for each sequence:

$$S_n=\sqrt{-2\sigma_d^2\ln P_{fa}}. \tag{144}$$

For the noisy signal (target present), the SNR becomes:

$$SNR=10\log\frac{A^2}{2\sigma_d^2}. \tag{145}$$

The pdf of the noisy signal is of Rice type:

$$p_{\hat{r}}(\hat{r}) = \frac{\hat{r}}{\sigma_d^2}\exp\left(-\frac{\hat{r}^2 + A^2}{2\sigma_d^2}\right) I_0\left(\frac{A\hat{r}}{\sigma_d^2}\right), \text{ for } \hat{r} \ge 0, \tag{146}$$

but now it is much narrower.

So, the separation between the pdfs of noise and noisy signal increases significantly in the case of denoising as opposed to the classical case. In consequence, the interval for the selection of the detection threshold is larger in the case of the proposed system.

Both cases were simulated in Matlab (with and without denoising systems) and we have compared their performance. We have used for the computation of the DWT the mother wavelets Symmlet 6 and the maximal number of decomposition levels.

The results of simulation are presented in Fig. 66. The threshold is computed when no target is present (noise only), corresponding to a value of the probability of false alarm of $P_{fa} = 10^{-4}$. In both cases, we took 1000 different realizations of noise, of length 1024 and N_0 = 1.

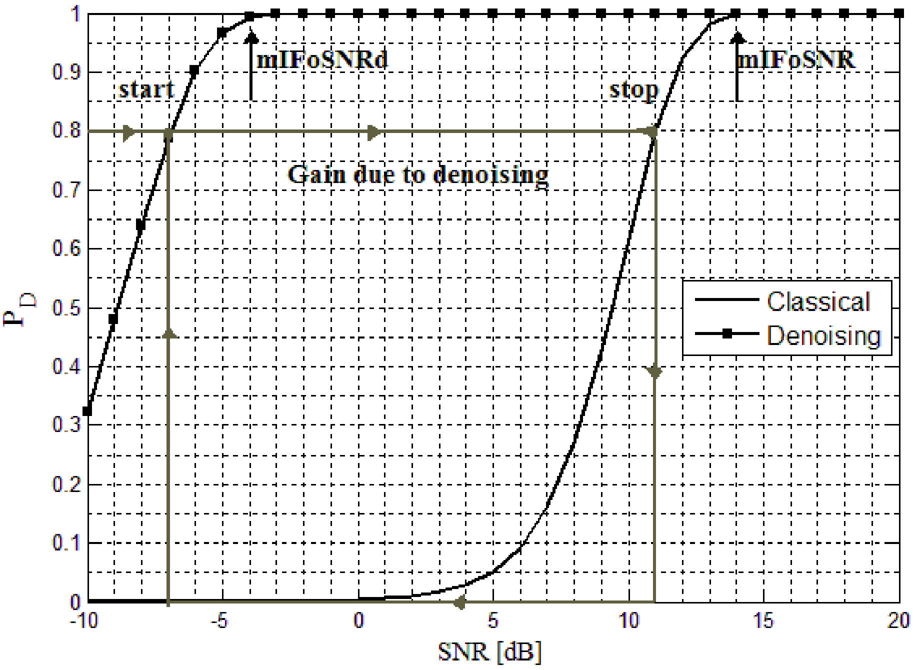

Fig. 66 A comparison of the detection probabilities for both cases.

For a false alarm rate of 10^{-4}, in the classical case, the threshold is $S = 4.29$. When using denoising, the new threshold is $S_n = \sqrt{-2\sigma_d^2 \ln P_{fa}} = 0.53$, obtained for the denoising threshold of $s = N_0\sqrt{2\ln(1024)} = 3.72$, where σ_d is estimated experimentally, at the value 0.12. In both cases, we verified that the false alarm rate is near 10^{-4} as we expect.

Next, we have considered the target + noise case (noisy input signals). SNR values are taken from -10 to 20 dB. For each case, we have taken 1000 realizations, each having a length of 1024, and we estimated the probability of detection. We have plotted the detection probability versus the input SNR in Fig. 66 for the case $P_{fa} = 10^{-4}$.

The SNR improvement brought by denoising versus the classical case is around 18 dB. For $P_d = 1$ we need in the classical case a value *mIFoSNR* = 14 dB.

Taking into account the SNR enhancement, the corresponding value of *mIFoSNRd* for the proposed method is -4 dB. Indeed, the corresponding value of the detection probability is 1 on the new probability detection curve.

The aim in [NafMacIsa14] is to propose the use of denoising methods for the envelope detection of radar signals, which could be of interest in CW Radar systems.

We have derived the performance of this system analytically and by simulation, verifying other equations established as well, and we have compared its performance by simulation with the classical case. Fig. 66 presents the performance of both systems. Denoting by $R_{\max}$ the radar maximum detectable range of the system equipped with the classical envelope detector and by ${}_{d}R_{\max}$ the radar maximum detectable range of the system equipped with the proposed system and applying (120), we obtain according to Fig. 66: ${}_{d}R_{\max} = 2.82R_{\max}$, which represents an improvement of the radar performance.

2.9.2 Building the range-Doppler map for multiple automotive radar targets

The selected waveform for automotive radar needs to be able to satisfy functional requirements such as the ability to resolve multiple targets in range and velocity simultaneously and unambiguously while keeping the measurement cycle time and transmitted power as low as possible. We analyze the main waveforms used in automotive radars and present a method for constructing the range-Doppler map [MacNafIsa14]. Simulations are performed using the rapid chirps waveform.

The technical challenge in automotive radar research and development is the simultaneous measurement of target range, radial velocity and azimuth angle. This must be done unambiguously for multiple targets inside a measurement cycle. The waveform design influences the fulfillment of these requirements. If the radars commonly seen in the defense industry are generally pulsed systems, the automotive sensors often use Frequency Modulated Continuous Waveform (FMCW) technology. This makes the radars smaller, cheaper to manufacture and use less power, the compromise being a much smaller distance which can be covered.

The objective in [MacNafIsa14] is to analyze some waveforms used in FMCW radars and to build the range-Doppler map by processing the simulated received radar waveform. This can be achieved by making use of different strategies and tools, depending on the chosen waveform. The main types of waveforms employed in automotive radars on 24 and 77-GHz are presented with their advantages and drawbacks. We focused on the rapid chirp waveform which is the latest development in the field. The theoretical considerations are validated by simulations which illustrate the capability of this waveform to resolve multiple targets simultaneously and unambiguously while keeping a low measurement cycle.

Waveforms Used in FMCW Automotive Radars

The requirements of automotive radars can be fulfilled by an appropriately chosen waveform. In general, this is a continuously transmitted modulated sinusoidal signal of instantaneous frequency f_T. The received echo signals are down-converted directly into the baseband by the instantaneous transmit frequency. There is a difference between the received frequency f_R and the transmitted frequency f_T which is called the beat frequency, f_B:

$$f_B = f_R - f_T. \tag{147}$$

The beat frequency is influenced by the propagation delay τ and the Doppler frequency f_D respectively. The propagation delay τ is related to the target range *R:*

$$\tau = 2\frac{R}{c}. \tag{148}$$

The radial velocity v_R determines the Doppler frequency:

$$f_D = -\frac{2}{\lambda} v_R. \tag{149}$$

If a moving target is observed, the beat frequency depends simultaneously on both the propagation delay and the Doppler frequency.

After being down-converted into baseband, the received signal is sampled and the beat frequency is measured by applying an FFT to the complex-valued vector. The challenge is how to identify the contributions of the range and radial velocity to the beat frequency.

The simplest continuous waveform which can be used in automotive radars is a non-modulated sine wave. It can measure the Doppler frequency precisely but has poor range measurement capabilities, because, in this case, the beat frequency is in fact equal to the Doppler frequency [GinMaiPat12]. The phase of the baseband signal is proportional to the range.

The next step taken in order to ensure a better range measurement capability is to consider the linear frequency modulation (LFM). The most important parameters in FMCW radars using this waveform are the carrier frequency f_C, the sweep bandwidth B_{sw} and the chirp duration T_{CPI}. The instantaneous frequency of the transmitted signal at time t is given by:

$$f(t) = f_C \pm \frac{B_{sw}}{T_{CPI}} t. \tag{150}$$

The sign of the slope indicates an up-chirp or down-chirp signal respectively.

In case of a moving target, the beat frequency of a single chirp contains two components, one owing to the target range and another to the Doppler frequency [GinMaiPat12]:

$$f_B = -\frac{2}{\lambda} v_R \mp \frac{B_{sw}}{T_{CPI}} \frac{2}{c} R = f_D \pm f_\tau. \tag{151}$$

This means that in a single chirp signal there will always be an ambiguity when attempting to measure range and radial velocity. Therefore, an up- and down-chirp transmitted as a concatenated sequence is necessary, as presented in Fig. 67.

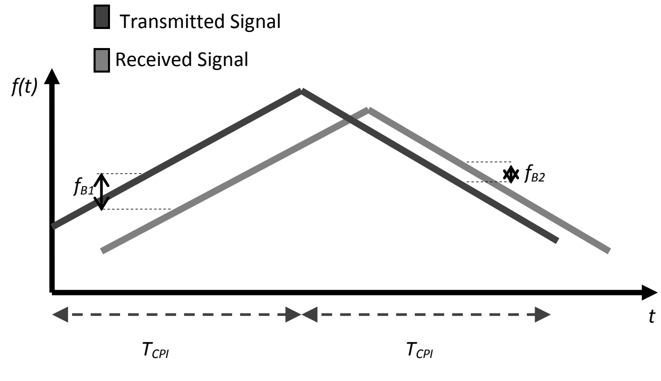

Fig. 67 Up- and down-chirp LFM waveform.

There are two different beat frequencies measured separately by performing two FFTs on both chirps, yielding two independent linear equations of the form presented in (151), with two unknowns, the radial velocity and target range. In a single target situation, the solving of this system means the calculation of an intersection point between two lines in the range-radial velocity plane.

But, in a situation with two targets, each of them will have a pair of beat frequencies associated with the up- and down-chirps. This means that there will be a total of four intersection points in the range-radial velocity plane, resulting in two additional ghost-targets. The more targets we have in the scenario, the more ghost targets will appear considering this type of waveform. In order to resolve such ambiguities, the transmit signal can be extended by two additional up- and down-chirp signals [FolRohLub05] [PouFegSch08] with different bandwidth. By using this variant, the range-Doppler ambiguities are eliminated even for multiple targets, but the measurement time is extended, which can be a disadvantage.

The frequency shift keying (FSK) waveform, on the other hand, is capable of resolving multiple targets with different ranges and radial velocities, but cannot resolve stationary targets with different ranges which will be detected on the same spectral line in the Doppler spectrum. This means the pure FSK has no range resolution capability [GinMaiPat12] [Roh10] (see Fig. 68).

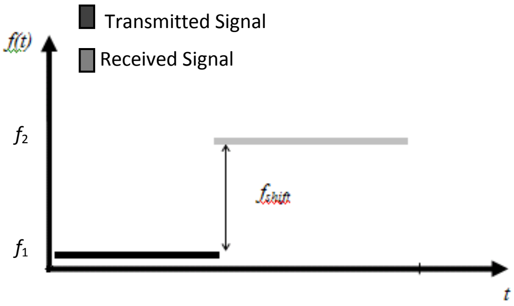

Fig. 68 FSK waveform.

However, a combination of LFM and FSK, called MFSK [RohMei01] achieves almost perfectly the performance requirements discussed so far. This waveform is presented in Fig. 69.

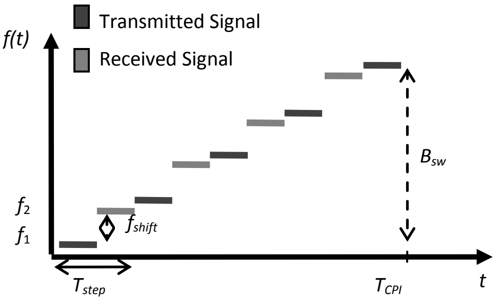

Fig. 69 MFSK waveform.

The MFSK consists of two stepwise linearly modulated signals with a frequency shift between them. They are transmitted in an intertwined way. The frequency difference (beat frequency) obtained from the received signal contains information about range and velocity. The phase shift between the two signals measured at the beat frequency also depends on range and velocity. Thus, a linear system of two equations can be solved for finding the two parameters of interest unambiguously even in multiple target environments [GinMaiPat12]:

$$f_B = -\frac{2}{\lambda} v_R - \frac{2B_{sw}}{cT_{CPI}} R, \tag{152a}$$

$$\Delta\phi = 2\pi\left(T_{step}\frac{2}{\lambda}v_R - f_{shift}\frac{2}{c}R\right). \tag{152b}$$

However, there is a concern in the fact that the phase measurement needs a high signal-to-noise ratio (SNR) for high accuracy.

The next improvement is a frequency modulated waveform composed of multiple chirps of very short duration. This waveform is analyzed.

The Rapid Chirps Waveform. This waveform consists of a sequence of chirps which have a very short duration T_{chirp}. The target range and velocity will be estimated by two independent frequency measurements, eliminating the need of phase estimation [Roh14]. This brings a higher accuracy and system performance at the expense of a greater computation complexity. The rapid chirps waveform is presented in Fig. 70.

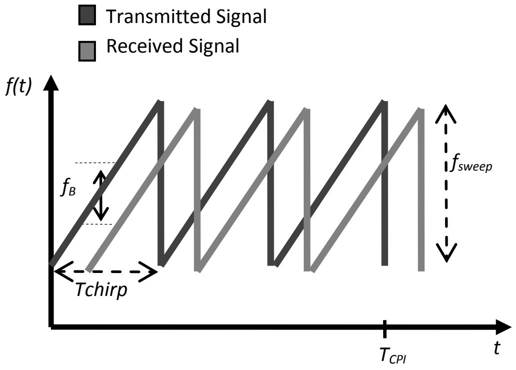

Fig. 70 Rapid chirps waveform.

If the transmitted signal, denoted by $s(t)$, is scattered back by P targets, we receive the signals $r_p(t)$, $p = 1,2,\ldots,P$. The signal received by the antenna has the expression:

$$r(t) = \sum_{p=1}^{P} r_p(t). \tag{153}$$

Assuming there is no noise affecting the received signal, and taking into account that the chirp is expressed as a frequency modulated signal with instantaneous phase φ_i and duration T_{chirp}, the received signal has the form:

$$r(t) = \sum_{p=1}^{P} A_p \sum_{m=0}^{M-1} \cos\varphi_i\left(t - mT_{chirp} - \tau_p\right)\exp\left(j2\pi v_p t\right). \tag{154}$$

where A_p denotes the amplitude corresponding to the signal reflected from target p, M is the number of chirps in the sequence, τ_p and v_p are the delay corresponding to the range and the Doppler shift respectively.

The frequency down conversion is made for both in phase and quadrature components of the received signal. The result of the down conversion is low-pass filtered, and the resulting components are added to obtain the beat signal, expressed as:

$$b(t) = b_{If}(t) + jb_{Qf}(t) = \sum_{m=0}^{M-1}\sum_{p=1}^{P} A_p \exp\left(j\varphi_{bmp}\right), \tag{155}$$

where

$$\varphi_{bmp} = \varphi_i\left(t - mT_{chirp}\right) - \varphi_i\left(t - mT_{chirp} - \tau_p\right) + 2\pi v_p t. \tag{156}$$

In the case of a chirp, the modulator signal is linear therefore the instantaneous phase has the expression:

$$\varphi_i(t) = \omega_C t + 2\pi k_f \alpha \frac{t^2}{2}, \tag{157}$$

where ω_C is the carrier angular pulsation, k_f is the frequency deviation and α is the modulator signal amplitude.

By substituting (157) into (156) and performing some calculations, we arrive at the following equation for the instantaneous phase of the received beat signal:

$$\varphi_{bmp}(t) = \varphi_{0mp} + 2\pi k_f \alpha \tau_p t + 2\pi v_p t, \tag{158}$$

where φ_{0mp} is a constant term that does not depend on the time.

The instantaneous frequency of the beat signal is obtained by taking the first derivative with respect to time:

$$f_{bimp}(t) = k_f \alpha \tau_p + v_p. \tag{159}$$

The instantaneous frequency of the beat signal has two components. The first component is proportional to the delay τ_p and is used for range estimation. The second component is equal with the Doppler frequency v_p and is used for target velocity estimation. By analyzing Fig. 70, we can see that the angular coefficient of the instantaneous frequency of each chirp can be expressed in such a way that (159) becomes:

$$f_{bmp}(t) = f_{bmp} = \frac{f_{sweep}}{T_{chirp}} \tau_p + v_p = f_{Rp} + f_{Dp}. \tag{160}$$

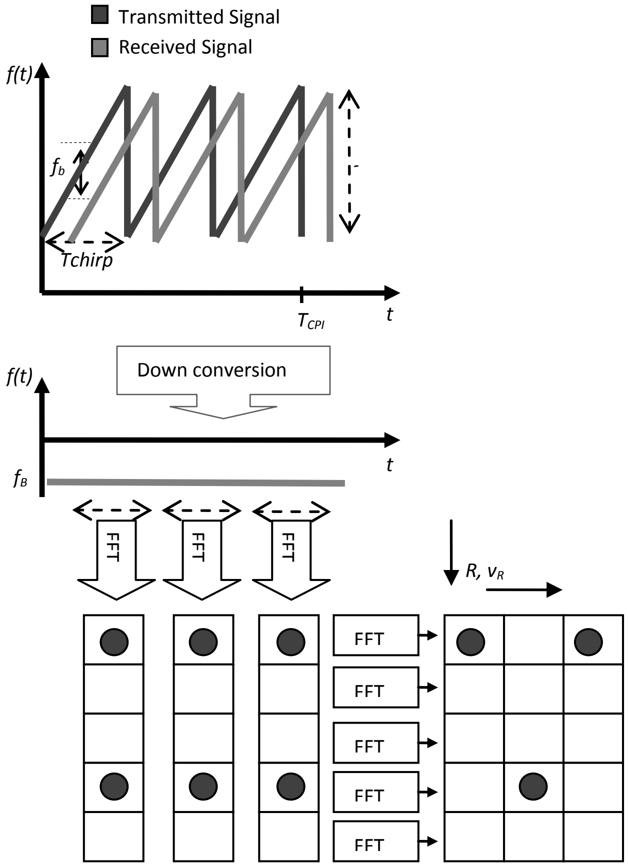

Fig. 71 Range and Doppler processing by two FFT operations.

In the case of the rapid chirps, we have $f_{Rp} >> f_{Dp}$, because T_{chirp} is very short, so $f_{bmp} \approx f_{Rp}$. After the sampling and analog to digital conversion of the signal $b(t)$ the digital range processing step is performed. The frequencies f_{Rp} are estimated by a first FFT computation round of the digital beat signals over each T_{chirp} duration. FFT is applied to each beat signal corresponding to a chirp, and the results are stored in the columns of a matrix, as shown in Fig. 71. The FFT magnitudes are proportional with the amplitudes of the targets (if at the considered frequency a target exists). The peaks in each FFT will correspond to the target ranges. The FFT phases in each column of the matrix have the values $\varphi_{0p} + 2\pi f_{Dp} m T_{chirp}$, where $\varphi_{0p} = \omega_0 \tau_p \text{-} \pi k_f \alpha \tau_p^2$ can be considered as constant for each target on the short duration T_{CPI} and m indexes the chirps. The target velocities, proportional with f_{Dp}, can be estimated now in the digital Doppler processing step, by a second FFT computation round. This second

FFT is applied on each row of the previous matrix taking into account the dependency of the phase of the complex numbers already mentioned on m. The resulting peaks will be placed at the Doppler frequencies f_{Dp}. A new matrix is obtained, which has peak values at the range and Doppler frequency of each target.

By performing windowed FFTs, we can also reduce unwanted effects such as a loss of information at some frequency components not visible due to the finite FFT frequency resolution.

Experimental Results. The algorithm described above was implemented in MATLAB and tested in a multiple target simulated environment. Some “worst case scenarios” such as targets with the same velocity or range were introduced to test the ability to determine their parameters unambiguously. We considered a carrier frequency of 24 GHz and a sweep bandwidth of 150 MHz. The maximum detectable range is R_{max} = 200 m and the maximum detectable radial velocity is v_{rmax} = 250 km/h. The transmitted signal consists of M = 256 chirps. Both FFTs are done on $NFFT$ = 2048 points. We consider three simulation scenarios: without and with noise (speckle and AWGN) in the received signal. In the first scenario, we consider that the received signal is not affected by noise. We take a number of P = 9 targets with the following range and radial velocity parameters:

$$R_p = [10 \quad 20 \quad 40 \quad 50 \quad 65 \quad 65 \quad 70 \quad 80 \quad 100] \ [\mathrm{m}]$$

$$v_{rp} = [30 \quad 30 \quad 45 \quad 55 \quad 60 \quad 120 \quad 20 \quad 10 \quad 75] \ [\mathrm{km/h}].$$

After down conversion, the in-phase and quadrature components of the beat signal corresponding to the 256th chirp are shown in Fig. 72. The signals are a sum of 9 sine waves with different beat frequencies. There is a continuous phase shift from one beat signal to the next which is proportional to the Doppler frequency. This feature will be exploited later on to find the radial velocity of the targets inside a range gate.

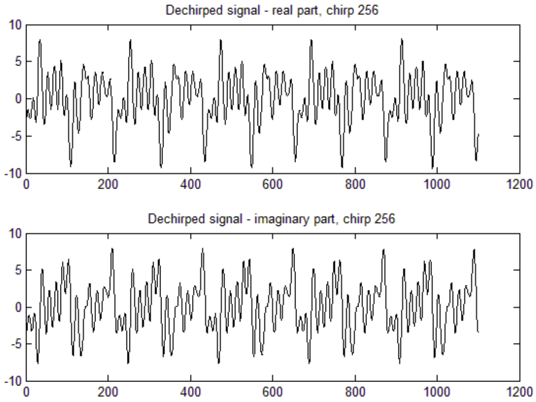

Fig. 72. Demodulated chirp signal components.

After combining the two components to form the complex signal, we look to find the target ranges. As stated before, an FFT is performed on each of the M chirps. The result of the FFT on the 256th chirp is shown in Fig. 73. We only have 8 peaks because there are two targets with the same range. Because the range component f_{Rp} is much larger than the Doppler frequency f_{Dp}, the two targets appear to have the same beat frequency and cannot be resolved at this stage.

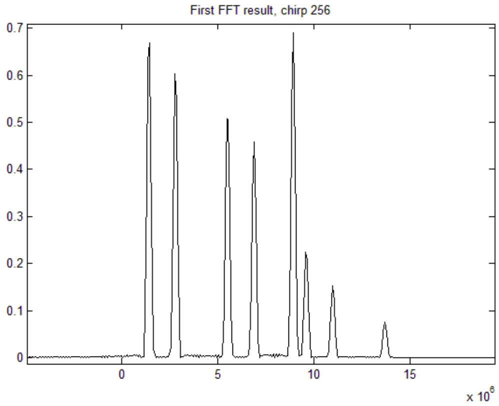

Fig. 73. Result of the first FFT computation.

At this point we have a matrix containing *M* columns and *NFFT* rows. On the lines of this matrix we perform the second FFT. This will separate the targets in Doppler frequency, so the targets with identical range can be unambiguously resolved. The two targets with identical radial velocities ($v_{r1} = v_{r2} = 30$ km/h) have already been resolved by the first spectral analysis. In Fig. 74 we have shown the result obtained for the range gate corresponding to the two targets with the same range ($R_1 = R_2 = 65$ m), but different radial velocities. It can be seen that they are resolved at this point in an unambiguous way.

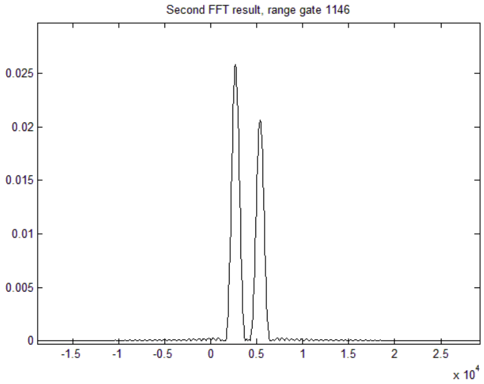

Fig. 74. Result of the second FFT computation.

The range-Doppler map will have *NFFT* x *NFFT* elements. After converting the axes to show the measures of interest, the result can be viewed in Fig. 75.

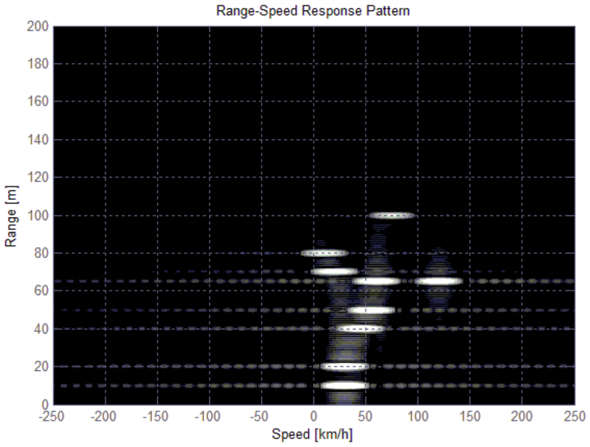

Fig. 75. Range-Doppler map for 9 targets (without noise).

It can be seen that all 9 targets are visible and detectable by a suitable thresholding performed in the amplitude domain. The artifacts which can be observed are due to the finite number of FFT points. A Hamming window was used in both FFT operations. For the first FFT, the window size is equal to the length of the down converted beat signal in T_{chirp}, while for the second FFT, the window length is equal to the number of chirps, M.

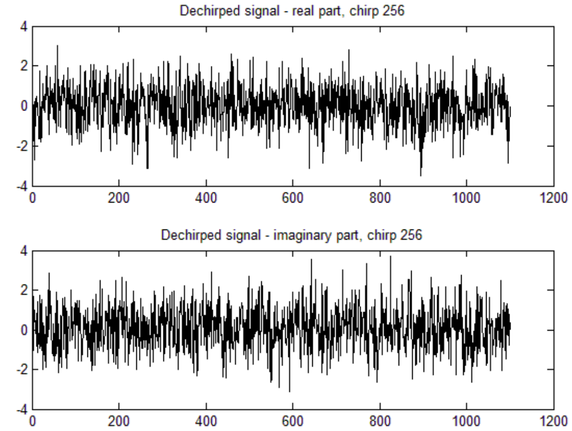

Fig. 76. Demodulated chirp signal components, affected by noise.

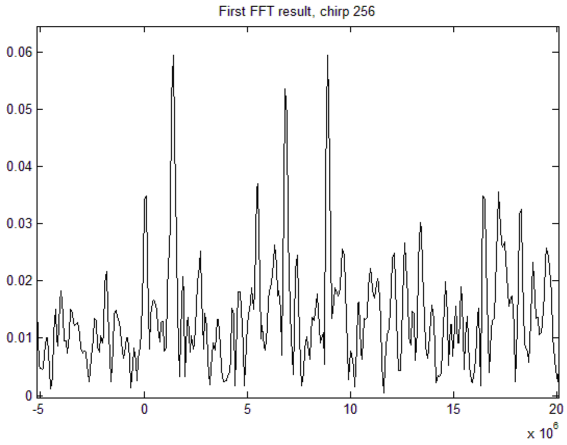

Fig. 77. Result of the first FFT computation on the noisy beat signal.

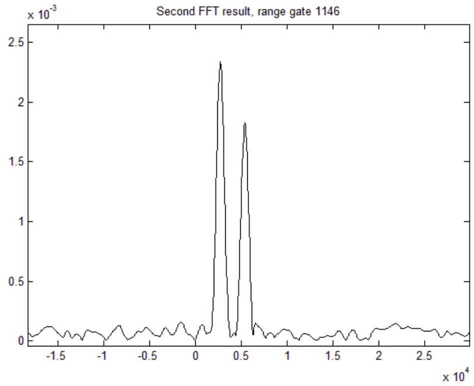

Fig. 78. Result of the second FFT computation on the noisy beat signal.

In the second scenario we consider speckle noise $s_p(t)$, which affects each signal reflected by a target, and receiver thermal noise, $w(t)$. The received signal is modeled as [HlaEde92]:

$$r(t) = \sum_{p=1}^{P} s_p(t) r_p(t) + w(t). \tag{161}$$

The Rayleigh-distributed speckle noise was obtained from two independent Gaussian distributions with zero mean and unitary variance. The receiver thermal noise is a Gaussian complex sequence of zero mean and unitary variance. The global Signal-to-Noise ratio at the receiver is -10 dB.

In the third scenario, we have nine targets affected by additive Gaussian white noise (AWGN), and for each target the SNR ranges from -15 to 25 dB with a step of 5dB:

$$r(t) = \sum_{p=1}^{P} r_p(t) + w(t). \tag{162}$$

The in-phase and quadrature components of the beat signal corresponding to the 256th chirp are shown in Fig. 76. The result of the first FFT on the 256th chirp is shown in Fig. 77. It is clear, by comparing figures 73 and 77 that the peaks corresponding to the targets are much more difficult to identify, in the second experiment, because the amplitudes of the peaks are affected by the two types of noise.

Fig. 78 shows the result of the second FFT corresponding to the range gate which contains the two targets with identical ranges. It can be seen that the peaks proportional to the Doppler frequencies are easier to identify, meaning that the noise does not affect the radial velocity measurement as much as the range measurement.

Finally, the range-Doppler maps for the second and third experiments are shown in Fig. 79 and 80. We can see that the targets situated at a greater range are very difficult to detect from the noisy background.

The paper [MacNafIsa14] presents some waveforms for automotive radar signal processing, focusing on the rapid chirps and a method for digital range and Doppler processing based solely on FFT computations. Simulation results prove that it is able to resolve multiple targets unambiguously in range and radial velocity by applying a two-dimensional FFT.

Depending on the number of points in which the FFTs are computed, the presented method for range and Doppler processing can be faster than other methods such as phase estimation, which also has lower accuracy. Furthermore, today's digital signal processors which implement the FFT are produced on a large scale with reduced costs, making the rapid chirps a feasible solution as far as production costs are concerned.

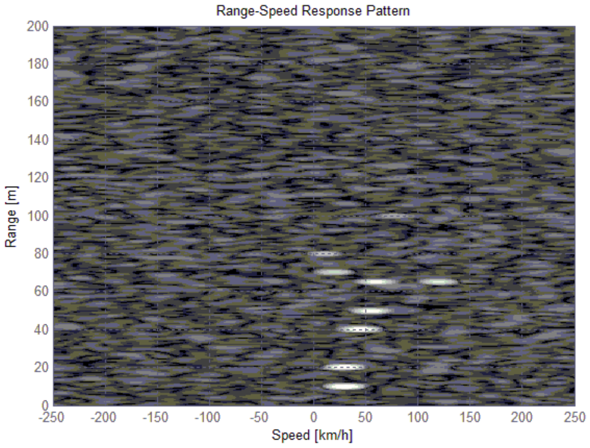

Fig. 79. Range-Doppler map for 9 targets – second experiment – received signal affected by speckle noise.

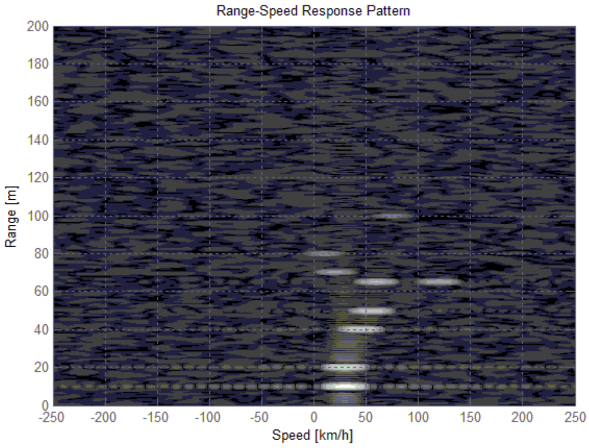

Fig. 80. Range-Doppler map for 9 targets – third experiment – received signal affected by AWGN noise.

2.10 Other topics

2.10.1 Biomedical signal processing: [ArvCosStoNafIsaToe11]; [ArvNafIsaCos11]

The collaboration with Dr. Beatrice Arvinti was focused on applying the wavelets theory for the ECGs and MCG signals transmission, problem that becomes nowadays actual due to the tremendous progress in communications. For the ECG signal, we have implemented denoising method, base line correction as well as compression. For the MCG signal, we have conceived a method for baseline wander reduction [ArvCosStoNafIsaToe11].

One of the major aspects of the ECG transmission is the source coding (compression). In [ISSCS2011], we propose a method for ECG compression using rejection of wavelet coefficients with the magnitude inferior to a given threshold in the DWT domain. This is equivalent with the filtering of wavelet coefficients with a hard thresholding filter. To evaluate the proposed method, we have proposed a quality factor $QF = CR^2 / PRD$ as the ratio of the square of the compression ratio and the distortion factor. For the evaluation of the distortions we used the Percent Root-Mean Square Difference (PRD),

$$PRD = \sqrt{\frac{\sum_{n=1}^{N}\left(x[n]-\hat{x}[n]\right)^2}{\sum_{n=1}^{N} x^2[n]}} \times 100\ [\%],$$

where x represents the input signal having N samples and $\hat{x}$ represents the reconstructed signal obtained after compression and reconstruction. The compression system is presented in Fig. 81. For the coding of the positions of the nulls wavelet coefficients we propose a run-length encoding (RLE) [IsaCubNaf02]. The best results are obtained using the Daubechies family of mother wavelets.

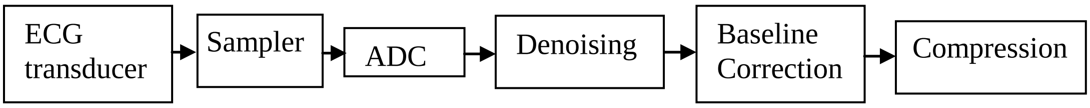

Fig. 81 The architecture of the acquisition chain.

In [ArvCosStoNafIsaToe11] we intended the development of a noninvasive method for removal of baseline drift of fetal magnetocardiograms (fMCG) based on the Stationary

Wavelet Transform (SWT). Usually, MCGs and ECGs are affected by biological noise due to the breathing or movement of the patient or interferences of the power line or other electronic devices. One of the results will be a drift of the baseline of the ECG or MCG, the opportunity of establishing a correct diagnosis being thus endangered. The method proposed involves computation of the SWT of the MCG; removal of detail coefficients, setting them to zero; back-conversion in the time domain of the new sequence, obtaining thus an estimation of the baseline drift; subtraction of the baseline estimation from the original signal, resulting in the removal of the baseline wander of the MCG. The estimation of the baseline drift is obtained through the low-pass filtering of the processed MCG (the detail coefficients resulted from the high-pass filter are eliminated). Fig.82 shows seven beats of the heart from the MCG signal before and after the baseline correction. We observe the method is very efficient, despite the noise.

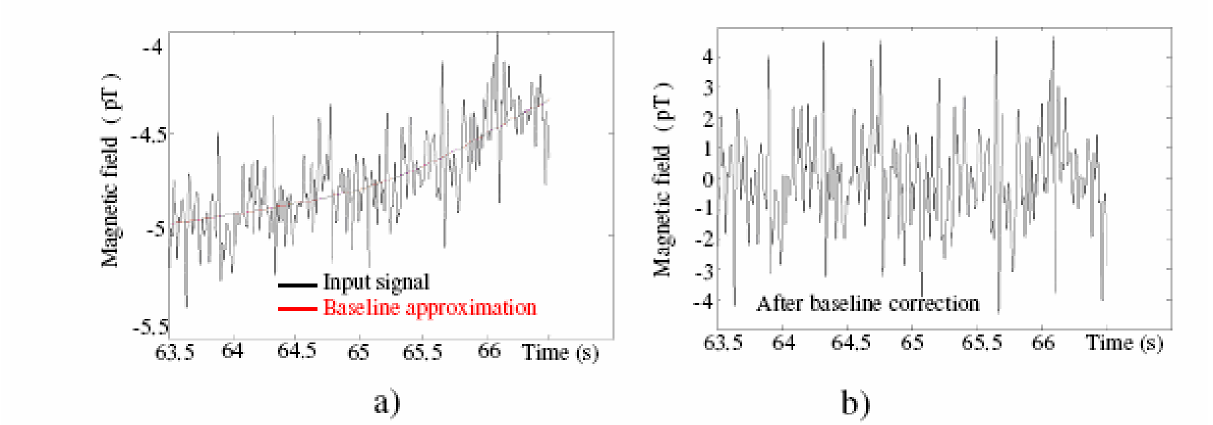

Fig.82 Seven beats of the recorded MCG before (left) and after the baseline correction (right).

2.10.2 PAPR reduction in telecommunications: [CutIsaNaf11a]; [CutIsaNaf11b]

Orthogonal Frequency Division-Multiplexing (OFDM) is one of the most popular technologies used in broadband wireless communication. One of the main practical issues of the OFDM is the Peak-to-Average Power Ratio (PAPR) of the transmitted signal. Large signal peaks requires the power amplifiers (PA) to support wide linear dynamic range. Higher signal level causes non-linear distortions leading to an inefficient operation of PA causing intermodulation products resulting unwanted out-of-band power.

In [CutIsaNaf11a] we proposed a PAPR reduction technique composed by a multiple symbol representations step followed by a signal clipping operation. This new PAPR reduction method combines the advantages of linearity from the first step with the reduced computation complexity of the second step, providing a better PAPR reduction with an insignificant bit error rate (BER) degradation.

In [CutIsaNaf11b] we proposed a hybrid PAPR reduction technique obtained by serialization of sequential tone reservation method and signal clipping method. This combines the advantages of linearity from the first step with the reduced computation complexity of the second step, providing a better PAPR reduction without any bit error rate (BER) degradation.

2.10.3 Riesz bases: [IsaIsaNaf11]

In [IsaIsaNaf11], we present a new method for the generation of Riesz bases with the aid of low-pass filters. The Riesz bases obtained can be used for the implementation of sampling systems for non-bandlimited signals. Each continuous in time low-pass filter impulse response generates a Riesz basis which corresponds to a Hilbert subspace of the space of finite energy signals.

2.11 Development and future work

My intention is to carry out academic and research activities in the field of signal and image processing, especially in statistical signal processing as well as estimation and detection. Statistical signal processing treats signals as stochastic processes, dealing with their statistical properties (mean, covariance, etc.). Signals are modeled as consisting of both deterministic and stochastic components. For example we consider a simple case, where the deterministic signal is affected by noise which can be often modeled as additive white Gaussian noise (AWGN). Even the deterministic component of the signal has some parameters which are unknown: for example the time when the signal begins.

Thus communications is based on stochastic signals, i.e. at least one signal parameter is random. Processing these signals is very important, and it completes the field of deterministic signal processing. In other words, information-bearing signals are random and also the noise affecting them is random.

For instance, in radiolocation the Neyman-Pearson detection is applied which is a classical strategy in the Statistical Signal Processing. On the other hand, when the useful signal is stochastic, having known statistical parameters, the Bayesian strategy is applied.

The detection process is based on one or many parameters which have to be estimated. Estimation is also an important problem, based on the Cramer-Rao theorem, the maximum-likelihood estimation, MLE, the minimum mean square error MMSE method, the method of moments etc.

The statistical performance of the estimators and detectors are evaluated always by simulations. Applications are: watermarking, denoising, texture classification, Hurst exponent estimation, segmentation, radar signal processing and so on. These can constitute both research projects as well as material for courses taught at the M.Sc. curriculum.

Consequently, my **teaching objectives** are the following:

1. Develop a teaching material for M.Sc. and Ph.D. students on statistical signal processing methods, including new trends worldwide, targeting the treatment of complex signals, complex statistical distributions and their use in signal processing, complex wavelet transforms, with particular emphasis on computer simulation.

2. After testing the efficiency of the material from point 1, I will develop a teaching material that may be published by a prestigious international publisher. I consider adopting the methods given by Vetterli and Goyal and others, and using my own research results in watermarking, texture classification, signal processing for automotive radar and tracking.

My **research objectives** are determined both by my previous work at UPT and LAPS laboratory, as well as the collaboration with researchers from abroad. The research activities developed in the framework of grants and contracts have also helped me train in the fields of statistical signal processing, complex signal processing, complex wavelet transforms, radar signal processing.

The main research activities can be done in collaboration with students, in connection mainly with the needs of the local and European industry and research centres. I do not exclude international cooperation with research centres and universities from outside the Europe. I have some research experience which comes from the cooperation with Prof.

Yannick Berthoumieu (ENSEIRB Bordeaux, France), Senior Lecturer James Nelson (Univ. College London UK), Prof. Hermann Rohling (TUHH, Germany) and contacts with: Prof. Deepa Kundur (Univ. of Toronto, Canada), Prof. Mauro Barni (Univ. of Siena, Italia), Prof. Tulay Adali (Univ. of Maryland, USA), and Prof. Ivan Selesnick (Polytechnic Institut of New York, USA).

I will most likely pursue the **following research themes**:

1. The continuation of the **image watermarking** research already established at Timisoara, developed in the framework of PhD thesis, in the wavelet transform domain, based on the papers of Prof. Selesnick, regarding the wavelet coefficient statistics and on our own research here in Timisoara. The watermark insertion in the phase of complex wavelet coefficients could be of major interest. I believe that the resulting research can be published in an ISI journal.

2. The continuation of the research made in cooperation with LAPS Bordeaux laboratory, in the framework of the bilateral grant Brancusi Romania-France „Classification de textures fondée sur la théorie des ondelettes hyper-analytiques et les copules” for **texture classification**, also in the framework of a PhD thesis. A first paper published by me treats the „distance” between two textures using Kullback-Leibler divergence. But I consider that there is a lot of work to do in this direction, possibly by simplifying the measurement on the „geodesic distance” between two probability distributions, introduced by Verdoolaege, to allow an easier way to compute this relationship (metric). On the basis of introducing a suitable measurement of the distance between two textures, I hope to contribute to the development of a mechanism for automatic image search in a database, as suggested by Do and Vetterli. The research results may be published in an ISI journal.

3. I will continue the research on the **complex wavelet transform** domain. I intend to cooperate with the team of prof. Tulay Adali and the team from LAPS to work for complex signal processing methods to be applied in telecommunications, image processing and biomedical signal processing. I have to mention here that I already went through a documentary research phase and I was able to make a correction to a calculation in an IEEE publication related to the complex distribution. These research can serve as a subject for a PhD thesis.

4. The research carried out in the framework of the European FP7 Grant ARTRAC, on **radar signal processing** for road safety has already led to some published results. This makes me believe that the application of wavelet transform and signal denoising after Donoho and Isar can significantly increase the probability of detection of a moving target while maintaining the required probability of false alarm (CFAR). Some results on the separation and tracking trajectories were obtained; extended Kalman filtering can be thus applied for this problem. These are two possible PhD research themes with a high applicability.

5. We have investigated the problem of **estimating the regularity of an anisotropic image**. In such images, for different directions, we obtain different regularity measure. It is important to separate preferential directions in the image. This can be done using a complex wavelet transform. Then on each direction, we estimate the degree of regularity (smoothness) through the Hurst exponent. We have already written two papers on the subject, one uses the Hyperanalytic wavelet packets and estimates the Hurst on each direction using a technique existing in the literature. The other paper, published at ICIP 2014, improves Hurst

(regularity) estimation by using lasso, in the field of the DTCWT. This second paper is written together with Professor Alexandru Isar, in collaboration with Senior Lecturer James Nelson (Univ. College London UK). To further improve this estimation we can replace the DTCWT with the HWPT.
There is of course, the possibility of continuation of the collaboration by articles and a PhD thesis.

6. As a member of the Adelaida Mateescu research centre, I will try to attract research contracts to support the major research directions presented. In this respect, I can mention that we already have two ongoing contracts with the European Space Agency, ESA, both using image processing techniques (**segmentation, denoising**). To the extent that we can successfully solve the themes proposed, we foresee the possibility to participate in other European space programs, together with PhD students from UPT.

I believe that the plan is realistic, since I already have accumulated some experience through contracts and publications, evidence shown by the fact that I was nominated as a reviewer for IEEE Trans. Information Forensics & Security, IEEE Trans. Multimedia, IEEE Trans. Signal Processing, IEEE Trans. Image Processing, EURASIP Journal on Information Security, IET Information Security, Research Letters in Electronics, Elsevier, Journal of Systems and Software, Elsevier, Signal Processing, Elsevier, IET Radar, Sonar & Navigation, Physical Communication.

I will also mention that I have access to the latest documentation, both through the UPT library and its subscribption to IEEE Proceedings, as well as my own subscriptions, as a member of IEEE (IEEE Trans periodicals. Information Forensics & Security, IEEE Trans. Multimedia, IEEE Trans. Signal Processing, IEEE Trans. Image Processing, IEEE Trans. Pattern Analysis and Machine Intelligence).

3. References

3.1 Personal publications 2008-2014

2014

[IsaNaf14] Isar, A.; Nafornita, C., On the statistical decorrelation of the 2D discrete wavelet transform coefficients of a wide sense stationary bivariate random process Digital Signal Processing Volume: 24 Pages: 95-105 Published: 2014, DOI: 10.1016/j.dsp.2013.10.001

[NafIsaNel14] Nafornita, C., Isar, A., and Nelson, J. D. B., Regularised, semi-local Hurst estimation via generalised lasso and dual-tree complex wavelets" IEEE International Conference on Image Processing ICIP 2014, Paris, France

[NafIsa14] Corina Nafornita, Alexandru Isar, Wavelet Based Contrast Enhancement for Still Images, 11th International Symposium on Electronics and Telecommunications (ISETC), 2014, 14-15 Nov. 2014, Timisoara, Romania, pp. 265-268.

[MacNafIsa14] Adrian Macaveiu, Corina Nafornita, Alexandru Isar, Andrei Campeanu, Ioan Nafornita, A Method for Building the Range-Doppler Map for Multiple Automotive Radar Targets, 11th International Symposium on Electronics and Telecommunications (ISETC), 2014, 14-15 Nov. 2014, Timisoara, Romania, pp. 151-156

[NafMacIsa14] Corina NAFORNITA, Adrian MACAVEIU, Alexandru ISAR, Ioan NAFORNITA, Andrei CAMPEANU, Envelope Detector with Denoising to Improve the

Detection Probability, pp 59-64. May 29-31, 2014, Bucharest, 10th International Conference on Communications, COMMUNICATIONS 2014

2013

[NafIsa13] Corina Nafornita, Alexandru Isar, Estimating directional smoothness of images with the aid of the hyperanalytic wavelet packet transform, Signals, Circuits and Systems (ISSCS), 2013 International Symposium on , IEEE Xplore, Iasi, Romania, ISBN 978-1-4799-3193-4 , 1, 4

2012

[NafBerNafIsa12] Nafornita, C; Berthoumieu, Y; Nafornita, I; Isar, A, KULLBACK-LEIBLER DISTANCE BETWEEN COMPLEX GENERALIZED GAUSSIAN DISTRIBUTIONS, 2012 PROCEEDINGS OF THE 20TH EUROPEAN SIGNAL PROCESSING CONFERENCE (EUSIPCO), Bucharest, ISBN 978-1-4673-1068-0, ISSN 2076-1465, AUG 27-31, 2012, 5 pag., WOS:000310623800372 Citations

[NafIsa12] Nafornita, C; Isar, A, A Complete Second Order Statistical Analysis of the Hyperanalytic Wavelet Transform, 2012 10TH INTERNATIONAL SYMPOSIUM ON ELECTRONICS AND TELECOMMUNICATIONS, IEEE, Timisoara, ISBN 978-1-4673-1176-2, NOV 15-16, 2012, 4 pag., 10th International Symposium on Electronics and Telecommunications (ISETC), 2012, WOS:000318702700052

[NafIsaNaf12] Nafornita, C; Isar, A; Nafornita, I, The Hyperanalytic Wavelet Packets - A Solution to Increase the Directional Selectivity in Image Analysis, 2012 10TH INTERNATIONAL SYMPOSIUM ON ELECTRONICS AND TELECOMMUNICATIONS, IEEE, Timisoara, ISBN 978-1-4673-1176-2, NOV 15-16, 2012, 4 pag., 10th International Symposium on Electronics and Telecommunications (ISETC), 2012, WOS:000318702700053

[SchBerTurNafIsa12] Schutz, A; Berthoumieu, Y; Turcu, F; Nafornita, C; Isar, A, Barycentric Distribution Estimation For Texture Clustering Based On Information- Geometry Tools, 2012 10TH INTERNATIONAL SYMPOSIUM ON ELECTRONICS AND TELECOMMUNICATIONS, IEEE, Timisoara, ISBN 978-1-4673-1176-2, NOV 15-16, 2012, 4 pag., 10th International Symposium on Electronics and Telecommunications (ISETC), 2012, WOS:000318702700081

2011

[IsaFirNafMog11] Alexandru Isar, Ioana Firoiu, Corina Nafornita and Sorin Moga (2011). SONAR Images Denoising, Sonar Systems, N. Z. Kolev (Ed.), ISBN: 978-953-307-345-3, InTech, Available from: http://www.intechopen.com/articles/show/title/sonar-images-denoising

[NafIsa11] Corina Nafornita and Alexandru Isar (2011). Application of Discrete Wavelet Transform in Watermarking, Discrete Wavelet Transforms - Algorithms and Applications, Hannu Olkkonen (Ed.), ISBN: 978-953-307-482-5, InTech, Available from: http://www.intechopen.com/articles/show/title/application-of-discrete-wavelet-transform-in-watermarking

[FirNafIsaIsa11] Firoiu, I.; Nafornita, C.; Isar, D.; Isar, A.; Bayesian Hyperanalytic Denoising of SONAR Images, Geoscience and Remote Sensing Letters, IEEE ; 27 June 2011 online early access (DOI : 10.1109/LGRS.2011.2155617)

[NafIsaIsa11] Nafornita, C.; Isar, D.; Isar, A.; Searching the most appropriate mother wavelets for Bayesian denoising of sonar images in the Hyperanalytic Wavelet domain; Statistical Signal Processing Workshop (SSP), June 2011

[ArvCosStoNafIsaToe11] Arvinti-Costache, B.; Costache, M.; Stolz, R.; Nafornita, C.; Isar, A.; Toepfer, H.; A wavelet based baseline drift correction method for fetal magnetocardiograms, New Circuits and Systems Conference (NEWCAS), 2011 IEEE 9th International, 2011, pp. 109 - 112

[ArvNafIsaCos11] Arvinti, B.; Nafornita, C.; Alexandru, Isar; Costache, M.; ECG signal compression using wavelets. Preliminary results, 2011 10th International Symposium on Signals, Circuits and Systems (ISSCS), 2011 , pp. 1 - 4

[CutIsaNaf11a] Victor Cuteanu, Alexandru Isar, Corina Nafornita, PAPR Reduction of OFDM Signals Using Multiple Symbol Representations -Clipping Hybrid Scheme, SPAMEC 2011, Cluj-Napoca

[CutIsaNaf11b] Victor Cuteanu, Alexandru Isar, Corina Nafornita, PAPR Reduction of OFDM Signals using Sequential Tone Reservation -Clipping Hybrid Scheme , SPAMEC 2011, Cluj-Napoca

[IsaIsaNaf11] Dorina Isar, Alexandru Isar, Corina Nafornita, Building Riesz Bases with the Aid of Low-Pass Filters , SPAMEC 2011, Cluj-Napoca

2010

[FirNafBouIsa10] Ioana Firoiu, Corina Nafornita, Jean-Marc Boucher, Alexandru Isar, Searching Appropriate Mother Wavelets for Hyperanalytic Denoising, Advances in Electrical and Computer Engineering, Issue 4, 2010, ISSN: 1582-7445, ISI (pdf)

[FirNafIsaBouIsa10] Ioana Firoiu, Corina Nafornita, Dorina Isar, Jean-Marc Boucher, Alexandru Isar, An Asymptotic Statistical Analysis of the Hyperanalytic Wavelet Transform, 5th European Conference on Circuits and Systems for Communications (ECCSC’10), November 23-25, 2010, Belgrade, Serbia (pdf) (ppt)

[NafFirIsaBouIsa10a] Corina Nafornita, Ioana Firoiu, Dorina Isar, Jean-Marc Boucher, A. Isar, A Second Order Statistical Analysis of the Hyperanalytic Wavelet Transform, Proceedings of the 9th IEEE International Symposium of Electronics and Telecommunications, ISETC 2010, Timisoara, Romania, November 2010, pp. 311-314, ISBN: 978-1-4244-8458-4 (pdf) (ppt) **Link:** Original publication is available at: ieeexplore.ieee.org

[NafFirIsaBouIsa10b] Corina Nafornita, Ioana Firoiu, Dorina Isar, Jean-Marc Boucher, Alexandru Isar, "A Second Order Statistical Analysis of the 2D Discrete Wavelet Transform", Proceedings of IEEE International Conference Communications 2010, Bucuresti, Romania, June 10-12, ISBN: 978-1-4244-6363-3, pp. 145-148. (pdf) (ppt) **Link:** Original publication is available at: ieeexplore.ieee.org

2009

[Naf09] Corina Nafornita, "Signals and Systems, vol. 1", Politehnica Publishing House, 2009, ISBN 978-606-554-013-2 (978-606-554-014-9 vol I), published in English. (table of contents) (Errata)

[FirNafBouIsa09] Ioana Firoiu (Adam), Corina Nafornita, Jean-Marc Boucher, Alexandru Isar, Image Denoising Using a New Implementation of the Hyperanalytic Wavelet Transform, IEEE Transactions on Instrumentation and Measurement, WISP special number, August 2009, vol. 58, no. 8, pp. 2410-2416, ISSN 0018-9456, Impact factor 0.978 (pdf)

[NafIsaKov09] Corina Nafornita, Alexandru Isar, Maria Kovaci, "Increasing Watermarking Robustness using Turbo Codes," IEEE International Symposium on Intelligent Signal Processing WISP 2009, Budapest, Hungary, 26-28 August 2009 pp. 113-118, ISBN 978-1-4244-5058-9 (pdf) (ppt)

[NafIsa09] Corina Nafornita, Alexandru Isar, On the Choice of the Mother Wavelet for Perceptual Data Hiding, Proceedings of IEEE International Symposium SCS'09, Iasi, Romania, July 9-10, 2009, ISBN 1-4244-0968-3, pp. 233-236, (pdf) (ppt)

2008

[Naf08] Corina Nafornita, "Culegere de probleme de teoria probabilitatilor şi procese aleatoare", (Problems of probability theory and random processes), online, Timisoara, 2008, published in Romanian. [pdf]

[NafIsa08] Corina Nafornita, Alexandru Isar, Watermarking Based on the Hyperanalytic Wavelet Transform, Acta Technica Napocensis-Electronics and Telecommunications, Vol. 49, nr. 3, pp. 19-26, ISSN 1221-6542 [pdf][ppt]

[NafNafIsaBor08] I. Nafornita, C. Nafornita, A. Isar, M. Borda, Perceptual Watermarks in the Wavelet Domain, Proceedings of Communications 2008 Workshop "New Technologies and Trends in IT and Communications", pp. 19-28, ISBN 978-606-521-008-0 [pdf][ppt]

[NafFirBouIsa08] C. Nafornita, I. Firoiu, J.-M. Boucher, A. Isar, A New Watermarking Method Based on the Use of the Hyperanalytic Wavelet Transform Proc. SPIE Europe: Photonics Europe, vol. 7000: Optical and Digital Image Processing 70000W, pp.70000W-1-70000W-12, ISBN 97808194 71987, Strasbourg, April 25, 2008 [pdf] [ppt]

3.2 Other references

[AbdGlaPan02] Abdulaziz, N.; Glass, A.; Pang, K.K. (2002). Embedding Data in Images Using Turbo-Coding, *6th Symposium on DSP for Communication Systems*, 28-31 Jan. 2002, Univ. of Wollongong, Australia.

[AdaNafBouIsa07] Adam, I.; Nafornita, C.; Boucher, J.-M. & Isar, A. (2007). A New Implementation of the Hyperanalytic Wavelet Transform, *Proc. of IEEE Symposium ISSCS 2007*, Iasi, Romania, ’07, 401-404.

[BalPer01] Balado F. & Perez-Gonzalez, F. (2001). Coding at the Sample Level for Data Hiding: Turbo and Concatenated Codes, *SPIE Security and Watermarking of Multimedia Contents*, San Jose CA, 22-25 Jan. 2001, San Jose CA , USA, 2001, 4314, 532-543.

[BarBarPiv01] Barni, M.; Bartolini, F. & Piva, A (2001). Improved wavelet-based watermarking through pixel-wise masking, *IEEE Trans. Image Processing*, 10, 5, May 2001, 783 – 791.

[BraMagMin96] Braudaway, G.W.; Magerlein, K.A. & Mintzer, F. (1996). Protecting publicly available images with a visible watermark, *Proc. SPIE – Int. Soc.Opt. Eng.*, vol. 2659, pp.126 – 133, 1996.

[Cox05] Cox, I. (2005). Robust watermarking, *ECRYPT Summer School on Multimedia Security*, Salzburg, Austria, Sept. 22, 2005

[CoxKilLeiSha97] Cox, I.; Killian, J.; Leighton, T. & Shamoon, T. (1997). Secure Spread Spectrum Watermarking for Multimedia, *IEEE Trans. Image Processing*, 6, 12, 1997, 1673-1687

[CoxMilBlo02] Cox, I.; Miller, M. & Bloom, J. (2002). *Digital Watermarking*, Morgan Kaufmann Publishers, 2002

[Dau80] Daugman, J. (1980). Two-dimensional spectral analysis of cortical receptive field profiles, *Vision Res.*, 20, ’80, 847-856.

[Gir89] Girod, B. (1989). The information theoretical significance of spatial and temporal masking in video signals, *Proc. SPIE Human Vision, Visual Processing, and Digital Display*, vol. 1077, pp. 178–187, 1989.

[HuaFow02] Hua, L. & Fowler, J. E. (2002). A Performance Analysis of Spread-Spectrum Watermarking Based on Redundant Transforms, *Proc. IEEE Int. Conf. on Multimedia and Expo*, Lausanne, Switzerland, ’02, vol. 2, 553–556.

[Kin00] Kingsbury, N. (2000). A Dual-Tree Complex Wavelet Transform with improved orthogonality and symmetry properties, *Proc. IEEE Conf. on Image Processing*, Vancouver, ’00, paper 1429.

[Kun00] Kundur, D. (2000). Water-filling for Watermarking?, *Proc. IEEE Int. Conf. On Multimedia and Expo*, NY, 1287-1290, Aug. 2000.

[KunHat98] Kundur, D. & Hatzinakos, D. (1998). Digital Watermarking using Multiresolution Wavelet Decomposition, *Proc. IEEE Int. Conf. On Acoustics, Speech and Signal Processing*, Seattle, Washington, Vol. 5, pp. 2969-2972, May 1998.

[KunHat01] Kundur, D. & Hatzinakos, D. (2001). Diversity and Attack Characterization for Improved Robust Watermarking, *IEEE Transactions on Signal Processing*, Vol. 49, No. 10, 2001, pp. 2383-2396.

[LinWuBlo01] Lin, C. Y.; Wu, M.; Bloom, J. A.; Cox, I. J.; Miller, M. L. & Lui, Y. M. (2001). Rotation, Scale, and Translation Resilient Watermarking for Images, *IEEE Trans. On Image Processing*, 10, 5, May 2001

[LooKin00] Loo, P. & Kingsbury, N. (2000). Digital Watermarking Using Complex Wavelets, *ICIP* 2000.

[MouMih02] Moulin, P. & Mihcak M.K. (2002). A Framework for Evaluating the Data-Hiding Capacity of Image Sources, *IEEE Trans. Image Processing*, 11(9), ’02, 1029-1042.

[NafIsaBor05] Nafornita, C.; Isar, A. & Borda, M. (2005). Image Watermarking Based on the Discrete Wavelet Transform Statistical Characteristics, *Proc. IEEE EUROCON* 2005, Serbia & Montenegro, 943-946.

[Naf08] Nafornita, C. (2008). *Contributions to Digital Watermarking of Still Images in the Wavelet Transform*, Ph.D. thesis, Feb. 2008, Technical University of Cluj-Napoca, Romania.

[Naf07a] Nafornita, C. (2007). A New Pixel-Wise Mask for Watermarking, *Proc. of ACM Multimedia and Security Workshop*, 2007, Dallas, TX, USA.

[NafIsaBor06a] Nafornita, C.; Isar, A. & Borda, M. (2006). Pixel-wise masking for watermarking using local standard deviation and wavelet compression, *Scientific Bulletin of the Politehnica Univ. of Timisoara, Trans. on Electronics and Communications*, 51(65), 2, pp. 146-151, ISSN 1583-3380, 2006.

[NafIsaBor06b] Nafornita, C.; Isar, A. & Borda, M. (2006). Improved Pixel-Wise Masking for Image Watermarking, *Multimedia Content Representation, Classification and Security*, September 11-13, 2006, Istanbul, Turkey, Lecture Notes in Computer Science, Springer-Verlag, 2006, pp. 90-97.

[Naf07b] Nafornita, C. (2007). Robustness Evaluation of Perceptual Watermarks, *IEEE Int. Symposium on Signal, Circuits and Systems ISSCS 2007*, 12-13 July 2007, Iasi, Romania.

[NikPit98] Nikolaidis, N. & Pitas, I. (1998). Robust Image Watermarking in the Spatial Domain, *Trans. Signal Processing*, Vol. 66, No. 3, pp. 385-403, 1998.

[RuaPun98] Ó Ruanaidh, J.J.K. & Pun, T. (1998). Rotation, Scale and Translation Invariant Spread Spectrum Digital Image Watermarking, *Signal Processing*, 66(1998), pp. 303-317.

[RuaDowBol96] Ó Ruanaidh, J.J.K; Dowling, W.J.; Boland, F.M. (1996). Phase watermarking of digital images, *Proc. IEEE Int. Conf. Image Processing*, 1996, pp. 239-242.

[PodZen98] Podilchuk, C. & Zeng, W. (1998). Image-Adaptive Watermarking Using Visual Models, *IEEE Journal on Selected Areas in Communications*, 16, 4, May 1998, 525-539

[SerAmbTomWad03] Serdean, C.V.; Ambroze, M.A.; Tomlinson, M. & Wade, J.G. (2003). DWT based high-capacity blind video watermarking, invariant to geometrical attacks, *IEE Proc.-Vis. Image Signal Process.*, 150, 1, Feb. 2003.

[XiaBonArc98] Xia, X.; Boncelet, C. G. & Arce, G. R. (1998). Wavelet Transform Based Watermark for Digital Images, *Optics Express*, Vol. 3, No. 12, 1998, pp. 497-505.

[AngBarMer08] Angela D'Angelo, Mauro Barni, and Neri Merhav, “Stochastic Image Warping for Improved Watermark Desynchronization,” EURASIP Journal on Information Security, vol. 2008, Article ID 345184, 14 pages, 2008.

[AbdGlaPan02] N. Abdulaziz, A. Glass, K.K.Pang, “Embedding Data in Images Using Turbo-Coding”, 6th Symposium on DSP for Communication Systems, 28-31 Jan. 2002, Univ. of Wollongong, Australia.

[SerAmbTomWad03] C.V. Serdean, M.A. Ambroze, M. Tomlinson and J.G. Wade, DWT-based high-capacity blind video watermarking, invariant to geometrical attacks, IEE Proc.-Vis. Image Signal Process., 150, 1, Feb. 2003.

[BalPer01] Felix Balado and Fernando Perez-Gonzalez, Coding at the Sample Level for Data Hiding: Turbo and Concatenated Codes, SPIE Security and Watermarking of Multimedia Contents, San Jose CA, 22-25 Jan. 2001, San Jose CA , USA, 2001, 4314, 532-543.

[Fea92] J. C. Feauveau, "Nonorthogonal Multiresolution Analysis using Wavelets, in Wavelets-A Tutorial in Theory and Applications", C. K. Chui (editor), Academic Press, 153-178, 1992.

[BerGlaThi93] C. Berrou, A. Glavieux, P. Thitimajshima , "Near Shannon limit error-correcting coding and decoding: Turbo-codes", Proc.ICC’93, Geneva, Switzerland, May 1993, 1064 – 1070.

[BerGla96] C. Berrou, A. Glavieux, "Near Optimum Error Correcting Coding and Decoding: Turbo-Codes", IEEE Trans. on Communications, 44, 10, Oct. 1996.

[DouBer05] C. Douillard, C. Berrou, "Turbo Codes With Rate-m/(m+1) Constituent Convolutional Codes", IEEE Trans. on Communications, 53, 10, Oct. 2005, 1630-1638.

[KovBalNaf06] M. Kovaci, H. Balta, M. Nafornita, "Performance of Multi Binary Turbo Codes on Rayleigh Flat Fading Transmission Channels", Annals of University from Oradea, Romania, Sect. Electronic, 2006, 64-67.

[Cro00] S. Crozier, "New High-Spread High-Distance Interleavers for Turbo-Codes", 20th Biennial Symposium on Communications, Kingston, Ontario, Canada, May 28-31, 2000, 3-7.

[DolDiv95] S. Dolinar, D. Divsalar, "Weight Distributions for Turbo Codes Using Random and Nonrandom Permutations", The Telecommunications and Data Acquisition Progress Report, TDA PR 42-122, Aug. 1995, pp. 56-65.

[KovBalNaf05] M. Kovaci, H. Balta, M. Nafornita, "The Performance of Interleavers used in Turbo Codes", Proc. Int. Symp. Signals, Circuits and Systems, ISSCS 2005, Iasi, July, 14-15, 2005, 363-366.

[VogFin00] J. Vogt, A. Finger, "Improving the Max-Log-MAP Turbo Decoder", Electron. Lett., 36, 23, 1937–1939, Nov. 2000.

[KovBalBayNaf07] M. Kovaci, H. Balta, A. De Baynast, M. Nafornita, "Performance Comparison of Punctured Turbo Codes and Multi Binary Turbo Codes", Proc. International Symposium on Signal, Circuits and Systems, ISSCS 2007, Iasi, Romania, July, 12-13, 2007, 485-488.

[USC09] USC-SIPI image database, http://sipi.usc.edu/database/

[Pic09] Pablo Picasso, Portrait of Igor Stravinsky, http://abcgallery.com/P/picasso/picasso25.html

[UnsBlu03] M. Unser, T. Blu, “Mathematical Properties of the JPEG2000 Wavelet Filters”, IEEE Trans. Image Processing, 12, 9, Sept. 2003, 1080-1090.

[GroMor84] A. Grossman and J. Morlet, “Decomposition of Hardy functions into square integrable wavelets of constant shape”, SIAM J. Math. Anal., vol. 15, ‘84, 723–736.

[BarNas04] S. Barber and G. P. Nason, “Real nonparametric regression using complex wavelets”, J. Roy. Stat. Soc. B, vol. 66, ’04, 927–939.

[Sel02] I. W. Selesnick, “The design of approximate Hilbert transform pairs of wavelet bases”, IEEE Trans. on Sig. Proc., vol. 50, ’02, 1144–1152.

[Sel01] I. W. Selesnick, “Hilbert transform pairs of wavelet bases”, IEEE Sig. Proc. Let., vol. 8, ’01, 170–173.

[LinMay95] J.-M. Lina and M. Mayrand, “Complex daubechies wavelets”, Appl. Comput. Harm. Anal., vol. 2, ‘95, 219–229.

[OlhMet06] S. C. Olhede and G. Metikas, “The Hyperanalytic Wavelet Transform”, Imperial College Statistics Section Technical Report TR-06-02, May, ‘06.

[LanGuoOdeBur96] M. Lang, H. Guo, J. E. Odegard, C. S. Burrus and R. O. Wells Jr., “Noise reduction using an undecimated discrete wavelet transform”, IEEE Sig. Proc. Let., vol.3, no.1, ‘96, 10-12.

[Abr94] P. Abry, "Transformées en ondelettes-Analyses multirésolution et signaux de pression en turbulence", Ph .D .dissertation, Université Claude Bernard, Lyon, France, ‘94.

[Hig84] J. R. Higgins, “Bases for the Hilbert space of Paley-Wiener functions”, Proceedings of Aachener Colloquium, ‘84, 274-278.

[Isa93] A. Isar, “ Nouvelles modalités de décomposition multiresolution des signaux à energie finie ”, Quatorzieme colloque GRETSI, Juan-les-Pins, France, ‘93, 93-97.

[FerSpaBur00] Felix C. A. Fernandes, Rutter L.C. van Spaendonck and C. Sidney Burrus “A New Framework for Complex Wavelet Transforms”, IEEE Trans. on Sig. Proc., vol. 51, no. 7, ‘00, 1825–1837 .

[SimFreAdeHee92] E. P. Simoncelli, W. T. Freeman, E. H. Adelson and D. J. Heeger, “Shiftable multi-scale transforms”, IEEE Trans. on Info. Th., vol. 38, ‘92, 587 – 607.

[AdaNafBouIsa07b] I. Adam, C. Nafornita, J.-M. Boucher and A. Isar, “A Bayesian Approach of Hyperanalytic Wavelet Transform Based Denoising”, Proc. IEEE Int. Conf. WISP’07, Alcala de Henares, Spain, October, ‘07, 237-242.

[FoiKatEgi07] Foi, A., V. Katkovnik and K. Egiazarian, “Pointwise Shape-Adaptive DCT for High-Quality Denoising and Deblocking of Grayscale and Color Images”, IEEE Trans. Image Proc., (5), ’07, 1395-1411.

[WalDat00] M. Walessa and M. Datcu, “Model-Based Despeckling and Information Extraction from SAR Images”, IEEE Trans. Geo. Rem. Sens., vol. 38, no. 5, ‘00, 2258- 2269.

[Shu05] P.-L. Shui, “Image Denoising Algorithm via Doubly Local Wiener Filtering With Directional Windows in Wavelet Domain”, IEEE Sig. Proc. Let., Vol. 12, No. 6, '05, 681-684.

[ZhoShu07] Z.-F. Zhou and P.-L. Shui, Contourlet-based image denoising algorithm using directional windows, Elect. Let., vol 43, no.2, ‘07.

[Olh06] S. C. Olhede, “Hyperanalytic Denoising”, Imperial College Statistics Section Technical Report TR-06-01 1, Department of Mathematics, Imperial College London, SW7 2AZ UK.

[AubAuj08] Gilles Aubert and Jean-François Aujol, “Variational Approach to remove Multiplicative Noise,” SIAM Journal on Applied Mathematics, volume 68, number 4, pages 925-946, January 2008.

[DenTupDarSig09] L. Denis, F. Tupin, J. Darbon and M. Sigelle. “SAR Image Regularization with Fast Approximate Discrete Minimization, ” IEEE Transactions on Image Processing, vol. 18, no. 7, July 2009, 1588-1600.

[AntFan96] Anestis Antoniadis and Jianqing Fan, "Regularization of Wavelet Approximations," Journal of the American Statistical Association, September 2001, Vol. 96, No. 455, pp. 939-967.

[IsaMogIsa09] Isar A., Moga S., Isar D., "A New Denoising System for SONAR Images," EURASIP Journal on Image and Video Processing, Hindawi Publishing Corporation, Volume 2009 (2009), Article ID 173841.

[ArgBiaAlp06] Argenti F, Bianchi T, Alparone L. "Multiresolution MAP despeckling of SAR images based on locally adaptive generalized Gaussian pdf modeling," IEEE Trans Image Process. 2006 Nov; 15(11): 3385-99.

[LajHus09] Lajevardi, S.M., Hussain, Z. M., Feature Extraction for Facial Expression Recognition based on Hybrid Face Regions, Advances in Electrical and Computer Engineering Journal, no. 3, pp. 63 – 67, 2009.

[WanCanAch09] Wan T., Canagarajah N., Achim A., „Segmentation-Driven Image Fusion Based on Alpha-Stable Modeling of Wavelet Coefficients," IEEE Transactions on Multimedia, vol. 11, no. 4, pp. 624-633, June 2009.

[ArgBiaScaAlp09] Argenti F., Bianchi T., di Scarfizzi G.M., Alparone L. (2009), LMMSE and MAP Estimators for Reduction of Multiplicative Noise in the Nonsubsampled Contourlet Domain, *Signal Processing*, vol. 89, no. 10, Oct. 2009, pp. 1891—1901, ISSN 0165-1684.

[Bua07] Buades A. (2007), *Image and film denoising by non-local means*, Ph. D. Thesis, Universitat de les Iles Baleares.

[FroStiShaHol82] Frost V. S., Stiles J. A., Shanmugan J. A. and Holtzman J. C. (1982), A Model for Radar Images and Its Application to Adaptive Digital Filtering of Multiplicative Noise, *IEEE Transactions on Pattern Analysis and Machine Intelligence*, Vol. PAMI-4, No. 2, March 1982, pp. 157 - 166 , ISSN 0162-8828.

[HolKroMor89] Holschneider M., Kronland-Martinet R., Morlet J. and Tchamitchian P. (1989), Wavelets. Time-frequency Methods and Phase Space, chapter *A Real-Time Algorithm for Signal Analysis with the Help of the Wavelet Transform*, pages 289–297, Springer-Verlag, ISBN-10: 3540530142, Berlin, Germany.

[JalBlaZer03] Jalobeanu A., Blanc-Féraud L. and Zerubia J., (2003), Natural image modeling using complex wavelets". In *Proc. of SPIE, Wavelets X*, Volume: 5207, 2003, pp. 480-494, ISBN: 9780819450807.

[KatEgiAst06] Katkovnik V., Egiazarian K. and Astola J. (2006), *Local Approximation Techniques in Signal and Image Processing*, SPIE Press, ISBN 0-8194-6092-3, Bellingham, Washington, USA.

[Kin98] Kingsbury N. G. (1998), "The dual-tree complex wavelet transform: a new efficient tool for image restoration and enhancement". In *Proc. European Signal Processing Conference, EUSIPCO 98*, Rhodes, pp. 319–322, ISBN 960-7620-05-4.

[KuaSawStr87] Kuan D. T., Sawchuk A. A. and Strand T. C., (1987), Adaptive restoration of images with speckle, *IEEE Trans. ASSP*, Vol. 35, No. 3, Mars 1987, pp. 373-383, ISSN**:** 00963518.

[Lee81] Lee J. S., (1981), "Speckle Analysis and Smoothing of Synthetic Aperture Radar Images", *Computer Graphics and Image Processing*, Vol. 17, no.1, September, 1981, pp. 24-32, ISSN: 0146-664X.

[Lur02] Lurton X., (2002), *An Introduction to Underwater Acoustics, Principles and Applications.* Springer, ISBN 3-540-42967-0, Chichester, UK.

[Sel08b] Selesnick I. W., (2008), "The Estimation of Laplace Random Vector in AWGN and the Generalized Incomplete Gamma Function", *IEEE Trans. on Signal Processing,* vol. 56, no. 8, August 2008, pp. 3482-3496, ISSN**:** 1053-587X .

[CohRazMal97] I. Cohen, S. Raz and D. Malah, “Orthonormal shift-invariant wavelet packet decomposition and representation”, Signal Processing, Elsevier, 57(3), 251-270, ‘97.

[PesKriCar96] J.C. Pesquet, H. Krim, H. Carfantan, “Time-invariant orthonormal wavelet representations”, IEEE Trans. Sig. Proc., 44, 1964-1970, ’96.

[BaySel08] I. Bayram and I. W. Selesnick, “On the Dual-Tree Complex Wavelet Packet and M-Band Transforms”, IEEE Trans. Signal Processing, 56(6) : 2298-2310, ‘08.

[AndKinFau05] R. Anderson, N. Kingsbury, J. Fauqueur, ”Determining Multiscale Image Feature Angles from Complex Wavelet Phases”, Proc. International Conference on Image Analysis and Recognition (ICIAR), Toronto, ‘05.

[KarFabBou08] I. Karaoui, R. Fablet, J.-M. Boucher, W. Pieczynski, J. M. Augustin, “Fusion of textural statistics using a similarity measure: application to texture recognition and segmentation”, Pattern Anal. Applic., 11, 425-434, ‘08.

[StaFadMur07] J.-L. Starck, J. Fadili, F. Murtagh, “The undecimated wavelet decomposition and its reconstruction”, IEEE Transactions on Image Processing, volume 16, Issue 2, 2007, 297-309.

[VanCor99] M. Vannucci and F. Corradi, “Covariance structure of wavelet coefficients: theory and models in a Bayesian perspective”, J. R. Statist. Soc. B, 61, Part 4, 1999, 971-986.

[CraPer05] P. F. Craigmile, D.B. Percival, “Asymptotic decorrelation of between-scale wavelet coefficients”, IEEE Trans. Inform.Theory 51 (3), March 2005, 1039–1048.

[AttPasIsa07] A. M. Atto, D. Pastor, A. Isar, “On the Statistical Decorrelation of the Within-scale Wavelet Packet Coefficients of a Band-Limited Wide-Sense Stationary Random Process”, Signal Processing, 87, Elsevier, 2007, 2330-2335.

[LiuMou01] J. Liu, J., P. Moulin, “Information-theoretic analysis of interscale and intrascale dependencies between image wavelet coefficients”, IEEE Trans. Image Process., 2001, 10, (11), 1647–1658.

[FouBenBou01] S. Foucher, G. B. Bénié, J. M. Boucher: “Multiscale MAP filtering of SAR images”. IEEE Transactions on Image Processing 10, (1), 2001, 49-60.

[ChaPesDuv07] C. Chaux, J.-C. Pesquet, L. Duval, “Noise Covariance Properties in Dual-Tree Wavelet Decompositions”, IEEE Transactions on Information Theory, vol. 53, no. 12, Dec. 2007, 4680-4700.

[Nas02] G. P. Nason, “Choice of wavelet smoothness, primary resolution and threshold in wavelet shrinkage”, Statistics and Computing, 12, 2002, 219-227.

[Dau92] I. Daubechies, “Ten Lectures on Wavelets”, Society for Industrial and Applied Mathematics, 1992.

[BluLui07] T. Blu and F. Luisier, “The SURE-LET approach to image denoising”, IEEE Trans. Image Process., vol. 16, no. 11, Nov. 2007, 2778–2786 .

[Pes99] B. Pesquet-Popescu, “Statistical Properties of the Wavelet Decomposition of Some Non-Gaussian Self-Similar Processes”, invited paper, Signal Processing, No. 75, 1999, 303-322.

[AttBer12] A. M. Atto and Y. Berthoumieu, “Wavelet transforms of non-stationary random processes: Contributing factors for stationarity and decorrelation,” IEEE Transactions on Information Theory, vol. 58, no. 1, January 2012, 317-330.

[GleDat06] D. Gleich, M. Datcu, “Gauss-Markov Model for Wavelet-Based SAR Image Despeckling”, IEEE Signal Processing Letters, vol. 13, no. 6, June 2006, 365-368.

[LuiBluUns07] F. Luisier, T. Blu, M. Unser, “A New SURE Approach to Image Denoising: Interscale Orthonormal Wavelet Thresholding, IEEE Transactions on Image Processing, vol. 16, no. 3, March 2007, 593-605.

[LuiBluUns11] F. Luisier, T. Blu, M. Unser, “Image Denoising in Mixed Poisson-Gaussian Noise”, IEEE Transactions on Image Processing, vol. 20, no. 3, March 2011, 696-709.

[LuiBluWol12] F. Luisier, T. Blu, P. J. Wolfe, “A CURE for Noisy Magnetic Resonance Images: Chi-Square Unbiased Risk Estimation”, IEEE Transactions on Image Processing, vol. 21, no. 8, August 2012, 3454-3466.

[PizPhi06] A. Pizurica and W. Philips, “Estimating the probability of the presence of a signal of interest in multiresolution single- and multiband image denoising,” IEEE Trans. Image Process., vol. 15, no. 3, Mar. 2006, 654-665.

[PorStrWaiSim03] J. Portilla, V. Strela, M. J. Wainwright, and E. P. Simoncelli, “Image denoising using scale mixtures of gaussians in the wavelet domain”, IEEE Trans. Image Process., vol. 12, no. 11, Nov. 2003, 1338–1351.

[ChaDuvBenPes08] C. Chaux, L. Duval, A. Benazza-Benyahia, and J.-C. Pesquet, “A Non-linear Stein-based estimator for multichannel image denoising,” IEEE Trans. Signal Process., vol. 56, no. 8, Aug. 2008, 3855-3870.

[AchKur05] A. Achim and E. E. Kuruoglu, “Image Denoising Using Bivariate α-Stable Distributions in the Complex Wavelet Domain”, IEEE Sig. Proc. Let., 12(1), ’05, 17-20.

[MilKin08] M. A. Miller and N. G. Kingsbury, “Image modelling using interscale phase properties of complex wavelet coefficients”, IEEE Transactions on Image Processing, 17, No. 9, September 2008, 1491-1499.

[ChaDuvPes06] C. Chaux, L. Duval, and J.-C. Pesquet, “Image analysis using a dual-tree M-band wavelet transform”, IEEE Trans. on Image Proc., vol. 15, no. 8, Aug. 2006, 2397–2412.

[KulLei51] S. Kullback and R.A. Leibler, “On Information and Sufficiency”, Annals of Mathematical Statistics, 22 (1), pp. 79–86, 1951.

[DoVet02] M. N. Do and M. Vetterli, “Wavelet-based texture retrieval using generalized Gaussian density and Kullback-Leibler distance”, IEEE Trans. Image Processing, vol. 11, pp. 146-158, Feb. 2002.

[NovAdaRoy10] M. Novey, T. Adali, and A. Roy, “A complex generalized Gaussian distribution-Characterization, generation, and estimation”, IEEE Trans. Signal Processing, vol. 58, no. 3, part. 1, pp. 1427-1433, March 2010.

[VerBacSch08] G. Verdoolaege, S. De Backer, P. Scheunders, “Multiscale colour texture retrieval using the geodesic distance between multivariate generalized Gaussian models”, ICIP'2008, pp.169-172.

[VisTex02] MIT Vision and modeling group, Vision texture, Available online: http://vismod.media.mit.edu/vismod/

[MatSkaBr02] J. Mathiassen, A. Skavhaug, and K. Bř, “Texture dissimilarity measure using Kullback-Leibler divergence between gamma distributions,” Computer Vision—ECCV, 2002.

[WouSchDyc99] G. Van de Wouver, P. Scheunders, and D. Van Dyck, “Statistical texture characterization from discrete wavelet representations,” Image Processing, IEEE Transactions on, 1999.

[KwiUhl08] R. Kwitt, and A. Uhl, “Image similarity measurement by Kullback- Leibler divergences between complex wavelet divergences between complex wavelet subband statistics for texture retrieval,” Image Processing, IEEE International Conference on, 2008.

[MalHasLasBer10] A.D.E. Maliani, M.E. Hassouni, N.-E. Lasmar, and Y. Berthoumieu, “Texture classification based on the Generalized Gamma distribution and the Dual Tree Complex Wavelet Transform,” I/V Communications and Mobile Network, International Symposium on, 2010.

[LasBer10] N.-E. Lasmar and Y. Berthoumieu, “Multivariate statistical modeling for texture analysis wavelet transforms,” Acoustics Speech and Signal Processing, IEEE International Conference on, 2010.

[HuZha09] Y. Hu, and C.-X. Zhao, “Unsupervised texture Classification by Combining Multi-Scale Features and K-Means Classifier,” Pattern Recognition, Chinese Conference on, 2009.

[ChoTon07] S.-K. Choy and C.-S. Tong, “Supervised texture classification using characteristic generalized gaussian density,” Journal of Mathematical Imaging and Vision, 2007.

[ComPes09] P. L. Combettes and J.-C. Pesquet, “Proximal splitting methods in signal processing,” Fixed-Point Algorithms for Inverse Problems, Springer, 2009.

[AmaNag07] S. Amari and H. Nagaoka, Methods of information geometry, Amer Mathematical Society, 2007.

[AmaDou98] S. Amari and S. C. Douglas, “Why natural gradient?,” Acoustics, Speech and Signal Processing, 1998 IEEE International Conference on, 1998.

[Pel90] E. Peli, “Contrast in complex images, ” J. Opt. Soc. Amer., A7, (10), (1990), 2032–2040, http://dx.doi.org/10.1364/JOSAA.7.002032.

[BegNeg89] A. Beghdadi, A. Le Negrate, “Contrast enhancement technique based on local detection of edges,” Comput. Vis. Graph. Image Process., 46, (2), (1989), 162–174.

[GonWoo08] R.C. Gonzalez and R.E. Woods, Digital Image Processing, Addison–Wesley Longman Publishing Co., Inc., Boston, MA, USA, 2008.

[PizJohEriYanMul90] S.M. Pizer, R. E. Johnston, J. P. Ericksen, B.C. Yankaskas and K.E. Muller, “Contrast-Limited Adaptive Histogram Equalization: Speed and Effectiveness,” Proc.first conference on Visualization in Biomedical Computing, 22-25 May, 1990, Atlanta, GA, 337-345.

[PisZonHem98] E. D. Pisano, S. Zong, B. M. Hemminger, M. De Luca, R. E. Johnston, K. E. Muller, M. P. Braeuning and S. M. Pizer, “Contrast limited adaptive histogram equalization image processing to improve the detection of simulated spiculations in dense mammograms,” J. Digit. Imaging 11, (4), (1998), 193–200.

[TsaYeh08] C.-M. Tsai and Z.-M. Yeh, “Contrast Enhancement by Automatic and Parameter-Free Piecewise Linear Transformation for Color Images,” IEEE Trans.Consumer Electronics, vol. 54, Issue 2, May 2008, 213-219.

[Zha10] Yong Zhao, “A Linear Programming Approach for Optimal Contrast-Tone Mapping,” PhD. Thesis, McMaster University, October 2010.

[LozBulHilAch13] A. Loza, D.R. Bull, P.R. Hill and A.M. Achim, “Automatic contrast enhancement of low-light images based on local statistics of wavelet coefficients,” Digital Signal Processing, 23, 2013, 1856–1866.

[Kin99] N. G. Kingsbury, “Image processing with complex wavelets,” Philos. Trans. R. Soc. Lond. Ser. A Math. Phys. Eng. Sci. 357, (1999), 2543–2560.

[Sel08] I.W. Selesnick. The estimation of spherically-contoured Laplace random vectors in additive white Gaussian noise. IEEE Trans. Signal Processing, 56(8):3482-3496, Aug. 2008.

[SenSel02] L. Sendur and I.W. Selesnick, “Bivariate shrinkage functions for wavelet-based denoising exploiting interscale dependency”, IEEE Trans. on Signal Processing, 50(11), ’02, 2744-2756.

[CoiDon95] R. Coifman, D. Donoho, Translation-invariant wavelet denoising, in: A. Antoniadis, G. Oppenheim (Eds.), Wavelet and Statistics, in: Lecture Notes in Statist., vol.103, Springer-Verlag, 1995, pp. 125–150.

[Deb14] P. Debevec, HDR Memorial source images, available at http://projects.ict.usc.edu/graphics/HDRShop

[Dul14] Aram Dulyan, Shutter speed in Greenwich, available at http://commons.wikimedia.org/wiki/File:Shutter_speed_in_Greenwich_(no_caption).jpg

[Rio93] O. Rioul, “Ondelettes régulières : application à la compression d'images fixes”, PhD thesis, ENST, Télécom Paris, Mar. 1993.

[AbrVei98] P. Abry, D. Veitch, “Wavelet Analysis of Long Range Dependent Traffic”, IEEE Trans. Info. Theory, vol. 44 (1), 1998, 2-15.

[VidNicGar07] B. Vidakovic, O. Nicolis, C. Garutti, “2-d Wavelet-based Spectra with Applications in Analysis of Geophysical Images”, ASA Joint Statistical Meetings, 2007.

[FirIsaBouIsa09] I. Firoiu, D. Isar, J.-M. Boucher, A. Isar, “Hyperanalytic Wavelet Packets”, Proc. WISP’09, Budapest, Hungary, 67-72.

[Kin01] N. G. Kingsbury, “Complex wavelets for shift-invariant analysis and filtering of signals”, J. of Appl. And Comp. Harm. Analysis, 10(3), May 2001, 234-253.

[Dav14] C. Davenport, “Commutative Hypercomplex Mathematics”, available online at http://home.comcast.net/~cmdaven/hyprcplx.htm last accessed November 25, 2014

[NelKin10a] J. D. B. Nelson and N. G. Kingsbury, “Fractal dimension based sand ripple suppression for mine hunting with sidescan sonar,” Int. Conf. Synthetic Aperture Sonar and Synthetic Aperture Radar, 2010.

[EchLev08] A. Echelard, J. Levy Vehel, “Wavelet denoising based on local regularity information,” European Signal Processing Program, 2008.

[VidKatAlb00] B. D. Vidakovic, G. G. Katul, J. D. Albertson, “Multiscale denoising of self-similar processes,” Journal Geophysical Research, 105, D22, 27049–27058, 2000.

[AbrGonLev09] P. Abry, P. Goncalves, J. Levy Vehel, Scaling Fractals and wavelets, Wiley, 2009.

[TibTay10] R. J. Tibshirani, J. Taylor, “The solution path of the generalised Lasso,” Annals of Statistics, 39, 3, 1335–1371, 2010.

[NelKin10b] J. D. B. Nelson, N. G. Kingsbury, “Dual-tree wavelets for estimation of locally varying and anisotropic fractal dimension,” IEEE Int. Conf. Image Processing, 341–344, 2010.

[SelBarKin05] I. W. Selesnick, R. G. Baraniuk, N. G. Kingsbury, “The dual-tree complex wavelet transform,” IEEE Signal Processing Magazine, 22, 6, 123–151, 2005.

[KapKuo96] L. M. Kaplan and C. C. J. Kuo, “An improved method for 2-d self-similar image synthesis,” IEEE Trans.Image Processing, 5, 5, 754–761, 1996.

[Frac14] Inria Saclay/Ecole Centrale de Paris Regularity Team, “Fraclab Toolbox,” http://fraclab.saclay.inria.fr, 2014.

[EhaSasMor94] N. Ehara, I. Sasase, S. Mori, “Weak radar detection based on wavelet transform”, IEEE International Conference on Acoustics, Speech and Signal Processing, vol. 2, 377-380, 19-22 Apr. 1994.

[DonJoh98] D.L. Donoho, I.M. Johnstone, “Minimax estimation via wavelet shrinkage”, Annals of Statistics, vol. 26, No. 3, 879-921, June 1998.

[Mal99] S. Mallat, A Wavelet Tour of Signal Processing, Second edition, Academic Press, 1999.

[DonJoh94] D.L. Donoho, I.M. Johnstone, “Ideal spatial adaptation by wavelet shrinkage”, Biometrika, vol. 81, no. 3, 425-455, September 1994.

[Don95] D.L. Donoho, “De-noising by soft-thresholding”, IEEE Transactions on Information Theory, vol. 41 , no. 3, 613 – 627, May 1995.

[DonJohKerPic95] D.L. Donoho, I.M. Johnstone, G. Kerkyacharian, D. Picard, “Wavelet shrinkage. Asymptopia”, J. Roy. Statist. Soc., vol. 57, 301—369, 1995.

[Roh12] H. Rohling, “Radartechnik und signalverarbeitung”, Technische Universität Hamburg-Harburg, 2012.

[Gal93] G. Galati – Editor, Advanced Radar Techniques and Systems, Peter Peregrinus Ltd., 1993.

[Sko90] M.I. Skolnik, Radar Handbook, 2nd edition, McGraw-Hill, 1990.

[GinMaiPat12] F. Gini, A. De Maio, L. Patton, Waveform Design and Diversity for Advanced Radar Systems, London, United Kingdom, 2012, p. 173 – 205.

[Roh10] H. Rohling, “Milestones in Radar and the Success Story of Automotive Radar Systems”, *Proceedings of the International Radar Symposium*, Vilnius, Lithuania, 2010.

[RohMei01] H. Rohling, M.-M. Meinecke, “Waveform design principles for automotive radar systems”, *Proceedings of the CIE International Conference on Radar*, pp. 1-4, Beijing, China, 2001.

[FolRohLub05] F. Folster, H. Rohling, U. Lubbert, “An automotive radar network based on 77GHz FMCW sensors”, *IEEE International Radar Conference*, Arlington, VA, USA, 2005.

[PouFegSch08] K. Pourvoyeur, R. Feger, S. Schuster, A. Stelzer, L. Maurer, “Ramp Sequence Analysis to Resolve Multi Target Scenarios for a 77-GHz FMCW Radar Sensor”, *11th International Conference on Information Fusion*, Cologne, Germany, 2008.

[Roh14] H. Rohling et al., “The ARTRAC Architecture”, http://artrac.org/file.php/ARTRAC_Architecture.pdf-2012-10-16, last accessed on 19.06.2014.

[HlaEde92] F. Hlawatsch, G. S. Edelson, “The ambiguity function of a linear signal space and its application to Maximum-Likelihood range/Doppler estimation”, *Proceedings of the IEEE-SP International Symposium, Time-Frequency and Time-Scale Analysis*, Victoria, BC, USA, 1992.

[IsaCubNaf02] A. Isar, A. Cubitchi, M. Nafornita, Algorithmes et techniques de compression, Orizonturi universitare, 2002.